UNIVERSITY OF MARIBOR
FACULTY OF MECHANICAL ENGINEERING

Doctoral Dissertation

INFLUENCE OF MICRODEFECT ON FATIGUE PROPERTIES IN WELD FINE GRAIN HEAT AFFECTED ZONE ON NICKEL MOLYBDENUM ALLOY STEEL

September, 2023

Fidan SMAILI

UNIVERSITY OF MARIBOR
FACULTY OF MECHANICAL ENGINEERING

Doctoral dissertation

INFLUENCE OF MICRODEFECT ON FATIGUE PROPERTIES IN WELD FINE GRAIN HEAT AFFECTED ZONE ON NICKEL MOLYBDENUM ALLOY STEEL

Doktorska disertacija

VPLIV MIKRONAPAKE NA LASTNOSTI PRI UTRUJANJU FINOZRNATEGA TOPLOTNO VPLIVANEGA PODROČJA V VARU NA NIKELJ MOLIBDENOVEM JEKLU

September, 2023

Author: Fidan SMAILI, Msc. of Mech. Eng. Sci.

Supervisor: Assist. Prof. Dr. Tomaž VUHERER, IWE, IWI

UDC: 620.178.3:621.791.053(043.3)

ACKNOWLEDGEMENTS

This thesis reports the research work carried out at the Institute of Welding, Department of Mechanical Engineering, at the University of Maribor.

Firstly, I would like to express my gratitude to my supervisor Assist. Prof. Dr. Tomaž VUHERER for his continuous guidance and support throughout my PhD study, for his patience, motivation, enthusiasm and for his great personality. The knowledge and inspirations from him will benefit my whole life.

My sincere thanks go also to Assist. Prof. Dr. Gorazd LOJEN and Assoc. Prof. Jožef PREDAN for their valuable inputs and insightful suggestions to the research project.

I thank my colleagues and friends in the Institute of Welding, Department of Mechanical Engineering, for the meaningful discussions, friendship and encouragements.

My appreciation also goes to the lab staff in the Institute of Welding Laboratory, Viljem Šprah and Uroš Orožim, for their kind assistance in the experimental work.

I would like to acknowledge the Research Scholarship provided by the University of Maribor and the Public Scholarship, Development, Disability and Maintenance Fund of the Republic of Slovenia.

Above all, my family, especially my mother and brothers, who have given me unending support and love, for which my mere expressions of thanks will never suffice.

VPLIV MIKRONAPAKE NA LASTNOSTI PRI UTRUJANJU FINOZRNATEGA TOPLOTNO VPLIVANEGA PODROČJA V VARU NA NIKELJ MOLIBDENOVEM JEKLU

Ključne besede: zvarni spoj, drobnozrnato toplotno vplivano področje, mehanske lastnosti, širjenje utrujenostne razpoke

POVZETEK

V doktorski disertaciji so predstavljeni rezultati raziskave mehanskih lastnosti drobnozrnate mikrostrukture toplotno vplivanega področja (TVP) na zvarnem spoju. Namen tega eksperimentalnega dela je bil ugotoviti vpliv mikronapak na trdnost pri utrujanju drobnozrnate mikrostrukture TVP na zvarnem spoju (zlasti na trajno dinamično trdnost). Da bi razložili ta pojav, je to delo razdeljeno na devet različnih poglavij:

1. *Uvod,*
2. *Pregled literature,*
3. *Raziskovalna metodologija,*
4. *Problem utrujanja zvarnih spojev,*
5. *Mikronapaka na FZ TVP zvarnem spoju,*
6. *Eksperimentalni rezultati,*
7. *Razprava,*
8. *Zaključki,*
9. *Literatura.*

V prvem poglavju te disertacije so predstavljeni: problem, cilji raziskave in hipoteze. Poznavanje lastnosti fino zrnatega toplotno vplivanega področja (FZ TVP) pri utrujanju na zvarnega spoja nas vodi k doseganju ciljev te raziskave.

Glavni raziskovalni cilji te raziskave so naslednji:

- *raziskati in analizirati FZ TVP na zvaru,*
- *raziskati vpliv prisotnosti mikronapake na dobo trajanja pri utrujanju,*
- *opazovati obnašanje in določiti lastnosti pri utrujanju FZ TVP na zvaru,*

- *določiti prag za širjenje utrujenostnih razpok v FZ TVP na zvaru,*
- *Določiti lomno žilavost v FZ TVP na zvaru;*
- *Določiti splošne mehanske lastnosti FZ TVP z namenom povečanja zanesljivosti zvarnih spojev, zlasti na varjenih konstrukcijah.*

Za dosego teh raziskovalnih ciljev so predstavljene tri hipoteze, ki jih je treba potrditi ali zavrniti. Te hipoteze so:

- *S fizikalno majhno napako v mikrostrukturi FZ TVP je mogoče raziskati vpliv širjenja začetne razpoke na utrujanje.*
- *Z uporabo modificiranega Chappetijevega modela bo mogoče pojasniti pojav začetnega širjenja razpoke skozi različne mikrostrukture (od FZ TVP do GZ TVP).*
- *Obstoj zaostalih napetosti v bližini mikronapake ima pomembno vlogo pri obnašanju razpoke v FZ TVP.*

Ločena obravnava samo enega dela TVP lahko privede do napak pri ocenjevanju celovitosti konstrukcij, medtem ko bi bila lahko določitev lastnosti pri utrujanju in lomne žilavosti v takem primeru precenjena ali podcenjena na zvarnih spojih. To je poseben izziv, ki doslej še ni bil v celoti raziskan. Razlog za to je, da ima TVP različne dele, kot so: grobozrnata TVP, drobnozrnata TVP, medkritična TVP in pregreta TVP zvara. Ta heterogenost TVP vodi tudi do različnih mehanskih lastnosti in vpliva na razvoj napetostnega polja na konici razpoke, zato gonilna sila za razvoj razpoke ni enaka za vsako pod področje. Da bi se spopadli s tem izzivom, smo podrobno preučili pristop k načinu utrujanja in mehaniki loma TVP zvarnega spoja, kot je opisano v pregledu literature oziroma v poglavju 2 te disertacije.

V metodologiji raziskave, predstavljeni v poglavju 3 tega dela, so bile podrobno opisane uporabljene eksperimentalne in numerične metode. Začetek tega poglavja se začne s predstavitvijo osnovnega materiala, realnega zvara in predstavitvijo metod toplotnih obdelav za pripravo mikrostrukture FZ TVP kot je prisotna v realnem zvaru. V tej raziskavi so bili vzorci z FZ TVP najprej simulirani z dvema različnima simulacijskima metodama, najprej z uporabo:

- *Avstenitizacije v laboratorijski peči, ki ji sledi kaljenje z vodo (AF+WQ) in*
- *Simulatorja toplotnega cikla varjenja (WTCS)*

Uporabljena sta bila simulator termičnega cikla varjenja Smithweld 1405 in laboratorijska peč Bosio EUP-K 20/1200. Cilj je bil doseči enako $\Delta t_{8/5}$ *in enako martenzitno mikrostrukturo FZ TVP, kot je bila opažena v FG TVP na realnem zvaru, kjer je bila povprečna velikost zrn približno 10* μ*m.*

Da bi potrdili enako FZ TVP mikrostrukturo kot v realnem zvaru, smo simulirane FZ TVP primerjali z realno mikrostrukturo na zvaru. Pri realnem zvaru je bil narejen enojni sočelni V-zvar na 15 mm debeli predgreti jekleni pločevini iz jekla 17CrNiMo6. Namen je bil, da se ustvari referenčna mikrostruktura. Parametri varjenja so bili določeni glede na želeni čas ohlajanja $\Delta t_{8/5}$ *= 10 s in v skladu s standardom SIST EN 1011-2, priloga D6, za dvodimenzionalno odvajanje toplote. Med varjenjem se je čas ohlajanja* $\Delta t_{8/5}$ *meril z vnaprej nameščenimi termoelementi.*

Po drugi strani je bila za vzorce AF+WQ izbrana najvišja temperatura, ki je nekoliko nižja kot pri vzorcih WTCS, da bi dosegli enako velikost zrn v obeh vrstah vzorcev, vendar še vedno dovolj nad A_{C3}*, da bi zagotovili homogeno transformacijo v avstenit. V peči so namreč vzorci izpostavljeni visokim temperaturam dlje kot v pravem zvaru ali v simulatorju termičnega cikla, saj se počasneje segrevajo, zato je za zagotovitev homogene mikrostrukture po celotnem prerezu potreben določen čas zadrževanja na tej temperaturi. V ta namen je morala biti temperatura nižja kot pri resničnem varjenju, da se prepreči prekomerna rast kristalnih zrn. S predhodnimi poskusi je bilo ugotovljeno, da je v peči, segreti na 870 °C, v 45 minutah (5 minut za segrevanje + 10 minut zadrževanja) mogoče doseči enako velikost avstenitnih zrn kot pri pravem termičnem ciklu varjenja.*

V obeh primerih, WTCS in AF+WQ, je bila hitrost hlajenja nadzorovana s termoelementi, ki so bili privarjenimi na vzorce. Medtem ko je bilo na simulatorju enostavno zagotoviti želeno $\Delta t_{8/5}$ *= 10 s, kjer želeno krivuljo ohlajanja zagotavlja računalniško krmiljen hladilni sistem, je bilo treba za kaljenje z vodo uporabiti posebno serijo vzorcev, da smo dosegli enako ohlajevalno hitrost in da je bil čas ohlajanja točno* $\Delta t_{8/5}$ *= 10 s.*

Za pregled mikrostruktur je bila uporabljena klasična metalografska priprava obrusov, sestavljena iz brušenja, poliranja in jedkanja. Za oceno velikosti zrn je bil uporabljen optični mikroskop Nikon Epiphot 300, opremljen z digitalnim fotoaparatom Olympus DP-12. Vsi mehanski preskusi so bili opravljeni pri sobni temperaturi. Za natezne preskuse in preizkuse udarne žilavosti - Charpyjeve preskuse so bili uporabljeni po 3 vzorci vsake vrste in 1 vzorec za določevanje rasti utrujenostne razpoke.

V nadaljevanju tega poglavja so predstavljene eksperimentalne preskusne metode, uporaba Chapettijevega modela in uporaba numeričnih metod (model MKE, izdelava mreže in določitev robnih pogojev in obremenitev). V tem poglavju je pri numeričnih metodah razložena uporaba Vickersove vtiskovanja na ravni površini in v utoru vzorcev, ki predstavlja umetno mikronapako.

V četrtem poglavju doktorske disertacije je predstavljen problem utrujanja zvarnega spoja. Na kratko so opisani dejavniki, ki najbolj vplivajo na lastnosti pri utrujanju zvarnega spoja, kot so: zaostale napetosti, okolje, srednja napetost, razmerje obremenitve ter hrapavost in faktor koncentracije napetosti.

Analiza toplotno vplivanega področja v zvarnem spoju, možnost njene umetne simulacije z uporabo dveh različnih metod in vpliv mikronapak na drobnozrnato mikrostrukturo so predstavljeni v petem poglavju doktorske disertacije.

V poglavju 6 doktorske disertacije, ki je osrednji del tega dela, so predstavljeni eksperimentalni rezultati te raziskave. Preiskave mikrostrukture vseh treh pripravljenih vzorcev so pokazale, da je v vseh treh vrstah pripravljenih vzorcev v mikrostrukturi prevladovala martenzitna mikrostruktura. Primerjava mikrostruktur je pokazala, da so bile mikrostrukturne sestavine obeh vrst simuliranih vzorcev zelo podobne mikrostrukturnim sestavinam FZ TVP na realnem zvaru. Povprečna velikost zrn je bila določena v skladu s standardom ASTM E112 z linearno metodo merjenja premerov zrn.

Za natezni preskus so bili uporabljeni standardizirani cilindrični vzorci s premerom 10 mm. Natezni preskusi so bili opravljeni z univerzalnim servohidravličnem trgalnem stroju Amsler 559/594 v skladu s standardom EN ISO 6892-1, metoda B, rezultati pa so navedeni v tem poglavju.

V naslednjem koraku so bile opravljene meritve trdote po Vickersu na vzorcu realnega zvara in na simuliranih vzorcih. Vickersova trdota HV 10 je bila izmerjena z merilnikom trdote Shimadzu HMV-2000 v skladu s standardom EN ISO 6507-1. ISO 9015-1 je bil upoštevan tudi za realni zvar in meritve FZ TVP realnega zvara. Pred meritvami so bili za brušenje uporabljeni papirji do P 1200 v skladu s standardom ISO 6344-3, da bi zagotovili gladke površine. Na vsakem vzorcu je bilo opravljenih petnajst meritev, nato pa so bile izračunane povprečne vrednosti.

Povprečna trdota dobavljenega (normaliziranega) materiala je bila po pričakovanjih bistveno nižja od trdote FZ TVP, kjer material ni bil zakaljen. Trdota vzorcev AF+WQ, vzorcev WTCS in

dejansko varjenih FZ TVP je bila zelo podobna. Potencialno, vendar zaradi enakih izmerjenih hitrosti ohlajanja je malo verjetno, da bi lahko bila nekoliko večja trdota vzorcev AF+WQ posledica različnih načinov ohlajanja.

Vzorci WTCS so bili vpenjani v vodno hlajene čeljusti, kar je povzročilo skoraj enodimenzionalni toplotni tok iz vročega osrednjega območja vzorca proti čeljusti na obeh straneh. Vzorci AF+WQ so bili ohlajeni z vodo, pri čemer so se vse površine ohlajale intenzivneje, toplotni tok iz središča vzorca pa je bil dvodimenzionalen. Poleg tega so se povprečne vrednosti razlikovale le za približno 1,5 %, kar je znotraj zahtevanega območja ponovljivosti (zahtevana so odstopanja < 4 %) v skladu s standardom ISO 6507-2. Zato lahko trdoto obeh vrst simuliranih vzorcev štejemo za praktično enako. Realni FZ TVP je imel nekoliko nižjo povprečno trdoto kot simulirani vzorci. Vendar je bila razlika med vzorci WTCS in realno zvarjeno FZ TVP še vedno v zahtevanem območju ponovljivosti manj kot 4 %. Zato lahko glede trdote realnega FZ TVP na zvaru in obe vrsti simuliranih vzorcev štejemo za praktično enake. Tako so meritve trdote in primerjava mikrostruktur potrdile, da so simulirani vzorci reprezentativni za realno zvarjeno FZ TVP in da so primerni za nadaljnje mehansko preskušanje.

V naslednjem koraku so bili izvedeni preskusi udarne žilavosti po Charpyjevi metodi. Ti preskusi so bili izvedeni na tritočkovnih upogibnih preskušanih za obe vrsti vzorcev (AF+WQ in WTCS). Instrumentirani udarni preskusi so bili izvedeni s Charpyjevim kladivom Amsler RPK300 s hitrostjo zbiranja podatkov $4 \cdot 10^6$ odčitkov na sekundo v skladu s standardom ISO 148-1. Za preskušanje so bili uporabljeni vzorci s standardno ISO - V-zarezo. Posneti so bili diagrami sile v odvisnosti od časa in energije v odvisnosti od časa. Z instrumentiranimi Charpy preskusi je bilo mogoče skupno energijo za lom E_t (E_t = KV8 v skladu s standardom ISO 148-1) razdeliti na energijo za nastanek razpoke E_i in energijo za širjenje razpoke E_p. Rezultati so pokazali, da imajo vzorci WTCS v povprečju nekoliko večjo udarno žilavost kot vzorci AF+WQ. Dejstvo, da je bila hitrost udarnega kladiva pri vseh izvedenih udarnih preskusih konstantna in da so udarni vzorci in vzorci WTCS absorbirali večjo količino energije udarca, kaže na manjšo gonilno silo za razvoj razpok. Nazadnje je treba poudariti, da je bila pri vseh preskusih energija za iniciacijo E_i bistveno večja od energije širjenja E_p. To kaže, da ne glede na metodo simulacije pri sobni temperaturi in brez prevelikih količin vodika material v FZ TVP ni posebej nagnjen k nastanku razpok. Vendar pa se razpoke, ko se enkrat pojavijo, z majhno porabo energije dokaj enostavno širijo in se verjetno

ne bodo ustavile. Ta ocena je kvalitativna in je potrjena z mehanskimi preskusi in izmerjeno lomno žilavostjo.

Lomno mehanski preskusi so bili opravljeni s testiranjem s tritočkovnim upogibom SENB z eno bočno zarezo. Geometrija preskusnih vzorcev SENB in zareza sta bili pripravljeni v skladu s standardom ASTM E1820. Obremenjeni so bili v kvazistatičnem režimu s konstantno hitrostjo obremenjevanja. Stabilna rast razpok je bila ocenjena z metodo normalizacije v skladu s standardom ASTM E1820. Ta metoda omogoča oceno rasti razpoke na podlagi izmerjenih začetnih in končnih dolžin razpok na lomnih površinah preskusnih vzorcev po preskusih.

Preskus rasti utrujenostne razpoke se je izvedel, da se ugotovi prag za širjenje dolgih razpok. Zato je bila v naši raziskavi uporabljena standardna preskusna metoda rasti utrujenostnih razpok v skladu s standardom ASTM E647-15e1. Geometrija vzorcev za preskus rasti utrujenostnih razpok je pripravljena v skladu s standardom. 1 mm globoka zareza je bila pripravljena z obdelavo z žično erozijo. Na stransko površino vzorca je bila pritrjena merilna folija, ki je omogočila natančnejše merjenje dolžine razpoke med utrujenjem, kot to zahteva standard. Preskusi so bili izvedeni na 160 Nm RUMUL Cractronic stroju, za merjenje rasti utrujenostnih razpok pa je bila uporabljena oprema Fractomat. Vsi preskusi so bili izvedeni z razmerjem upogibne obremenitve R = 0,1.

Rezultati preskusov utrujanja so bili predstavljeni na šestih različnih S-N krivuljah (Vöhlerjeve krivulje). Trajna dinamična trdnost pa je določena za vse vrste vzorcev v obeh pogojih. Po določitvi trajne dinamične trdnosti je bila opravljena ocena rezultatov v skladu s Chapettijevim modelom, za ugotovitev kritične dolžine razpoke pa je bil izdelan Kitagawa Takahashi diagram.

Nazadnje je bil za upoštevanje vpliva zaostalih napetosti na kritično dolžino razpoke uporabljen vpliv zaostalih napetosti okoli mikronapak, ki je bil vzet iz rezultatov numeričnih metod, saj je znano, da Chapettijev model ne upošteva učinka zaostalih napetosti okoli mikronapake. Po upoštevanju vpliva zaostalih napetosti so diagrami ponovno narisani in glede na rezultate je razvidno, da je vpliv zaostalih napetosti znaten.

V poglavju 7. in 8. doktorske disertacije so predstavljene razprave in zaključki o eksperimentalnih ugotovitvah, ki izhajajo iz rezultatov poskusov.

V poglavju 9. so predstavljeni vsi viri, ki so bili uporabljeni pri delu na tej raziskavi.

INFLUENCE OF A MICRODEFECT ON THE FATIGUE PROPERTIES IN A WELD FINE GRAIN HEAT AFFECTED ZONE ON NICKEL-MOLYBDENUM ALLOY STEEL

Keywords: weld joint, Fine Grain Heat Affected Zone, mechanical properties, fatigue crack growth

ABSTRACT

This research presents two possibilities to prepare and test the Fine Grain of a Heat Affected Zone, which, practically, could be considered as the weakest part of welded joints in the presence of any microdefect. It is a narrow zone located between the fusion zone and the unaffected base material; therefore, only a few methods are suitable to test its mechanical properties. The 18CrNiMo7-6 steel was used as the base material. As this steel is usually used for the production of dynamically loaded components, testing of its fatigue behaviour and fracture toughness was crucial, but also measurement of its hardness and impact toughness. To investigate the mechanical properties of a Fine-Grain Heat-Affected Zone (FG HAZ), two different methods were used in this research: A weld thermal cycle simulator (WTCS) and austenitising in a laboratory furnace + water quenching (AF+WQ). The microstructures of the simulated specimens were very similar to a real weld FG HAZ. The WTCS specimens exhibited hardness of 419 HV, KV = 101.5 J, ΔK_{thR} = 3.40 MPam$^{0.5}$, C = 1.64×10^{-11}, m = 2.4465. The AF+WQ specimens exhibited hardness of 425 HV, KV = 73.1 J, ΔK_{thR} = 4.33 MPam$^{0.5}$, C = 1.73×10^{-11}, m = 2.5114. The hardness of the real weld FG HAZ was 405 HV. Comparison of the results for both types of simulated specimens, with the results for a real weld HAZ, confirmed that both types of simulated specimens are suitable for mechanical tests of individual HAZ subzones. The residual stresses introduced by artificially prepared micro defect played significant role on crack initiation and propagation.

TABLE OF CONTENTS

LIST OF FIGURES

LIST OF TABLES

LIST OF THE SYMBOLS USED

$k_{surface}$ Correction coefficient for the surface condition [-],

k_{size} Correction coefficient for the geometry [-],

k_{load} Correction coefficient for the loading condition [-],

$k_{temp.}$ Correction coefficient for the temperature environment [-],

$k_{reliability}$ Correction coefficient of reliability [-],

σ_f (σ_e) Corrected strength [MPa],

σ'_f (σ'_e) Strength determined from a standardised test [MPa].

da/dN Crack growth rate [mm/cycle],

m Constant coefficient of the material for a fixed range of stress $\Delta\sigma$ and R (load rate) [-],

C Coefficient of the material for a range of fixed stress $\Delta\sigma$ and R (load rate) [-],

ΔK Range of the stress intensity factor [MPa$\sqrt{m}$],

$Y(a/W)$ Dimensionless function that depends on the geometry of the component and the crack size (a) [-],

ΔK_{th} Range of the stress intensity factor threshold [MPa$\sqrt{m}$],

ΔK_{IC} Range of fracture toughness of the material for mode I [MPa$\sqrt{m}$].

K_{IC} Critical stress intensity factor [MPa$\sqrt{m}$].

σ_f Critical stress [MPa],

a Crack length [mm],

M_k Factor which considers the presence of the weld [-],

M_S Correction factor of the free surface area near the crack tip [-],

M_i Correction factor of the free surface in the crack tip [-],

ϕ Angle of the ellipse[rad or degree],

K Stress intensity factor [MPa$\sqrt{m}$],

σ Applied stress [MPa],

K_{max} Maximum stress intensity factor [MPam$^{0.5}$],

R Load ratio [-],

ΔK_{op} Crack opening stress intensity [MPam$^{0.5}$],

$R_{p0.2}$ Yield strength [MPa],

R_m Ultimate tensile strength [MPa],

A_5 Permanent elongation [%]

HV Vickers hardness [-],

E_t Total energy for fracture (= KV_8 according to ISO 148-1) [J],

E_i Energy for crack initiation [J],

E_p Energy for crack propagation [J],

K_t Theoretical stress concentration factor [-],

K_f Fatigue stress concentration factor [-],

K_1, K_2, K_3, K_4 Coefficients of theoretical stress concentration factor [-],

D Hight of fatigue specimen [mm],

h Depth of fatigue specimen [mm],

r Radius of fatigue specimen [mm],

d Location of the strongest microstructural barrier (for example, grain size) [μm],

$\Delta\sigma_{eR}$ Material's plain fatigue limit [MPa]

ΔK_{dR} Microstructural or intrinsic threshold [Mpam$^{0.5}$]

ΔK_{CR} Extrinsic component threshold [Mpam$^{0.5}$]

ΔK_{th} Long crack threshold [Mpam$^{0.5}$]

k Material coefficient [-]

u_1, u_2, u_3 Displacement in corosponding axis 1, 2, 3 [mm],

ϕ_1, ϕ_2, ϕ_3 Rotation in corosponding axis 1, 2, 3 [deg/degree],

F Force on the pyramid [N],

M_z Bending moment of model [Nm],

$M_{z\,spec.}$ Bending moment of specimen in fatigue limit [Nm],

$S_{\sigma,max}$ Maximum normal stresses in a stress cycle [MPa],

$S_{\sigma,min}$ Minimum normal stresses in a stress cycle [MPa],

Mσ Mean stress sensitivity factor [MPa],

γ_w Mean stress fitting parameter [-],

$S_{\sigma,ar}$ Fully reserved stress amplitude [MPa],

$S_{\sigma,m}$ Moderate mean stress [MPa],

$S_{\sigma,a}$ Stress amplitude [MPa],

N_i Fatigue life [cycles]

Kc Fracture toughness [Mpam$^{0.5}$]

ΔK Stress intensity range [Mpam$^{0.5}$]

γ Refers to the ratio between spacing and depth of the asperities,

R_z 10-point roughness [μm],

ρ Effective profile valley radius of the surface texture [μm],

Δe Nominal stress amplitude [MPa],

T_{max} Maximum temperature [°C],

T_m Steel melting point temperature [°C],

A_1 Austenite starting temperature [°C],

A_3 Austenite homogenisation temperature [°C],

I Current [A],

U Tension [V],

Q Heat input during welding [kJ/mm]

d Diagonal of pyramid [μm],

h Depth value of the pyramid [μm],

$area^{1/2}$ Defect's size parameter [μm],

E Elastic modulus [MPa],

J_{IC} Critical values of the J-integral [kJ/mm^2],

δ_{IC} Critical value of crack opening [mm],

K_{IC} Critical values of the stress intensity factor [MPam$^{0.5}$],

v Poisson's ratio [-],

α Coefficient of the material [-],

a_c Critical crack size [mm],

M_1 Bending moment of model for σ_{eR} =550 MPa [Nm],

M_2 Bending moment of model for σ_{eR} =675 MPa [Nm],

s_{11} Stress distribution [MPa],

R_{local} Local stress ratio [-].

LIST OF SYMBOLS ABBREVIATIONS USED

18CrNiMo7-6 Designation of the steel according to the Standard DIN EN 1008:2008-06

HAZ	Heat Affected Zone
CG HAZ	Coarse Grain Heat Affected Zone
FG HAZ	Fine Grain Heat Affected Zone
IC HAZ	Intercritical Heat Affected Zone
OT HAZ	Over Tempered Heat Affected Zone
PWHT	Post-Weld Heat Treated
NDT	Nondestructive Testing
LCF	Low Cycle Fatigue
HCF	High Cycle Fatigue
ASME	American Society of Mechanical Engineers
LEFM	Linear Elastic Fracture Mechanics
EPFM	Elastic Plastic Fracture Mechanics
SIF	Stress Intensity Factor
FCGR	Fatigue Crack Growth Rate
FCG	Fatigue Crack Growth
PICC	Plasticity Induced Crack Closure
WRSs	Welding Residual Stresses
FEM	Finite Element Method
CCT	Continuous Cooling Transformation
AF+WQ	Austenitising in a laboratory furnace followed by water quenching
WTCS	Weld thermal cycle simulator

WoRS	without residual stress
WRS	with residual stress
SEM	Scanning Electron Microscopy
ABAQUS/CEA	Computer-Aided Engineering Software
C3D8	8-node brick finite element
SENB	Single Edge Notched Bend
CTOD	crack tip open displacement
CMOD	crack mouth open displacement
SC	short crack
LC	long crack
MSC	microstructurally short crack
PSC	physically short crack

1 INTRODUCTION

1.1 Background

Nowadays, the welding process is becoming one of the most significant manufacturing processes. Heat generated as a result between the electrode and base material melts the material and also affects the base material in a wider zone, which is not melted, but is the subject of significant changes known as a Heat Affected Zone (HAZ). A HAZ is a very complex zone, and it is divided into sub-zones such as a Coarse Grain HAZ (CG HAZ), a Fine Grain HAZ (FG HAZ), an intercritical HAZ (IC HAZ), a over tempered HAZ (OT HAZ), which is over tempered but did not reach a eutectic temperature.

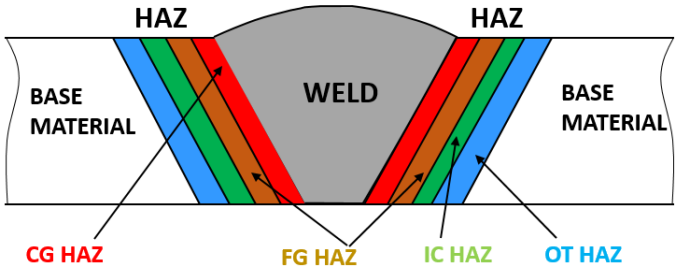

Figure 1. 1 Welded joint; Base material, HAZ, Weld material.

Each of the above mentioned sub-zones has different properties because of their microstructure arrangement. While the HAZ is the critical part of the weld toe, to assure adequate properties of weld joints in high strength steels, the selection of an appropriate welding technology demands a lot of attention [1, 2, 3]. Also, preheating before welding is necessary, to avoid cold hydrogen cracking [4]. Failure of weld toe occurs inside of the HAZ because of the defects which are present on the microstructure of the material. The critical areas of weld joints are Heat Affected Zones (HAZs). Upon heating and subsequent rapid cooling, unfavourable changes occur in the microstructure, which can result in unacceptable mechanical properties of the material. Therefore,

most of the weld joints need to be post-weld heat treated (PWHT) with controlled heating and cooling [5].

If a defect is detected by nondestructive testing (NDT) methods inside of these zones, as designers we have to be able to predict and monitor the crack growth rate (crack propagation) so as to discard the component from usage before catastrophic failure can occur. Therefore, knowing mechanical properties of each particular subzone is crucial.

The reliability of welded structural components depends on many factors, while the weld process itself is complex from the view of the effect in the microstructure of the welded material. During the process of welding, but also in other manufacturing methods, defects are present, even under optimal operation conditions. Due to poor NDT sensitivity and sometimes the negligible work of an inspection operator, small defects in weld joints usually remain undetected, and these defects cause stress concentrations, which can potentially lead to initiation of cracks from the defects. There are many accidents which end up with human fatalities, and also with financial losses due to undetected defects from NDT operators. During cycle loading, cracks start to initiate and propagate from these small defects, even at loads below the fatigue limit, depending on the size of the defect in comparison to the grain size of the HAZ microstructure. For reliability of the weld joint`s welded structural components it is crucial that each part of the weld joint has adequate properties, in order to prevent catastrophic and sudden breakage of the welded constructions [6]. Defects in the microstructure will react as stress risers and stress concentration, and so the crack initiates firstly from such defects [7]. A HAZ can be in many cases the critical part of the weld joint, and usually failure of the weld toe occurs inside of this zone because of the defects, which can be present on the microstructure of the material. If a defect is detected by NDT methods at a welded joint, the designers have to be able to predict and monitor the crack growth rate (crack propagation), so as to discard the component from usage before catastrophic failure can occur.

1.2 Problem statement

Manufacturing processes, as well as the weld process itself, is followed by defects. Since the material is heated to a very high temperature (to melting point in most cases as the welding process requires), metallurgical changes take place in the parent metal, particularly in the vicinity of a

joint, known as a HAZ. These changes are followed by deterioration of the mechanical properties, and loss of the ductility is a major problem which especially affects the HAZ. Microstructure changes due to the weld process are followed by defects. Defects in a welded joint happen, even at optimal operation conditions, but sometimes they could also be the subject of a wrong welding procedure specification, inadequate edge preparation of parts, etc. In such a condition different flaws, such as porosity, cracks, slag inclusions, etc. take place in the weld joint, which becomes critical for the life of the welded joint. A HAZis very complex in its nature and heterogeneous and it is divided into sub-zones such as a CG HAZ, a FG HAZ, an IC HAZ, and a OT HAZ, which is an over tempered zone. A HAZ in the welding field is known as an Achilles heel, due to its susceptibility to crack initiation and propagation.

The aim of this scientific work is the investigation of the mechanical properties of a FG HAZ and its behaviour in the presence of a small defect under cyclic loading. The influence of an artificially small physical defect (Vickers indentation) on the FG HAZ on crack initiation and propagation will contribute to increasing of the reliability of 18CrNiMo7-6 steel. This steel is used mostly in industry for heavy loads in automotive parts which are dynamically loaded. The investigation will help us to make recommendations to industry about the estimation of how much is the risk for a welded joint failure due to such defects` size and find an allowable defect size. Furthermore, this particular steel is susceptible to solidification cracks, and the welding operation is recommended to be carried out with very low hydrogen electrodes, in order to prevent hydrogen cracking in the solidification phase. A tensile test, a Charpy experimental test, fracture toughness and fatigue tests of specimens with a FG microstructure were used for the investigation of the behaviour of cracks in this particular HAZ of the steel.

1.3 Research objectives

In order to prepare the microstructure in as welded conditions, specimens from the material 18CrNiMo7-6 with FG HAZ have been simulated in two different ways: (in a laboratory furnace and by using a weld thermal welding simulator). In these conditions the preparation of different specimens with artificial micro-defects in their FG HAZ microstructure with or without residual stress caused by artificially made defects will be possible. A Vickers indenter will be used as an

artificially made small physical defect. After that, the specimens will be tested in fatigue in order to design Vöhler curves. The influence will be explained of the residual stress on initiation and early crack propagation. A Chapetti model will be used to explain the initiation and propagation of a crack from a physically small defect. It is known that the Chapetti model does not take into account the acting of residual stress around the defect, so this needs to be taken into consideration for early crack initiation and propagation from the defect, ss the objective of this research work is the investigation of the behavior of the crack initiation and early crack propagation of the microstructure of an FG HAZ. Using the knowledge of the behaviour of the CG HAZ zone properties of 18CrNiMo7-6 steel under cyclic load, done from an earlier investigation, after investigation of the FG HAZ properties of 18CrNiMo7-6 steel on the fatigue threshold and fatigue crack growth, a clear mirror of behaviour will be discovered during the cyclic loading of HAZ of 18CrNiMo7-6 steel. The behaviour of an FG HAZ in crack initiation and early crack propagation are the main objectives. The fatigue crack growth data for the FG HAZ will be necessary in order to explain its behaviour. Determination of the FG HAZ properties will be a helpful contribution for the welding industry, while it is well known that welded joints fail mostly in the HAZ, and if we know the FGHAZ and CGHAZ properties exactly, we can describe the effect of the heat input rate in changing the base material microstructure, and also give an answer to the behaviour of cracks in a HAZ. According to this, it is worth saying that, in future, it will be necessary to make improvements in the weld machines and weld technics in order to reduce the HAZ effect without reduction of the weld quality.

The objectives and assumption of this research are described as follows:

- To investigate and analyse the FG HAZ of a weld;
- To investigate the influence of the presence of the physical microdefect on fatigue life;
- To find and observe the fatigue properties of the FG HAZ of a weld;
- To investigate the fatigue crack threshold of the FG HAZ of a weld;
- To find the fracture toughness of the FG HAZ of a weld;
- To identify in general the mechanical properties of the FG HAZ in order to enhance the reliability of the welded joints, particularly in welding constructions.

Topics related to the fatigue and fracture of a weld joint are to be covered in order to explain the research problem.

1.4 Structure of Doctoral Thesis

The Doctoral Thesis is organised in six Chapters, described as follows:

Chapter 1 – generally provides an overview, as well as an introduction to the research. Described are the research background, problem definition, research objectives and the structure of the Doctoral Thesis .

Chapter 2 - provides a literature review, with the emphasis on the fatigue and fracture of a weld joint. It presents the current literature on the fracture and fatigue of a weld joint. The application of fatigue and fracture of a weld joint in engineering fields is shown at the end.

Chapter 3 – a description of the research methodology is included under this chapter. The research begins with an explanation of the methods used during the research work and a description of the experimentl procedure is given after that. This chapter also describes the preparation and calculation of the stress intensity factor K_t as in a welded joint.

Chapter 4 - deals with the factors that influence fatigue in a weld joint, and the stress range, load ratio R and mean stress value effect, roughness and stress concentration factor are explained in this chapter. The influence of these factors in a weld joint has a significant effect on the total life of the welded joint.

Chapter 5 – The influence of small physical defects on the FG HAZ of a weld joint, an analysis of the FG HAZ on the weld joint and the possibility of the preparation of a FG HAZ in a welding simulator and laboratory furnace are described in this chapter. This chapter also contains the welding cycle which was used to prepare the specimens for the investigation. The experimental results are presented and discussed in **Chapter 6** respectively.

Chapter 7 - Analysis of the experimental results, microstructure photographs, evaluation of the S-N curve (Vöhler curve), evaluation of the *da/dN- ΔK* curve (Paris law), fracture toughness,

residual stress effect around a micro defect, implementation of the Chapetti model and KT-diagram are covered under these two chapters.

Finally, **Chapter 8** is reserved for the conclusion of this research work.

1.5 Hypothesis

These hypothesis could be written:

1. By putting of physical small defect on to FG HAZ microstructure the influence of initial crack on fatigue could be investigated.

2. Using of the modified Chappeti model will be able to explain phenomenon of crack propagation through to different microstructure (from FG HAZ to CG HAZ).

3. Existence of the residual stresses in vicinity of the defect play significant role for crack behaviour in FG HAZ.

1.6 Original scientific contribution

The scientific work of this research project has been published in several papers. The first article derived from this investigation was published in the International Journal of Fatigue, the second article in Materials MDPI, And the third article in the Metalurgija Journal. Procedia Structural Integrity is another international journal where a part of this investigation has been published. Research work from this project has been presented in some international and national conferences, such as: The 22nd European Conference on Fracture - ECF22 26-31.,August, 2018, Belgrade and LMZ conference - 31.05.2018, Maribor. The behaviour of FG HAZ and its properties in relation to crack initiation and propagation have been explained in detail for 18CrNiMo7-6 steel.

2 LITERATURE REVIEW

2.1 Introduction

The welding process is followed by defects inside the microstructure due to different factors which are part of the process and also the solidification process [8]. Defects in the microstructure of a welded joint, such as small cracks, voids, flaws, pores` chemical inhomogeneities in the weld metal, including solute segregation, banding, inclusions, and gas porosity into the microstructure of the welded materials appear, even if very professional technology is applied [9, 10, 11]. These defects in the microstructure have a tendency to grow after applied repetition static or dynamic load on the material; therefore, such defects are the most significant factor of the reduction of the life of a welded joint, such as metal constructions: (excavator, automotive industry, bridges, shafts, railways, pipelines, aircraft, bicycle pedals, etc. [12, 13, 14, 15]. Such small defects are the centre of stress appearance, and it is known that stress concentration is one of the significant factors of destroying welded joints [15]. Since the metal to be joined is held by clamping and local boundary heating and cooling happen during the annealing process, residual stresses develop in the region of the weld. These residual stresses are often tensile in nature, and affect the behaviour of the weld joint under fatigue loading greatly. Residual stresses may be removed and metallurgical changes reversed by heat treatment (annealing and normalising), but sometimes we have to deal with large welded structures where heat treatment is difficult to perform and it is too expensive.

The fracture and fatigue phenomena of welded joints are well known to be problematic and very often faced in real life, and it’s known as the failure of welded joints due to rupture or fatigue strength. Fatigue is a formation of a crack or cracks as a result of the repeated application of loads under the endurance limit of the material, each of which is insufficient by itself to cause normal static failure. Some defects in the microstructure of the HAZ are shown in Figure 2.1.

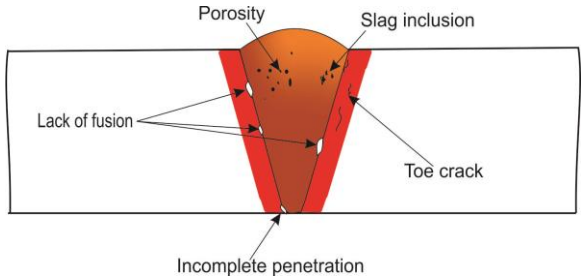

Figure 2. 1 Defects in the microstructure of a HAZ

Fatigue is a process of accumulative damage produced by the fluctuation of stress and strains, even when both stress and strains are below the static resistance level of the material. The damage is accumulating cycle by cycle, and after a certain number of repetitions a failure will occur. The fatigue process is normally divided into three phases:

- Phase 1: crack initiation;
- Phase 2: crack growth;
- Phase 3: final fracture.

Most metals with a body centred cubic crystal structure have a characteristic response to cyclic stresses. These materials have a threshold stress limit below which fatigue cracks will not initiate. This threshold stress value is often referred to as the endurance limit. In steels, the life associated with this behaviour is generally accepted to be $2x10^6$ cycles. In other words, if a given stress state does not induce a fatigue failure within the first $2x10^6$ cycles, future failure of the component is considered unlikely. For spring applications, a more realistic threshold life value would be $1x10^7$ cycles. Metals with a face centred cubic crystal structure (e.g. aluminium, austenitic stainless steels, copper, etc.) do not typically have an endurance limit. For these materials, fatigue life continues to increase as stress levels decrease; however, a threshold limit is not typically reached below which infinite life can be expected. Based on the magnitude of stress and the number of cycles, fatigue process is divided into two regions:

- LowCycle Fatigue (LCF) less than 10^4 cycles
- HighCycle Fatigue (HCF) more than 10^4 cycles

The difference between Low Cycle Fatigue (LCF) and High Cycle Fatigue (HCF) has to do with the deformations. LCF is characterised by repeated plastic deformation (i.e. in each cycle), whereas

HCF is characterised by elastic deformation. The number of cycles to failure is low for LCF and high for HCF, hence the terms Low and High Cycle Fatigue.

Transition between LCF and HCF is determined by the stress level, i.e. the transition between the plastic and elastic deformations. That implies that there is no fixed transition life, e.g. 10^4, but that the transition life depends on the ductility of the material [14]. In the Figure 2.2 applied fatigue strength range is described over a number of stress cycles.

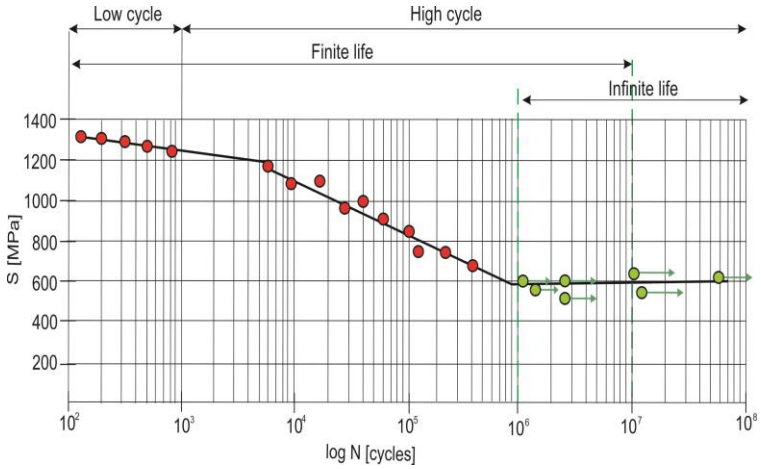

Figure 2. 2 The fatigue strength vs. number of stress cycles (S-N) diagram

When the crack reaches a critical dimension, one additional cycle causes sudden failure. This means that the material has exceeded its fatigue strength (σ_f) or endurance limit (σ_e), and so the welded joint or construction has failed as s result.

The fatigue strength (σ_f) and the endurance limit (σ_e) for some materials can be estimated from the following relations:

Steel: $\sigma_e = 0.5\,\sigma_{ut}$ for $\sigma_{ut} < 1400MPa\ (200ksi)$

$\sigma_e = 700$ MPa (100 ksi) for $\sigma_{ut} \geq$ 1400 MPa (200 ksi)

Iron: $\sigma_e = 0.4\,\sigma_{ut}$ for $\sigma_{ut} <$ 400 MPa (60 ksi)

$\sigma_e = 160$ MPa (24 ksi) for $\sigma_{ut} \geq$ 400 MPa (60 ksi)

Aluminium: $\sigma_e = 0.4\,\sigma_{ut}$ for $\sigma_{ut} <$ 330 MPa (48 ksi)

$\sigma_f = 130$ MPa (19 ksi) for $\sigma_{ut} \geq$ 330 MPa (48 ksi)

The fatigue strength or endurance limit are typically determined from the standard material tests (e.g. the rotating beam test). However, they must be modified appropriately to account for the physical and environmental differences between the test specimen and the actual part being analysed:

$$\sigma_f(or\ \sigma_e) = k_{surface} \cdot k_{size} \cdot k_{load} \cdot k_{temperature} \cdot k_{reliability} \cdot \sigma_f'(\ or\ \sigma_e') \qquad (2.1)$$

Where:

$k_{surface}$ - is the correction coefficient for the surface condition [-],

k_{size} - is the correction coefficient for the geometry [-],

k_{load} - is the correction coefficient for the loading condition [-],

$k_{temperature}$ - is the correction coefficient for the temperature environment [-],

$k_{reliability}$ - is the correction coefficient of reliability [-],

$\sigma_f(or\ \sigma_e)$ - is the corrected strength [MPa],

$\sigma_f'(\ or\ \sigma_e')$ - is the strength determined from a standardised test [MPa].

Referring to the last equation of the fatigue strength or endurance limit calculation it is clear that there are so many coefficients which determine the value of fatigue strength or endurance limit, but the significant factor is the homogeneity of the materials` microstructure. if the microstructures of the materials contain any defects, so that it is not homogeneous, it will affect the welded joint directly and the possibility to destroy it will be increased.

Authors have devoted energy to identifying the influence of a microdefect on fatigue strength in a CG HAZ [15]. The fatigue strength of a FG HAZ of the weld in the presence of a physical microdefect was investigated in our research work [16, 17, 18]. The schematic of the influence of the physical microdefect on two different types of microstructure is shown in Figure 2.3.

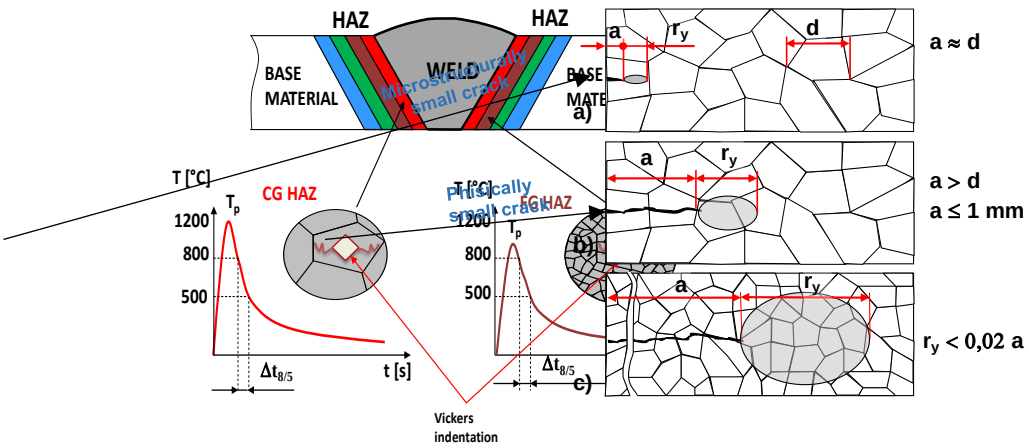

Figure 2. 3 Schematic of the influence of the physical microdefect on two different types of microstructure and a welding cycle diagram.

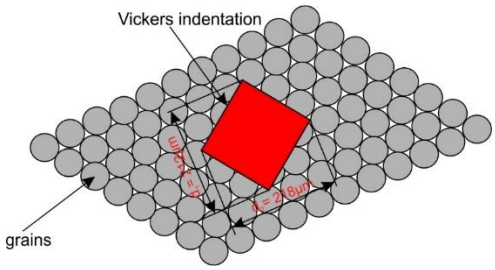

Figure 2. 4 Schematically described artificially small physical defect (Vickers pyramid) introduced on a region of a FG HAZ of a weld joint

Welding as a manufacturing method is followed by defects as a result of heat input and microstructure reorganisation. A welding defect is any flaw that compromises the usefulness of a weldment, and has been observed by one of the NDT inspection methods. There is a great variety of welding defects. Welding imperfections are classified according to the Standard EN ISO 6520, while their acceptable limits are specified in Standard EN ISO 5817 and Standard EN ISO 10042 (for aluminium alloys) for visual inspection.

According to the American Society of Mechanical Engineers (ASME), causes of welding defects can be broken down as follows:

a) 41% poor process conditions,
b) 32% operator error,

c) 12% wrong technique,
d) 10 % incorrect consumables, and
e) 5% bad weld grooves.

The above mentioned defects become critical when welded joints are subjected to cyclic loading, and that could cause failure due to fatigue. Fatigue results from this cyclic loading, as well as strains in the material. Throughout a welded assembly's life, cracks which reduce the fatigue life of a joint could initiate, propagate and grow, causing the assembly to fail, even if these cyclic stresses are low and smaller than the base material and weld filler material yield stress. Hence, the fatigue strength of a welded joint does not correlate to the fatigue strength of the base material, and therefore incorporating design considerations in the development phase can reduce failures due to fatigue in welded joints [16].

Over recent years, significant research has been carried out in the field of The fracture and fatigue of welded joint. In this chapter literature reviews are presented that are related to the structure of the Doctoral Thesis. The area of concern consists mainly of the following categories:

Literature reviews on the fracture of a welded joint,

Literature reviews on the fatigue of a welded joint.

2.2 Current literature on the fracture of welded joints

One of the common failure phenomena in welded joints and structural engineering materials as well is fracture of the welded joints due to fatigue. This is associated with the presence of flaws or defects in the microstructure of the material, or any geometric detail, such as discontinuities, which, after a certain number of load cycles, serve as generator for the initial fatigue crack. Either through manufacturing or created by situations of use, pre-existing flaws create the critical conditions from which the material breakage can be developed. fracture mechanic`s purpose is to analyse and determine the mechanical behaviour of structural elements, when considering the existence of flaws in the material to define the conditions or criteria of breakage [17] [18].

The first theory that explains the fracture of cracked solids, known as linear elastic fracture mechanics (LEFM), was proposed initially by Griffith at the beginning of the last century, and

subsequently developed later by Irwin. Up to its appearance, only the failure by plastic collapse, where the material deforms plastically without any fracture, had well-structured physical and mathematical foundations. The LEFM came to fill the gap that existed in the opposite situation of the plastic collapse, when the fracture occurs in conditions of a small deformation, and in stress levels that are much lower than those that lead to the start of the material plastic deformation processes [18]. Using the principles of the LEFM, it is possible to assess the stable propagation of fatigue cracks in welded joints when using the empirical relationship proposed by Paris and Erdogan [7] given in equation 2.2.

$$da/dN = C(\Delta K)^m = C(Y\Delta\sigma\sqrt{\pi a})^m \tag{2.2}$$

$$\Delta K_{th} \leq \Delta K \leq \Delta K_{IC} \tag{2.3}$$

where:

da/dN– is the crack growth rate [mm/cycle],

m – is the constant coefficient of the material for a fixed range of stress $\Delta\sigma$ and R (load rate) [-],

C – is the constant coefficient of the material for a range of fixed stress $\Delta\sigma$ and R (load rate) [-],

ΔK - is the range of the stress intensity factor [MPa$\sqrt{\text{m}}$],

$Y\left(\frac{a}{W}\right)$ - is a dimensionless function that depends on the geometry of the component and the crack size (a) [-],

ΔK_{th} - is the range of the stress intensity factor threshold [MPa$\sqrt{\text{m}}$],

ΔK_{Ic} - is the range of fracture toughness of the material for mode I [MPa$\sqrt{\text{m}}$].

When the stress intensity factor reaches a critical value, and the Standard ASTM E399 and Standard ASTM D5045 requirements are met, the critical value can be regarded as a material property called fracture toughness for plane-strain, K_{IC}. For that value, the crack starts its unstable spread, fracturing the component into two parts. In this way, the local fracture approach on Mode I is determined on the basis of the following expression shown in equation 2.4:

$$Y\sigma_f\sqrt{\pi a} \rightarrow K_{IC} \tag{2.4}$$

$Y\left(\frac{a}{W}\right)$ - is a dimensionless function that depends on the geometry of the component and the crack size (a) [-],

K_{Ic} - is the critical stress intensity factor [MPa$\sqrt{\text{m}}$].

σ_f - is the critical stress [MPa],

a - is the crack length [mm].

In welded joints, the stress fields in front of the crack are more complex to determine, due to the microstructural changes that occur as a result of the thermal cycle [19]. The crack tip in a weld can be described as a semi-elliptical curve with depth (a) and length ($2c$). In general, using Mode I, the stress intensity factor is given by [20] as in equation 2.5

$$K_I = Y\,\sigma\sqrt{\pi a} \tag{2.5}$$

where:

K_I -is the applied stress at mode I [MPa$\sqrt{\text{m}}$],

σ -is the applied stress [MPa],

a – is the crack length [mm]

$Y\left(\frac{a}{W}\right)$ - is a correction factor dependent on the load and the geometry of the crack size [-].

The Y parameter is influenced by a number of factors that can be represented as follows by equation 2.6::

$$Y = \frac{M_k + M_s + M_t}{\emptyset^o} \tag{2.6}$$

where:

M_k -is a factor which considers the presence of the weld [-],

M_s -is a correction factor of the free surface area near the crack tip [-],

M_t -is a correction factor of the free surface in the crack tip [-],

$\emptyset^0$ - is the integral of the ellipse. The integral of the ellipse $\emptyset^0$ can be expressed as in equation 2.7:

$$\emptyset^o = \int_0^{\pi/2} \{1 - \left(1 - \frac{a^2}{c^2}\right) sen^2\,\emptyset\}^{1/2} d\emptyset \tag{2.7}$$

where:

$\emptyset$ [rad or degree] -is defined as the angle of the ellipse.

The values of M_s and M_t depend on the joint geometry, and failing to evaluate them can lead to an error that is normally about 0.13%. The latter is due to the fact that the stress field is low-intensity when the distance is greater from the weld toe. Therefore, it can be avoided [21].

A number of researchers have determined expressions for the calculation of M_k, such as Lie and Zhao, and Maddox and Andrews, who made a review of the British Standards PD6493 and BS7608, for the steel structures` cruciform design subjected to fatigue, establishing a value of M_k between 0.83 and 1.00 for cracks located at the weld of a toe [22, 23].

Maddox presented equation 2.8, a dimensionless factor M_k which allows for the estimation of the influence of stresses that are generated by the geometric profile of the welded joints on the stress intensity factor [23].

$$M_k = \frac{K}{\sigma\sqrt{\pi a}} \tag{2.8}$$

where:

M_k - is a factor which considers the presence of the weld [-],

K - is a stress intensity factor [MPa$\sqrt{\text{m}}$],

σ - is the applied stress [MPa],

a – is the crack length [mm].

The researcher [20, 24] carried out a comparative analysis between the estimated models by Maddox, Andrews and Hobbacher for the determination of the weld magnification factor M_k. In this work, it was determined that the crack depth is a parameter that affects between 15% and 65% of the parametric equation for the calculation of M_k.

Researcher Brennan [25] developed a comparative parametric equation for the determination of the weld magnification factor in a cruciform welded joint. In addition, the results were compared with those developed previously by the researchers [21, 13], establishing a good level of correspondence between the magnitudes encountered and the previous research.

In the case of welded joints in test tubes with cruciform geometry, Zhao and Lie [22] included a set of equations for estimating the effect of misalignment on different types of welded joints with a semi-elliptical surface crack. Nadot, Y. [26] gave detailed information about fatigue from defects and their effect on service life. Numerical methods were used by Friedman [27] in 1980 for the transient thermal behaviour of the welding process. Among the numerical methods used to carry

out the study of transitional period thermal behaviour, is the Finite Element Method, which is one of the most popular methods. This technique has gained special importance, mainly when it includes a mesh refinement around the tip of the crack, besides the effect of the thermal cycle in the stress intensity factors K_I assessment and the weld magnification factor M_k. Although, conceptually, the factors are obtained in a direct way, Finite Element Analysis, with conventional elements near the crack tip, underestimates the stress increase in gradient and displacement. Instead of using ever smaller elements, size $1\sqrt{r}$, some researchers [28, 29] introduced a direct method by moving the composed node of 8-noded quadrilateral elements up the quarter points in the crack tip, and relocating the nodes of the mid-point to a fourth at the end of the crack.

Once the field of stress is established the parameters of fracture are obtained [30]. Certain configurations of elements and nodes produce unique displacements. While this type of behaviour is undesirable for the majority of the analyses, it is ideal for elasticity problems in cracks. By forcing elements in the crack tip to have a unique deformation, $1\sqrt{x}$ can improve the accuracy and reduce the need for a high degree of refinement of the mesh in the crack tip. This singular deformation is only applied in the crack tip.

Some contributions of this research are the three-dimensional computational analysis of a welded joint by using the Finite Element Method (FEM), and another contribution is the surface weld bead and the differentiation in the mechanical properties of the fusion zone, the HAZ and the base material zone. In addition, the use of an initial residual stress field for the welded joint and adjacent region to emulate the actual experimental model.

The fundamentals of Fracture Mechanics were employed in the numerical modelling of the welded joint with the presence of a surface crack semi-elliptical type discontinuity at the weld toe. The latter is defined as a semi-elliptical surface crack with a small aspect. Because of this study, a set of mathematical models for the weld magnification factor were obtained for cruciform welded joints, which can be used in the prediction of the fatigue life of this type of welded joint.

2.3 Current literature on the fatigue of welding joint

The term “fatigue” was first mentioned in the 19th century to describe the failure of a structure or structural element subjected to cyclic loading. Research on fatigue was first carried out by August

Wöhler, who investigated the failure of train axles. He detected that structural loading that is well below its static resistance does not cause any damage. However, in the case of repeating the same loading over a prolonged period of time, it can cause the failure of the structure or structural element. In the 19th century fatigue was a mysterious phenomenon, because fatigue damage could not be seen and failure occurred without any warning.

In the 20th century, it became known that cyclic (repeated) structural loading initiates the fatigue mechanism, and, respectively, crack initiation and propagation. Since this fatigue phenomenon became recognised much research has been conducted, and significant progress in developing fatigue assessment methods has been made, understanding the mechanism of fatigue of structures and materials and the designing of fatigue resistant details.

High strength steels are taking a significant role in the design of structural components, as well as modern shipbuilding and marine structures. The demand for high load carrying capacity of these structures has put forward the use of high strength steels with a martensitic type microstructure, which is generally understood as possessing the best tensile properties. However, the problem is that martensitic material has poor toughness due to its brittleness. Welding has been applied as a commonly used technique in the connection of high strength steels. It has been known that the tendency of cold cracking gets higher in the welded joint when the strength of the steel increases. On the other hand, the unavoidable welding defects which serve as potential crack initiation sites give rise to the occurrence of fatigue failure. It is generally accepted that the mechanical properties of the weld metal, from both a strength and toughness point of view, are very much dependent on its microstructure feature. Acicular ferrite, first described in the early 1970s, was regarded as the optimum microstructure, due mainly to its nature of small grain size and high angle boundaries [31]. It was introduced purposefully into the welding of “hard and brittle” high strength steels to improve the toughness of their joints.

The welded structures are often exposed to complex cyclic wave loadings, and fatigue failure has been a major cause of failure. As argued by numerous researchers, e.g. Hobbacher [32] , due to the inherent weld imperfections that can serve as initial cracks, the fatigue life of welded joints can be treated largely as crack propagation life. Damage tolerance design based on fracture mechanics concepts is needed under this circumstance [33].

Guang Tao Xu et al. [34] investigated the characterisation of fracture toughness for the surface-modified layer of 18CrNiMo7-6 alloy steel after carburising heat treatment by the indentation method, and found that the variation of fracture toughness exists with the depth of the surface-modified layer.

Zhang et al. [35], while investigating the effect of microstructure on fatigue-crack propagation of 18CrNiMo7-6 high-strength steel, found that, when the crack propagation encounters a high-angle boundary or passes through different crystal orientations, the crack deflects, and expands when it encounters a low-angle boundary.

Shengwei Qin et al. [36] in the research of the effect of the carburising process on the high cycle fatigue behaviour of 18CrNiMo7-6 steel, found that the fatigue strength of carburised specimens has an increase-decrease trend with the increase of the effective case depth.

Since FCG data are critical inputs for damage tolerant design, it should be investigated extensively to ensure the safety of marine structures. The relation between the FCGR and the SIF range was first detected by Paris and Erdogan [37]. They found that a fairly good linear relation was achieved when plotting the FCGR data against the nominal SIFs on a double logarithmic scale. Therefore, the well-known Paris-Erdogan law was proposed, which was an empirical power law based on test data:

$$da/dN = C(\Delta K)^m \tag{2.9}$$

where:

da/dN– is the crack growth rate [mm/cycle],

m – is the constant coefficient of the material for a fixed range of stress $\Delta\sigma$ and R (load rate) [-],

C – is the constant coefficient of the material for a fixed range of stress $\Delta\sigma$ and R (load rate) [-],

ΔK -is the range of the stress intensity factor [MPa$\sqrt{\text{m}}$],

Several factors affect the FCGR of a material. The most significant one may be the stress ratio-R. Although an apparently anomalous behaviour, in that there was a very weak R-ratio dependency in the Paris regime reported for some steels by Jones et al. [38], the effect of the R-ratio on FCGR has been investigated extensively as a common phenomenon for many materials during the past few years. Conventional representation of crack growth rates as a function of a single driving force

as depicted by Eq. (2.9) is considered as inadequate to correlate the R-ratio effect. In general, two methods are often used, namely, the two-parameter method and the crack closure method, to attain an effective crack driving force that can correlate the R-ratio effect with some physical basis.

(1) The two-parameter model (also referred to as the superposition method, or the effective stress ratio method, in some studies)

The two-parameter model is generally considered to be based on the Smith-Watson-Topper fatigue damage parameter [39], which believes that it is the product of the maximum stress σ_{max} and half of the strain range $\Delta\varepsilon/2$ ahead of the crack tip that controls the damage process of fatigue. Because there are only two independent variables between the stress intensity factor range ΔK, the maximum stress intensity factor K_{max} and stress ratio R, any two of them is able to represent the whole information of a cyclic loading.

The R-ratio effect on FCGR was first discussed by Walker [40]. Based on experimental data, Walker pointed out that the FCG driving force is controlled by a combination of R and ΔK, which is called the two-parameter driving force.

Nooriz et al. [43] also derived an analogous two-parameter model based on the elastic–plastic crack tip stress–strain field analysis in the material volume adjacent to the crack tip. Other two-parameter models include those proposed by Huang and Moan [44], Li et al. [45] and Zhan et al. [46]. Sadananda and Vasudevan [47] insisted that an unambiguous description of fatigue crack growth requires two loading parameters: ΔK and K_{max}. They also pointed out that, by introducing the two-parameter method, many effects, including the R-ratio, can be explained without invoking any extraneous factors, such as the crack closure concept.

Generally, it can be summarised that the FCGR equation in the intermediate regime can be characterised by a unified form: $da/dN = C\,(\Delta K \cdot f(R))^m$. This means that the crack growth driving force can be represented by the multiplication of ΔK and a function of the stress ratio, $f(R)$.

(2) The crack closure model (also called the effective stress intensity factor range method)

Another explanation for the so-called R-effects was provided by Elber [48], who introduced the concept of Plasticity Induced Crack Closure (PICC). Closure involves the premature contact of the crack faces during the unloading portion of a fatigue cycle at a load above the minimum load, and as such reduces the effective driving force for crack propagation.

This model seems to have a more physical basis. Although other crack closure mechanisms have been proposed, PICC is regarded as the dominant crack closure mechanism in the intermediate crack regime [49]. The effect of SIF can be expressed as (K_{max}-K_{op}), where K_{op} is the SIF corresponding to the crack opening force.

Although the crack closure assertion has been debuted by a few investigators, it still attracts extensive application by numerous investigators, such as Newman [50] and McEvily and Ritchie [51]. The key issue of the crack closure model lies in the determination of the crack opening/closing force. Over the past few years, both experimental measurement and numerical analysis have been applied to determine the crack opening/closing force. Experimental measurement of the opening stress in the conventional ASTM Standard [52] is to find a 2% compliance deviation. However, it is well documented that the crack opening force may not be a unique value. It depends on the experimental location and the technique employed. Both global and local compliance techniques have been employed to determine the crack opening force. COD gauges, or strain gauges attached to varied places on the crack mouth adjacent to the expected crack plane, across that plane, or even on the back-face, have been employed in the literature. In general, measurements taken at locations remote from the crack tip would yield lower apparent opening loads than measurements taken near the crack tip. Regarding the compliance offset criterion in experimental determination of the crack opening force, aside from the recommended 2% offset method, a 0% offset method or 4% offset method have also been used for different materials, e.g. structural steels [53]. In addition, the idea of partial crack closure has been proposed by Donald [54]. Up tonow , both the two-parameter method and the crack closure method have been employed extensively, and are found to be equally effective in correlating the crack growth data in a wide range of materials, load ratios and stress intensity levels. For the two parameter method, a proper choice of the effective crack growth driving force is crucial. For the crack closure method, the discrepancies lie in the determination of K_{op}. In the present paper, both methods have been evaluated concerning their ability to correlate the *R*-ratio effect on FCGR.

For an engineering structure without any welds that undergoes in service cyclic loading, a lead crack usually originated from a small naturally occurring material discontinuity, as reviewed by Jones [55], whereas, for a welded joint, it starts to propagate typically from a relatively large crack-like weld defect or irregularity, such as incomplete joint penetration, lack of fusion and/or hot/cold/ delayed cracks [56]. In addition, Welding Residual Stresses (WRSs) also play a vital role in the

FCG of a welded joint. Most published reports have focused on the effect of acicular ferrite on impact toughness and cold cracking [57] for high strength steel welds. The FCG behaviours of high strength steel welds are addressed very seldom. In our previous study, we reported the I-II mixed mode FCG behaviour in the welded joint of a new generation Ni-Cr-Mo-V high strength steel [58]. Qiang Wang [59] investigated the damage tolerance design of the Ni-Cr-Mo-V high strength steel welded joints employed in modern marine structures.

In order to shed light on the remaining life prediction for these welded structures, more fracture mechanics investigations were carried out in this study, with a focus on the effects of several important factors, including stress ratio, microstructure, specimen thickness and Welding Residual Stresses (WRSs) on long crack growth behaviour, which is often seen during fatigue cracking in welded joints due to the nearly unavoidable weld defects that act like cracks. The effects of stress ratio, microstructure, specimen thickness and Welding Residual Stresses (WRSs) were studied extensively. Although the attained FCGR data might not necessarily represent the in-service crack growth behaviour for the base material due to the lack of small crack data, we hope that these results were helpful for the practical engineering damage tolerance design of the welded joints of Ni-Cr-Mo-V high strength steel employed in modern marine structures. As per the Standard ASTM E647-13a [60] the in-service performance of this steel requires the direct measurement of small crack growth rates.

2.4 Numerical analysis methods

The Finite Element Method (FEM), sometimes called Finite Element Analysis (FEA), is a numerical technique used to obtain a solution of problems in engineering [61]. FEM is wide-spread and used in different engineering fields, such as automotive, aerospace, the wind industry, etc.

Analysis of permanent connections such as welded joints of mechanical systems is often a difficult task, because their geometries are often very complex and the applied loads differ significantly. These systems can be described using the differential equations of the system. In many cases, the solution of the differential equation is very difficult, or even impossible, except when the loading and boundary conditions of the problem are simple, which makes direct integration possible [62].

When the geometry and loading conditions are complex, it is impossible to solve the problem based on analytical methods. Such problems can be solved successfully by using numerical methods. The FEM is a numerical method, and one of the more powerful methods for solving engineering problems.

The exact time of the early development of FEM is difficult to determine. In 1943, R. Courant used an assemblage of triangular elements and the principle of minimum potential energy to study a torsion problem. This was the basis of the FEM. The term finite elements was first used by Clought in 1960 in the context of plane stress analysis, and it has been used since that time [63]. The first paper on FEM was published by Argyrisa in 1954, and the first book was published in 1967 by Zienkiewicz and Cheoung.

In recent years a lot of energy has been devoted by different authors to investigate the effect of microdefects such as a Vickers indentation on crack initiation of different materials (brittle and ductile) [65, 66, 67].

K. Zeng [68] presented a comparison of a three-dimensional finite element numerical analysis of Vickers indentation with an experimentally observed indentation load—depth (P—h) relation on brittle materials. The technique of putting a Vickers indentation to measure the residual stress field around an indentation at the surface of material with an FEM numerical calculation has also been used from authors [69, 67].

Additionally, Nguyen et al. [70, 71] developed an analytical model utilising LEFM and FEA, the dimensional analysis technique and superposition approaches, to assess the impact of residual stresses, weld geometry and undercut on the fatigue life of butt-welded joints. The conventional method of fatigue analysis for welded structural components is based on the S-N curve of accepted standards for calculating total life.

On the other hand, the means of FEM numerical methods in estimation of the fatigue of welded structure were presented from Mustafa [72], and the Influence of fillet end geometry on fatigue behaviour of welded joints is given by [73]

3 RESEARCH METHODOLOGY

The main research methods employed during this research can be identified as the experimental methods and numerical analysis methods. The usage of these methods is needed in order to solve the addressed problem. The schematic of the research methodology is presented in Figure 3.1.

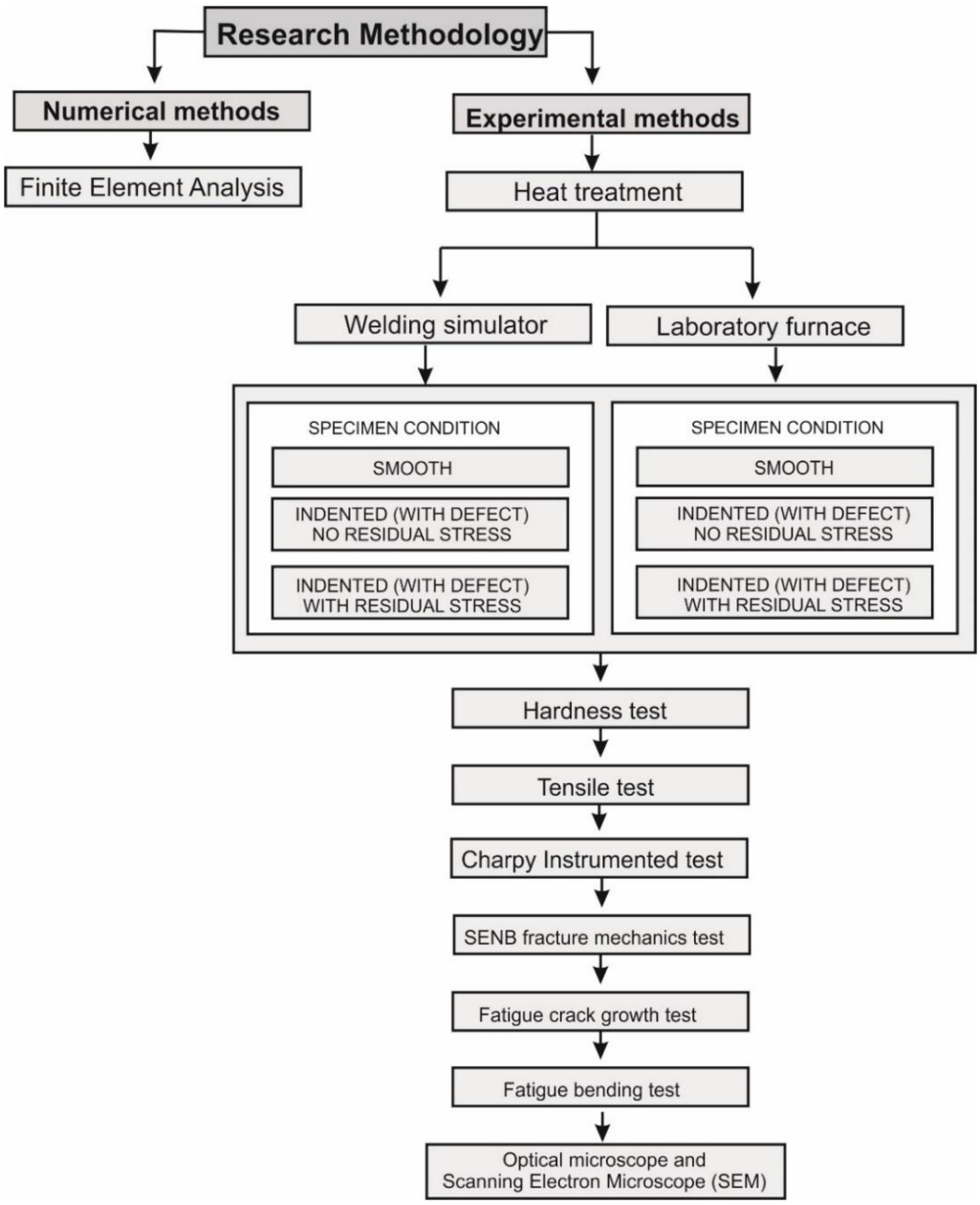

Figure 3. 1 Research methodology of the investigation

As it is shown schematically in Figure 3.1 the research methodology included experimental methods and numerical methods to investigate the phenomena of the crack`s behaviour in the FG HAZ and the residual stress effect around the micro defect. Determination of the exact properties of the fine grain microstructure in the HAZ required the usage of:

1. Heat treatment for microstructure preparation
2. Tensile test,
3. Hardness measurement (Vickers hardness),
4. Instrumented Charpy impact test,
5. SENB fracture mechanics test,
6. Fatigue crack growth rate test,
7. Fatigue bending test,
8. Optical microscope and Scanning Electron Microscope (SEM).

The intention of the usage of these methods will be explained separately in more detail in the next subchapter. The numerical analysis methods were used as a tool for evaluation of the residual stress effect in the vicinity of a defect in the fine grain microstructure, while the experimental measurements were impossible due to the position of the defect on the surface of the specimen.

3.1 Experimental methods

The material used in this study was the nickel molybdenum low alloy steel 18CrNiMo7-6, which is a case hardening steel with high toughness. This steel is used widely for heavy dynamically loaded components. Unfortunately, it is susceptible to cold cracking, although the danger of embrittlement and cold cracking can be decreased by preheating and maintaining the temperature during welding. The chemical composition of the steel in as-delivered condition, according to the Material Certificate, is given in Table 3.1.

Table 3. 1 Chemical composition of 18CrNiMo7-6 alloy steel (weight %)

C	Si	Mn	P	S	Cr	Ni	Cu	Mo	Al
0.18	0.22	0.43	0.012	0.028	1.56	1.48	0.15	0.28	0.023

3.1.1 Base material

The *18CrNiMo7-6* alloy steel in as-delivered condition has these mechanical properties: yield strength (R_{p02}) 484 MPa, ultimate tensile strength (R_m) 634 MPa, (A_5) permanent elongation 26%. Other physical properties of the steel specified by the manufacturer are as follows: modulus of elasticity 210 000 MPa, density 7.870 kg /m^3, thermal conductivity 38 W/ mK, electrical resistance 0.18 Ωmm^2/m, specific thermal conductivity 460 J / kgK, coefficient of linear thermal expansion 11.2·10^{-6} K^{-1} temperature A_{c1} 705 °C, between 20-100 °C and 13.9 ·10^{-6} K^{-1} between 20-500 °C, temperature A_{c1} 705 °C, temperature A_{c3} 790 °C, and the temperature of the beginning of the martensite formation M_s 450 °C. To determine the actual mechanical properties of the starting material, we performed three tensile tests on standard test pieces with a diameter of 12 mm according to standard DIN EN 10002.

3.1.2 Real weld

First, a multi-pass single-V butt weld was made on a 15 mm thick preheated plate, in order to produce a reference microstructure. The welding parameters were determined with respect to the desired cooling time $\Delta t_{8/5}$ = 10 s, according to SIST EN 1011-2, Annex D6 [65], for two-dimensional heat flow. During welding, the cooling time $\Delta t_{8/5}$ was measured with preinstalled thermocouples. The parameters are summarised in Table 3.2.

Table 3. 2 Welding parameters for real welding

I / A	105
U / V	24.2
v_{welding} / cm min^{-1}	14.6
Q / kJ cm^{-1}	8.9
Coated electrode EN ISO 18275-A [66]	E 89 4 ZB62 H5, ϕ3.2 mm
T_{preheat} / °C	200
$T_{\text{interpass}}$ / °C	250
$\Delta t_{8/5}$ / s	10

3.1.3 Heat treatment and microstructure preparation

Heat treatment has been used as a method for microstructure simulation in real weld conditions of a HAZ. The treatment is done according to the Continuous Cooling Transformation diagram (CCT diagram) of *18CrNiMo7-6* steel, which is shown in Figure 3.2 to ensure the required hardness.

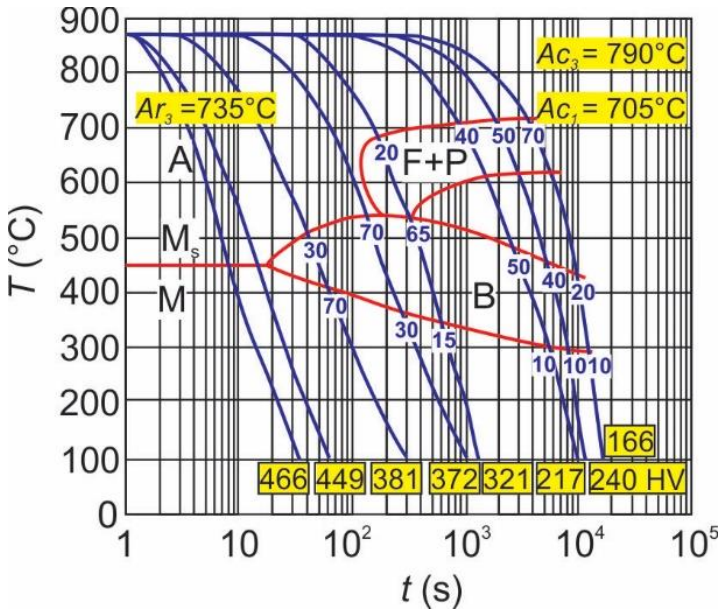

Figure 3. 2 CCT diagram of 18CrNiMo7-6 steel [76]

Two groups of specimens with fine grain microstructures were prepared artificially - simulated by using:

1) A Weld Thermal Cycle Simulator (WTCS), and

2) Austenitising in a laboratory furnace followed by Water Quenching (AF+WQ).

The weld thermal cycle simulator Smitweld 1405 and laboratory furnace Bosio EUP-K 20/1200 were used, respectively. The goal was to achieve the same $\Delta t_{8/5}$ and the same martensitic FG HAZ microstructure as was observed in a real weld FG HAZ, where the average grain size was around 10 μm. The cooling time $\Delta t_{8/5}$ (cooling time between 800 °C and 500 °C) was measured using thermocouples during real welding and during water quenching from 870 °C. In both cases, the $\Delta t_{8/5}$ was 10 s. Therefore, the same $\Delta t_{8/5}$ was used in our investigation, and the parameters used during the experiment are summarised in Table 3.3.

Table 3. 3 Thermal cycles of the simulated specimens

	WTCS	AF + WQ
Heating rate	150 °C s^{-1}	15 min in the preheated furnace
$\Delta t_{8/5}$	10 s	10 s
T_{peak}	1100 °C	870 °C
$T_{preheat}$	200 °C	-

The machine used to simulated FG HAZ specimens is presented below, together with the monitoring display after finishing the simulation.

Figure 3. 3 a) Welding simulator and b) real heat treatment diagram (WTCS)

The WTCS was used to prepare specimens under various conditions, including:

- Without artificial microdefect smooth specimens (SMOOTH),
- With artificial microdefect without residual stress (WoRS),
- With artificial microdefect with the presence of residual stress (WRS).

The second set of specimens was prepared by austenitising in a lab furnace, then quenching in water (AF+WQ). These conditions led to the preparation of specimens in various conditions:

- Without artificial microdefect smooth specimens,
- With artificial microdefect without residual stress,
- With artificial micro-defect with the presence of residual stress.

Figure 3.4 shows the laboratory furnace that was used to simulate the FG HAZ specimens.

Figure 3. 4 Furnace for heat treatment of the specimens

Consequently, the microstructures in the simulated (i.e. artificially prepared) HAZs developed under the same cooling rates as in real welding. The thermal cycles of the simulated FG HAZ specimens are presented graphically in Figure 3.5.

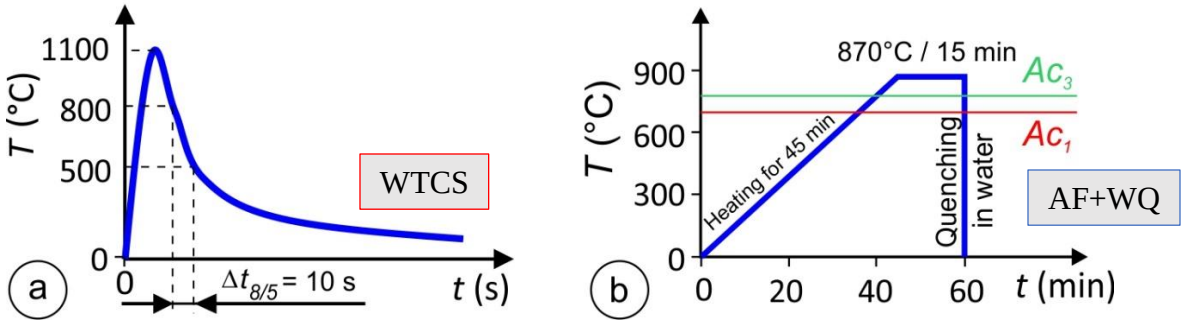

Figure 3.5 Heat treatment of specimens: a) Welding simulator; b) Laboratory furnace

For the AF+WQ specimens, a lower peak temperature was selected compared to the WTCS specimens, in order to obtain similar grain sizes in both types of specimens. Namely, in a furnace, the specimens were inevitably exposed to high temperatures much longer than in a real weld or in the thermal cycle simulator. Consequently, the temperature had to be lower, to prevent excessive grain growth.

In both cases, the cooling rates were controlled via thermocouples, welded onto the specimens. While it was easy to do on the simulator, where the desired cooling curve is assured by the computer-controlled cooling system, for water quenching a special series of specimens was used, to adjust the flow rate of water in the quenching bath.

Two steel states were developed, and these steel states were also used to produce specimens for different test methods like: Tensile, Hardness, Charpy Instrumented test, SENB fracture mechanics and the FCGR test and Fatigue bending test. Also, specimens for SEM (Scanning Electron Microscopy) were prepared in the same conditions. In Table 3.4 are presented the number of specimens also which were prepared for each particular test method.

Table 3. 4 Simulated of WTCS and AF+WQ test specimens for all test methods

WELD THERMAL CYCLE SIMULATOR (WTCS) SPECIMENS									
			Number of simulated specimen						
State	Material	Peak Temp [°C]	Tensile test	Hardness test	Instr. Charpy test	SENB Fracture mechanics	Fatigue crack growth	Fatigue bending test	SEM
SMOOTH	18CrNiMo7-6	1100	2	15	2	2	2	11	1
WoRS	18CrNiMo7-6	1100	-	-	-	-	-	18	-
WRS	18CrNiMo7-6	1100	-	-	-	-	-	13	-
AUSTENITISING IN A LABORATORY FURNACE AND WATER QUENCHING (AF+WQ) SPECIMEN									
			Number of simulated specimen						
State	Material	Peak Temp [°C]	Tensile test	Hardness test	Instr. Charpy test	SENB Fracture mechanics	Fatigue crack growth	Fatigue bending test	SEM
SMOOTH	18CrNiMo7-6	870	2	15	2	2	2	16	1
WoRS	18CrNiMo7-6	870	-	-	-	-	-	15	-
WRS	18CrNiMo7-6	870	-	-	-	-	-	12	-

3.1.4 Hardness test

Vickers hardness *HV* 10 was measured with a Shimadzu HMV-2000 hardness tester in compliance with Standard ISO 6507-1 [77]. ISO 9015–1 [78] was also considered for the real weld FG HAZ. Prior to the measurements, papers up to P 1200, according to Standard ISO 6344-3 [79], were applied for grinding to assure smooth surfaces. The force of 98.1 [N] was applied for 30 seconds to determine the hardness number of the prepared microstructure. Fifteen measurements were taken on a flat surface of each type of specimen, followed by calculation of the average values. After measurement of the hardness number, an artificial microdefect was indented at the notch of the specimens prepared for the bending test in the same applied conditions of the loaded force and time of duration according to the Standard ISO 6507-1 [77].

3.1.5 Tensile test

In the tensile tests 3 specimens were used for investigation of the mechanical properties. The tensile tests were performed with a universal servo hydraulic testing machine, Amsler 559/594, according to the Standard EN ISO 6892-1, method B [80]. Standardised cylindrical specimens were used, with a diameter of 10 mm. The geometry and real shape of the tensile specimen are shown in Figure 3.6.

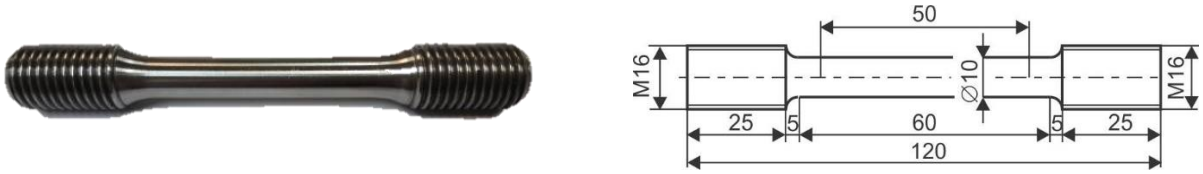

Figure 3. 6 Specimen geometry for the tensile test

3.1.6 Charpy test

The instrumented impact tests were carried out with a Charpy pendulum Amsler RPK300, with a data acquisition rate of 4×10^6 readings per second, according to Standard ISO 148-1 [81]. Standard ISO-V-notch specimens were used for testing and their geometry is shown in Figure 3.7.

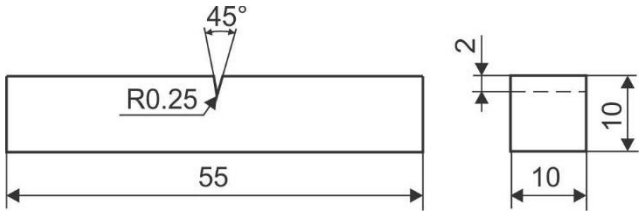

Figure 3. 7 Specimen geometry of the Charpy test

Force versus time and energy versus time diagrams were recorded. The instrumented tests allowed the total energy for fracture E_t (= KV_8 according to Standard ISO 148-1 [81]) to be split into the energy for crack initiation E_i and the energy for crack propagation E_p.

3.1.7 SENB Fracture Mechanics test

Standardised SENB specimens according to Standard ASTM E1820 [82], were used to derive the fracture toughness. The geometry of the specimen is shown in Figure 3.8.

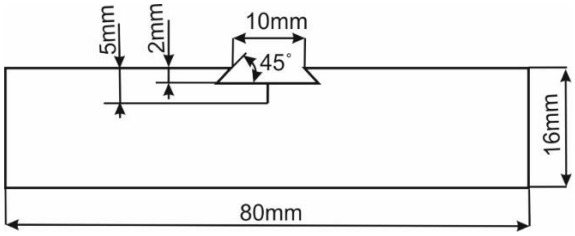

Figure 3.8 Fracture toughness, SENB specimen geometry and dimensions

The specimens were heat treated in similar conditions as for thefatigue test. Fracture toughness testing of the FG HAZ samples was carried out using a Rumul Cracktronic machine, as shown in Figure 3.9, and according to the ASTM Standard E1820-20 [82].

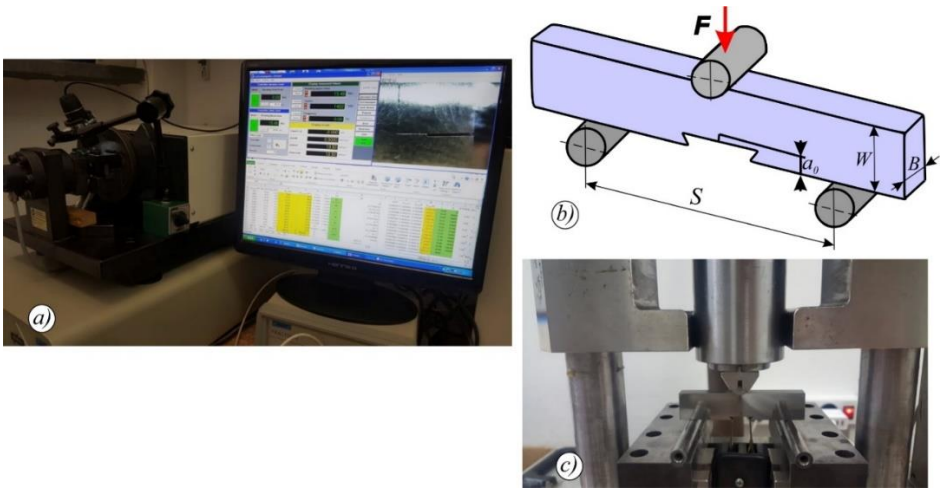

Figure 3. 9 Fracture toughness testing setup on a Rumul Cracktronic; (a) Pre-cracking fatigue (b) Bend test fixture design. (Specimen: B - width; W – height; a_0 – initial crack size; S – support distance; F - load) and (c) photo from the experiment

The range of the initial fatigue crack length corresponded to the guidelines reported in the ASTM E1820 Standard [82], where the following condition should be satisfied: $0.45 \leq a_0/W \leq 0.55$ (W =16 mm and B=7.98 mm for the specimen). The prepared specimens were then subjected to the cyclic bending loading at room temperature on round supports $S = 4 \cdot W = 4 \cdot 16 = 64$ mm (Figure 3.9b) apart with the load applied in the middle, on the opposite side of the initial crack. The bending force and Crack Mouth Opening Displacement (CMOD) were measured until breakage, as specified in the ASTM E1820 Standard [82] (Figure 3.9b).

3.1.8 Fatigue crack growth test

To investigate the crack growth behaviour in a

FG HAZs under cyclic load specimens were prepared, and the geometry of the fatigue crack growth specimens is shown in Figure 3.10.

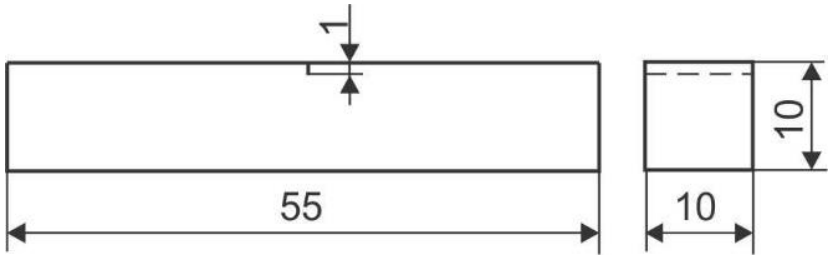

Figure 3. 10 Fatigue specimen: Geometrical shape and Real shape.

The geometry of the specimens was similar to the Charpy specimen, but the notch was different (1 mm deep) and it was prepared by electro erosion machining. The strain gauge foils were attached on the side surface of the specimen, which were used for crack length measurement during testing.

The fatigue crack growth tests were carried out according to Standard ASTM E647-15e1 [52] on a 160 Nm RUMUL Cractronic machine, and Fractomat equipment was used for the fatigue crack growth measurement, Figure 3.11. In order to determine the threshold of the FG HAZ of AF+WQ and WTCS specimens, all tests were performed with a bending load ratio R = 0.1.

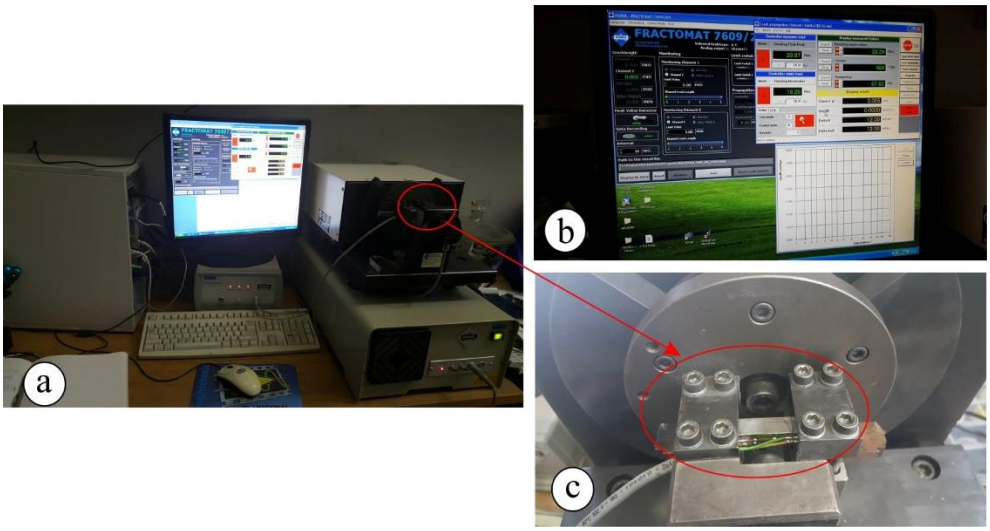

Figure 3. 11 a) The RUMUL Crakctronic and Fractomat machine; b)Set up for loading specimen, and c) Clamping of the fatigue crack growth specimen

3.1.9 Fatigue bending test

In order to find the fatigue strength and endurance limit of the FG HAZ microstructure special specimen geometry was selected to ensure the stress concentration factor of ($K_t = 1.74$). According to Roarks Formulas for stress and strain [74], the geometrical shape of the specimens were prepared in a way which corresponded to, or was equal with the value of the stress intensity factor on the FG HAZ. The calculation of the stress intensity factor was done by using Excel, and the procedure is shown below.

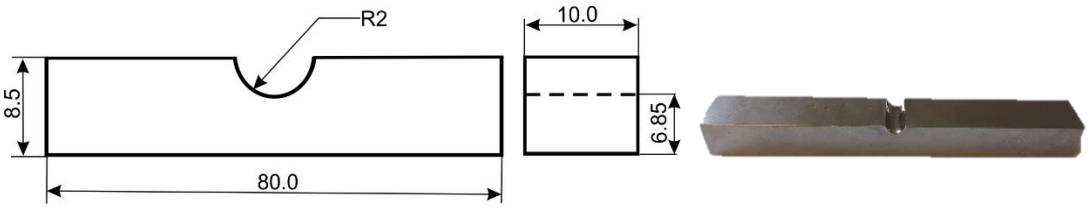

Figure 3. 12 Fatigue specimen: Geometrical shape and Real shape.

According to Roarks Formulas for stress and strain [83], the K_t factor calculation is derived by using equations 3.1 to 3.6 as follows:

:

$$K_t = K_1 + K_2 \cdot \left(\frac{h}{D}\right) + K_3 \cdot \left(\frac{h}{D}\right)^2 + K_4 \left(\frac{h}{D}\right)^3 \tag{3.1}$$

where: $0.5 \leq h/r \geq 4.0$

$$K_1 = 0.721 + 2.394 \cdot \sqrt{\frac{h}{r}} - 0.127 \cdot \frac{h}{r} \tag{3.2}$$

$$K_1 = 0.721 + 2.394 \cdot \sqrt{\frac{h}{r}} - 0.127 \cdot \frac{h}{r} \tag{3.3}$$

$$K_2 = -0.426 - 8.827 \cdot \sqrt{\frac{h}{r}} + 1.518 \cdot \frac{h}{r} \tag{3.4}$$

$$K_3 = 2.161 + 10.968 \cdot \sqrt{\frac{h}{r}} - 2.455 \cdot \frac{h}{r} \tag{3.5}$$

$$K_4 = -1.456 - 4.535 \cdot \sqrt{\frac{h}{r}} + 1.064 \cdot \frac{h}{r} \tag{3.6}$$

for: $D = 8.5\ mm; d = 6.85mm; h = 1.6mm; r = 2mm$

The result of the after calculations of shape geometry of the specimens using Excel, the stress intensity factor ws derived to be $K_t = 1.74$, where:

K_1, K_2, K_3, K_4 - Coefficients of theoretical stress concentration factor [-].

The groove was prepared on the geometry of all specimens for the fatigue bending test according to the calculation mentioned above. The SMOOTH specimens underwent heat treatment directly on both conditions and and after that they were tested for fatigue bending. In the WoRS (without residual stress) specimens, an artificial microdefect was first induced in order to generate stress

concentration, and after that the specimens were heat treated. This procedure resulted in the release of residual stresses induced by the microdefect. Lastly, the WRS specimens (specimens with residual stress), first underwent heat treatment, and then an artificial microdefect was induced, which caused the stress concentration and residual stress remaining in the microstructure (see Table 3.5 for details).

Table 3. 5 Preparation of AF+WQ and WTCS test specimens for the fatigue banging test

WTCS SPECIMENS					
State	Designation of the specimen	Heat treatment	Cause of stress concentration	Type of micro defect	Number of simulated specimens
SMOOTH	S_{WTCS}	After preparing the groove	-	-	11
WoRS	$WoRS_{WTCS}$	After preparing the groove and induced microdefect	Artificial microdefect	Vickers pyramid	17
WRS	WRS_{WTCS}	After preparing the groove and before induced microdefect	Artificial microdefect	Vickers pyramid	13
AF+WQ SPECIMEN					
State	Designation of the specimen	Heat treatment	Cause of stress concentration	Type of microde fect	Number of simulated specimens
SMOOTH	S_{AF+WQ}	After preparing the groove	-	-	16
WoRS	$WoRS_{AF+WQ}$	After preparing the groove and induced microdefect	Artificial microdefect	Vickers pyramid	15
WRS	$WoRS_{AF+WQ}$	After preparing the groove and before the induced microdefect	Artificial microdefect	Vickers pyramid	11

All specimens were loaded at the load ratio R=0.1.

3.1.10 Chapetti model

The limit of stable fatigue crack propagation will be determined by applying the Chapetti model to evidence gathered from experiments conducted using the formulas below. As Miller [75] stated, the existence of a microstructural and mechanical threshold is what distinguishes fatigue resistance. The material's intrinsic microstructural properties affect the microstructural threshold directly. It is the minimum stress required for a Microstructurally Short Crack (MSC) to pass through the strongest microstructural barrier, which is typically a distinctive microstructural dimension like grain size. Evidence from earlier research by Chapetti et al. [76, 77] shows that this intrinsic threshold stress level corresponds to the material's simple fatigue limit. Considering this, the Chapetti model's [76] definition of the microstructural or intrinsic threshold ΔK_{dR} is calculated by equation 3.7 as follows:

$$\Delta K_{dR} = Y \Delta \sigma_{eR} \sqrt{\pi d} \tag{3.7}$$

where:

ΔK_{dR} - microstructural or intrinsic threshold [Mpam$^{0.5}$]

d - is the location of the strongest microstructural barrier (for example, grain size) [μm],

Y - is the geometric correction factor [-],

$\Delta \sigma_{eR}$ - is the material's plain fatigue limit [Mpa].

The geometric correction factor Y was set to be 0.65, since MSCs nucleated at surfaces are typically thought to be semi-circular [78]. The 'R' subscript indicates that as $\Delta \sigma_{eR}$ is R-ratio dependent, ΔK_{eR} is also.

The Chapetti model predicts that the crack propagation threshold also consists of an "extrinsic" component, K_C, which depends on crack length in addition to the microstructural threshold. When this component has developed fully, it reaches the maximum value (for long cracks), K_{CR}, which is constant for a specific material and load ratio. The difference between the microstructural threshold, K_{dR}, and the long crack propagation threshold, K_{thR}, is what is referred to as the maximal extrinsic component, which is calculated by equation 3.8 as:

$$\Delta K_{CR} = \Delta K_{thR} - \Delta K_{dR} \tag{3.8}$$

An exponential function of the following form presented in by equation 3.9 can be used to describe the development of K_C as a function of crack length:

$$\Delta K_C = \Delta K_{CR}\left(1 - e^{-ka}\right) \tag{3.9}$$

where:

a - is the crack length,

k - is a material coefficient [-]

R - load ratio (dependent constant that defines the shape of the ΔK_C curve) [-].

The material threshold as a function of crack length is then defined by equation 3.10 as:

$$\Delta K_{th} = \Delta K_{dR} + \Delta K_C = Y\Delta\sigma_{th}\sqrt{\pi d} \quad a \geq d \tag{3.10}$$

From expressions (3.8) and (3.9) can be derive equation 3.11:

$$\Delta K_{th} = \Delta K_{dR} + (\Delta K_{thR} - \Delta K_{dR})\left[1 - e^{-k(a-d)}\right] \quad a \geq d \tag{3.11}$$

It is now important to define the value of the constant k, responsible for the behaviour of ΔK_C, the extrinsic component of ΔK_{th}.

The initial hypothesis that this model takes into account is that the strongest microstructural barrier, which is located at position d, defines the plain fatigue limit, or $\Delta\sigma_{eR}$. This model's second hypothesis is that the threshold stress level for cracks longer than d must be equal to or lower than the plain fatigue limit.

The final form used to estimate the parameter k, is by using equation 3.12:

$$k = \frac{1}{4d}\frac{\Delta K_{dR}}{(\Delta K_{thR} - \Delta K_{dR})} = \frac{1}{4d}\frac{\Delta K_{dR}}{\Delta K_{CR}} \tag{3.12}$$

This expression was later proved to work very well with experimental data for eight different materials. More details are given in reference [76].

It can be seen that the Chapetti model is defined fully once $\Delta\sigma_{eR}$, ΔK_{thR} and d are known, all being parameters that can easily be obtained from common standardised fatigue tests and metallographic analysis.

Finally, we have to consider that the Chapetti model does not take into account the effect of residuals` stresses. For measurement of the residual stresses the numerical analysis was used, and were implemented on a KT-diagram (see Subchapter 6.8).

3.2 Numerical analysis methods

Due to the geometry of the specimens, especially due to the rounded groove where the indented artificial microdefect was induced, it was impossible to get the correct value of the residual stresses levels around the microdefect by using standard measuring methods. Therefore, our approach to get a solution was oriented on numerical analysis methods, to measure the residual stresses around the defect correctly. In this case, we used ABAQUS/CEA as a software for the FEA simulation.

The determination of residual stresses due to Vickers pyramid indentation is simulated on a flat surface and also in a groove, and four different models were simulated for this:

1. Vickers pyramid indentation on a flat surface
2. Vickers pyramid indentation on a groove with residual stress (WRS condition)
3. Vickers pyramid indentation on a groove without residual stress (WoRS condition taking into account the shape of indentation only)
4. Smooth model

3.2.1 FEM model of Vickers pyramid indentation on a flat surface

To determine the residual stresses in the vicinity of the Vickers pyramid indentation, we used the results of the instrumented indentation, and also used them to construct and control the applied numerical model. The experimental data for FG HAZ were obtained by indentation on a flat surface. This is a diagram of the applied force - depth during loading and unloading of the Vickers pyramid. Therefore, we simulated the indentation numerically first on a flat surface to adjust the correct coefficient of friction.

The full model of the Vickers pyramid was defined for the numerical model. We developed a geometric model, which is shown in Figure 3.13. The material properties for FG HAZ were prescribed in (Chapter 6). We have also prescribed an analytical rigid face represented by a full model of the Vickers pyramid. It was assumed that the coefficient of friction between the FG HAZ and the analytical rigid face was 0,07.

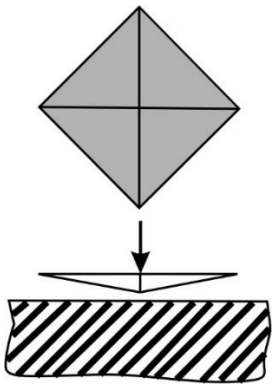

Figure 3. 13 The shaded part of the Pyramid was prepared for the numerical model of the FEA.

Figure 3.14 shows the numerical model mesh. The mesh, in the indented area, is structured and dense. For the grid we used the 8-node brick element labelled C3D8.

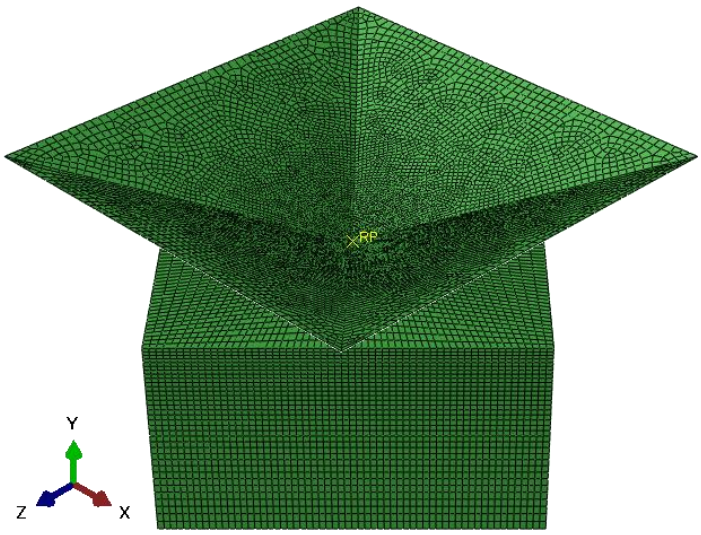

Figure 3. 14 Geometric model and the numerical model with a mesh grid.

Table 3.6 gives the number and type of elements used in the numerical model with FEM.

Table 3. 6 Number of elements and nodes used.

Location	Type of element	Number of elements	Number of nodes
Material to be stamped	C3D8	42000	393766
Vickers pyramid	C3D8	2536	2602
Total		44536	396368

The model was implemented on symmetry planes, where symmetry boundary conditions were given, which are shown in Figure 3.15.

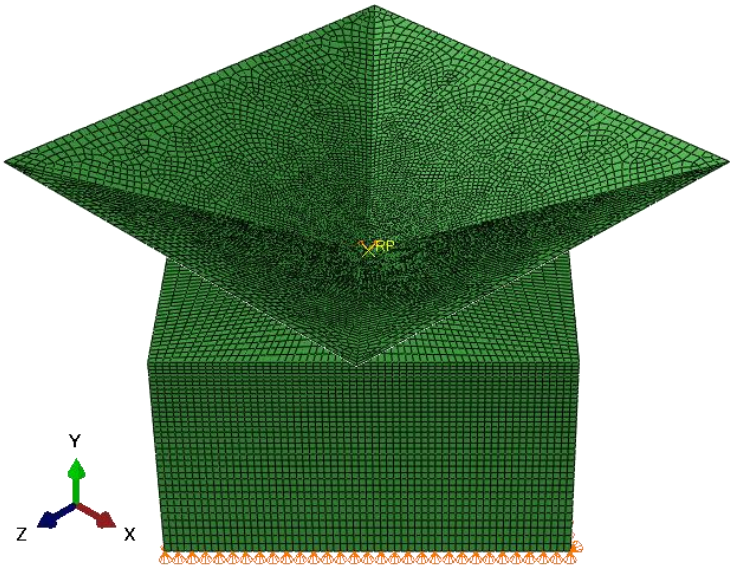

Figure 3. 15 Clamping boundary conditions view $u_1=u_3=\phi_1=\phi_2=\phi_3=0$. Support from down plane (XZ) + load y direction F = -98,1N

A discrete rigid body was used as the Vickers pyramid, and used to define the load boundary conditions. The pyramid was then compressed progressively up to a force of 98.1 N. Equilibrium was established between the resistance of the steel and the compressive force on the pyramid. The pyramid was stationary. The pyramid was then removed in the direction of displacement u_2.

Table 3.7 gives the boundary conditions of the load at each step. A 3D elasto-plastic analysis was used and the Von Mises yield criterion.

Table 3. 7 Load boundary conditions.

Step	Operation	Implementation in the numerical model	Boundary conditions load in the numerical model	Load
1	Indentation	Force on the pyramid	$u_1=u_3=0,\phi_1=\phi_2=\phi_3=0$	F_2= -98.1N, u_2=results
2	Pyramid lifting	Pyramid displacement	$u_1=u_3=0,\phi_1=\phi_2=\phi_3=0$	$F_2=0$, $u_2=0$

3.2.2 FEM model for Vickers pyramid indentation on a groove with residual stress (WRS)

The experience gained from the simulation of the indentation of a Vickers pyramid on a flat surface was used to simulate the indentation of a Vickers pyramid in the groove of a cuboid test specimen. The experimental force-depth of indentation diagrams for the loading and unloading of the Vickers pyramid for this case could not be measured due to shape of the groove with radius 2 mm. The shaded and hatched parts of the test specimen in Figure 3.16 were used for the numerical model with FEM.

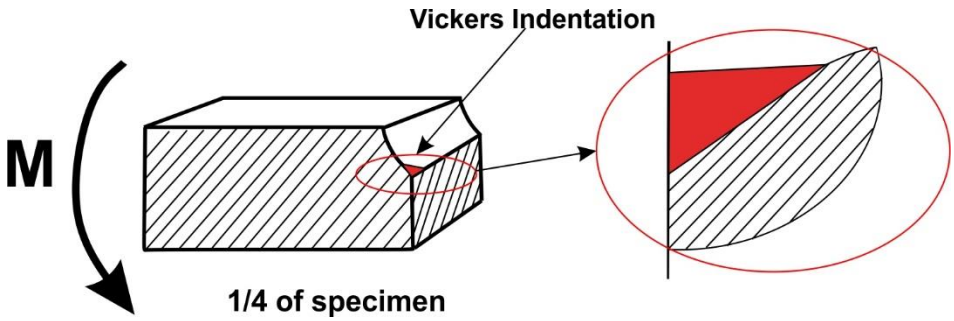

Figure 3. 16 Model used for the numerical calculation (FEM)

Since the specimen was two time plane symmetrical, so we used a ¼ specimen and a ¼ Vickers pyramid. From these we constructed a geometric model. We prescribed the material properties of FG HAZ in (Subchapter 3.1.1). In addition, we modelled two analytical rigid surfaces, one representing the Vickers pyramid and the other used to define the bending load at the end of the specimen. We defined the same coefficient of friction between the FG HAZ and the analytical rigid face of Vickers indenter and specimen in the groove as before (0.07). The adequacy of the Vickers pyramid indentation simulation results was checked by the achieved Vickers pyramid indentation depth, which could be determined experimentally after the indentation due to groove shape with radius 2 mm.

Figure 3.17 shows the numerical model with the mesh. The mesh was condensed and structured in the area of the Vickers pyramid indentation. Within this area, we used three dimensional rigid elements with a 8-node brick element labelled C3D8.

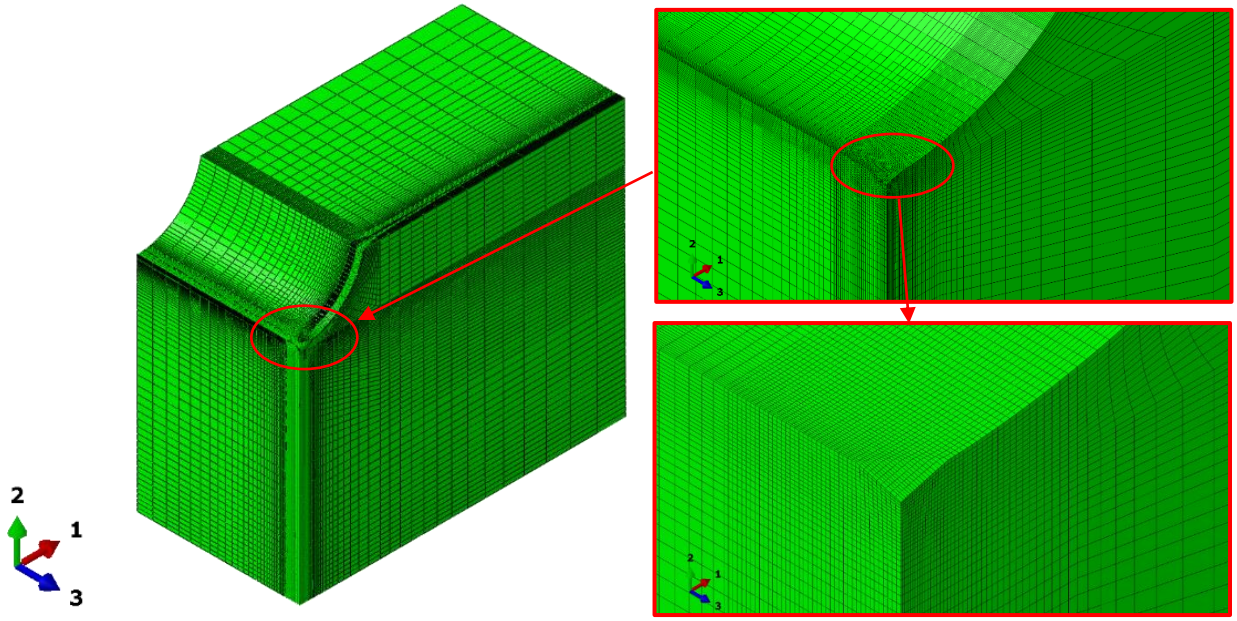

Figure 3. 17 Geometric model and the numerical model with mesh and detail of the structured mesh for the simulation of the Vickers pyramid indentation.

Table 3.8 gives the number of elements and nodes used in the numerical model.

Table 3. 8 Number of elements and nodes used.

Location	Type of element	Number of elements	Number of nodes
The specimen body	C3D8	42000	393766
Discrete rigid body - load	C3D8	2536	2602
Total		44536	396368

We imposed symmetry boundary conditions on the symmetry planes of the model, to prevent displacements in the normal direction of these planes and twists outside these planes. The clamping boundary conditions are shown in Figure 3.18.

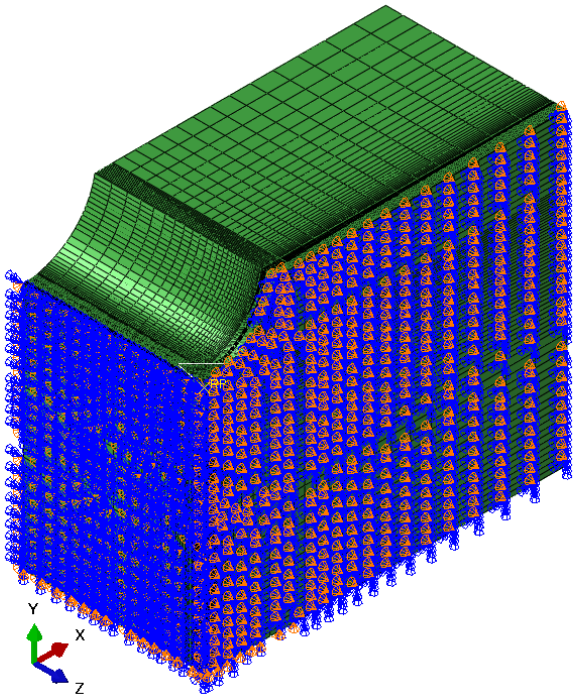

Figure 3. 18 Symmetry boundary condition of the clamping, indentation support from down side

The load boundary conditions are given on an analytically rigid surface representing the surface of the Vickers pyramid, and are shown in Figure 3.19.

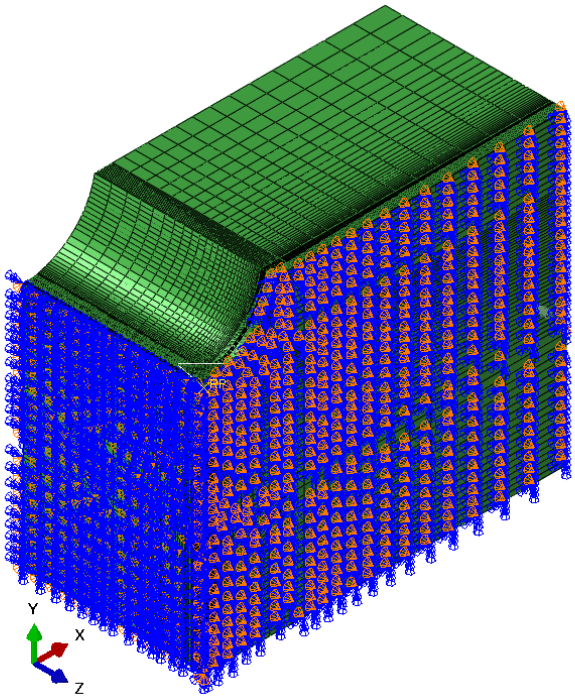

Figure 3. 19 Load boundary conditions of indented specimen loaded by moment Mz not supported from down side in Y direction

The load on the pyramid was applied by displacing an analytically rigid surface representing the face of the pyramid, in the direction of displacement u_2 until equilibrium with material response of specimen was reached. After this stage pyramide (analytically rigid surface) was removed out indentation. In next stage bending moment $M_{z\ specimen}$ = 30782 N·m was applied to specimen. The value of the bending moment was the same as in experiment where fatigue limit was reached. A detailed description is given in Table 3.9, in ¼ model of the specimen in FEA model we actually used just ½ $M_{z\ specimen}$, what correspond to the loading of M_z = 15391 N·m on endurance limit at this condition σ_{eR} = 675 MPa.

Table 3. 9 Load boundary conditions

Step	Operation	Implementation in the numerical model	Boundary conditions` load in the numerical model	Load
1	Indentation	Force on the pyramid	$u_1=u_3=0, \phi_1=\phi_2=\phi_3=0$	F_2 = -98.1N, u_2 = results
2	Pyramid lifting	Pyramid displacement		F_2= 0, u_2=0
3	Loading to the fatigue limit	Moment bending	$u_1=u_3=0, \phi_1=\phi_2=\phi_3=0$	M_z=15391Nm

3.2.3 FEM model of Vickers pyramid indentation on a groove without residual stress (WoRS)

The experience gained from the simulation of the indentation of a Vickers pyramid on a flat surface was used to simulate the indentation of a Vickers pyramid in the groove of a cuboid test specimen. The force-depth of the indentation diagrams for the loading and unloading of the Vickers pyramid for this case could not be measured. The shaded and hatched parts of the test specimen in Figure 3.20 were used for the numerical model with FEM.

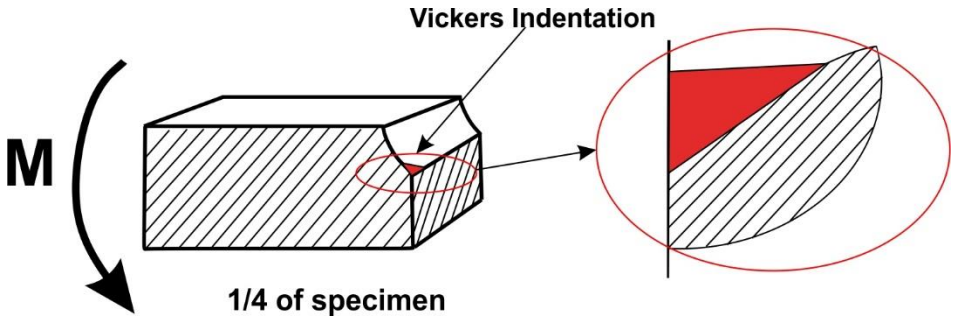

Figure 3. 20 Model used for the numerical calculation (FEM)

Since the specimen was 2 times plane symmetry, we used a ¼ subject and a ¼ Vickers pyramid. From these we constructed a geometric model. We prescribed the material properties of FG HAZ in (Subchapter 3.1.1). In addition, we modelled two analytical rigid surfaces, one representing the Vickers pyramid and the other used to define the bending load at the end of the specimen. We defined the same coefficient of friction between the FG HAZ and the analytical rigid face of Vickers indenter and specimen in the groove as before (0.07). The adequacy of the Vickers pyramid indentation simulation results was checked by the achieved Vickers pyramid indentation depth, which could be determined experimentally after the indentation due to groove shape with radius 2 mm. Figure 3.21 shows the numerical model with the grid. The grid was condensed and structured in the area of the Vickers pyramid indentation. Within this area, we used three-dimensional rigid elements with an 8-node brick element which is called C3D8.

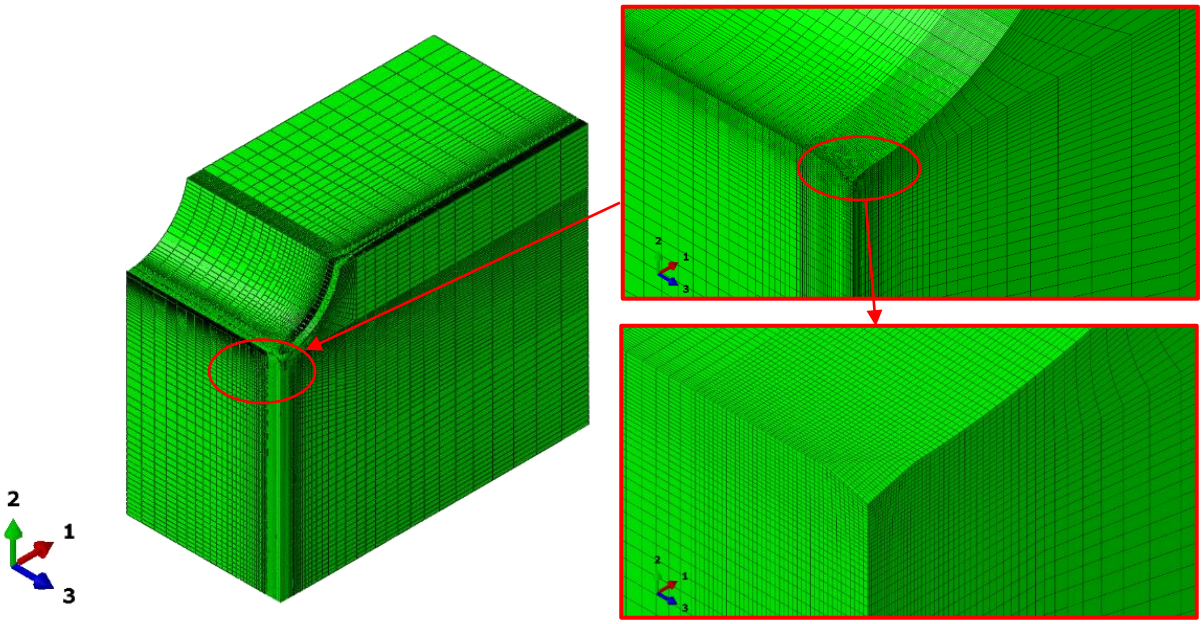

Figure 3. 21 Geometric model and the numerical model with mesh grid.

Table 3.10 gives the number of elements and nodes used in the numerical model.

Table 3. 10 Number of elements and nodes used.

Location	Type of element	Number of elements	Number of nodes
The specimen body	C3D8	42000	393766
Discrete rigid body - load	C3D8	2536	2602
Total		44536	396368

We imposed symmetry boundary conditions on the symmetry planes of the model to prevent displacements in the normal direction of these planes and twists outside these planes. The clamping boundary conditions are shown in Figure 3.22.

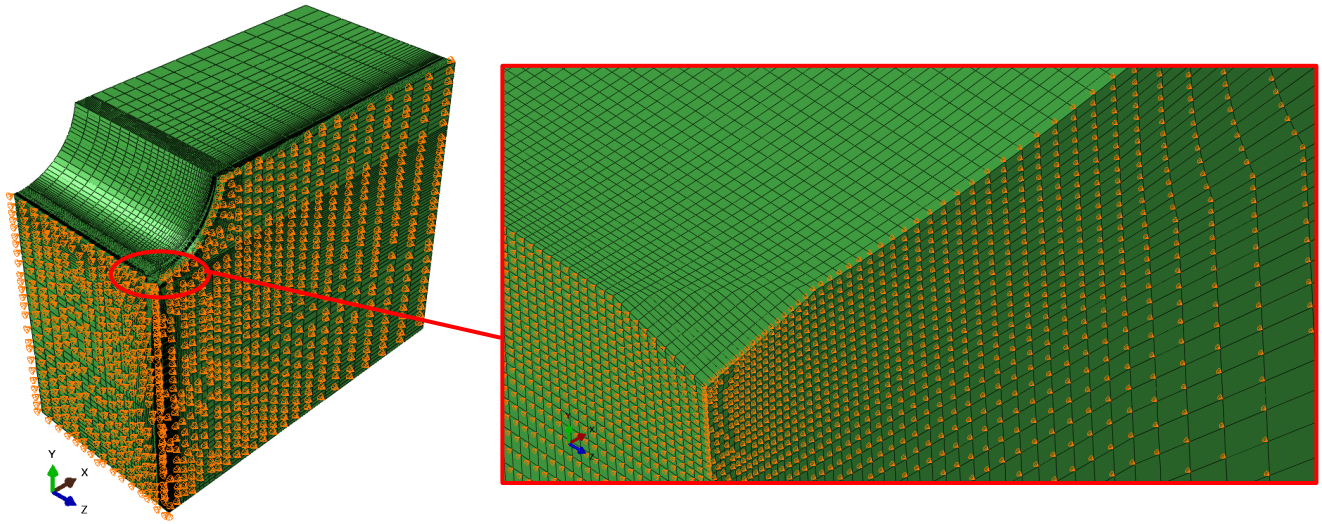

Figure 3. 22 Symmetry boundary condition of the clamping; 1/4 numerical model (a), model detail at indentation of the Vickers pyramid (b).

The load boundary conditions are given on an analytically rigid surface representing the surface of the Vickers pyramid, and are shown in Figure 3.23.

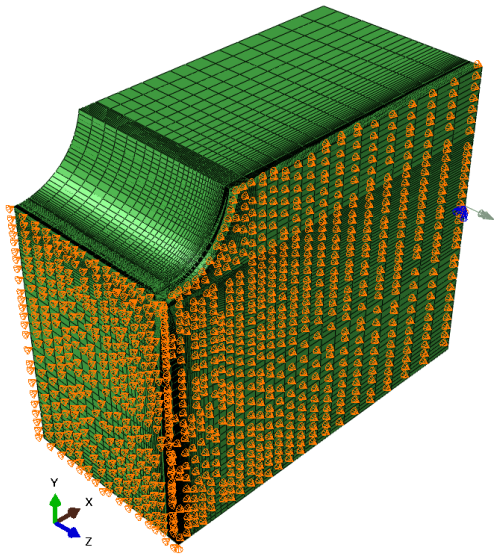

Figure 3. 23 Load boundary conditions

The load on the pyramid was applied by displacing an analytically rigid surface representing the face of the pyramid in the direction of displacement u_2. This particular case was loaded to the fatigue limit by including residual stresses.

The load on the pyramid was applied by displacing an analytically rigid surface representing the face of the pyramid, in the direction of displacement u_2 until equilibrium with material response of specimen was reached.

After this stage pyramide (analytically rigid surface) was removed out indentation. In next stage bending moment $M_{z\ specimen}$ = 30782 N·m was applied to specimen. The value of the bending moment was the same as in experiment where fatigue limit was reached. A detailed description is given in Table 3.11, in ¼ model of the specimen in FEA model we actually used just ½ $M_{z\ \text{specimen}}$, what correspond to the loading of M_z = 12541 N·m on endurance limit at this condition σ_{eR} = 550 MPa.

Table 3. 11 Load boundary conditions

Step	Operation	Implementation in the numerical model	Boundary conditions` load in the numerical model	Load
1	Indentation	Force on the pyramid	$u_1=u_3=0, \phi_1=\phi_2=\phi_3=0$	F_2= -98.1N, u_2=results
2	Indentation	Pyramid displacement	$u_1=u_3=0, \phi_1=\phi_2=\phi_3=0$	F_2= 0, u_2=0
3	Removed RS	(due to the deformed geometry of the Vickers indentation remaining, the stress- strain field was removed)		
4	Loading to the fatigue limit	Moment bending	$u_1=u_3=0, \phi_1=\phi_2=\phi_3=0$	M_z=12541 N·m

3.2.4 FEM model of a Smooth model

Simulation of this type of specimen was done without putting an indentation. Moment banding was applied to the test specimen, as shown in Figure 3.24 for the numerical model with FEM.

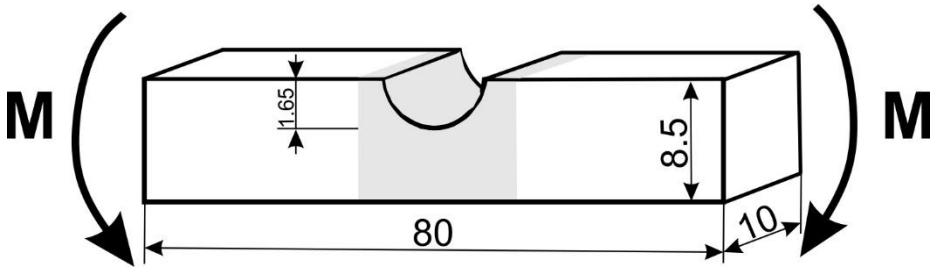

Figure 3. 24 Test specimen with a groove was used for the numerical model.

Since the specimen was 2 times plane symmetry, we used a ¼ subject and a ¼ Vickers pyramid. From these we constructed a geometric model. We prescribed the material properties of FG HAZ in (Subchapter 3.1.1).

In addition, we modelled two analytical rigid surfaces, one representing the Vickers pyramid and the other used to define the bending load at the end of the specimen. We defined the same coefficient of friction between the FG HAZ and the analytical rigid face of Vickers indenter and specimen in the groove as before (0.07).

The adequacy of the Vickers pyramid indentation simulation results was checked by the achieved Vickers pyramid indentation depth, which could be determined experimentally after the indentation due to groove shape with radius 2 mm. Figure 3.25 shows the numerical model with the grid. The grid was was condensed and structured in the area of the Vickers pyramid indentation.

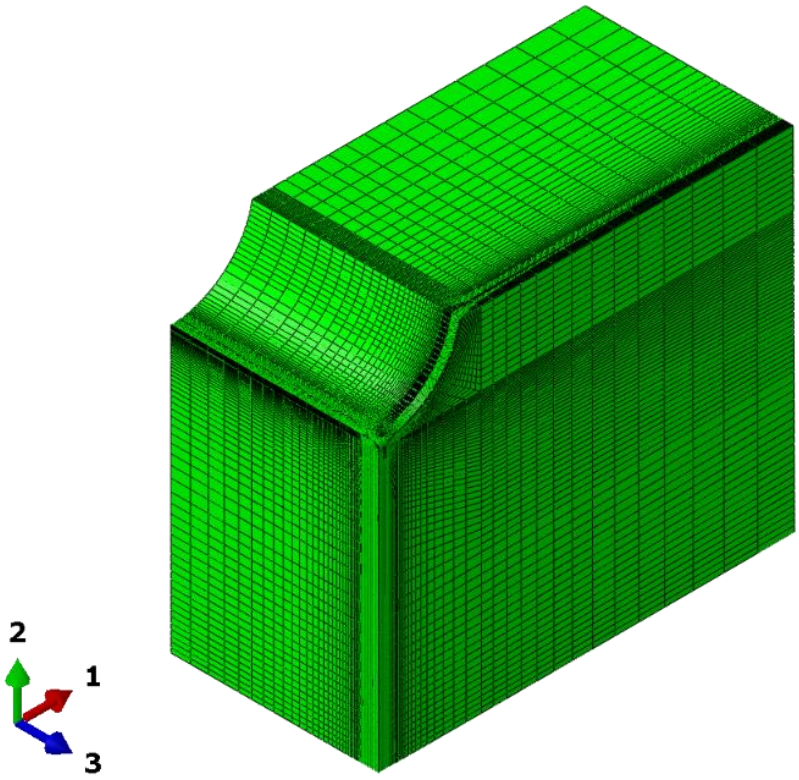

Figure 3. 25 Geometric model and the numerical model with mesh grid

The grid was condensed and structured in the area of the groove. Within this area, we used three-dimensional rigid elements with a 8-node brick element, labelled C3D8.

Table 3.12 gives the number of elements and nodes used in the numerical model.

Table 3. 12 Number of elements and nodes used.

Location	Type of element	Number of elements	Number of nodes
The specimen body	C3D8	42000	393766
Discrete rigid body - load	C3D8	2536	2602
Total		44536	396368

We imposed symmetry boundary conditions on the symmetry planes of the model to prevent displacements in the normal direction of these planes and twists outside these planes. The clamping boundary conditions are shown in Figure 3.26.

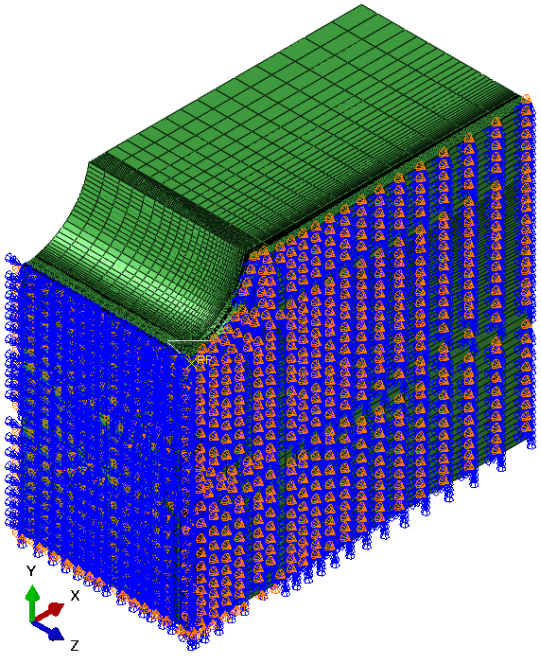

Figure 3. 26 Symmetry boundary condition of the clamping full numerical model

The load on the pyramid was applied by displacing an analytically rigid surface representing the face of the pyramid, in the direction of displacement u_2 until equilibrium with material response of specimen was reached. After this stage pyramide (analytically rigid surface) was removed out indentation. In next stage bending moment $M_{z\ specimen}$ = 30782 N·m was applied to specimen. The value of the bending moment was the same as in experiment where fatigue limit was reached. A detailed description is given in Table 3.13, in ¼ model of the specimen in FEA model we actually used just ½ $M_{z\ \text{specimen,}}$ what correspond to the loading of M_z = 15391 N·m on endurance limit at this condition σ_{eR} = 675 MPa.

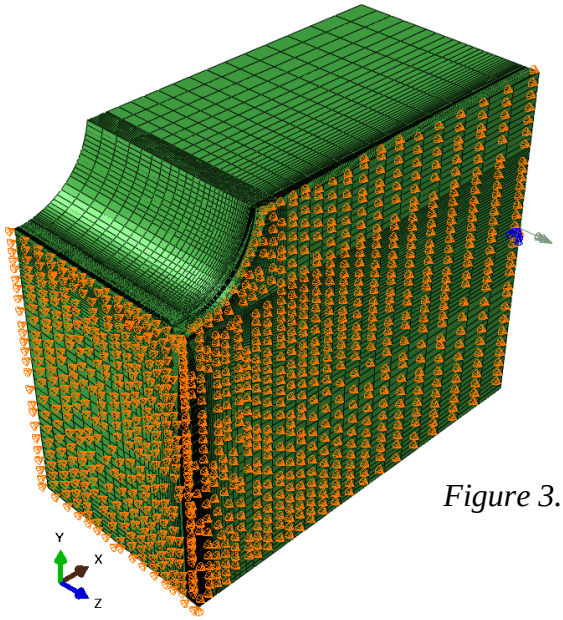

Figure 3. 27 Load boundary conditions

Table 3. 13 Load boundary conditions

Step	Operation	Implementation in the numerical model	Boundary conditions load in the numerical model	Load
1	Loading to the fatigue limit	Moment bending	$u_1=u_3=0, \phi_1=\phi_2=\phi_3=0$	M_z= 15391 N·m

4 FATIGUE PROBLEM OF A WELD JOINT

4.1 Factors that influence fatigue in a weld joint

Some factors, which affect the fatigue life of a welded joint significantly are explained shortly and in separation form as follows:

4.1.1 Effect of welding residual stresses

During the welding process, due to the heat generated by the arc, residual stresses remain in the area of the weld, either in the HAZ or fusion zone. The mean stress a welded joint may face in application, can be altered due to the welding processes implementing residual stresses, changing the fatigue life, and can render S-N laboratory testing results. Welded assemblies, with geometrical imperfections, can also introduce residual stresses. Removal of residual stresses by stress relief methods can only be achieved partially. Residual stresses can still remain in a welded joint, even after some of these stress relief methods have been achieved. It found that the welding residual stresses influence the fatigue strength and fatigue life of the support greatly. Consequently, the welding residual stresses must be minimised or eliminated at the key areas of the support.

4.1.2 Effect of the thickness of the member

Looking at things from a statistical point of view, a larger population contains more extreme defect sizes, both large and small. The presence of larger defects leads to crack growth and failures at lower stress levels, hence, a lower endurance limit. An increase in the thickness of a base material will contribute to a decrease of the fatigue strength, due to increasing the possibilities of the presence of small defects or irregularities in the base material. This can also be due to an increase in the residual stress concentrations in thick material cross-sections.

4.1.3 Effect of material type

All materials have varying physical and mechanical properties. As a material`s ultimate tensile strength increases, this does not lead to an increase in fatigue strength. This is not the case when evaluating materials that do not contain welded joints. Therefore, stress-cycle curves for welded joints cannot be correlated to the material`s ultimate tensile strength. Most design information has been developed for structural steels.

4.1.4 Effect of the welding process

Many welding processes are available for various applications and environments. Stress-cycle curves are not available for all of these processes, and still need to be developed so that proper fatigue analysis can be performed. The most abundant process found in stress-cycle curves is developed from specimens prepared by arc welding.

4.1.5 Effect of the Environment

The surrounding environment can affect the fatigue life of a welded assembly, often lowering it. Points such as temperature, moisture and geographical location are considered part of the surrounding environment. Environments which contain sea water may see decreased fatigue life due to the increase in crack growth rates. Little information is available in this area, but it is known that, if a base material is subjected to corrosion, the fatigue strength can decrease to what is similarly found in welded joints.

4.1.6 Avoiding Fatigue Failures of a Welded Joint

Since the presence of cracks reduces fatigue life and accelerates failure, it is important to avoid all cracking mechanisms in order to prolong the fatigue life of a welded joint. Other weld defects, such as inclusions and lack of penetration, should also be avoided, due to these defects being the source of where cracks can initiate. A detailed review of the welded joint during the design is another way to reduce failures. Ensuring that the design is able to handle the cyclic loading profile will prevent premature failures. Additional resources through design handbooks are also available to aid in designing the welded joint to optimise fatigue life. Finite Element Analysis can also be used to predict fatigue failure successfully.

4.2 Mean stress and load ratio R effect

4.2.1 Mean Stress Effect

Mean stress is one of the significant factors which effect the fatigue life of structural components. From the perspective of applied cyclic stresses, the fatigue damage of a component correlates strongly with the applied stress amplitude or applied stress range, and is also influenced by the mean stress. The mean stress effect should be considered seriously in fatigue analyses. In the HCF regime normal mean stresses have a significant effect on the fatigue behaviour of components.

Mean normal stresses are responsible for the opening and closing state of micro-cracks. Since the opening of micro-cracks accelerates the rate of crack propagation and the closing of micro-cracks retards the growth of cracks, tensile mean normal stresses are detrimental, and compressive mean normal stresses are beneficial in terms of fatigue strength. There is very little or no effect of mean stress on fatigue strength in the LCF regime, where the large amount of plastic deformation reduces any beneficial or detrimental effect of the mean stress significantly.

At high mean stress, the decrease in fatigue life is associated with multiple crack initiation sites at the specimen`s surface. The fatigue limit is affected highly by the tensile mean stress and stress ratio, R = 0.7, since the maximum stress approaches near yield stress and causes cyclic ratcheting.

The mean normal stress effect can be represented by the mean stress ($S_{\sigma,m}$) or the stress ratio (R). Both are defined as follows:

$$S_{\sigma,\mathrm{m}} = \frac{(S_{\sigma,\max} + S_{\sigma,\min})}{2} \tag{4.1}$$

$$R = \frac{S_{\sigma,\min}}{S_{\sigma,\max}} \tag{4.2}$$

where:

$S_{\sigma,\max}$ - are the maximum normal stresses in a stress cycle [MPa],

$S_{\sigma,\min}$ - are the minimum normal stresses in a stress cycle [MPa],

R - load ratio [-].

For an example of a fully reversed condition it can be found that $S_{\sigma,m} = 0$ and $R = -1$. The early models to account for the mean stress effect, such as Gerber [79], Goodman [80], Haigh [81], Soderberg [82], and Morrow [83], were usually plotted against empirical data in constant life plots of stress amplitude ($S_{\sigma,a}$) versus mean stress ($S_{\sigma,m}$). In Germany, these constant life plots are called Haigh's diagrams; in North America they are referred to commonly as Goodman's diagrams.

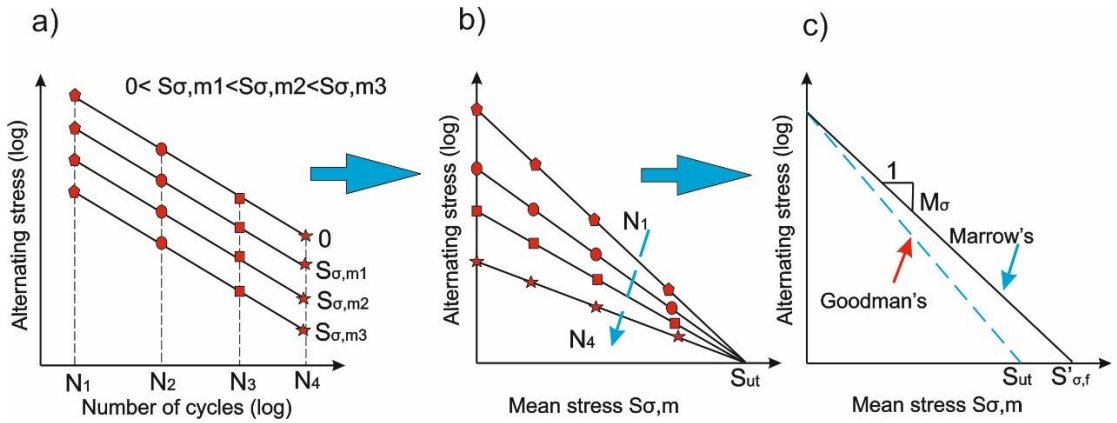

Figure 4. 1 Construction of constant life plots on normal stress in the $S_{\sigma,a}$ and $S_{\sigma,m}$ coordinates.

As illustrated schematically in Figure 4.1, a Haigh's diagram can be determined from a family of constant amplitude $S_{\sigma,a} - N$ curves (Wohler curves) with various mean stress values (0, $S_{\sigma,m1}$, $S_{\sigma,m2}$, and $S_{\sigma,m3}$). The equivalent fully reversed stress amplitude ($S_{\sigma,ar}$) is the generic interception point of the $S_{\sigma,a}$ axis, which is used to determine the fatigue life (N_i) from a corresponding component *S-N* curve.

According to Goodman's and Morrow's models as illustrated in Figure 4.1(c) and equations 4.3-4.6, the ultimate tensile strength ($S_{t,u}$) and the fatigue strength coefficient ($S_{\sigma,f}$) are the physical limits to $S_{\sigma,m}$ and the interception of the $S_{\sigma,m}$ axis, respectively. Alternatively, Haibach in the FKM-Guideline introduces the mean stress sensitivity factor (M_σ) to define the Haigh diagram, which is the absolute value of the slope of the constant life plot. The $M\sigma$ factor depends on the type of materials and loading condition.

Even though numerous models have been developed to account for the mean stress effect and load ration on fatigue strength and lives, the four commonly used formulas were chosen for discussion: Goodman's [80], Morrow's [83], Smith–Watson–Topper's [84], and Walker's [85].

The differences between the four models can be observed from the following expressions of the fully reserved stress amplitude in the case of moderate mean stress values:

- Goodman's:

$$S_{\sigma,\mathrm{ar}} = \frac{S_{\sigma,\mathrm{a}}}{1 - \frac{S_{\sigma,\mathrm{m}}}{S_{t,\mathrm{u}}}} \tag{4.3}$$

- Morrow's:

$$S_{\sigma,\mathrm{ar}} = \frac{S_{\sigma,\mathrm{a}}}{1 - \frac{S_{\sigma,\mathrm{m}}}{S^{f}{}_{\sigma,\mathrm{f}}}} \tag{4.4}$$

- SWT's:

$$S_{\sigma,\mathrm{ar}} = \sqrt{S_{\sigma,\mathrm{max}} S_{\sigma,\mathrm{a}}} = \sqrt{(S_{\sigma,\mathrm{a}} + S_{\sigma,\mathrm{m}}) S_{\sigma,\mathrm{a}}} \tag{4.5}$$

- Walker's:

$$S_{\sigma,\mathrm{a}} = S^{1-\gamma_w}{}_{\sigma,\mathrm{a}} S^{\gamma_w}{}_{\sigma,\mathrm{a}} = (S_{\sigma,\mathrm{a}} + S_{\sigma,\mathrm{m}})^{1-\gamma_w} S^{\gamma_w}{}_{\sigma,\mathrm{a}} \tag{4.6}$$

where:

γ_w - is a mean stress fitting parameter

The SWT and the Walker equations predict that a fatigue crack will not initiate if the maximum normal stress in a cycle is less than or equal to zero, meaning $S_{\sigma,max} \leq 0$ [86].

4.2.2 Load ratio (R)

Load ratio R is defined as the ratio of the minimum and maximum loads during the fatigue loading. Without environmental effects, the load ratio has a more significant effect on the stages I and III fatigue crack growth rates than in Stage II, as illustrated in Figure 4.2 [14]. In Stage I the fatigue threshold tends to decrease with increasing *R*, and hence the da/dN is higher at higher *R* at the same ΔK. In Stage III, the higher da/dN at higher *R* is a consequence of the critical condition that the maximum stress intensity factor K_{max} which can be calculated as $\Delta K/(1-R)$, approaches the fracture toughness *Kc*. In Stage II, the fatigue crack growth rate is controlled by *ΔK* (Paris law) and is relatively insensitive to the load ratio.

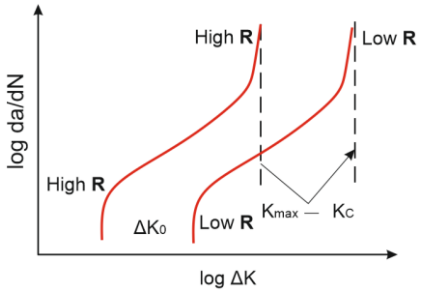

Figure 4. 2 Schematic of the effect of load ratio on da/dN

It is clear that the stress ratio has a significant impact on fatigue life: the higher the *R* value, for a given maximum stress, the greater the number of cycles until breakage. Passing from *R* = 0.1 to *R* = 0.7 can improve fatigue life by two decades.

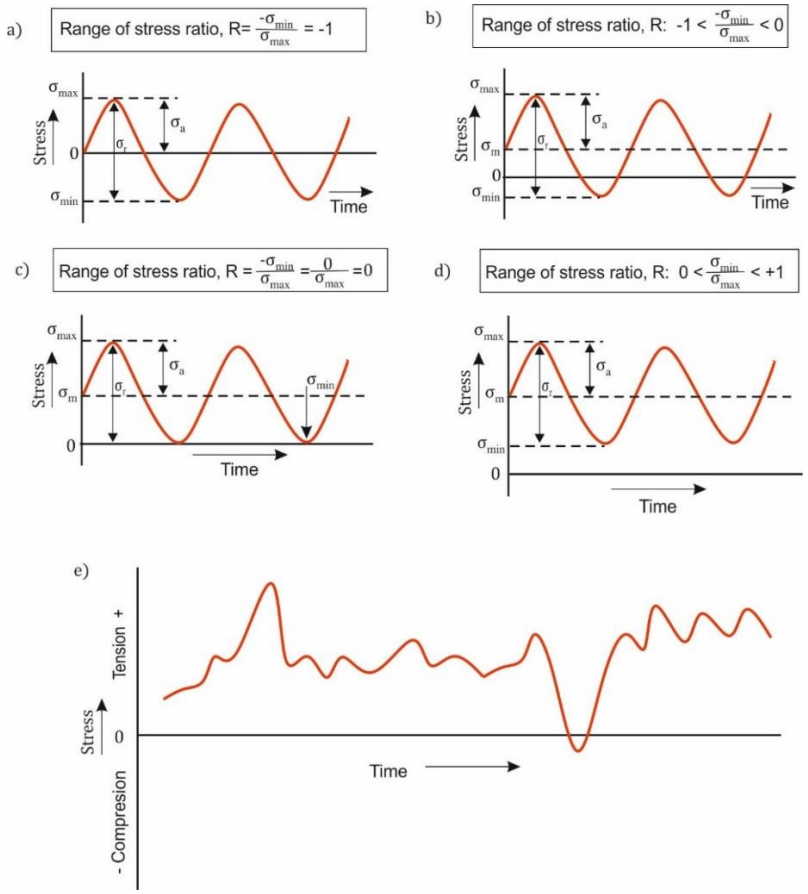

Figure 4. 3 Typical time-varying fluctuating stress cycles in fatigue: a) Completely reversed stress cycle; b) Partly reversed tension-compression; c) Pulsating stress; d)Tension-tension type pulsating; e) Irregular or random stress cycle

4.3 Roughness and stress concentration factor

Surface roughness and surface integrity resulting from manufacturing processes are both important considerations in fatigue design. In fact, the effects of surfaces on the fatigue life of metals have been recognised for many years [87], [88]. Fatigue damage on the surface of a component typically develops due to the surface integrity resulting from manufacturing, and the presence of stress concentrations originating from the surface topography. In general, the fatigue strength of engineering components increases with a decrease in the surface roughness [89]. However, standard surface roughness parameters cannot always be used for a reliable measure of the reduction in fatigue strength attributed to surface texture [90], [12], [91]. Theoretically, an uneven geometric profile has a lot of side-by-side micro notches lying on the surface of the machined specimen, from where stress concentration initiates. Therefore the stress concentration factor can be defined as:

$$K_t = 1 + 2\sqrt{\gamma \cdot \frac{R_z}{\rho}} \tag{4.7}$$

where:

K_t - denotes the stress concentration factor [-],

γ - refers to the ratio between spacing and depth of the asperities, which approximately equals to 1,

R_z is the 10-point roughness [μm],

ρ - is the effective profile valley radius of the surface texture [μm].

It is known that the if machined surface becomes rougher, it will lead to larger R_z and smaller ρ. According to this it is easy to conclude that K_t has an increscent trend. Then the stress amplitude $\Delta\sigma$ in the notch is the nominal stress amplitude Δe multiplied by K_t, as expressed in Equation (4.8).

$$\Delta\sigma = K_t \cdot \Delta e \tag{4.8}$$

Attention should be drawn to the fact that the stress concentration factor K_t is always greater than 1. Based on the theory of the local stress-strain method, fatigue life depends on the local stress-strain field, and a greater local stress-strain leads to lower fatigue life. Generally speaking, the

fatigue life is reduced as the surface roughness is increasing under the premise of the same load condition. The theory of the stress concentration factor presents a qualitative explanation for the phenomenon that fatigue life is inversely proportional to roughness. However, little attention has been paid to the quantitative relationship between them.

Attempts have been made to find the character of this kind of relationship through the fatigue experiment, and the preliminary results are shown in Figure 4.4. [92]

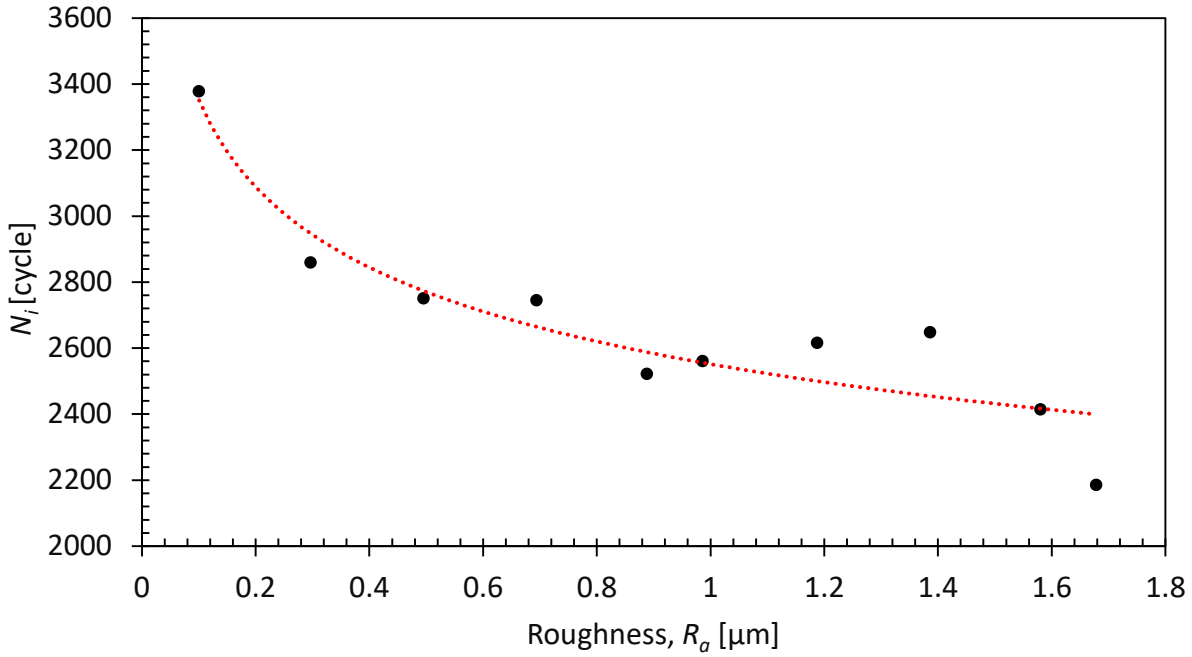

Figure 4. 4 Relationship between the roughness and the fatigue life

A power function curve was used to fit these data. As a result, the curve is expressed by Equation (4.9).

$$N_i = 2559 \cdot R_a^{-0.1166} \tag{4.9}$$

It can be seen that the curve reflects the relationship between the two variables well. The result provides some reference significance for engineering application, because the roughness of most structures or components belongs to the range from 0.2µm to 1.6µm.

5 PHYSICAL MICRODEFECT ON THE FG HAZ OF A WELD JOINT

5.1 Analyse of the HAZ on weld joint

A HAZ formed during welding, is an area in which some structural changes in the welded material take place as the result of the experienced temperature. The knowledge of a whole area weld joint and its subareas of the HAZ is important from a practical point of view, since, as shown in [93], a FG HAZ is in a critical place in terms of fatigue and creep strength. This applies in particular to those technological operations in which welding technologies are used for manufacturing or repair. The HAZ adjacent to the native material ixpact by heat has a lower fatigue resistance than the native material and only at maximum load (immediate tensile strength) appears at a trans–crystalline breakthrough in the native material, as shown in [93]. The cracking of the material beyond the HAZ indicates good ultimate strength of the joint, but does not guarantee a good fatigue and creep strength. In the case of fatigue and creep, the most dangerous place in the welded joint is (as mentioned earlier) is the area of fine-grained structure lying in the HAZ.

The structure of a HAZ is created as a result of welding effects [94], and it has:

- a tendency of the joint to the formation of cold cracks,
- an impact on the performance and properties of the welded construction, and in particular its resistance to brittle cracking in the presence of a microdefect.

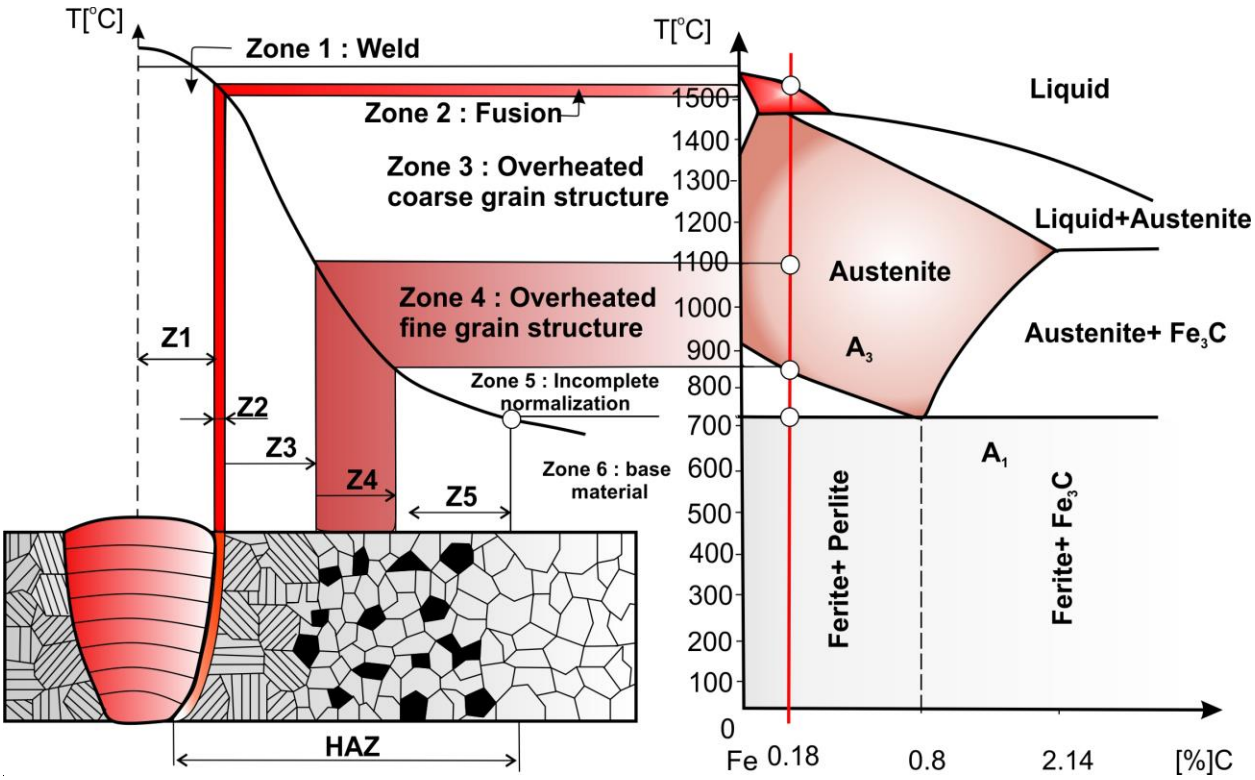

Figure 5. 1 An example of a HAZ structure for carbon steel containing 0.18% C

From a comparison of Figure 5.1 the following designations could be described:

CG HAZ - zones 2 and 3 – HAZ with coarse grain structure, heated to a temperature of (1100 ^{o}C $\leq T_{max} \leq T_m$),

where: T_m – is the steel melting point,

FG HAZ - zone 4 – HAZ with a fine grain structure, heated to a temperature above A_3 ($900 \leq T_{max.} \leq 1100^{o}$C),

IC HAZ - zone 5 – a HAZ heated to a temperature above A_1 in the range A_1-A_3 ($700 \leq T_{max.} \leq 900^{o}$C),

OT HAZ - zone 6 – a HAZ heated to a temperature below A_1 in the range ($600 \leq T_{max.} \leq 700^{o}$C).

For carbon steel of carbon content < 0.8% in a temperature below A_1 no structural changes occur in the welded material, see Figure 5.1. An austenitic change occurs at A_1 temperature. The homogenisation of austenite occurs above A_3. In the temperature range A_1 to A_3 the growth occurs of austenite grains. For steels with a carbon content of ≥ 0.8% points A_1 and A_3 overlap. Steel

containing 0.8% C is called a eutectoid. High temperatures occurring during the welding process promote austenitisation and the growth of austenite grains. Contrarily, a high heating rate and short holding time at high temperature limit the growth of grains.

5.2 HAZ prepared in a welding simulator

A HAZ microstructure can be prepared by using different procedures, for instance, by using a weld thermal simulator or by using a furnace and quenching. For the process of the HAZ microstructure formation it is important to know welding, the heat input during welding (welding parameters) and the thickness of the base material. All these parameters have an influence on the width of the HAZ regions and cooling rate. The process of FG HAZ simulation by using a welding simulator is explained schematically in Figure 5.2.

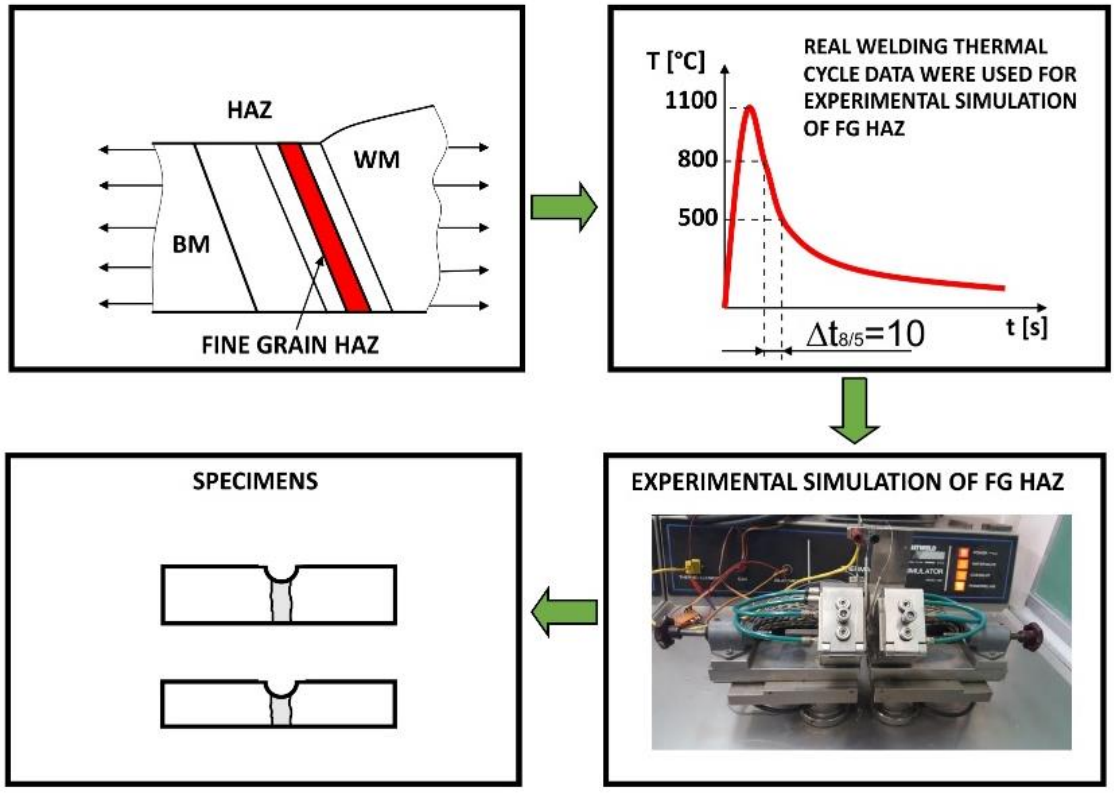

Figure 5. 2 HAZ preparation by using a weld thermal simulator. Redrawn [95]

Because most of the transformations happened on this steel between the temperatures 800 and 500°C, the cooling time $\Delta t_{8/5}$ is crucial for the microstructure formation. The cooling time $\Delta t_{8/5}$ is easy to measure, or it can be calculated from the welding parameters by using the EN ISO 1011-2 Standard procedure. The other important parameters for the simulation of the specific part of the HAZ on the weld thermal simulator are: Peak temperature reached in the HAZ during welding, preheating temperature, holding time on the peak temperature and the end temperature of the simulation. It is possible to measure all these parameters during welding of a real weld, or calculated by using the EN ISO 1011-2 Standard procedure. Recalling equations of the moving heat source are used for the construction the influence of the weld thermal cycle during welding on FG HAZ material. These data are used for the simulation, which was performed on unaffected base material (top left and top right parts of Figure 5.2). In the case of an FG HAZ of the steel 18CrNiMo7-6, the parameters were measured during the real weld, where the cooling time $\Delta t_{8/5}$ was 10 s and the peak temperature was 1100°C. All the parameters necessary for the simulation are in Table 5.1, and the entire influence of the weld cycle used for FG HAZ microstructure preparation is shown in Figure 5.3.

Table 5. 1 Parameters for FGHAZ simulation by using a weld thermal simulator

Heating rate (°C/s)	Preheating temp. (°C)	Peak temperature (°C)	Holding time at peak temperature (s)	Cooling time Δt8/5 (s)	Finish time (s)
150	50	1100	3	10	70

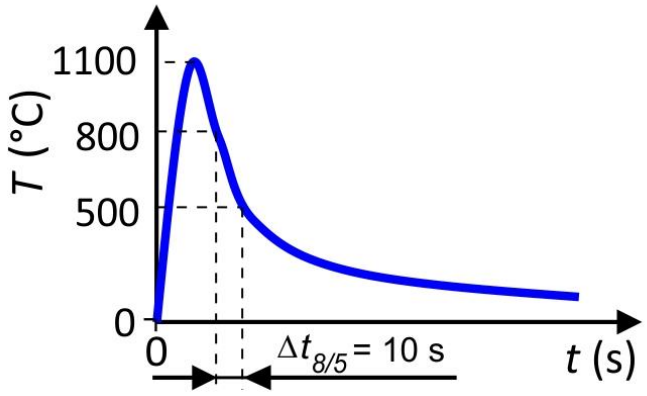

Figure 5. 3 Influence of the weld thermal cycle used for the FG HAZ microstructure preparation

5.3 HAZ prepared in a laboratory furnace

Preparation of the FG HAZ in the furnace is more complicated than in the case of using a weld thermal simulator, but the advantage in compression in the case of a fine grain microstructure prepared by the welding simulator is that the entire specimen has a unified microstructure. Therefore, the preparation of the microstructure in the furnace is required to be precise and accurate according to the holding time and temperature to get an appropriate FG HAZ microstructure.

The first step is coarsening the austenite grains, where coarsening of the grain can be obtained by high temperatures for short periods, or lower temperatures for a longer time. The target size of the crystal grains in our case was 12.8μm, which appeared during the real welding FG HAZ. The temperature of 870°C was chosen in order to achieve the size of the grains. The holding time on the temperature was determined experimentally by simulating and observing the grain size. Samples of the base material were heated and held in the furnace at a temperature of 870°C for 15 mins, and they were finally quenched in water. Consequently, the martensitic microstructures were formed with differently small grains.

The diagram of the heat simulation for two different temperatures (870°C and 1100°C) are compared and shown in Figure 5.4, which explains practically that the higher heat input the slower cooling rate, and vice versa [96].

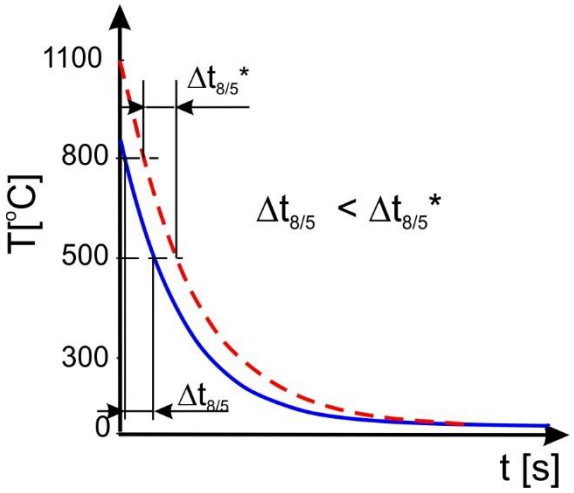

Figure 5. 4 $\Delta t_{8/5}$ measurements at quenching in water.

In this investigation the average target size of the microstructure was 12.8μm, and by holding specimens at 870°C it was required to stay for 15mins for the formation of the martensitic microstructure. This holding time was chosen for further investigation.

For the appropriate FG HAZ microstructure formation the cooling rate during quenching should be the same as during welding. This means that the cooling time $\Delta t_{8/5}$ needs to be the same. The cooling time during quenching was measured experimentally. Investigation revealed that by cooling in water at a temperature of 870°C it is possible to reach a cooling time of $\Delta t_{8/5}$ 10 s, but by cooling in water at a temperature of 1100°C, this time is longer [97]. The reason behind this is accumulated heat in the specimen, which cannot allow the specimen to cool down so fast in contact with the water.

The schematic of heat treatment of the preparation of the FG HAZ microstructure in the furnace can be seen in Figure 5.5. The first step of the FG HAZ preparation was heating to 870°C for 45min and then holding at a temperature of 870°C for 15min. The intention was to achieve grain coarsening (an austenite microstructure) and then followed by water quenching to achieve the proper cooling rate and right FG HAZ microstructure.

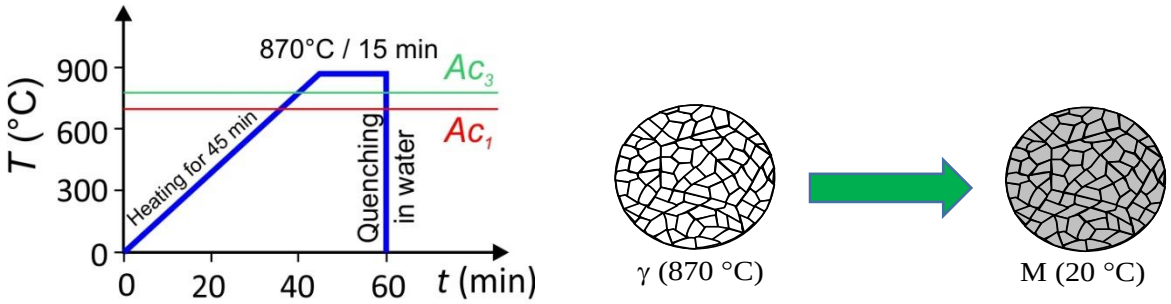

Figure 5. 5 FG HAZ microstructure preparation regime in the furnace

5.4 Influence of a physical defect in the FG HAZ

It is useful to think about solids in terms of a regular repeating pattern of planes of particles, but, in reality, it is important to recognise that solids` crystallography is seldom perfectly ordered. Defects are always present in the microstructure, and depending on their size and shape, in short,

a weld defect is any flaw or imperfection that compromises the intended use of a weldment. These are classified according to ISO 6520-1:2007 [98].

This also implies a flaw or imperfection that may not compromise the weld, and a weld is said to have a discontinuity when this occurs. So, a weld can have a discontinuity and not be considered defective. These acceptable limits are specified in ISO 5817 [99] and ISO 10042 [100].

However, if enough discontinuities exist (i.e., they exceed the limit as defined in an applicable code or specification), then the discontinuities become classified as defects, and the weld is rejected. A weld must be strong enough for the intended purpose at the most basic level, and many defects can weaken a joint. However, in some cases, your weld must be aesthetically pleasing too. Therefore, most defects either weaken a weld or make it look ragged and unpresentable. As a design engineer we expect and want to avoid having failure of welds due to defects. Therefore , it is required to know the types of defects that can occur and how to avoid them.

According to the Standard ISO 6520-1:2007 [98], defects are typically classified into 13 common types. There are many types of welding defects, but, in general, the most common weld defects are: Cracks, Inclusions, Lack of fusion, Porosity, Undercut, Poor penetration, Burn through, Under-fill, Excess reinforcement, Spatter, Over-roll/Overlap, Whiskers, Mechanical damage. The nature and severity of a defect determines in which of the categories it belongs. However, when a particular defect occurs, you want to know which parameter needs adjusting so you can fix it. Therefore, a list by defect type, along with how to correct the problem, is helpful.

However, defects also appear in the HAZ of a weld joint, and their presence in the fine grain microstructure can deteriorate the reliability of whole welded joint. Due to the sensitivity of the microstructure and weakness of the grain borders as a result of defects` presence or short cracks, the microstructure cannot decelerate or even stop the crack initiation, and further propagation orginates from such short cracks.

An important consequence of the fatigue behaviour of short cracks is that a transition crack length exists, below which the threshold stress intensity range ΔK_{th} is smaller than that for long cracks, and such a length is dependent on the material`s microstructure.

The overall dependence of threshold stress intensity range on the crack length (crack-size effect) is described by a ΔK_{th} against a plot, known as a ‘Kitagawa-Takahashi diagram’ (Figure 5. 6).

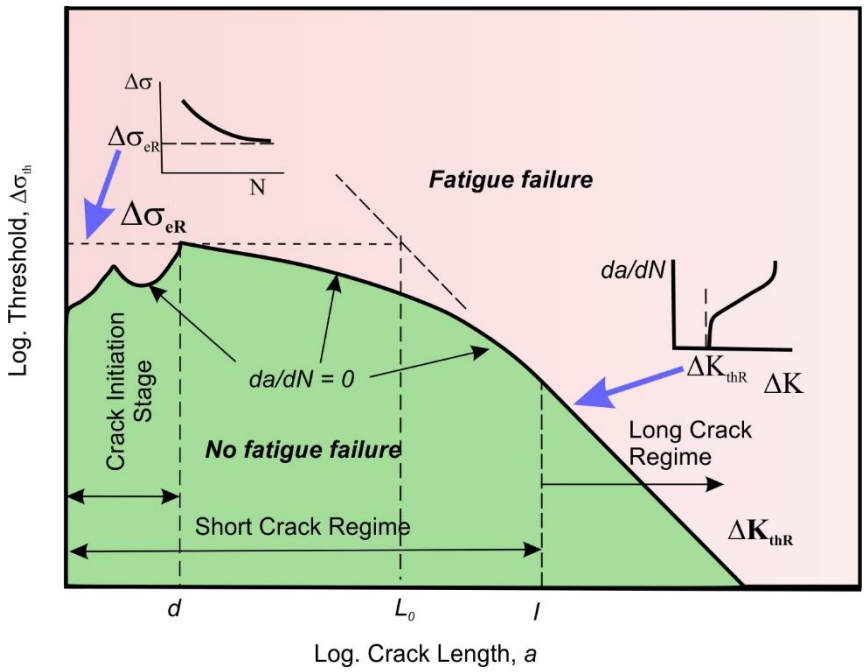

Figure 5. 6 Schematic representation of the Kitagawa-Takahashi diagram [75]

Similarly to fracture toughness, which defines the limit of unstable crack propagation, the threshold ΔK_{th} defines the limit of stable fatigue crack propagation. The threshold stress intensity range is calculated experimentally for a conventional very low propagation rate *da/dN* (usually 10^{-11} m/cycle), and is typically determined for long fatigue cracks. For such crack sizes, the threshold stress intensity range ΔK_{th} is found to be a property of the material independent of the crack length.

The results of our investigation after fatigue testing of specimens with fine grain microstructure in presence of a microdefect revealed that the microdefect on a fine grain microstructure acts as a crack, and it propagates all the time once it initiates.

6 EXPERIMENTAL RESULTS

The results of the micrographs and the experimental testing data for all test methods which were used during the investigation of the mechanical properties of a fine grain microstructure are presented in this Chapter.

6.1 Real weld and the fine grain microstructure

Specimens with fine grain microstructures have been the subject of grinding, polishing and etching in order to ensure appropriate micrographs. The grinding process was done using plates from P100 to P1200, and, after that, the polishing process with aluminium suspension (Al_2O_3), and finally the surface of specimens was the subject of an etching process for 30 seconds with etchant H_3PO_4. The surface microstructures of the specimens are presented in Figure 6.1 for a real weld, as well as for the Weld Thermal Cycle Simulator (WTCS) specimens and for the Austenitising in a laboratory Furnace followed by Water Quenching (AF+WQ) specimens are presented in Figure 6.2.

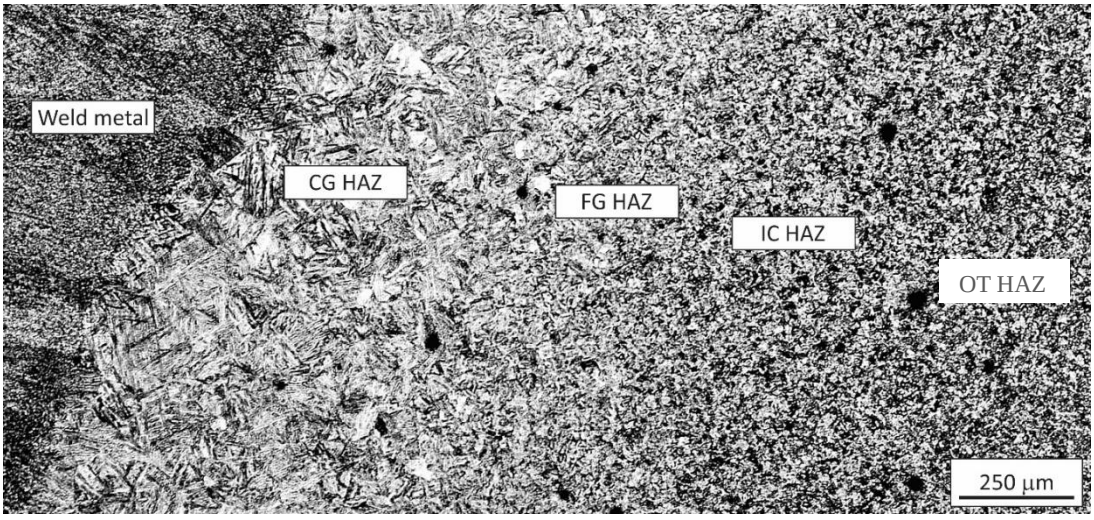

Figure 6. 1 Real weld and HAZ microstructure

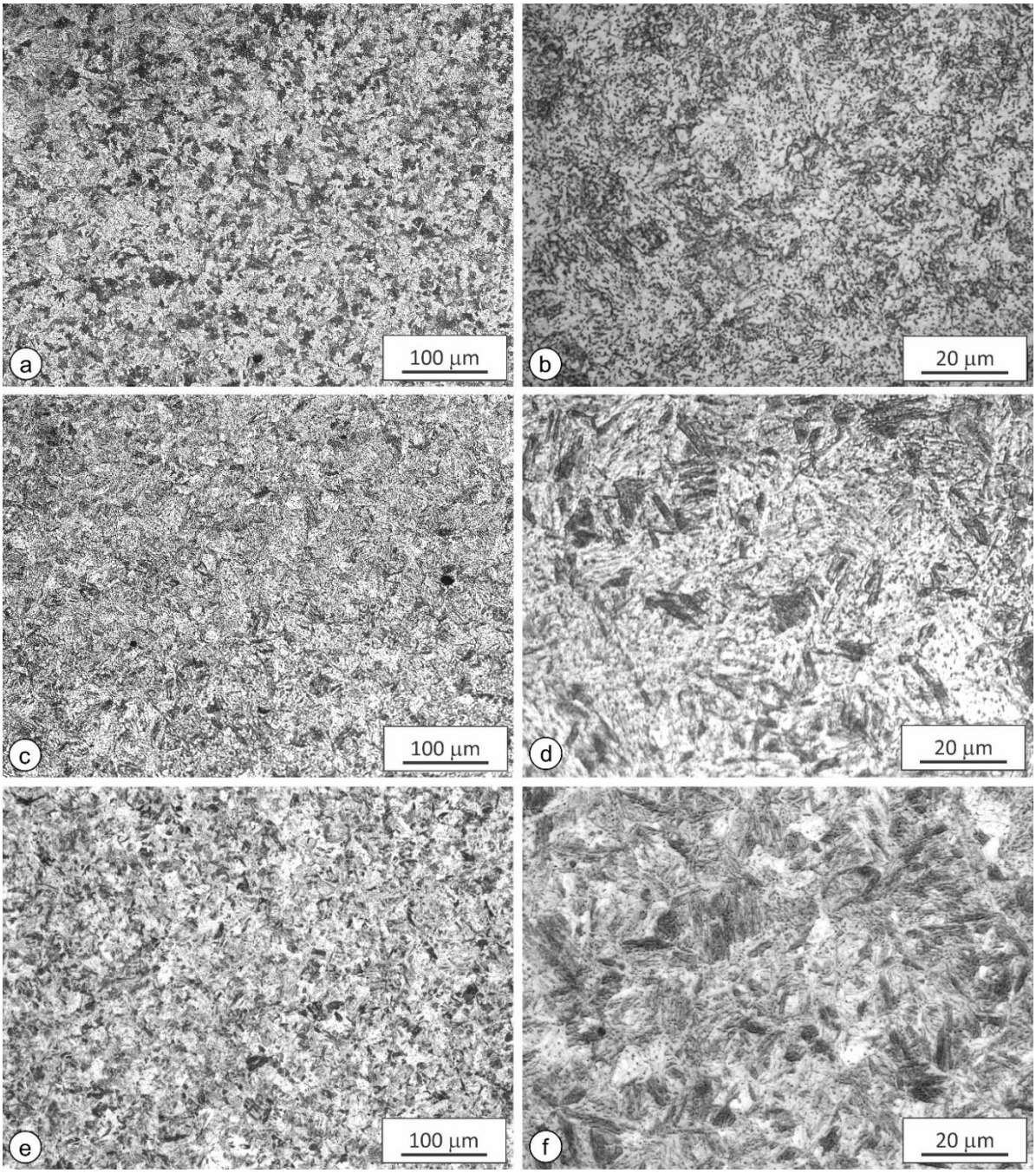

Figure 6. 2 Microstructure of different FG HAZs: a,b - FG HAZ in a real weld (200× and 1000×); c,d - WTCS specimen (200× and 1000×); e,f- AF + WQ specimen (200× and 1000×).

After performing a series of grain measurements, the average of the diameter of grains` sizes was derived for both microstructures, and the results wre 10.9 µm for the AF+WQ specimens and 12.6 µm for the WTCS specimens.

6.2 Hardness test

The results of the examined specimen's instrumented hardness test are depicted in the Figure below. Figure 6.3 demonstrates the loading-unloading diagram used during the experiment.

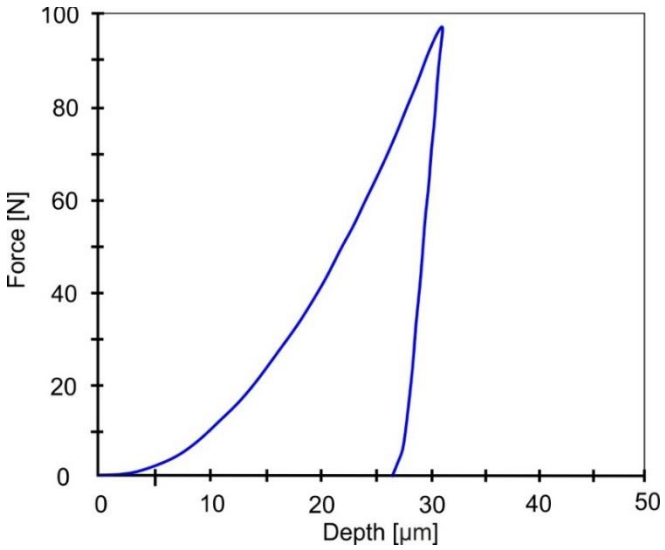

Figure 6. 3 Loading-unloading curve during introducing an artificial microdefect (Vickers Pyramid) in the notch of specimen

After the maximum loads were applied to the magnitude of 98.1 N, the indentation depth went up to 30.32 μm, but when the Vickers pyramid started to unload the material started to recover itself due to elastic-plastic behaviour, and, finally, the indentation depth ended up at 26.898 μm.

The depth of the pyramid-shaped Vickers indentation on the flat surface and on the specimen's groove was measured using a KEYENCE microscope and the findings are displayed in the Figure below. At least three cutting plane measurements were performed, and upon the photograph of the indentation the curvature or the shape of the indentation is plotted down the photographs and also on the side of indentation. The measurements of the depth and the diagonal of microdefect on a flat surface is presented in Figure 6.4. Also, here, three cutting plane measurements were performed, and upon the photograph of the indentation, the curvature or the shape of the indentation is plotted down the photographs and also on the side of indentation. The Cyan colour line represents the cutting plane on which the measurements took place.

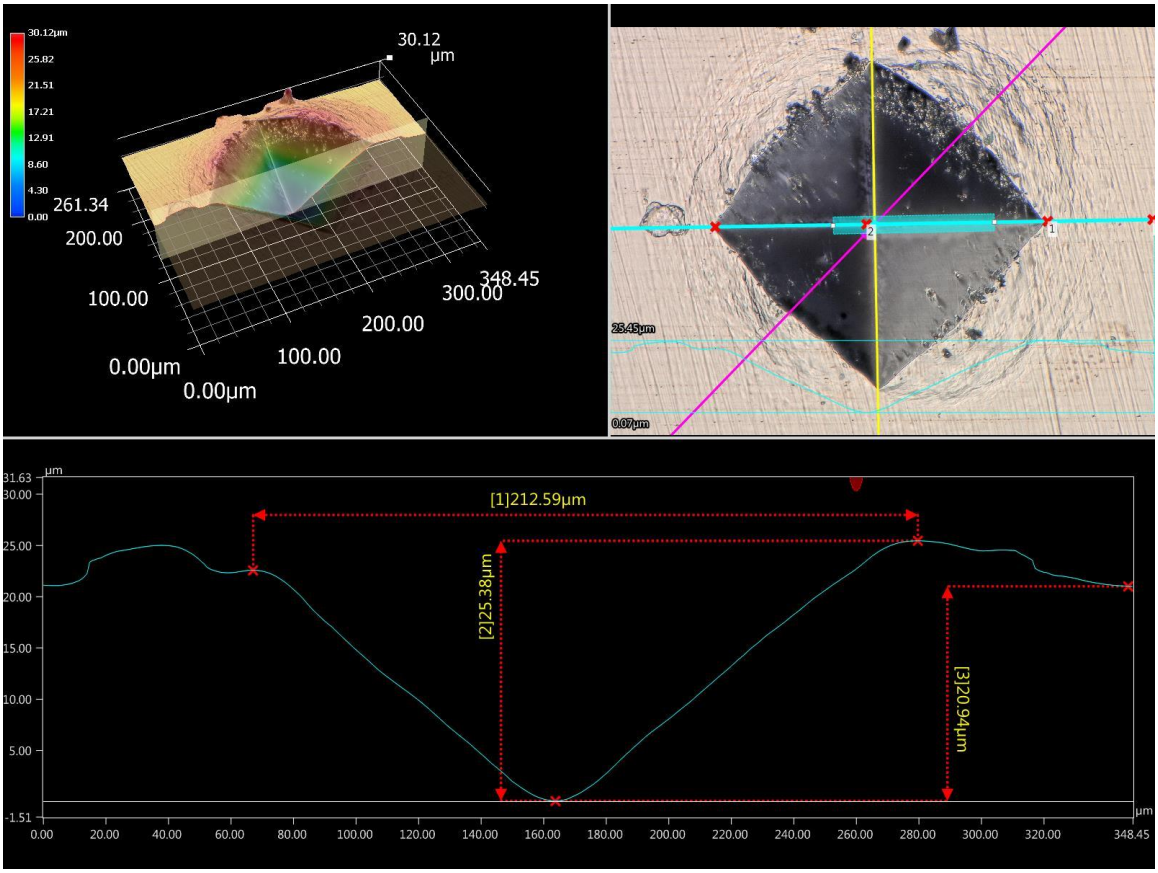

Figure 6. 4 Measurement of a microdefect on the flat surface

The microdefect (Vickers indentation) on the specimen's groove is shown in Figure 6.5.

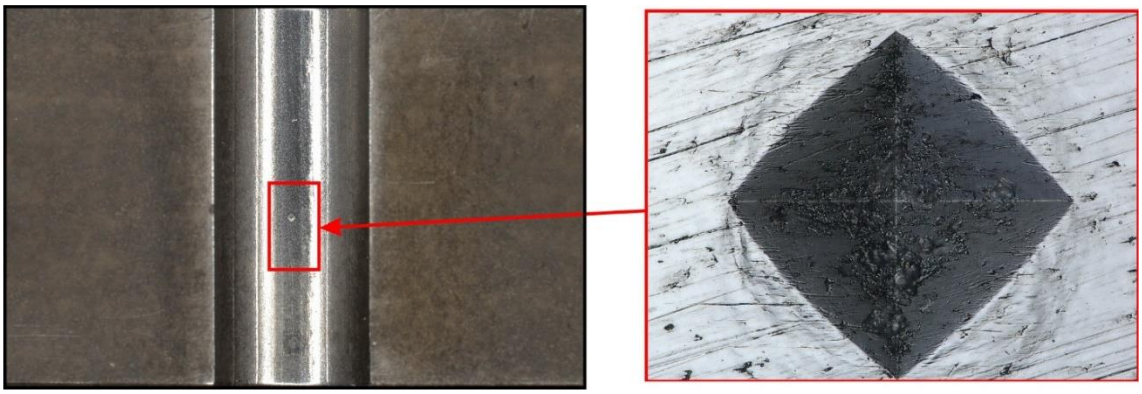

Figure 6. 5 Physical microdefect on the groove of the bending specimen

In Figure 6.6 the lilac color line represents the cutting plane on which the measurements took place. This is the diagonal from which the crack propagated during the fatigue bending test. The results of the crack propagation from the microdefect will be presented in the section of the fatigue.

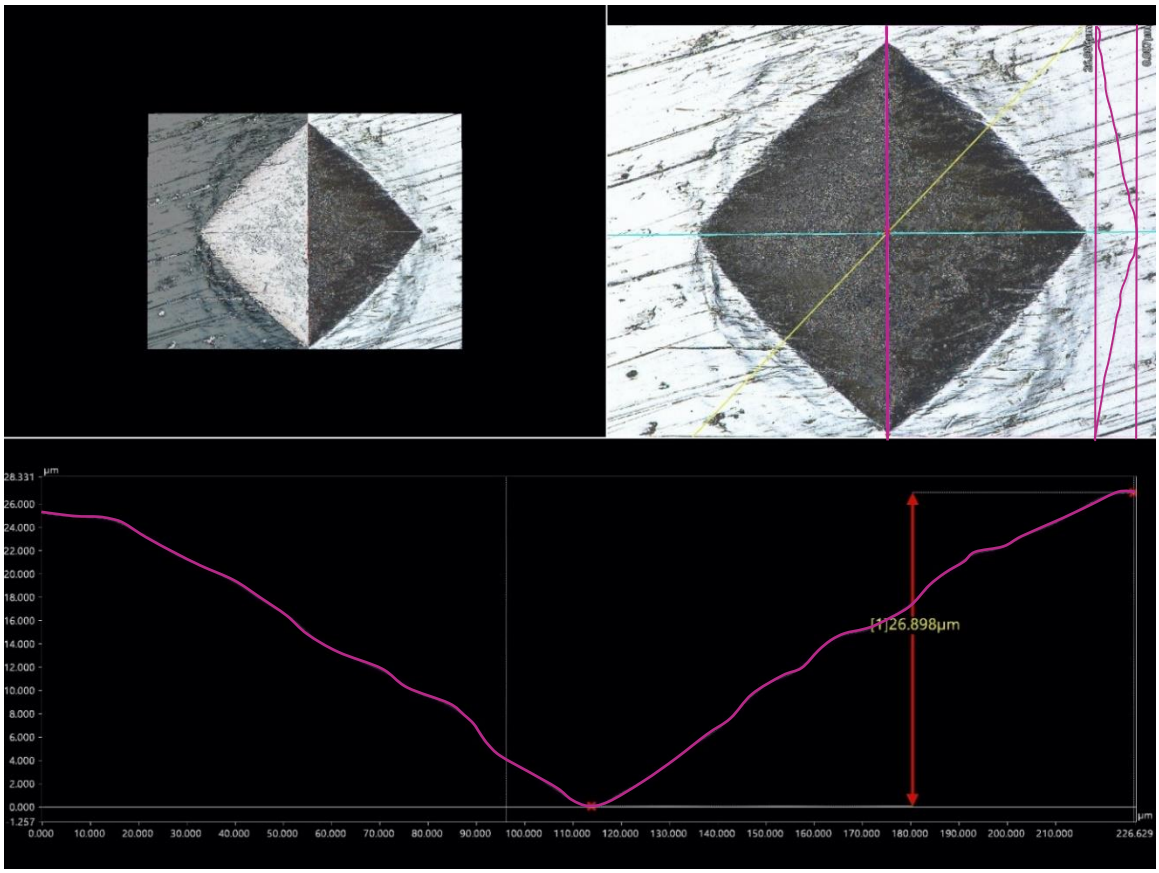

Figure 6. 6 Measurement of the microdefect on the groove specimen

On the flat surface the depth of the indentation was slightly smaller in comparison with the depth on the groove. The depth of the indentation on flat surface, as it can be seen, was 25.38 µm, while, on the other hand, the depth of the indentation at the groove was 26.898 µm.

The reason behind such behavior was the contact surface between the pyramid and the surface of the specimen. In the first case, the contact between the sides of the pyramid and the surface of the specimen exists all the time, from the moment of starting the load until the unloading took place. In the second case, the groove has a shape which allowed less contact with the side of the pyramid to the surface of the specimen, therefore the pyramid had less contact resistance.

The results of the hardness tests measurements for the AF+WQ, WTCS specimens along with a real weld FG HAZ are presented in Table 6.1.

Table 6. 1 Results of the hardness tests.

Material condition	As delivered	AF + WQ	WTCS	Real-weld FG HAZ
HV 10 / -	193	425	419	405

The average hardness of as-delivered (normalised) material was, as expected, significantly lower than the hardness of the FG HAZs, where the material was quench-hardened. The hardness of the AF+WQ samples, WTCS samples and real-weld FG HAZ was very similar. The slightly higher hardness of the AF+WQ samples could be caused by different ways of cooling. The WTCS samples were clamped into water-cooled jaws, which resulted in a nearly one-dimensional heat flow from the hot central area of the specimen towards the jaws on both sides. The AF+WQ specimens were water quenched, whereby all surfaces were cooled more intensively, and the heat flow from the centre of the specimen was two-dimensional. However, the average values differed only by about 1.5 %, which is within the required repeatability according to the Standard ISO 6507-2 [68]. Therefore, the hardness of both types of simulated specimens can be regarded as practically equal. The real weld FG HAZ exhibited slightly lower average hardness than the simulated specimens. However, the difference between the WTCS specimens and the real weld FG HAZ was still within the required repeatability range according to the Standard ISO 6507-2 (< 4 %). Therefore, with respect to hardness, the real weld FG HAZ and both types of simulated specimens can be regarded as very similar. Thereby, the hardness measurements, as did the comparison of the microstructures, also confirmed that the simulated specimens were representative of a real-weld FG HAZ, and that they were suitable for the intended further mechanical testing.

In WoRS (without residual stress) and WRS (with residual stress) specimens where the microdefect was introduced in the centre of the groove, the parameter $\sqrt{area}$ [μm] was calculated according from the depth of the indentation.

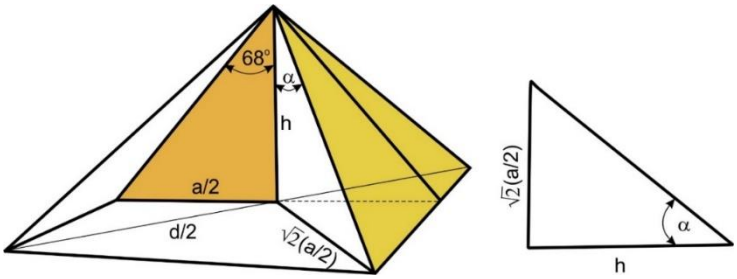

Figure 6. 7 Schema of the pyramid for parameter $\sqrt{area}$ calculation

From the calculation of the geometry of the pyramid and according to the trigonometry this relationship was derived, as is shown in equation 6.1:

$$tg\alpha = \frac{\frac{a\sqrt{2}}{2}}{h} \; and \; tg68° = \frac{a/2}{h} \tag{6.1}$$

From trigonometry using Pythagoras theorem equation 6.2 was derived:

$$\left(\frac{d}{2}\right)^2 = \left(\frac{a}{2}\right)^2 + \left(\frac{a}{2}\right)^2 \tag{6.2}$$

$$\frac{d}{2} = \sqrt{2}\left(\frac{a}{2}\right) \; , for \; d = 212.59 \; [\mu m] \; it \; was \; derived \; that: \; \frac{a}{2} = 150.34 \; [\mu m] \tag{6.3}$$

Therefore, the depth value of the pyramid was calculated to be $h = 30.3719$ $[\mu m]$ according to equation 6.1.

Based on the relationship of the geometry we found out the value of angle α from equation 6.4 as:

$$tg\alpha = \frac{\frac{a\sqrt{2}}{2}}{h} = \frac{\frac{a\sqrt{2}}{2}}{30.3719} \Rightarrow \; \alpha = 74.05° \tag{6.4}$$

Then we calculated area/2 based on equation 6.5:

$$\frac{area}{2} = \frac{a/2 * h}{2} = \frac{75.173 * 30.3719}{2} = \frac{2283.1468}{2} \tag{6.5}$$

Finally, the parameter area is presented in equation 6.6:

$$\sqrt{area} = 47.78\ [\mu m] \tag{6.6}$$

6.3 Tensile tests

Tensile tests were performed according to the Standard *EN ISO 6892-1* [71] using method B. Standardised cylindrical specimens with the diameters 12 mm and 10 mm were used for tensile testing. A diagram of the tensile test is shown in Figure 6.8.

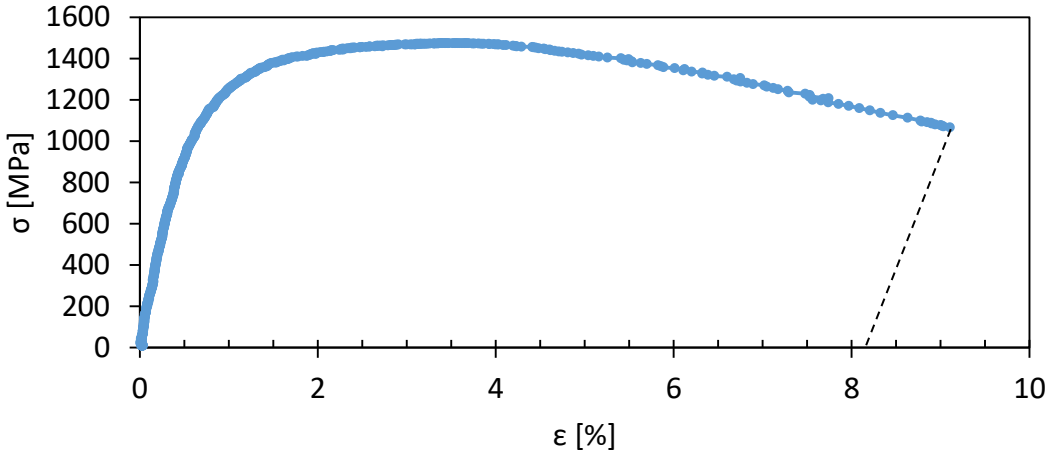

Figure 6. 8 Diagram of the tensile test

In Table 6.2 were tabulated data of the reaction of the specimen in the tensile test of a fine grain microstructure.

Table 6. 2 Results of the tensile test

Elastic modulus	Yield Strength	Ultimate Tensile Strength	Elongation
E	$R_{p0.2}$	R_m	A_5
206494	*1121*	*1475*	*8.2*
[MPa]	*[MPa]*	*[MPa]*	*[%]*

6.4 Charpy instrumented test

Instrumented impact tests of the AF+WQ specimen were carried out on an Instrumented Amsler Charpy Pendulum AMSLER 300 according to Standard EN ISO 148-1 [101] and StandardASTM E2298-18 [102]. The standardised specimens are shown in the previous Chapter (Figure 3.7).

6.4.1 Charpy instrumented test on the AF+WQ specimens

Force versus time and energy versus time diagrams of the quenched specimen were recorded during the tests and are presented in Figure 6.9 and Figure 6.10.

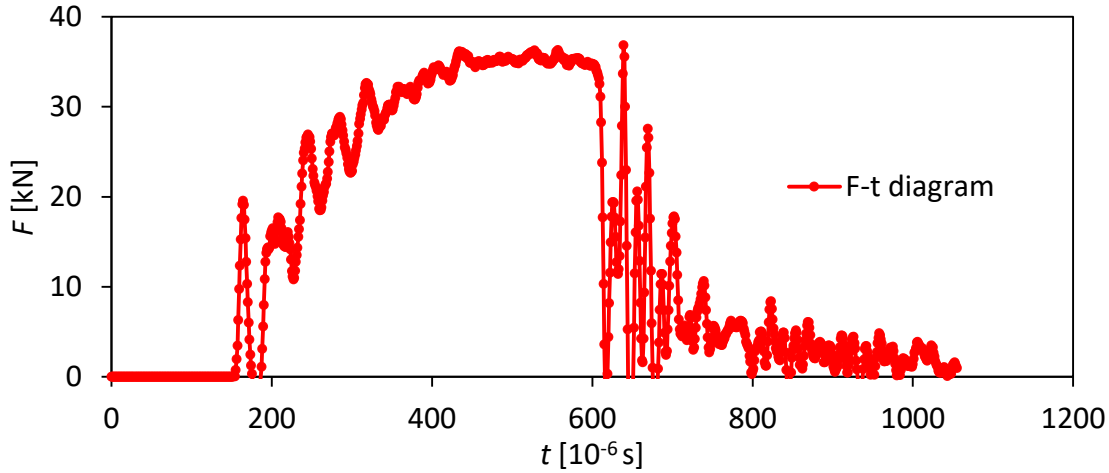

Figure 6. 9 F-t diagram of the AF+WQ specimen (nonfiltered signal)

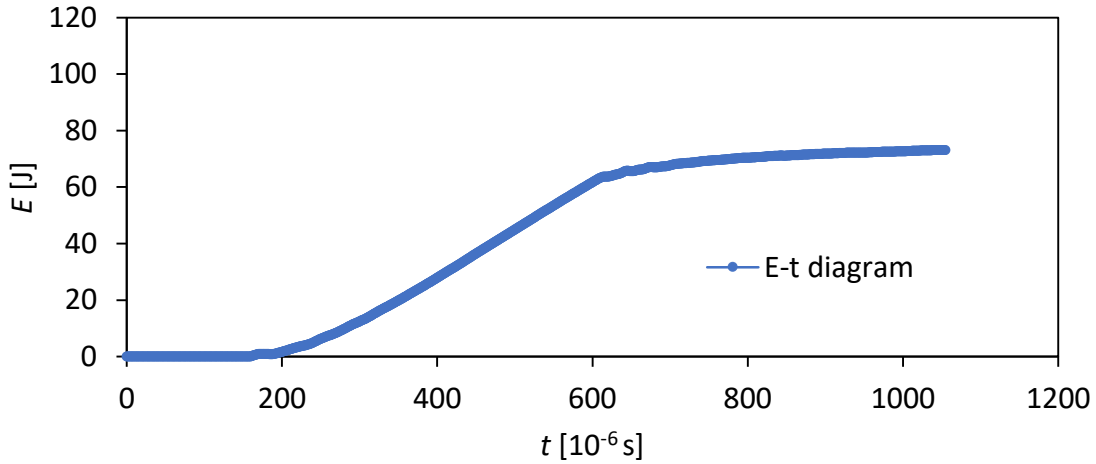

Figure 6. 10 E-t diagram of the quenched FG HAZ

Comparison of the *F-t* vs *E-t* diagrams of AF+WQ specimens, together with the fracture surface of the specimens and results of the instrumented Charpy test, are plotted in Figure 6.11. The total energy for fracture was split into the energy for initiation and the energy for propagation, which were used for both types of tested specimens. Testing was performed at room temperature.

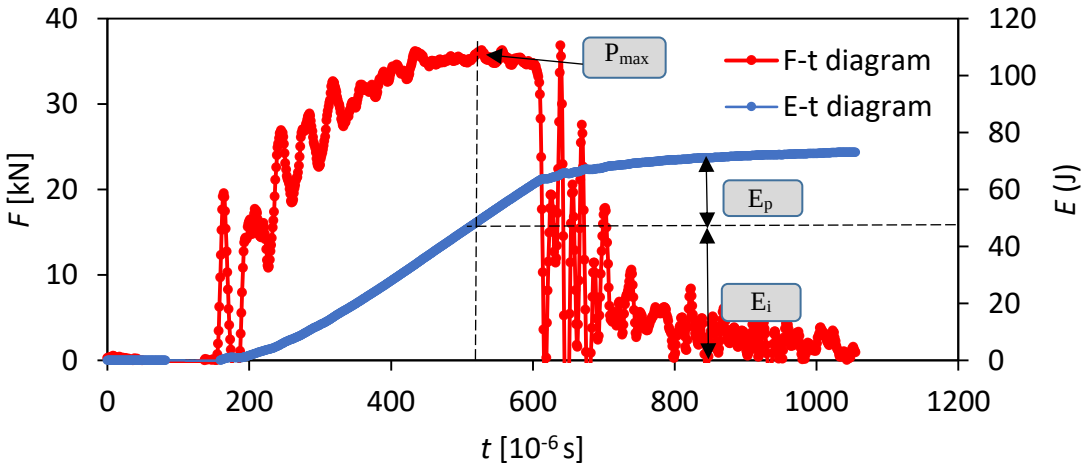

Figure 6. 11 Derivation of energies (Ep and Ei) from the F-t vs E-t diagrams of the AF+WQ specimens (nonfiltered signal)

Fractographs taken from the SEM examination at different magnifications (100x and 500x) of the impact fracture surface of the AF+WQ specimens showed a ductile fractured appearance.

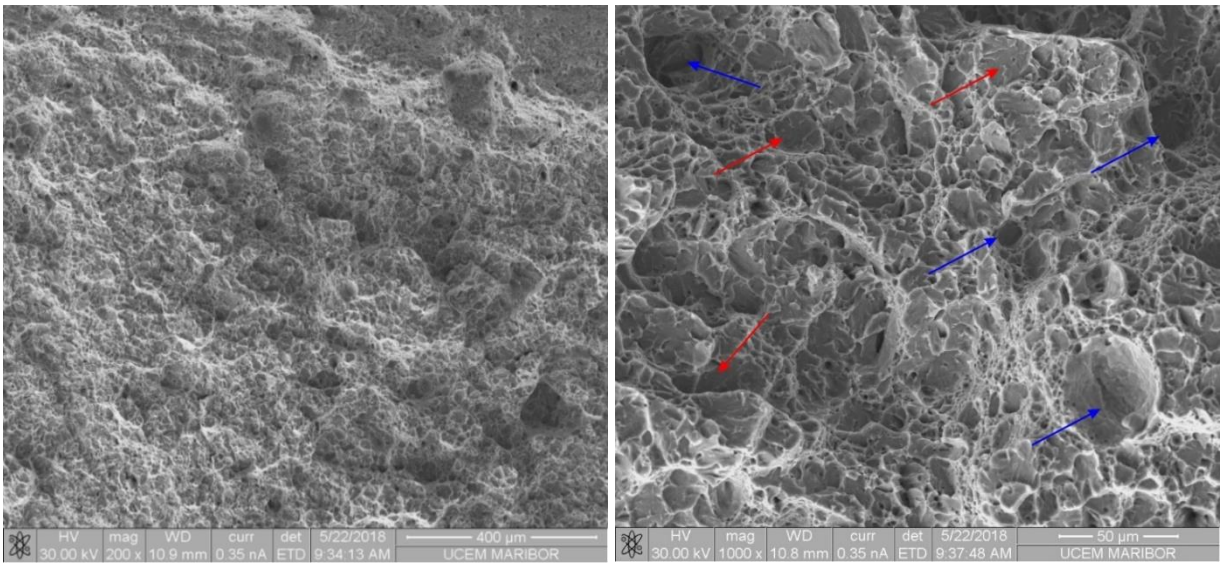

Figure 6. 12 Fracture surface of the AF+WQ specimens at 100x (left) and 500x (right)

From the SEM photograph at 100x magnification of the impact fracture surface of the AF+WQ specimens shown in Figure 6.12, the most important point is the clear visible dimples, indicating a ductile fracture surface of the microstructure (the red arrows in Figure 6.12).

On the other hand, in the 500x magnification photograph, besides ductile voids (blue arrow), the fractograph showed the presence of localised regions of quasi-cleavage fracture, indicated in Figure 6.12 with the red arrows. The presence of those features deteriorates the impact toughness of the fine-grained microstructure specimens, and also has an influence on the *F-t* diagram, where a steeper drop line after the maximum load P_{max} can be seen.

6.4.2 Charpy instrumented test on the WTCS specimens

Force versus time and energy versus time diagrams of the simulated specimen were recorded during the tests and are presented in Figure 6.13 and Figure 6.14.

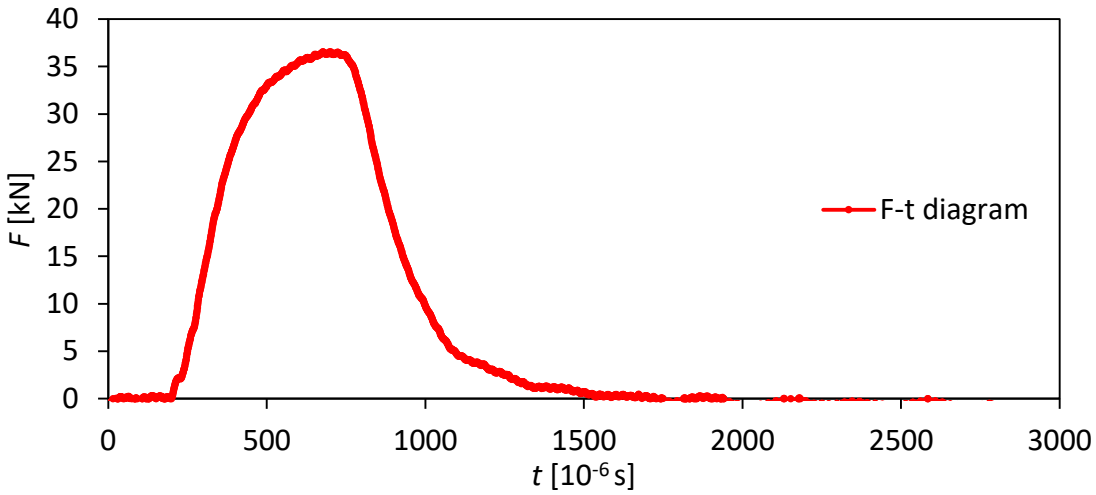

Figure 6. 13 F-t diagram of the WTCS specimen (filtered signal)

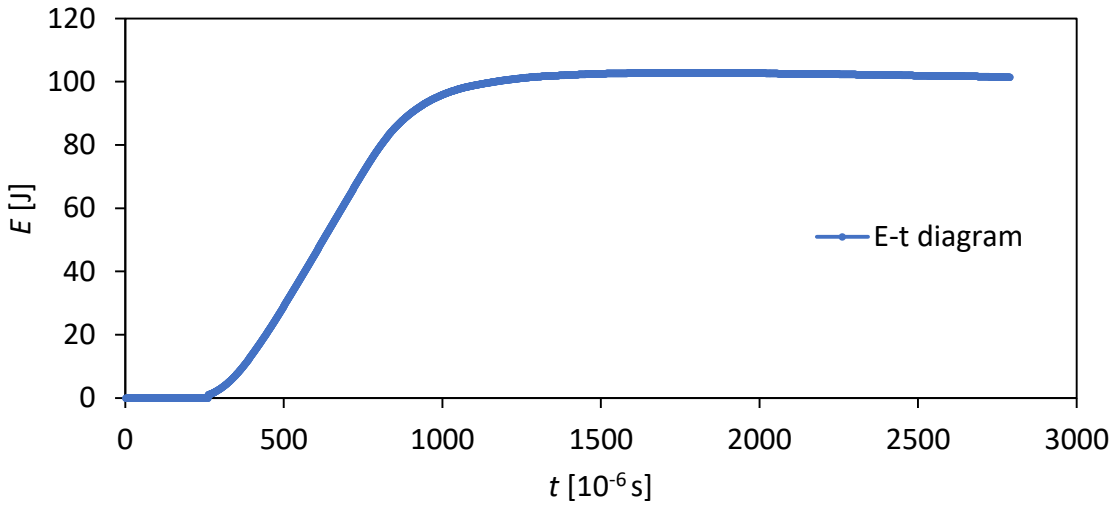

Figure 6. 14 E-t diagram of the WTCS specimen

The F-t vs *E-t* diagrams of the WTCS specimen, together with the fracture surface of the specimen and results of the instrumented Charpy test are plotted in Figure 6.15, and the final comparison of the AF+WQ vs WTCS specimens is listed in Table 6.3. The total energy for fracture was split into the energy for initiation and the energy for propagation, which were used for both types of tested specimens. Testing was performed at room temperature.

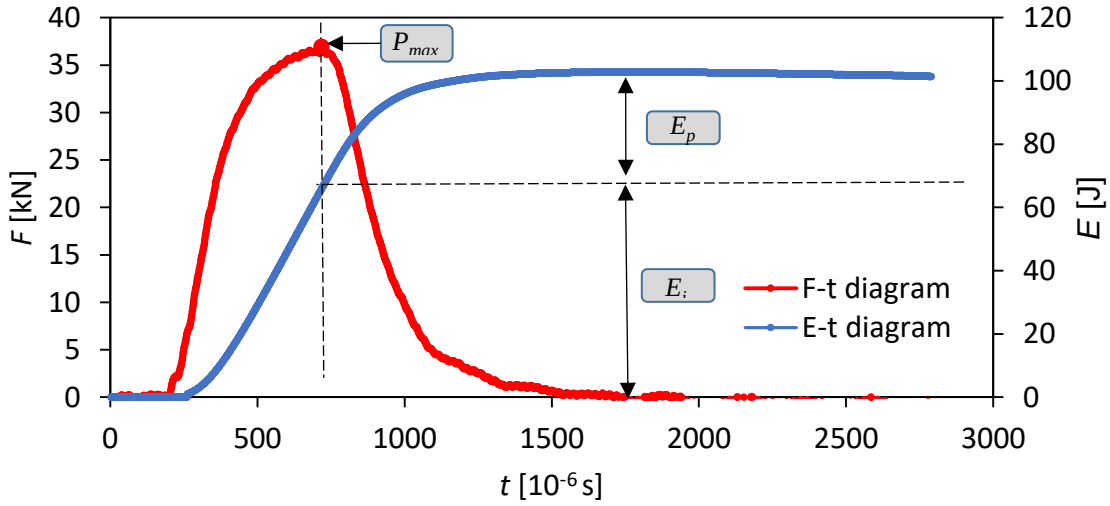

Figure 6. 15 Derivation of energies (Ep and Ei) from the F-t vs E-t diagrams of the WTCS specimen

Fractographs taken from the SEM examination at different magnifications (100x and 500x) of the impact fracture surface of the WTCS specimen also showed a ductile fractured appearance.

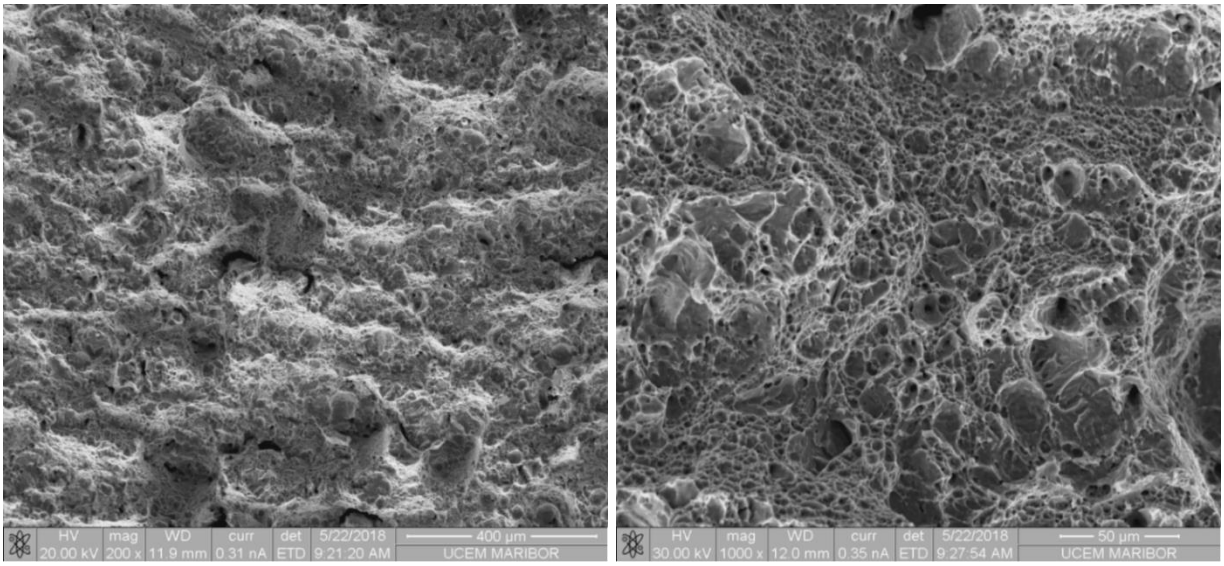

Figure 6. 16 Fracture surface of the WTCS specimen at 100x (left), 500x (right)

An example of the SEM photograph at 100x magnification of the impact fracture surface of the AF+WQ specimen is shown in Figure 6.16. The most important point is the clearly visible dimples, indicating a ductile fracture surface as a result of the microstructure.

On the other hand, at 500x magnification, the photograph, besides ductile voids, showed a lesser presence of localised regions of quasi-cleavage fracture. The presence of those features deteriorated the ductility of the fine-grained microstructure and also had an influence on the *F-t* diagram, where a steeper drop line after the maximum load P_{max} is reached can be seen. Based on this, the energy of propagation would be expected to be greater than for the AF+WQ specimen.

6.4.3 Comparison of the AF+WQ vs WTCS specimens

The results taken from tests at both prepared condition AF+WQ and WTCS and tested on the Charpy instrumented test were compared, in order to distinguish the differences between them. The comparison of the *F-t* vs *E-t* diagrams were shown in Figure 6.17 and Figure 6.18 respectively.

The WTCS, in comparison with the AF+WQ specimens, showed slightly greater values in terms of energies. The energy can also be derived from the area down the blue curve with respect to the abscissa for the WTCS specimen, and for the AF+WQ specimen the area down the red curve with respect to the abscissa.

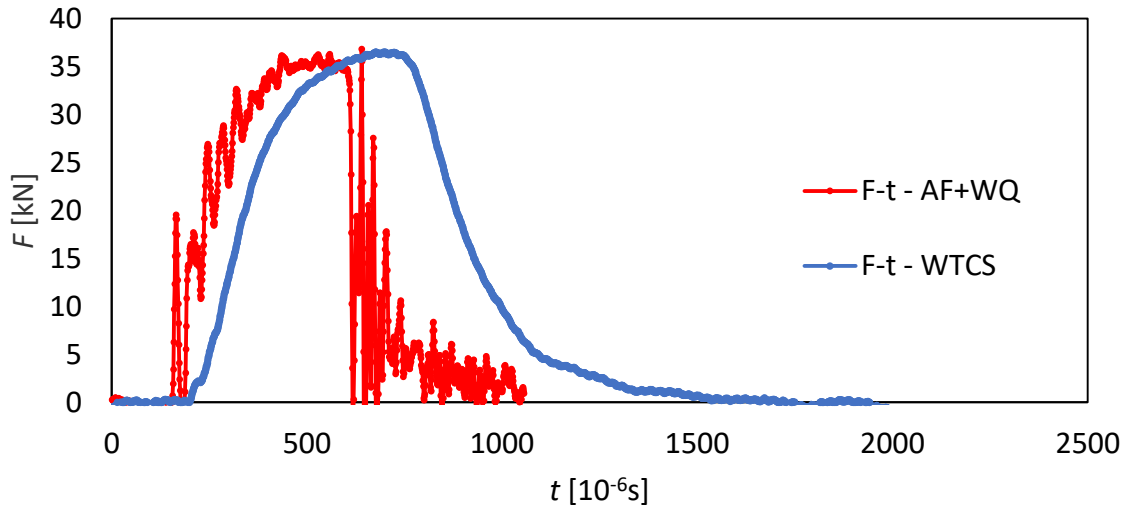

Figure 6. 17 Comparison of the F-t diagrams of the AF+WQ and WTCS specimens

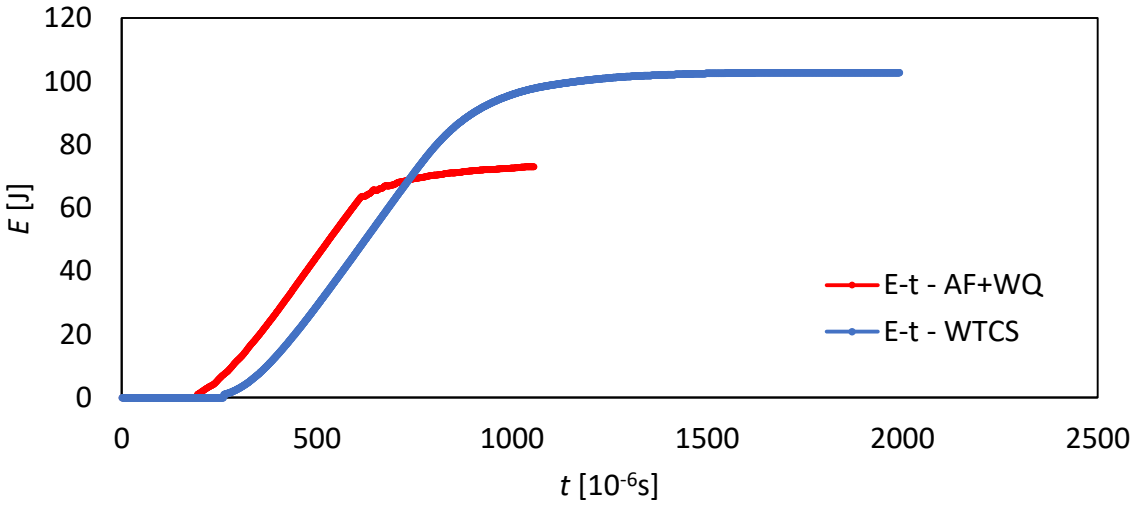

Figure 6. 18 Comparison of the E-t diagrams of the AF+WQ and WTCS specimens

The experiments results of the instrumented Charpy test are presented in Table 6.3.

Table 6. 3 Results of the AF+WQ and WTCS of the instrumented Charpy test

Microstructure	$A_v = E_t$/J	E_i/J	E_p/J	KV/J/cm^2	Part of ductile fracture /%
FG HAZ AF+WQ	73.11	49.70	23.41	91.38	55.41
FG HAZ WTCS	101.49	58.94	42.55	126.86	51.89

As can be seen from Table 6.3, the absorbed impact energies of the WTCS specimens were higher (*KV* = 101.49 J) than the energies of the AF+WQ specimens (*KV* = 73.11 J). However, due to the utilisation of the WTC simulator, the microstructure of the WTCS specimens was much less homogeneous than the microstructure of the AF+WQ specimens. Therefore, the more ductile material in the vicinity of the fracture surface of the WTCS specimens could influence the results. Consequently, the difference between the WTCS and AF+WQ specimens was less significant than indicated by the results of the Charpy impact tests. Both types of specimens absorbed substantially more energy for crack initiation E_i than for crack propagation E_p.

6.5 SENB Fracture Mechanics test of the AF+WQ specimens

The fatigue precracking procedure in conformance with the ASTM E1820-20 [73] Standard waas followed to introduce the crack in the specimen. The fatigue precracking protocol is shown in Figure 6.19.

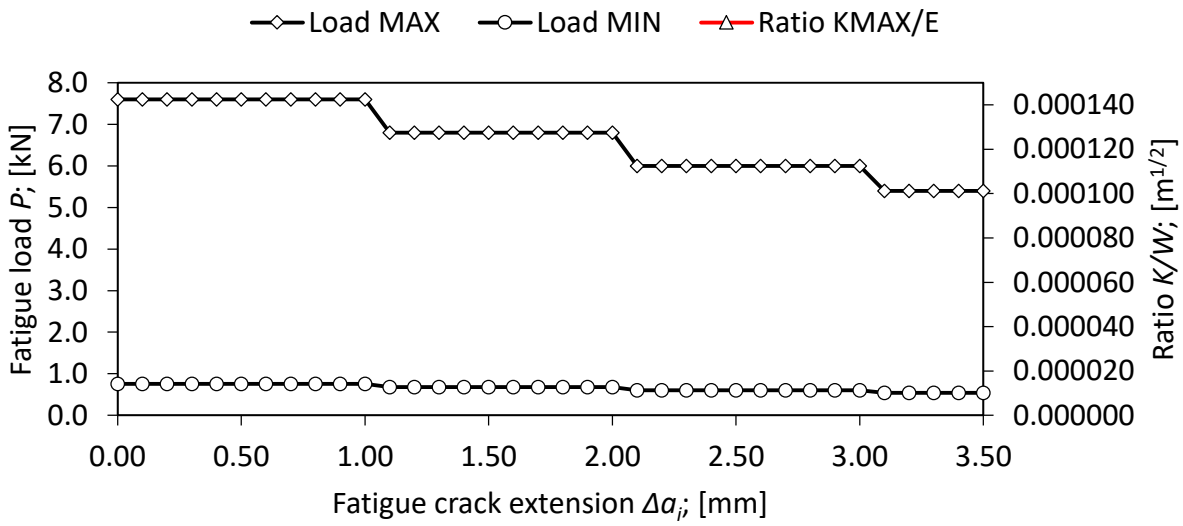

Figure 6. 19 Fatigue precracking protocol

The results of fracture toughness are plotted in diagram F vs CMOD (force vs crack mouth open displacement) and the *J*-*R* curve, as well as δ vs *R* taken from the experimental testing (Figure 6.20).

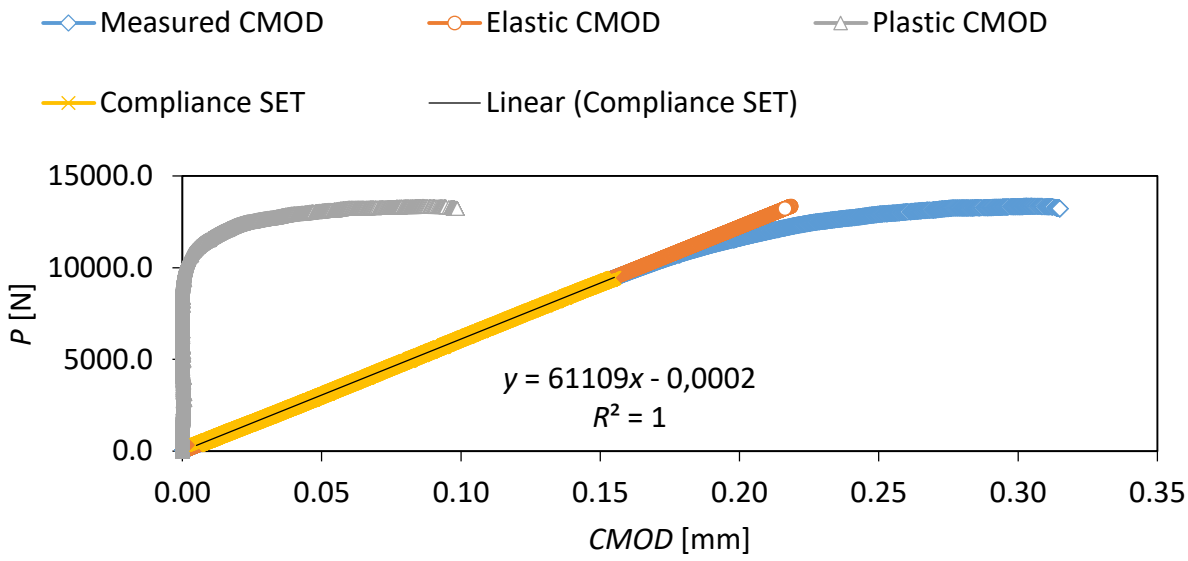

Figure 6. 20 Chart Applied Load vs. Crack Mouth Opening Displacement

The Normalisation Data Reduction technique calculations were used for the experimental data according to the Standard ASTM E1820-20 [73].

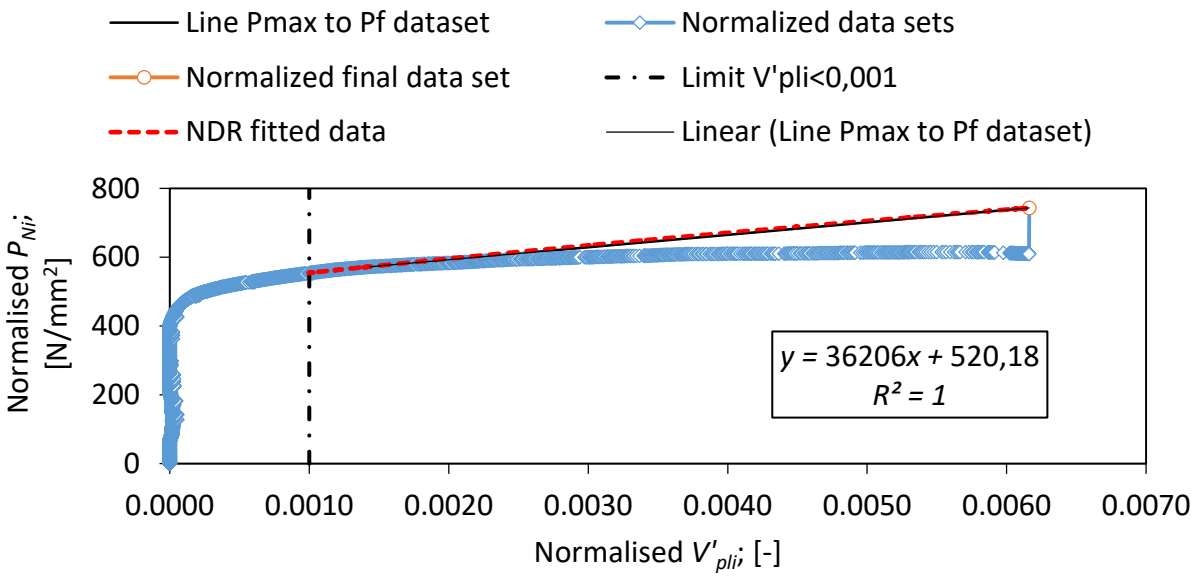

Figure 6. 21 Normalised data chart

After performing the normalisation technique to experimental data in compliance with Standard ASTM E1820-20 [73], the results of *J-R* curve, as well as δ vs *R* were derived, which are plotted in the Figures below.

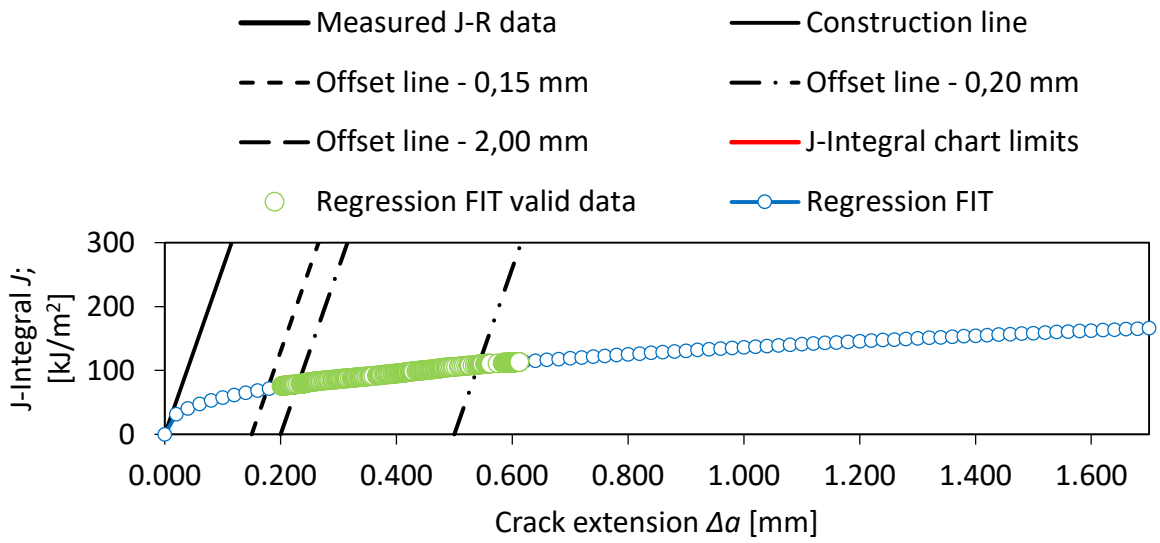

Figure 6. 22 J-Integral resistance curve (J-R)

Obtaining the critical values of the J-integral, J_{IC}, as well as the critical values of crack opening, δ_{IC}, for the FG of the HAZ of welded joints was determined after evaluation of the results.

The critical values of the J-integral—J_{IC} were determined based on the Standard ASTM E1820 [73], and its value was 78.565 [kJ/mm^2]. On the other hand, the critical value of crack opening, δ_{IC} was evaluated to be 0.032 [mm].

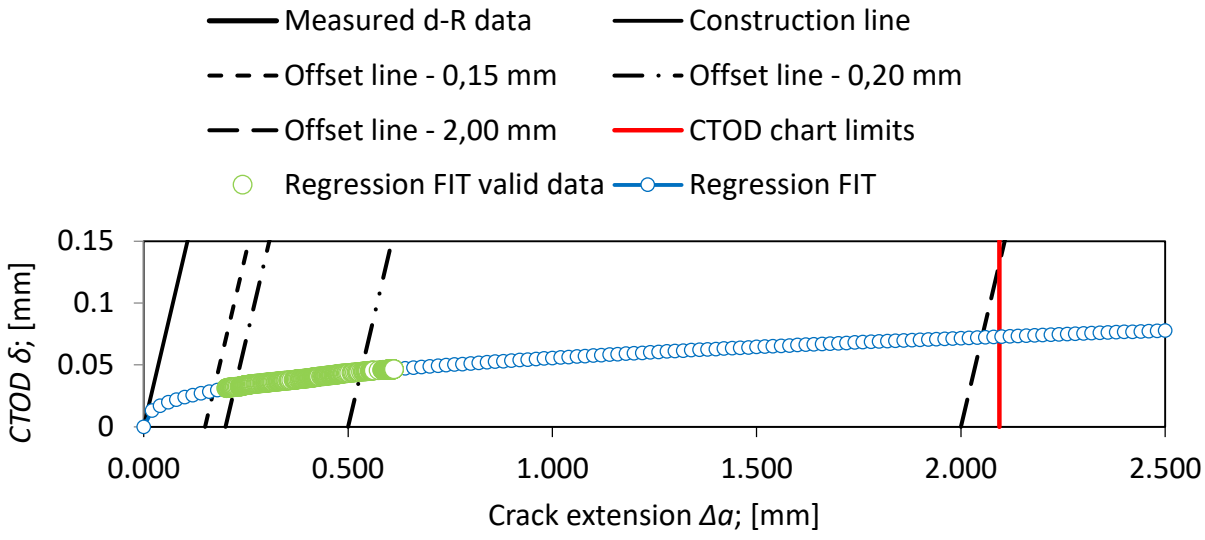

Figure 6. 23 CTOD resistance curve (δ-R)

Finally, the value of fracture toughness was determined by the expression:

$$K_{IC} = \sqrt{\frac{E \cdot J_{IC}}{1 - \nu^2}} \tag{6.7}$$

where:

ν – is the Poisson's ratio [-],

E – is modulus of elasticity [MPa]

By analysing the results of fracture toughness, it can be concluded that the fine-grain microstructure of the HAZ of a welded joint has a quite high fracture toughness, calculated from equation 6.2. The value of K_{IC} was 134.63 MPam$^{0.5}$, which is characterised by a higher ability to dissipate the energy caused by external load in comparison to the coarse grain microstructure.

A photograph of the plastic zone introduced after loading of the specimen during the experiment is presented in the Figure 6.24, which gives an indication that the specimen has enriched the yield point of the load and the crack has been encountered in the elastic-plastic region.

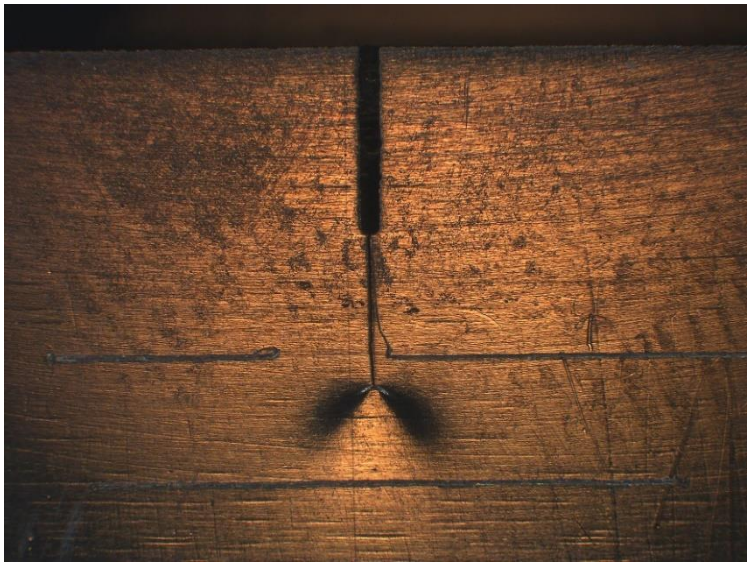

Figure 6. 24 Plastic zone introduced after loading of the specimen during the experiment

The specimen was loaded until the break, and after that the experimental determination of the fracture mechanics` parameters in the conditions of elastic-plastic fracture mechanics was done in accordance with the Standard ASTM E 1820 [73].

Finally, the SEM fractographic analysis was performed of the fracture surfaces of the Single Edge Notched Bend (SENB) specimens for the fine-grain microstructure of the heat affected zone of a welded joint.Figure 6.25 and Figure 6.26 show the photographs taken by the light microscope of the fracture surface of the specimen FG1, while Figure 6.27, shows the region of the stable crack growth zone of this specimen at higher magnification.

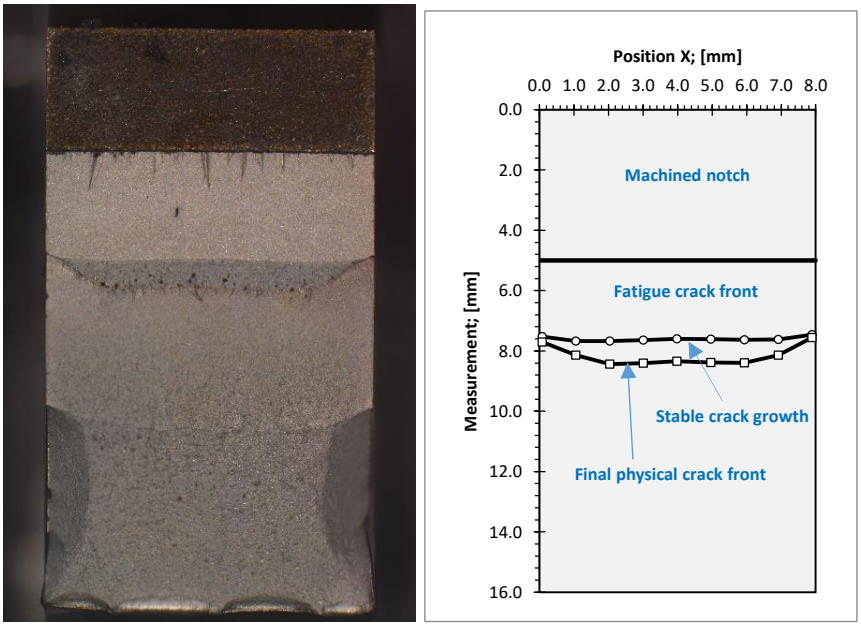

Figure 6. 25 Fractographs of the crack surface (surface 1 of the FG1 specimen)

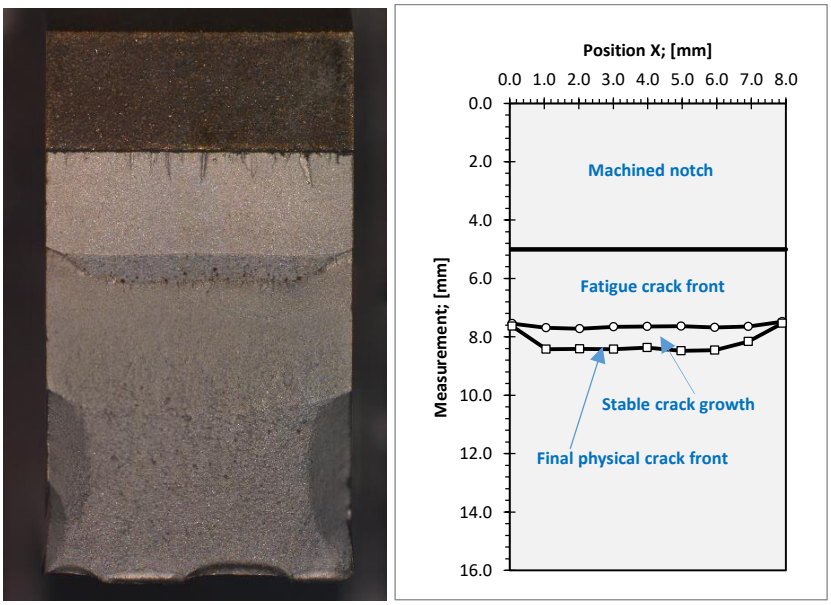

Figure 6. 26 Fractographs of the crack surface (Surface 2 of the FG1 specimen)

Figures 6.25 and Figure 6.26 demonstrate various locations where the crack length was measured on the specimen's fracture surface. According to the Standard ASTM E 1820 [73], there should be nine measurements in total for the correct evaluation of the fracture toughness. The final physical crack front represented the maximum crack length until where the stable crack growth ended and the final fracture occurred. The fatigue crack front, on the other hand, is the area where cracks are microstructurally short in length, and have not yetgrown to meet the zone of stable crack growth.

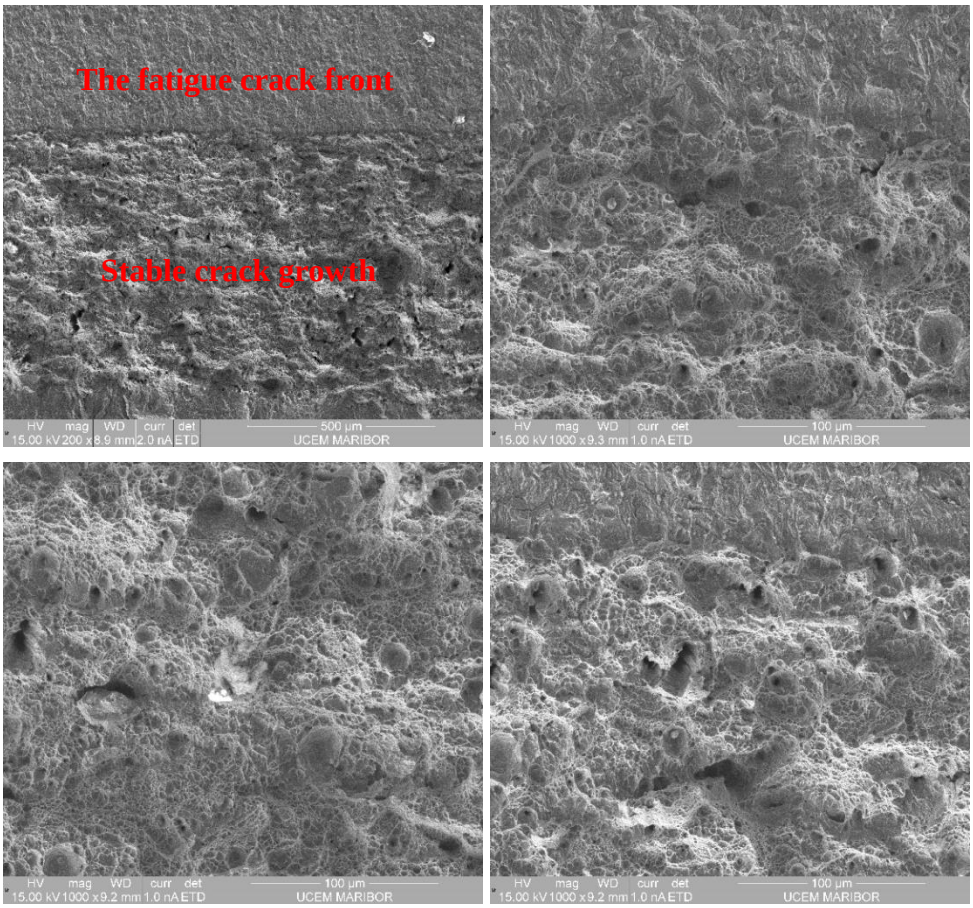

Figure 6. 27 Fractographs of the surface of the FG1 specimen at different locations at 100x and 500x: macro and stable crack growth zone.

The SEM photograph of 100x magnification of the fracture surface of the AF+WQ specimen shows that there are hills and valleys on the surface of the specimens, which indicate that the crack has changed direction during its growth process. On the other hand, at 500x magnification, the presence of some ductile small voids is visible in the fractograph.

6.6 Fatigue crack growth- experimental results (da/dN- ΔK curve)

The fatigue crack growth thresholds for long crack propagation ΔK_{thR} were determined for both cases. The adopted criterion for the threshold for long crack propagation ΔK_{thR} was less than 1μm/10^6 cycle.

The cuboid notched shape specimens were loaded in R= 0.1. The threshold for long crack fatigue propagation ΔK_{thR} was found to be $\Delta K_{thR} = 4.3\ \mathrm{MPa}\sqrt{m}$ for the quenched specimen and $\Delta K_{thR} = 3.4\ \mathrm{MPa}\sqrt{m}$ for the simulated specimens.

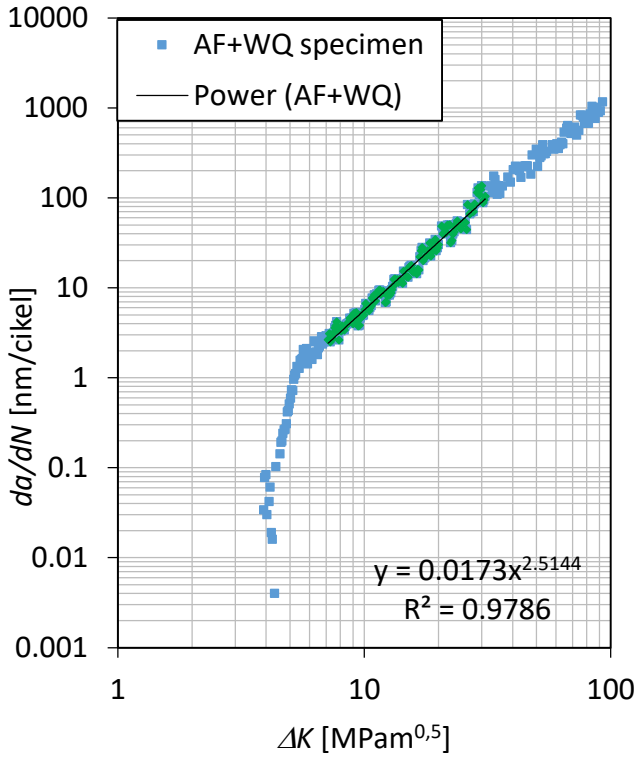

Figure 6. 28 Fatigue crack growth test of the AF+WQ specimen

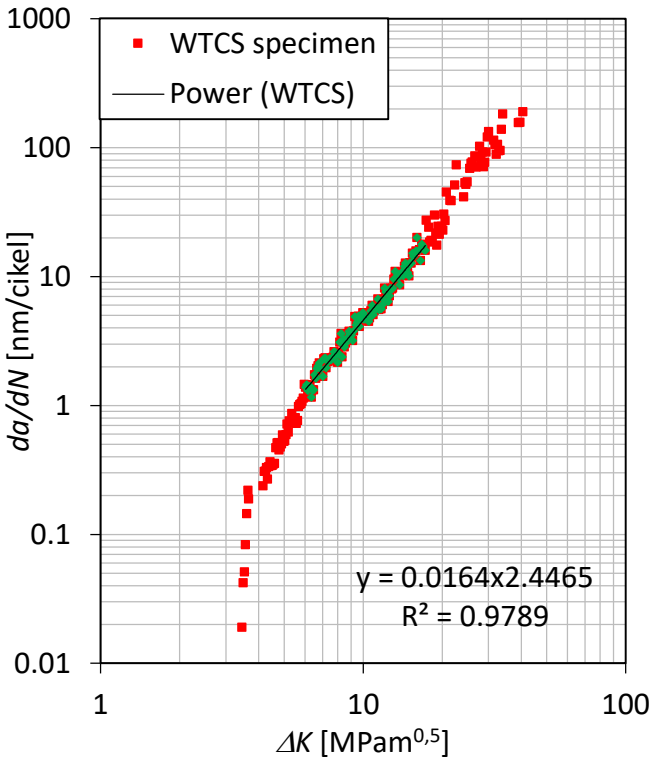

Figure 6. 29 Fatigue crack growth test of the WTCS specimen

Determination of the coefficients C and m of the Paris curve was done according to the Paris law equation 6.5. The FG HAZ- microstructures are presented in Table 6.4.

$$da/dN = C \cdot \Delta K^{m} \tag{6.8}$$

Table 6. 4 Results of the fatigue crack growth tests.

	R / -	ΔK_{thR} / MPa m$^{0.5}$	C	m
AF+WQ	0.1	4.33	1.73×10^{-11}	2.5114
WTCS	0.1	3.4	1.64×10^{-11}	2.4465

6.7 Fatigue bending test - experimental results (S-N diagrams)

The S-N diagrams of two different types of specimen prepared under the conditions AF+WQ (Austenitising in a laboratory furnace followed by Water Quenching) and WCTS (Weld Thermal Cycle Simulator) were derived and constructed from the experimental results. Besides the smooth specimens, where no indentation had been introduced at WoRS (without residual stress) and WRS (with residual stress), specimens where the microdefect was introduced in the centre of the groove and the parameter $\sqrt{area}$ which is the defect's size parameter in [μm], was calculated according to the depth of the indentation.

According to Murakami, the fatigue limit and threshold stress intensity factor calculated by equations 6.6 – 6.8 for polycrystalline metals could be calculated from the parameter $\sqrt{area}$ and hardness [103, 104] as:

$$\sigma_{eR} = \frac{1.43(HV + 120)}{\left(\sqrt{area}\right)^{1/6}} \cdot \left(\frac{1-R}{2}\right)^{\alpha} \tag{6.9}$$

$$\Delta K_{th} = 3.3 \cdot 10^{-3}(\mathrm{HV} + 120) \cdot \sqrt{area}^{1/3} \cdot \left(\frac{1-R}{2}\right)^{\alpha} \tag{6.10}$$

$$\alpha = 0.226 + HV \cdot 10^{-4} \tag{6.11}$$

where:

σ_{eR}	– is the fatigue limit in [MPa],
ΔK_{th}	– is the threshold stress intensity factor in [MPa m$^{1/2}$],
HV	-is the Vickers hardness number [-],
R	-is the load ratio [-],
α	- is the coefficient of the material [-],
$\sqrt{area}$	- is the defect's size parameter in [μm].

$for\ HV = 425$ and $\sqrt{area} = 47.78\ [\mu m]$

The fatigue limit predicted by Murakami for R= 0.1 was: $\sigma_{eR} = 330.32\ MPa$.The threshold stress intensity factor predicted by Murakami for R= 0.1 was $\Delta K_{th} = 5.26\ \left[MPam^{1/2}\right]$

6.7.1 Austenitising in a laboratoryfFurnace followed by Water Quenching (AF+WQ) of smooth specimens

To determine a fatigue limit in accordance with the British Standard *BS ISO 12107:2003* [114], the specimens were subjected to bending loading using the step 25. In Table 6.5 are shown the loading stress range values and number of cycles to failure; therefore, in Figure 6.30, the results are plotted in an S-N diagram.

Table 6. 5 Loading stress range values and number of cycles to failure

Designation	Stress[MPa]	N- [cycles]	Designation	Stress[MPa]	N- [cycles]
S_{AF+WQ} 1	1200	37800	S_{AF+WQ} 9	825	121400
S_{AF+WQ} 2	1100	51300	S_{AF+WQ} 10	800	251900
S_{AF+WQ} 3	1050	71200	S_{AF+WQ} 11	750	10000000
S_{AF+WQ} 4	1000	76000	S_{AF+WQ} 12	750	10000000
S_{AF+WQ} 5	1000	56184	S_{AF+WQ} 13	725	10000000
S_{AF+WQ} 6	950	91075	S_{AF+WQ} 14	700	176600
S_{AF+WQ} 7	900	103813	S_{AF+WQ} 15	650	10000000
S_{AF+WQ} 8	850	109041	S_{AF+WQ} 16	650	10000000

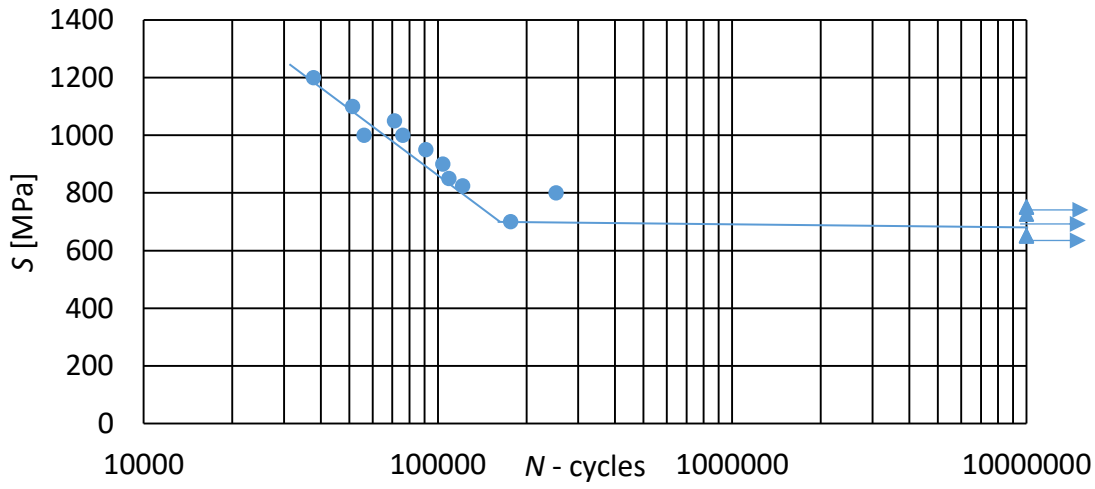

Figure 6. 30 S-N diagram of smooth quenched specimens

The fatigue strength (endurance limit) of the smooth specimens prepared for the laboratory furnace was determined to be $\sigma_{eR} = 675\ MPa$ after the evaluation of the experimental data in accordance with the British Standard *BS ISO 12107:2003* [114].

6.7.2 Austenitising in a laboratory Furnace followed by Water Quenching (AF+WQ) specimens with an artificial microdefect without RS (WoRS)

The specimens were the subject of bending loading with the step of 25 in order to find a fatigue limit according to the British Standard *BS ISO 12107:2003* [114]. In Table 6.6 are shown the loading stress range values and number of cycles to failure; therefore, the results are plotted in Figure 6.31.

Table 6. 6 Loading stress range values and number of cycles to failure

Designation	Stress[MPa]	N- [cycles]	Designation	Stress[MPa]	N- [cycles]
$WoRS_{AF+WQ}$ 1	1200	26600	$WoRS_{AF+WQ}$ 9	575	375700
$WoRS_{AF+WQ}$ 2	1100	57000	$WoRS_{AF+WQ}$ 10	575	279700
$WoRS_{AF+WQ}$ 3	1100	43900	$WoRS_{AF+WQ}$ 11	550	339300
$WoRS_{AF+WQ}$ 4	1000	65500	$WoRS_{AF+WQ}$ 12	550	1000000
$WoRS_{AF+WQ}$ 5	900	80000	$WoRS_{AF+WQ}$ 13	550	1000000
$WoRS_{AF+WQ}$ 6	800	120800	$WoRS_{AF+WQ}$ 14	525	1000000
$WoRS_{AF+WQ}$ 7	700	200200	$WoRS_{AF+WQ}$ 15	500	1000000
$WoRS_{AF+WQ}$ 8	600	516900			

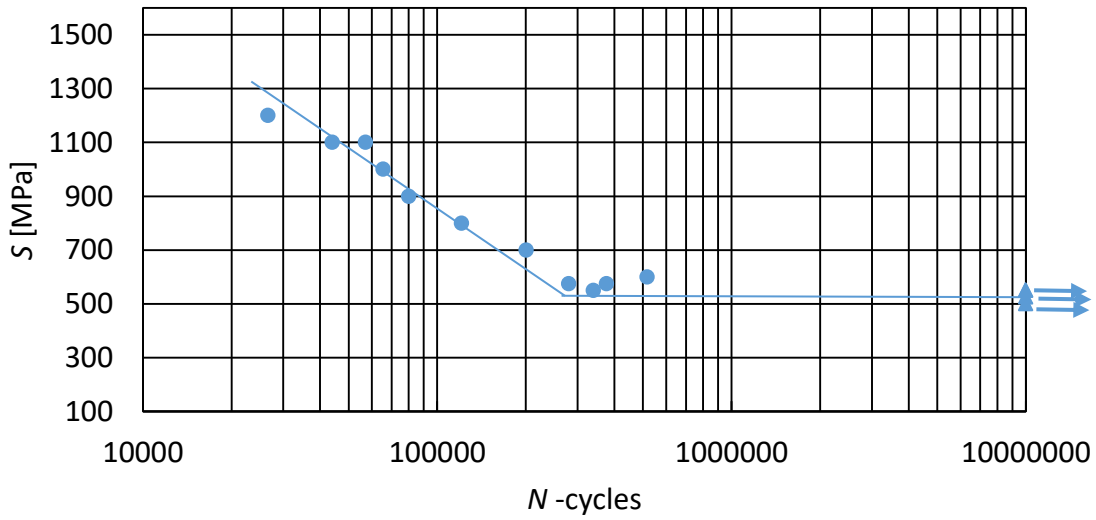

Figure 6. 31 S-N diagram of the quenched specimen impressed without residual stress

After evaluation of the experimental data according to the British Standard *BS ISO 12107:2003* [114] the fatigue strength (endurance limit) of the impressed specimens without residual stress prepared in the laboratory furnace was determined to be $\sigma_{eR} = 550\ MPa$.

6.7.3 Austenitising in a laboratory Furnace followed by Water Quenching (AF+WQ) specimens with an artificial microdefect with RS (WRS)

The specimens were subjected to bending loading according to the British Standard *BS ISO 12107:2003* [114]. Based on the loading stress range values and cycles to failure listed in Table 6.7, the findings are shown in an S-N diagram in Figure 6.32.

Table 6. 7 Loading stress range values and number of cycles to failure

Designation	Stress[MPa]	N- [cycles]	Designation	Stress[MPa]	N- [cycles]
WRS_{AF+WQ} 1	1000	102013	WRS_{AF+WQ} 7	775	403200
WRS_{AF+WQ} 2	950	122400	WRS_{AF+WQ} 8	675	7750000
WRS_{AF+WQ} 3	900	130300	WRS_{AF+WQ} 9	650	10000042
WRS_{AF+WQ} 4	992	90485	WRS_{AF+WQ} 10	625	10000000
WRS_{AF+WQ} 5	875	259900	WRS_{AF+WQ} 11	600	10000000
WRS_{AF+WQ} 6	850	261600			

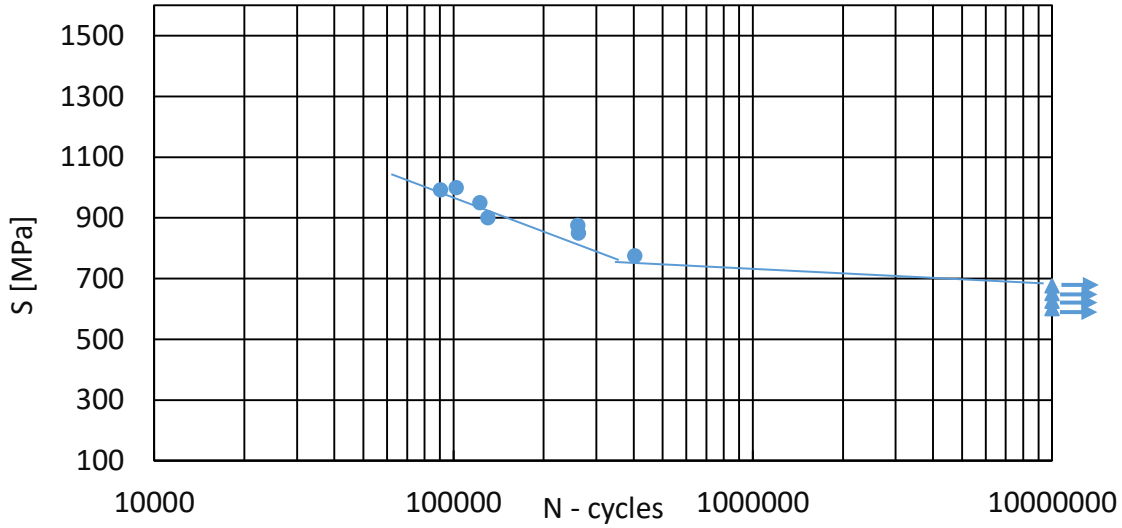

Figure 6. 32 S-N diagram of quenched specimen impressed with residual stress

After evaluation of the experimental data according to the British Standard *BS ISO 12107:2003* [105] the fatigue strength (endurance limit) of the smooth specimens prepared in the laboratory furnace was determined to be $\sigma_{eR} = 675\ MPa$.

6.7.4 Weld Thermal Cycle Simulator (WTCS) smooth specimens

In order to determine the fatigue limit in accordance with British Standard BS ISO 12107:2003 [114], the specimens were subjected to bending loading using the step 25. The loading stress range values and number of cycles to failure are presented in Table 6.8, and, finally, the results were plotted in an S-N diagram in Figure 6.33.

Table 6. 8 Loading stress range values and number of cycles to failure

Designation	Stress[MPa]	N- [cycles]	Designation	Stress[MPa]	N- [cycles]
S_{WTCS} 1	1000	46900	S_{WTCS} 7	650	10000000
S_{WTCS} 2	900	70010	S_{WTCS} 8	625	10000000
S_{WTCS} 3	900	71568	S_{WTCS} 9	600	10000000
S_{WTCS} 4	800	104200	S_{WTCS} 10	550	10000000
S_{WTCS} 5	750	99300	S_{WTCS} 11	525	10000000
S_{WTCS} 6	700	156384			

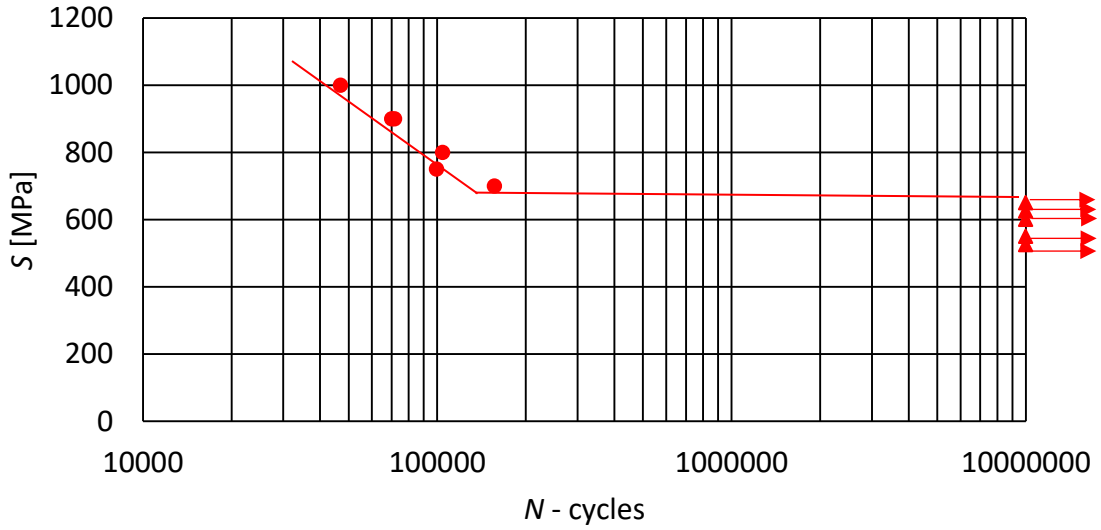

Figure 6. 33 S-N diagram of smooth WTCS specimens

After evaluation of the experimental data according to the British Standard *BS ISO 12107:2003* [105] the fatigue strength (endurance limit) of the smooth specimens prepared in the laboratory furnace ws determined to be $\sigma_{eR} = 675\ MPa$.

6.7.5 Weld Thermal Cycle Simulator (WTCS) specimens with an artificial microdefect without RS (WoRS)

The specimens were the subject of bending loading according to the British Standard *BS ISO 12107:2003* [114]. The loading stress range values and number of cycles to failure are shown In Table 6.9; therefore, the results are plotted in Figure 6.34.

Table 6. 9 Loading stress range values and number of cycles to failure

Designation	Stress[MPa]	N- [cycles]	Designation	Stress[MPa]	N- [cycles]
$WoRS_{WTCS}$ 1	1100	50500	$WoRS_{WTCS}$ 10	700	257800
$WoRS_{WTCS}$ 2	1000	51500	$WoRS_{WTCS}$ 11	650	180400
$WoRS_{WTCS}$ 3	900	82687	$WoRS_{WTCS}$ 12	625	189500
$WoRS_{WTCS}$ 4	800	84500	$WoRS_{WTCS}$ 13	600	278900
$WoRS_{WTCS}$ 5	800	91053	$WoRS_{WTCS}$ 14	600	454795
$WoRS_{WTCS}$ 6	775	142900	$WoRS_{WTCS}$ 15	575	10000000
$WoRS_{WTCS}$ 7	750	146740	$WoRS_{WTCS}$ 16	550	10000000
$WoRS_{WTCS}$ 8	650	151845	$WoRS_{WTCS}$ 17	500	10000000
$WoRS_{WTCS}$ 9	700	154089			

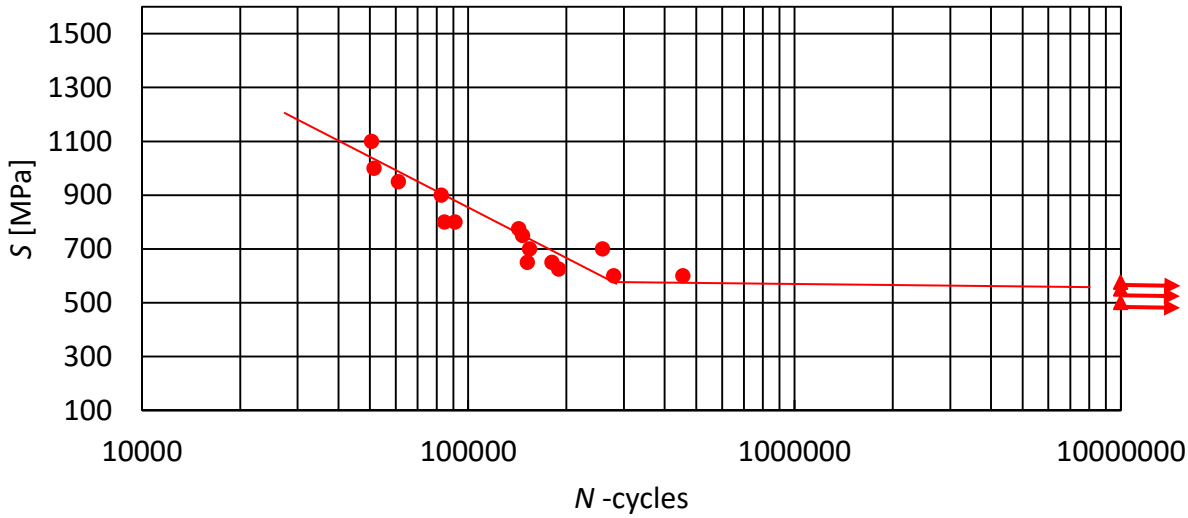

Figure 6. 34 S-N diagram of the WTCS specimens impressed without residual stress

After evaluation of the experimental data according to the British Standard *BS ISO 12107:2003* [115] the fatigue strength (endurance limit) of the smooth specimens prepared in the laboratory furnace was determined to be $\sigma_{eR} = 550\ MPa$.

6.7.6 Weld Thermal Cycle Simulator (WTCS) specimens with an artificial microdefect with RS (WRS)

In accordance with the British Standard *BS ISO 12107* [114], the samples were subjected to bending load using the step 25 in order to determine the fatigue limit. The loading stress range values and number of cycles until failure are reported in Table 6.10, and, finally, the results are plotted in an S-N diagram in Figure 6.35.

Table 6. 10 Loading stress range values and number of cycles to failure

Designation	Stress[MPa]	N- [cycles]	Designation	Stress[MPa]	N- [cycles]
WRS_{WTCS} 1	1000	86700	WRS_{WTCS} 8*	700	302100
WRS_{WTCS} 2	900	88000	WRS_{WTCS} 9	675	10000000
WRS_{WTCS} 3	900	104000	WRS_{WTCS} 10	600	10000000
WRS_{WTCS} 4	800	161600	WRS_{WTCS} 11*	650	10000000
WRS_{WTCS} 5	800	202600	WRS_{WTCS} 12	550	10000000
WRS_{WTCS} 6	750	110700	WRS_{WTCS} 13	525	10000000
WRS_{WTCS} 7*	725	188500	* crack out of indentation		

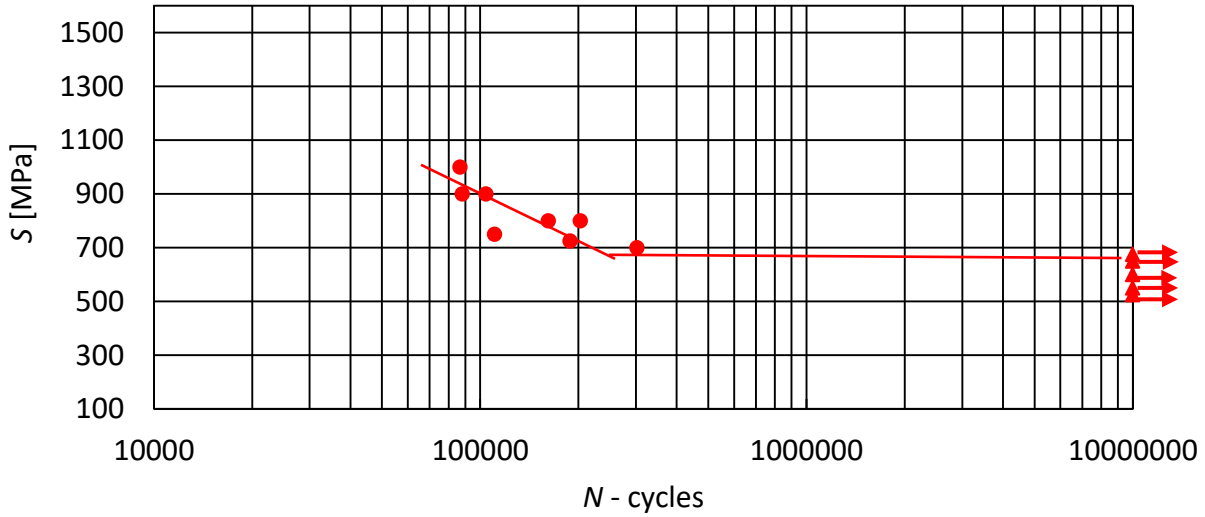

Figure 6. 35 S-N diagram of WTCS specimens impressed with residual stress

After evaluation of the experimental data according to the British Standard *BS ISO 12107:2003* [114], the fatigue strength (endurance limit) of the smooth specimens prepared in the laboratory furnace was determined to be $\sigma_{eR} = 675\text{MPa}$.

6.8 Chapetti model without FEA RS results

The methodology described in Section 3.1.10 was implemented, and using Excel for evaluation of the experimental data, the magnitude of the parameters of our interests were determined, such as: microstructural thresholds ΔK_{dR} , $\Delta K_{CR,}$ the extrinsic component of ΔK_{thR} and the intrinsic crack length a_0.

To estimate the fatigue life, the Chapetti model simply required measurements of the long crack propagation threshold, ΔK_{thR}, the fatigue limit or endurance, $\Delta\sigma_{thR}$, and the value of d as defined by the strongest microstructural barrier located at position d.

6.8.1 Chapetti model in a KT-type diagram for the AF+WQ smooth specimens

The estimation of the fatigue threshold for propagation and non-propagation of cracks is explained with a Kitagawa-Takahashi diagram. The experimental data of the stress threshold as a function of crack length were plotted for AF+WQ smooth FG HAZ microstructure specimens prepared in the laboratory furnace and presented in Figure 6.36 and Figure 6.37. The thresholds for short crack and long crack propagation were calculated and the threshold limit was found. In the KT-diagram the red circles represent the threshold stress range in the function of the threshold for long crack propagation (known as a long crack regime), while the blue circles represent the threshold for non-propagation of cracks (known as a short crack regime). Also, the vertical green dashed line represents the size area $\sqrt{area}$ of the artificial defect, which, for our case, was calculated to be $\sqrt{area} = 47$ μm. This mean that the size of the defect was smaller than the a_i (the critical crack size to behave as a long crack), which was $a_i = 0.039$ mm, and the threshold ΔK_{thR} becomes critical for further propagation.

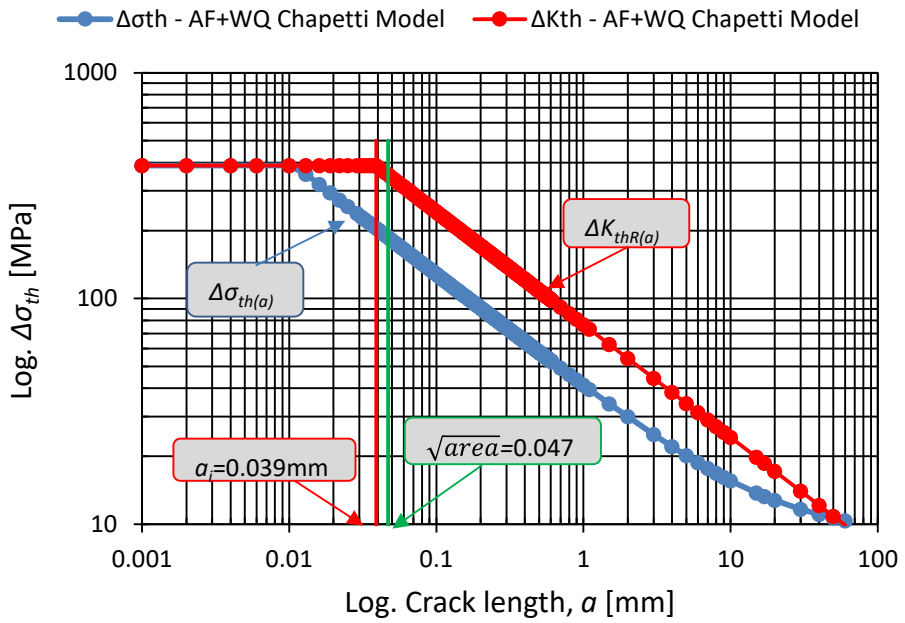

Figure 6. 36 Kitagawa-Takahashi diagram of the AF+WQ smooth specimens

As the microstructural threshold ΔK_{dR} was a small value, the conditions for crack propagation were fulfilled and the crack soon started to propagate. Consequently, this influenced the endurance limit of the specimens, which was evaluated to be σ_{eR}= 675 MPa.

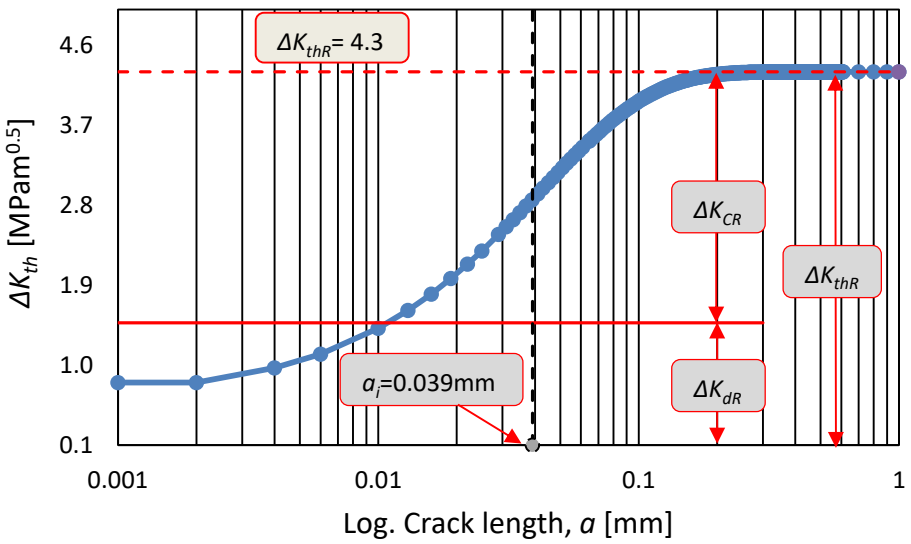

Figure 6. 37 Crack propagation threshold as a function of crack length (logarithmic scale) according to Chapetti's model

6.8.2 Chapetti model in a KT type diagram for the AF+WQ specimens WoRS

The Kitagawa-Takahashi diagram was used to explain the estimation of the fatigue threshold for propagation and nonpropagation of cracks. The experimental data of the stress threshold as a function of crack length were plotted for the AF+WQ without residual stress FG HAZ microstructure specimens prepared in the laboratory furnace, and presented in Figure 6.38 and Figure 6.39. The threshold limit was determined and the thresholds were calculated for both short crack and long crack propagation.

In the KT-diagram the red circles represent the threshold stress range in the function of the threshold for long crack propagation (known as a long crack regime), while the blue circles represent the threshold for non-propagation of cracks (known as a short crack regime). Also, the vertical green dashed line represents the size area $\sqrt{area}$ of the artificial defect, which, for our case, was calculated to be $\sqrt{area} = 0.047$ mm. This means that the size of the defect was smaller than the a_i (the critical crack size to behave as a long crack) which was $a_i = 0.058$ mm, and the threshold ΔK_{thR} becomes critical for further propagation.

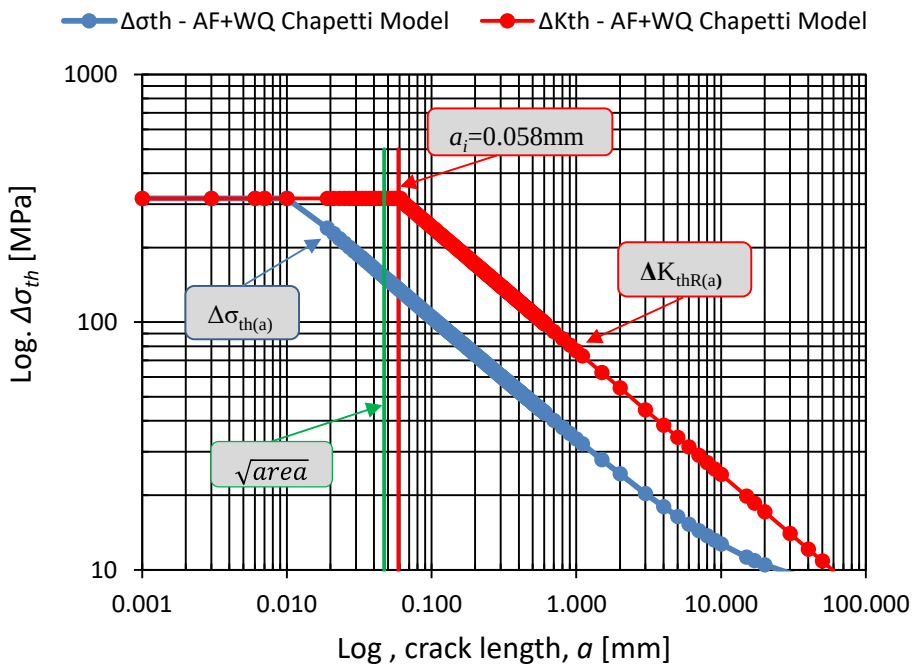

Figure 6. 38 Kitagawa-Takahashi diagram of AF+WQ without residual stress specimens

As the microstructural threshold ΔK_{dR} was a small value, the conditions for crack propagation were fulfilled and the crack soon started to propagate. Consequently, this influenced the endurance limit of the specimens, which was evaluated to be σ_{eR} = 550 MPa.

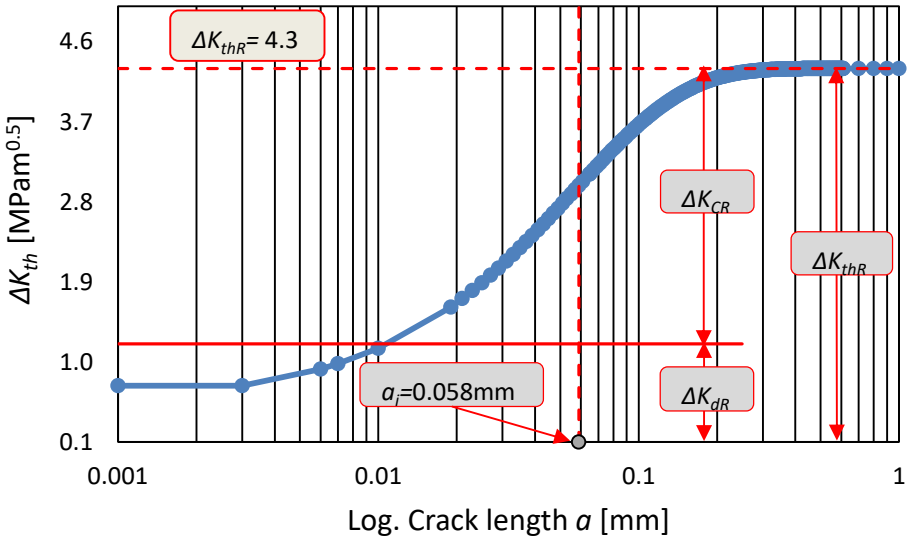

Figure 6. 39 Crack propagation threshold as a function of crack length (log scale)

6.8.3 Chapetti model in a KT- type diagram for AF+WQ specimens WRS

The Kitagawa-Takahashi diagram was used to explain the estimation of the fatigue threshold for cracks that propagate and nonpropagated cracks. Figures 6.40 and Figure 6.41 provide experimental data of the stress threshold as a function of crack length for AF+WQ with residual stress FG HAZ microstructure specimens. The thresholds for short crack and long crack propagation were calculated and the threshold limit was found. In the KT-diagram the red circles represent the threshold stress range in the function of the threshold for long crack propagation (known as a long crack regime), while the blue circles represent the threshold for non-propagation of cracks (known as a short crack regime). Also, the vertical green dashed line represents the size area $\sqrt{area}$ of the artificial defect, which, for our case, was calculated to be $\sqrt{area} = 0.047$ mm. This means that the size of the defect was smaller than the a_i (the critical crack size to behave as a long crack) which was $a_i = 0.039$ mm, and the threshold ΔK_{thR} becomes critical for further propagation.

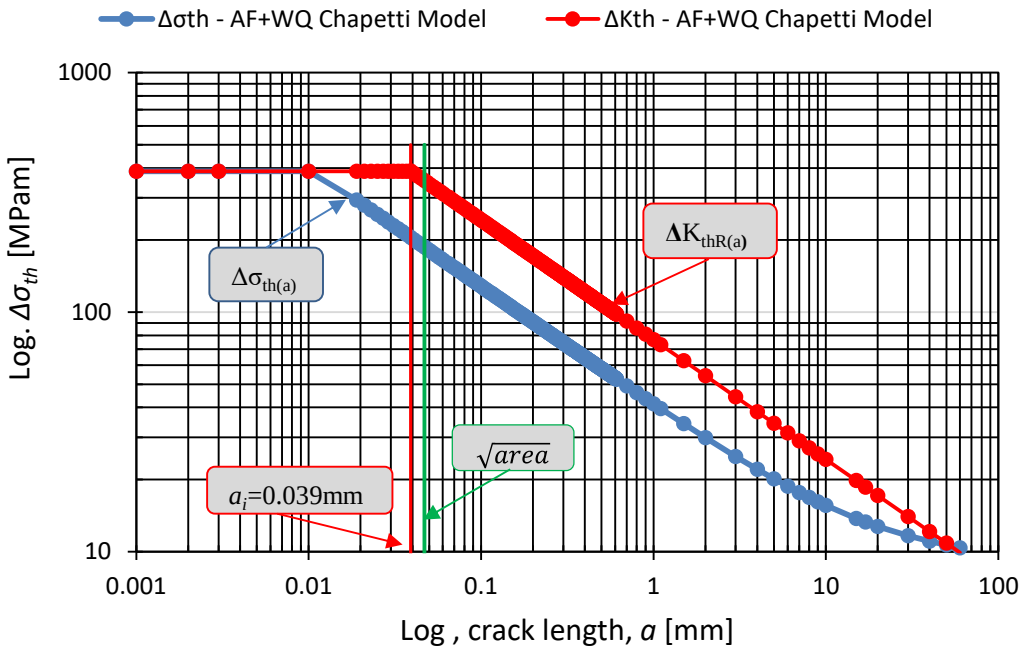

Figure 6. 40 Kitagawa-Takahashi diagram of the AF+WQ WRS specimens

The requirements for crack propagation were met, since the microstructural threshold ΔK_{dR} was a tiny number, and the crack soon started to propagate. As a result, this affected the specimens' endurance limit, which was determined to be σ_{eR} = 675 MPa.

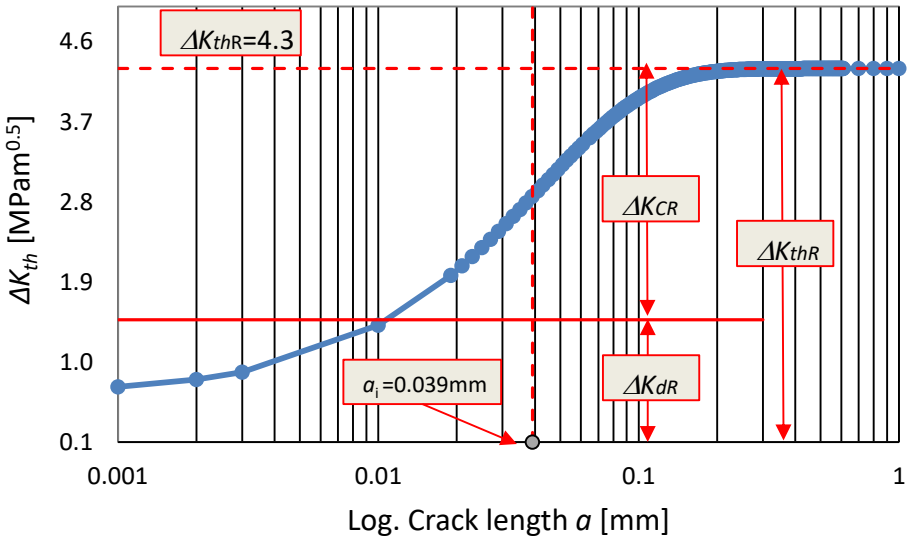

Figure 6. 41 Crack propagation threshold as a function of crack length (log scale)

6.8.4 Chapetti model in a KT- type diagram for the WTCS smooth specimens

The estimation of the fatigue threshold for propagation and non-propagation of cracks is explained with the Kitagawa-Takahashi diagram. The experimental data of the stress threshold as a function of crack length were plotted for the WTCS smooth specimens and are presented in Figure 6.42 and Figure 6.43. The thresholds for short crack and long crack propagation were calculated and the threshold limit was found. In the KT-diagram the red circles represent the threshold stress range in the function of the threshold for long crack propagation (known as a long crack regime), while the blue circles represent the threshold for non-propagation of cracks (known as a short crack regime). Also, the vertical green dashed line represents the size area $\sqrt{area}$ of the artificial defect, which, for our case, was calculated to be $\sqrt{area} = 0.047$ mm. This means that the size of the defect was smaller than the a_i (the critical crack size to behave as a long crack) which was $a_i = 0.024\ mm$, and the threshold ΔK_{thR} becomes critical for further propagation.

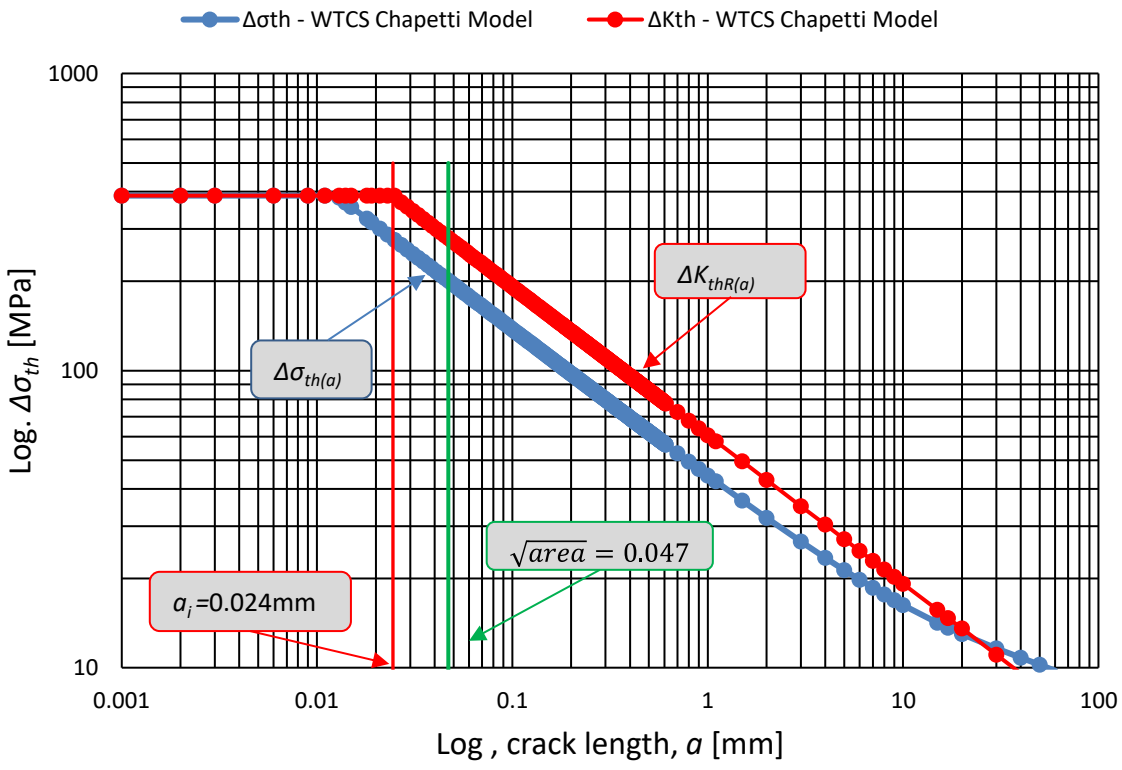

Figure 6. 42 Kitagawa-Takahashi diagram of the WTCS smooth specimens

As the microstructural threshold ΔK_{dR} was a small value, the conditions for crack propagation were fulfilled and the crack soon started to propagate. Consequently, this had an influence on the endurance limit of the specimens, which was evaluated to be σ_{eR} = 675 MPa.

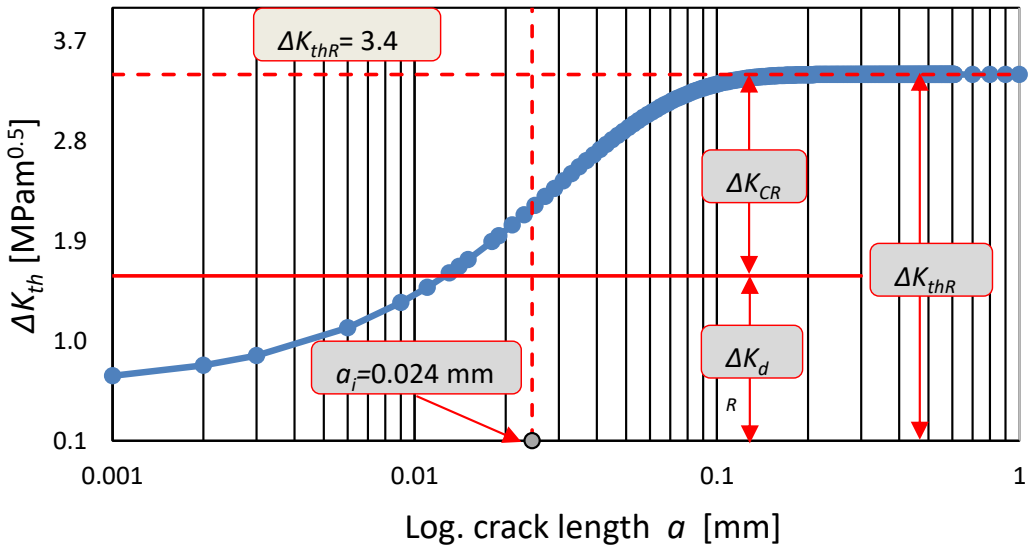

Figure 6. 43 Crack propagation threshold as a function of crack length (log scale)

6.8.5 Chapetti model in a KT- type diagram for the WTCS specimens WoRS

The experimental data of the stress threshold as a function of crack length were plotted for WTCS without residual stress, and are presented in Figure 6.44 and Figure 6.45. In the KT-diagram the red circles represent the threshold stress range in the function of the threshold for long crack propagation (known as a long crack regime), while the blue circles represent the threshold for non-propagation of cracks (known as a short crack regime). Also, the vertical green dashed line represents the size area $\sqrt{area}$ of the artificial defect, which, for our case, was calculated to be $\sqrt{area} = 47$ µm. This means that the size of the defect was smaller than the a_i (the critical crack size to behave as a long crack), which was $a_i = 0.036$ mm, and the threshold ΔK_{thR} becomes critical for further propagation.

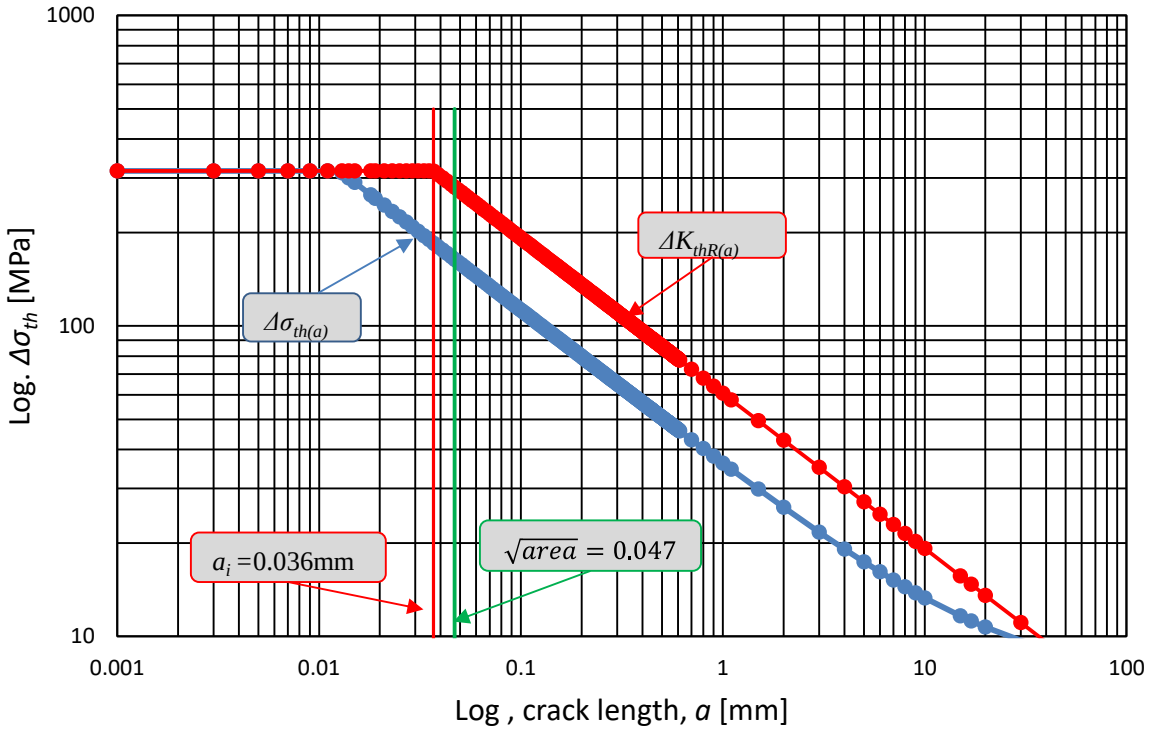

Figure 6. 44 Kitagawa-Takahashi diagram of WTCS without residual stress specimens

As the microstructural threshold ΔK_{dR} was a small value the conditions for crack propagation were fulfilled and the crack soon started to propagate. Consequently, this had an influence on the endurance limit of the specimens, which was evaluated to be σ_{eR} = 550 MPa.

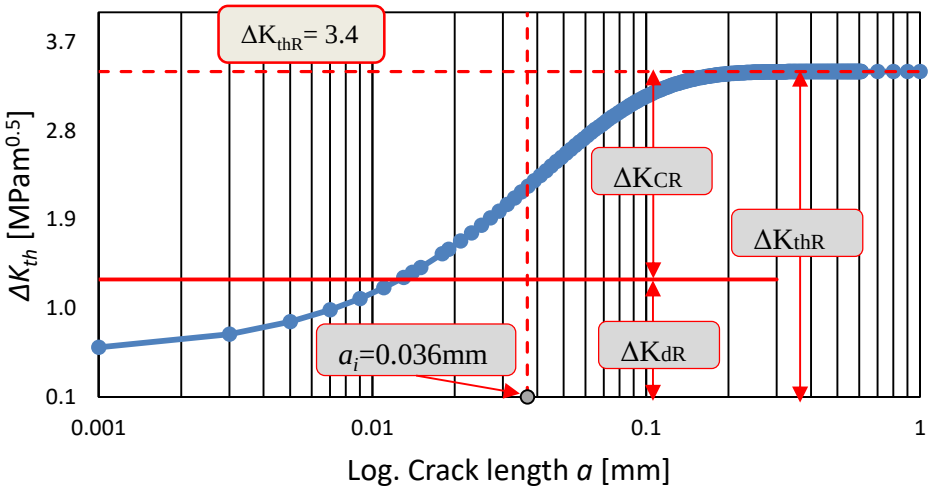

Figure 6. 45 Crack propagation threshold as a function of crack length (log scale)

6.8.6 Chapetti model in KT type diagram for WTCS specimens WRS

The xperimental data of the stress threshold as a function of crack length were plotted for the WTCS with residual stress specimens in a welding simulator and are presented in Figure 6.46 and Figure 6.47. The thresholds for short crack and long crack propagation were calculated and the threshold limit was found. In the KT-diagram the red circles represent the threshold stress range in the function of the threshold for long crack propagation (known as a long crack regime), while the blue circles represent the threshold for non-propagation of cracks (known as a short crack regime). Also, the vertical green dashed line represents the size area $\sqrt{area}$ of the artificial defect, which, for our case, was calculated to be $\sqrt{area} = 0.047$ mm. This means that the size of the defect was smaller than the a_i (the critical crack size to behave as a long crack) which was $a_i = 0.024$ mm, and the threshold ΔK_{thR} becomes critical for further propagation.

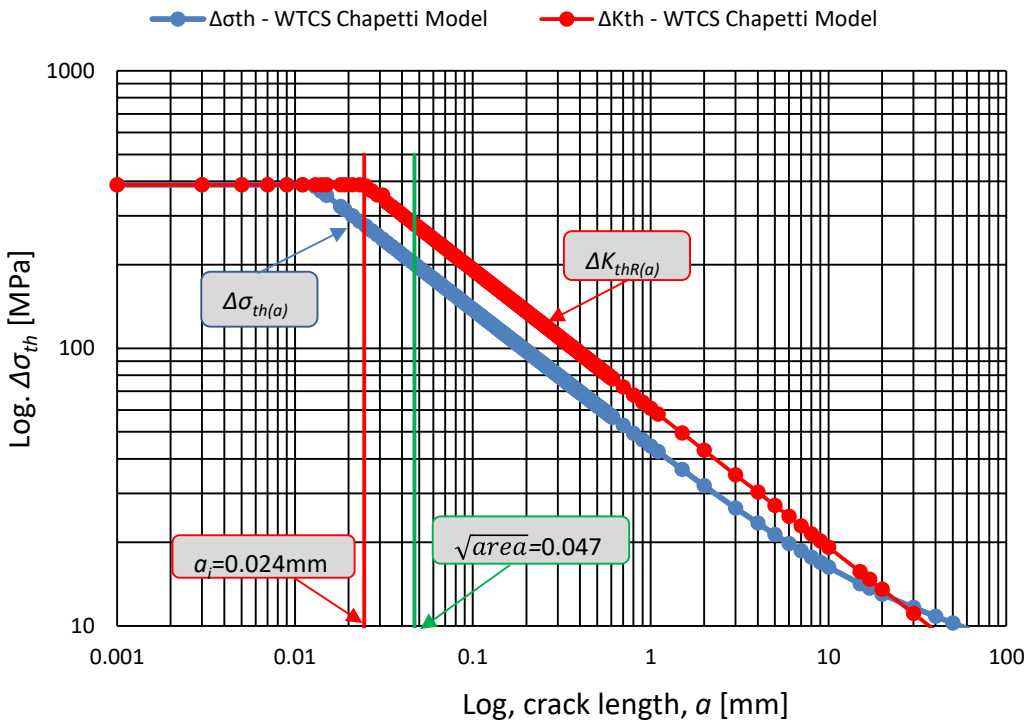

Figure 6. 46 Kitagawa-Takahashi diagram of WTCS without residual stress specimens

As the microstructural threshold ΔK_{dR} was a small value, the conditions for crack propagation were fulfilled and the crack soon started to propagate. Consequently, this had an influence on the endurance limit of the specimens, which was evaluated to be $\sigma_{eR} = 675$ MPa.

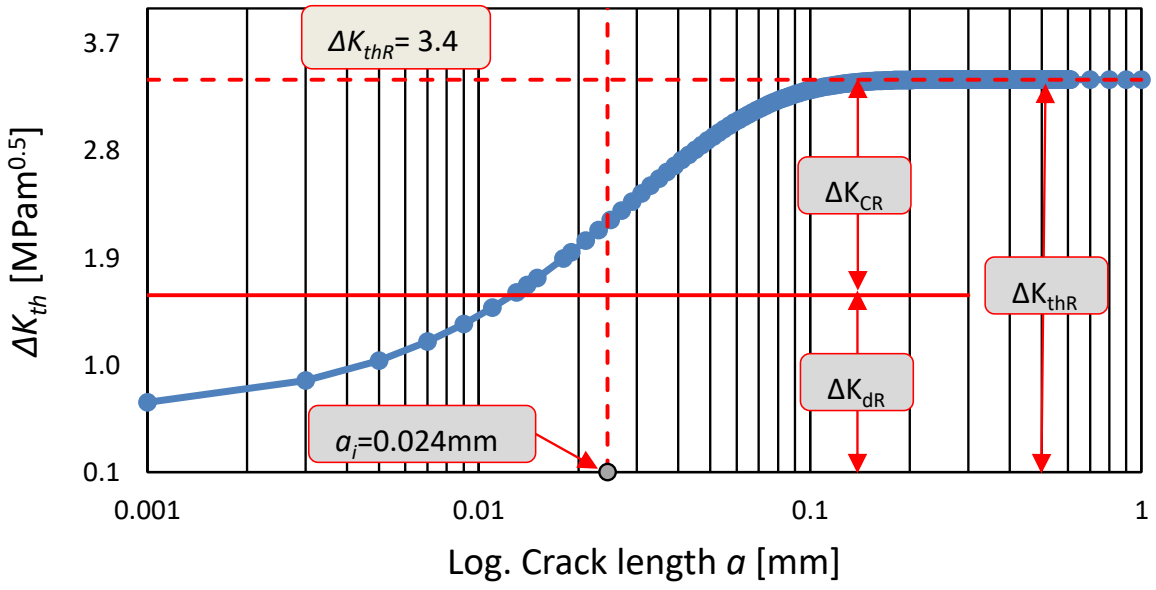

Figure 6. 47 Crack propagation threshold as a function of crack length (log scale)

6.8.7 Chapetti model parameters for the AF+WQ vs WTCS specimens

On the basis of the experimental findings and their assessments, the following Table was created to provide a clear image of how the specimens performed during the fatigue loading test and in fatigue crack growth. The parameters derived from the implementation of the Chapetti's model in the experimental data of the AF+WQ and WTCS specimens are also compared in Table 6.11. The minor difference in grain size preparation could be the explanation of the slight difference in the matching results, which were relatively close. For the AF+WQ specimens, the critical crack length for crack propagation was in the range of 0.024 mm to 0.058 mm, whereas, for the WTCS specimens, the critical crack length for crack propagation was in the range of 0.024 mm to 0.036 mm. This indicates that only WoRS (without residual stress) specimens could be identified to have non-propagation cracks. However, in other specimens the crack propagated constantly because of the magnitude of the intentionally created flaw, which was $\sqrt{area} = 0.047$ mm.

Table 6. 11 Experimental data taken from the Chapetti's model for AF+WQ and WTCS specimens

AF+WQ specimens								
	R	$\Delta\sigma_{eR}$, MPa	ΔK_{th}, MPa $m^{0.5}$	$d_{awerage}$, μm	ΔK_{dR}, MPa $m^{0.5}$	ΔK_{CR}, MPa $m^{0.5}$	$\Delta K_{dR}/\Delta K_{CR}$ -	a_i. mm
Smooth	0.1	675	4.3	10.9	1.48	2.82	0.52	0.039
WoRS	0.1	550	4.3	10.9	1.2	3.10	0.39	0.058
WRS	0.1	675	4.3	10.9	1.48	2.82	0.52	0.039
WTCS specimens								
	R	$\Delta\sigma_{eR}$, MPa	ΔK_{th}, MPa $m^{0.5}$	$d_{awerage}$, μm	ΔK_{dR}, MPa $m^{0.5}$	ΔK_{CR}, MPa $m^{0.5}$	$\Delta K_{dR}/\Delta K_{CR}$ -	a_i. mm
Smooth	0.1	675	3.4	12.6	1.59	1.81	0.87	0.024
WoRS	0.1	550	3.4	12.6	1.29	2.11	0.61	0.036
WRS	0.1	675	3.4	12.6	1.59	1.81	0.49	0.024

6.9 Residual stress effect around the micro defect

6.9.1 Stress destribution on the flat surface due to the Vickers pyramid

The results of the numerical model analysis of the Vickers pyramid indentation on the flat surface are shown in Figures 6.48 to 6.51. The full Vickers pyramid indentation and the distribution of the stresses are visible in its immediate vicinity.

Figures 6.48 show the distribution of Von Mises stress when the pyramid was loaded in the cross-section, and in the ground plane view at the maximum indentation depth when the pyramid was in equilibrium with the reaction of the material. The maximum tensile stresses resulting from the pyramid's pressure on the material will occur at the top edge of the impression, and the maximum compressive stresses occur at the bottom of the indentation. The distribution of stress components

were at the maximum indentation depth, when the pyramid was in equilibrium with the material reaction. The depth after impression was 30.32 μm,when pyramid was loaded by the force of F = 98.1 N.

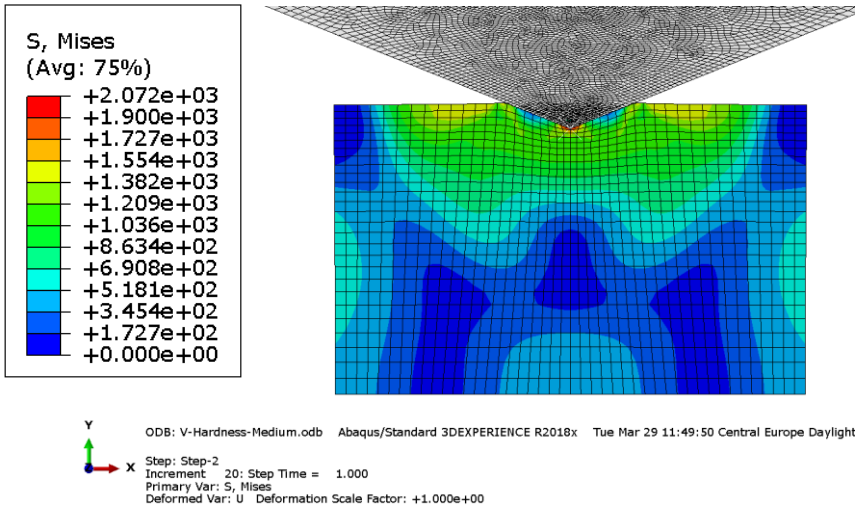

Figure 6. 48 Distribution of Von Mises stress when the pyramid was loaded at F = 98.1 N

Figure 6.49 shows the stresses $\sigma_{xx,}$ this time a top view, when the pyramid was loaded. As the numerical model only included one/fourth, the results are shown so that we can see the stresses around the entire indentation of the Vickers pyramid. After the pyramid had been removed, the stress distribution at the Vickers pyramid's maximum depth, as well as on the diagonals, is clearly visible. This explains perfectly the reason why the crack originated from the bottom and why it propagates through the diagonals.

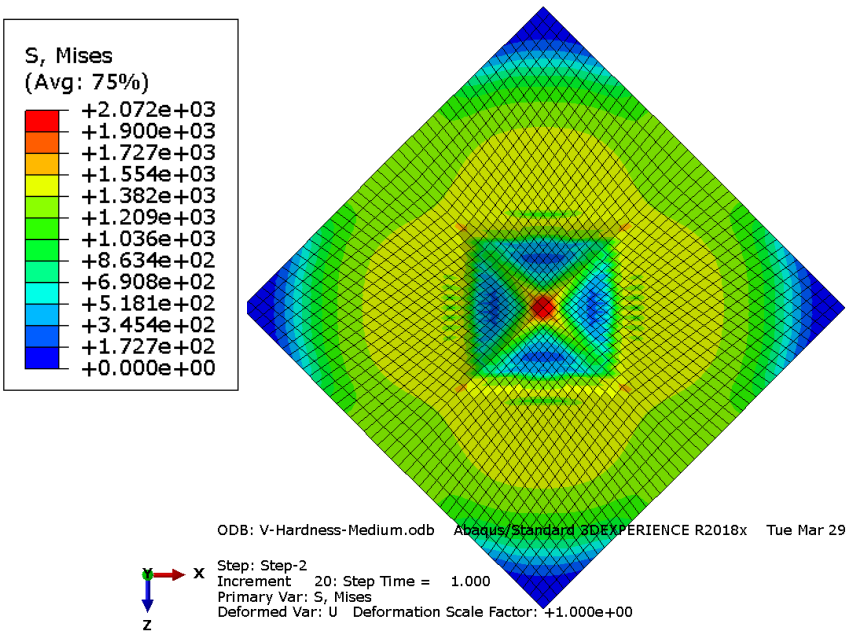

Figure 6. 49 Van Mises stresses in the flat surface at a load of F=98.1 N of the pyramid

The PEEQ value around the Vickers indentation when the pyramid is removed represents the residual stresses that remained due to indenting, simulated by using FEA on a flat surface were presented on Figure 6.50.

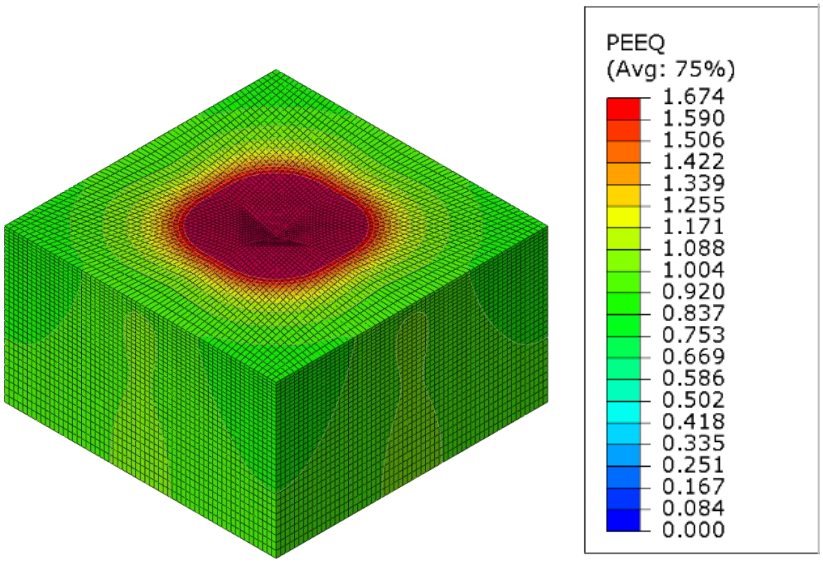

Figure 6. 50 Von Mises stress destribution remained on the flat surface due to the Vickers pyramid

In the other hand the Von Mises stress distribution results from the Vickers indentation when pyramid is removed simulated by using FEA on flat surface were presented on Figure 6.51.

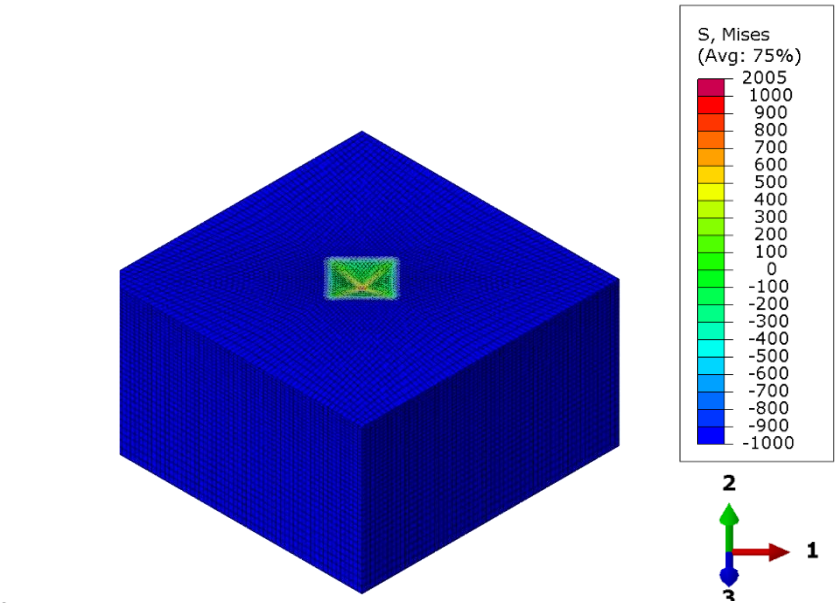

Figure 6. 51 The plastic strain equivalent on the flat surface due to the Vickers pyramid

6.9.2 Stress destribution due to the Vickers pyramid on the groove

In the model created on Abaqus the outcomes of the Vickers pyramid indentation simulation using FEA were as follows, and are presented in Figures 6.52 to 6.53. The mesh, as well as the boundary conditions for each specimen were explained (see Subchapter 3.2).

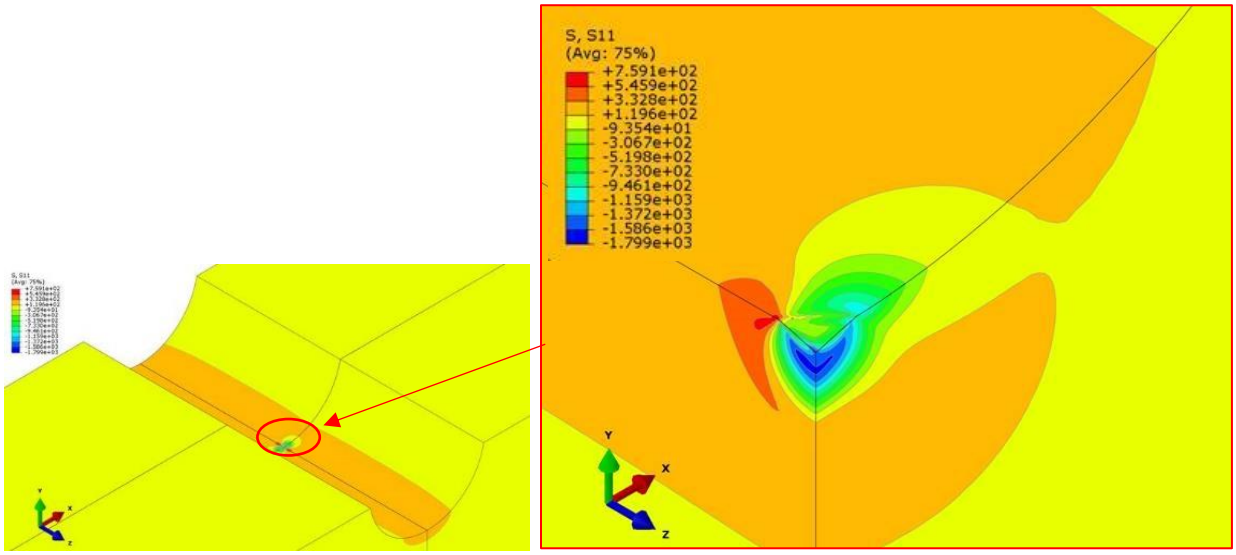

Figure 6. 52 Residual stresses σ_{xx} after indentation on the groove

These stresses in Figure 6.52 represent the distribution of residual stresses in plane yz of the future loading of the specimen through the artificial defect – Vickers indentation.

Finally, the Vickers indentation simulated by using FEA on the groove and on the flat surface were compared with the experimental results in the diagram of load vs depth during the process of introducing the microdefect, and are presented in Figure 6.53. The load vs. depth plot during the microdefect impression showed a small difference between the results from the experimental work (the blue line on the diagram) and FEA simulation at the groove of the specimen (the red line on the diagram). Due to the Vickers pyramid's unloading causing elastic material recovery, the unloading curves in the experiment and FEA did not match perfectly. Comparing the results of FEM into groove with them taken from the measurement with microscope we have found 3.6% difference, in the other hand comparing results of flat plate a 6.1% difference is derived.

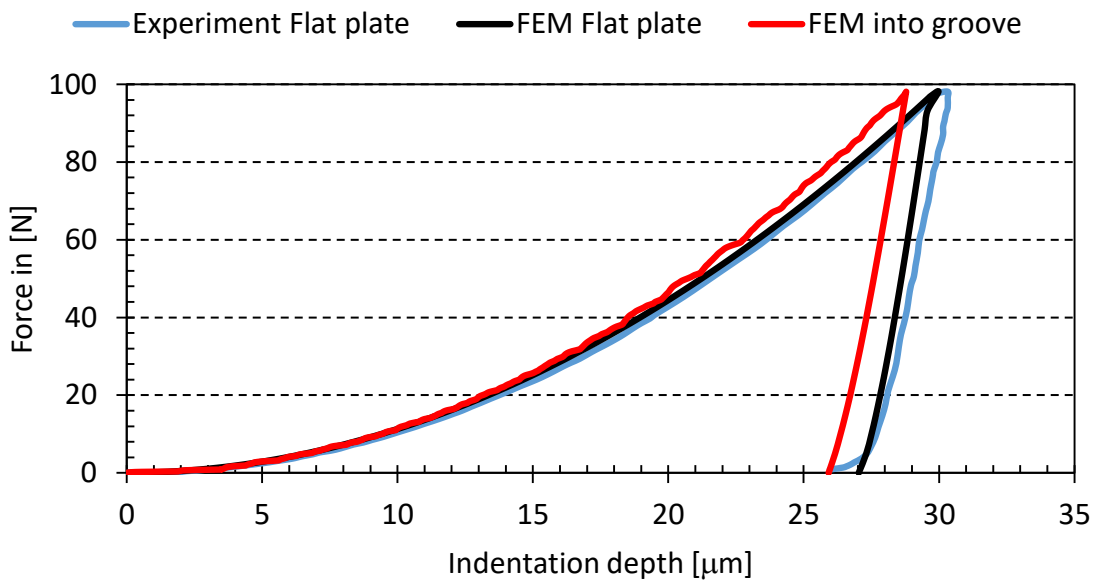

Figure 6. 53 Comparison of the force-depth diagram (experiment, flat surface and groove)

6.9.3 S11 distribution in With Residual Stresses (WRS) specimens

After loading the specimen to the fatigue limit σ_{eR} =675 MPa, and the model with the bending moment of M_2 = 15391 N·m which was ½ of the global bending moment of the specimen (30782 N·mm), the stress distribution was generated and concentrated mostly around the Vickers pyramid (artificially prepared microdefect). The magnitude of the stress distribution generated was in units of megapascal (MPa). Based on Figure 6.54, it can be seen that the tensile stresses in the microdefect's diagonals can reach a maximum value of 1089 MPa, while compressive stresses can reach a maximum value of 1168 MPa on the microdefect's bottom.

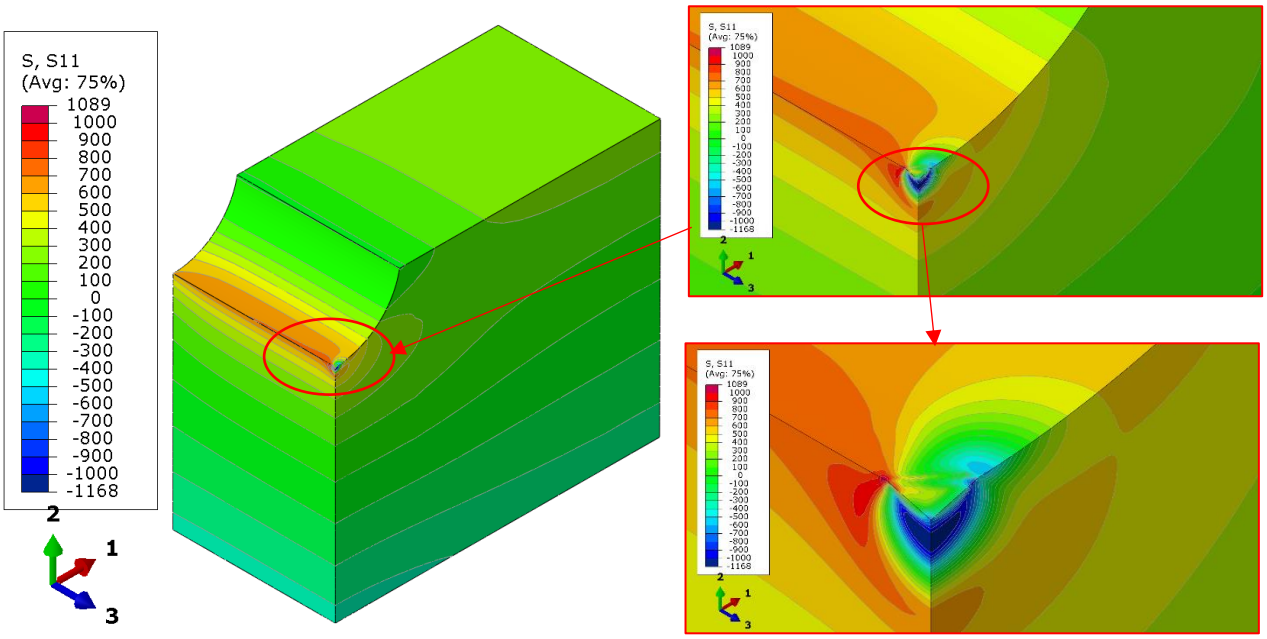

Figure 6. 54 S11 stress distribution after applying bending moment M_2=15391 N·m

The plot of the stress distribution s_{11} in plane 23 along the path distance for specimens in WRS conditions are presented in Figure 6.55. The high level of tensile stress are in vicinity of the diagonals of Vickers indentation and this explain the reason why the crack initiated from the diagonals in case of WRS specimens. The compressive stresses were high in bottom and have a blocked effect of crack initiation. The s11_RS_Fo curve represents the condition when the pyramid was removed, and that is the magnitude of the remaiing residual stresses after applying the F_{max} (10kg or 98.1 N).

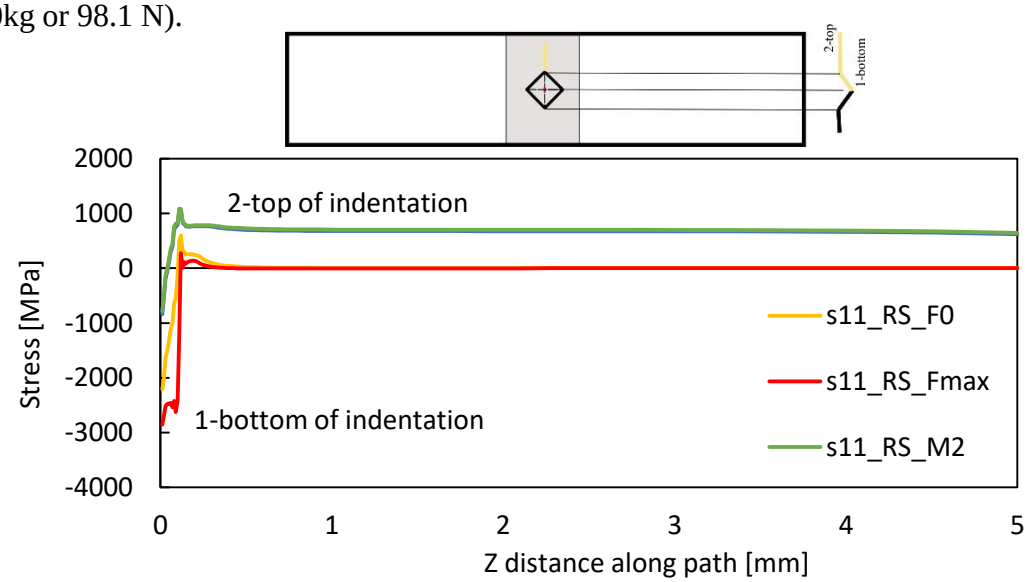

Figure 6. 55 Stress distribution along the path distance

On the other hand, the PEEQ magnitude results are presented after applying the M_2 maximum stress on the WRS specimen. Figure 6.56 shows the area where the main plastic strain equivalents (PEEQ) ε_{PEEQ} were the greatest. In the red area, the plastic strain was greater than 0.2%.

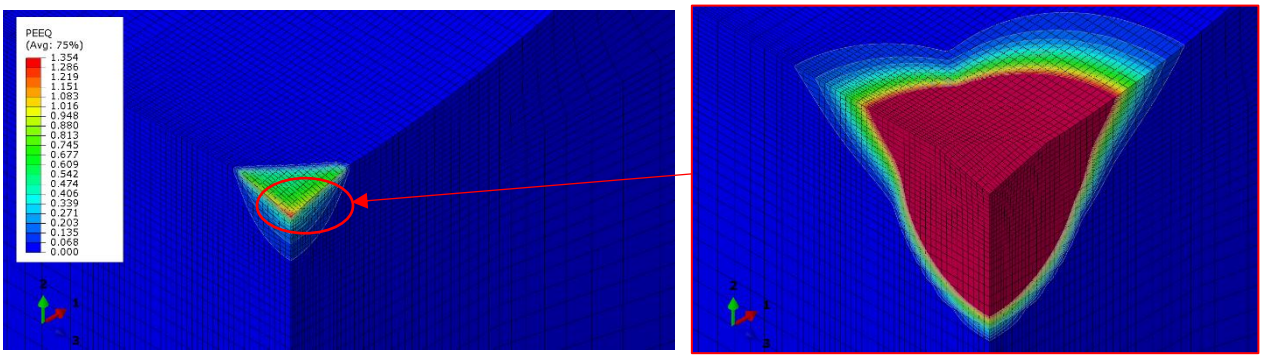

Figure 6. 56 The plastic strain equivalent (PEEQ) after applying the M_2 bending moment

6.9.4 Displacement along the u_2 of the WRS specimens

The displacements along the u_2 of the WRS specimens as result of applying maximum force F_{max} and F_0 are presented in Figure 6.57. Displacements slightly bigger than 0.025 mm, or 25 μm, were derived. The maximum displacement occurred at the indentation, and no displacements at all were identified along the path of the Z distance. The reason behind is due to elastic relaxation of the material when pyramid is removed. Blue line represent maximal load on the pyramide and represent profile when pyramide is in and maximal loaded, while red line represent profile of indentation after indentation is removed. Diagrams of displacement are presented on Figure 6.57, the enlarged diagram (right) shows the reaction in vicinity of indentation.

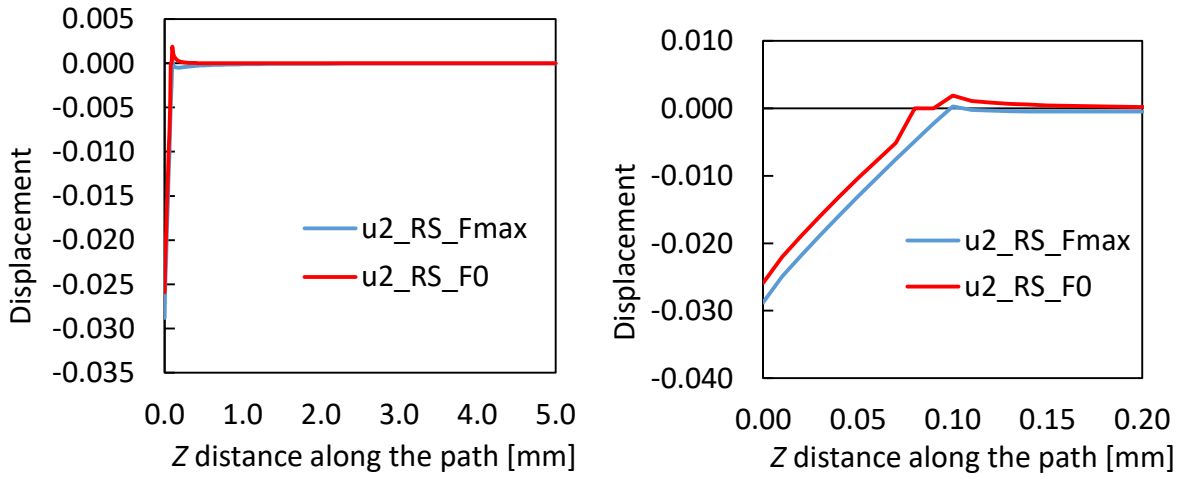

Figure 6. 57 Displacement along the u_2 of the WRS specimens at load F_0 and F_{max}

6.9.5 S11 distribution in Without Residual Stresses (WoRS) specimens

After loading the specimen to the fatigue limit σ_{eR} = 550 MPa, and the model with the bending moment of M_1 = 12541 N·m, which was ½ of the global bending moment of the specimen (25082 N·mm), the stress distribution was generated, and it is shown in Figure 6.58. The tensile stresses in the microdefect's diagonals can reach a maximum value of 1124 MPa.

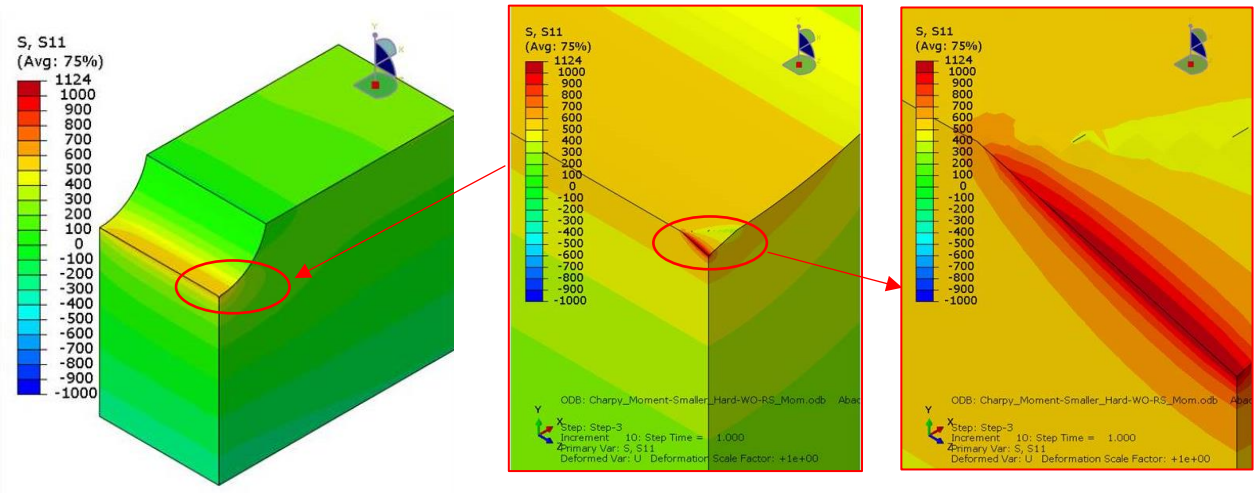

Figure 6. 58 S_{11} stress distribution after applying M_1=12541 N·m

Figure 6.58 shows that the high level of tensile stress are at bottom of the of Vickers indentation and this explain the reason why the crack initiated from the bottom and not from upper edges like case of WRS specimens.

The PEEQ magnitude results after applying the M_1 bending moment on the WoRS specimen are presented. Figure 6.59 shows the area where the main plastic strain equivalents (PEEQ) ε_{PEEQ} were the greatest. In the red area the plastic strain was greater than 0.2%.

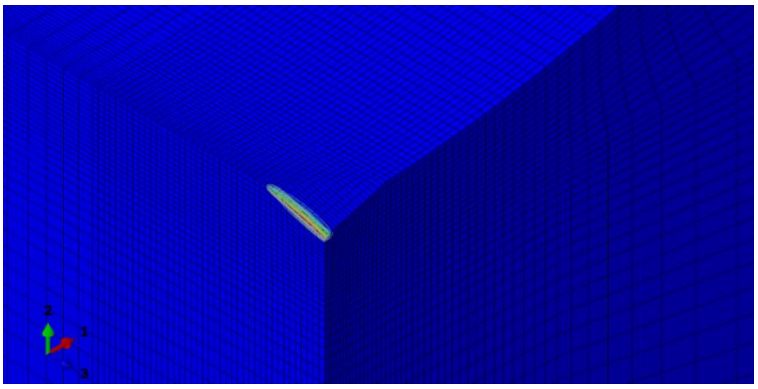

Figure 6. 59 The plastic strain equivalent (PEEQ) after applying M_1=12541 N·m

The case of loading of the FEM model with bending moment M_1 = 12541 N·m, actually represent loading of the specimen to its endurance limit σ_{eR} = 550 MPa for the W_0RS condition. In the other hand the case of loading of FEM model with bending moment M_2 = 15391 N·m, represent loading of the specimen to above the endurance limit on stress σ_{eR} = 675 MPa. This situation is shown in Figures 6.60 and 6.61. The tensile stresses in the microdefect's diagonals can reach a maximum value of 1301 MPa. This explain the fact that why in the fatigue test experiment at this stress loading level specimen were broken through indentation.

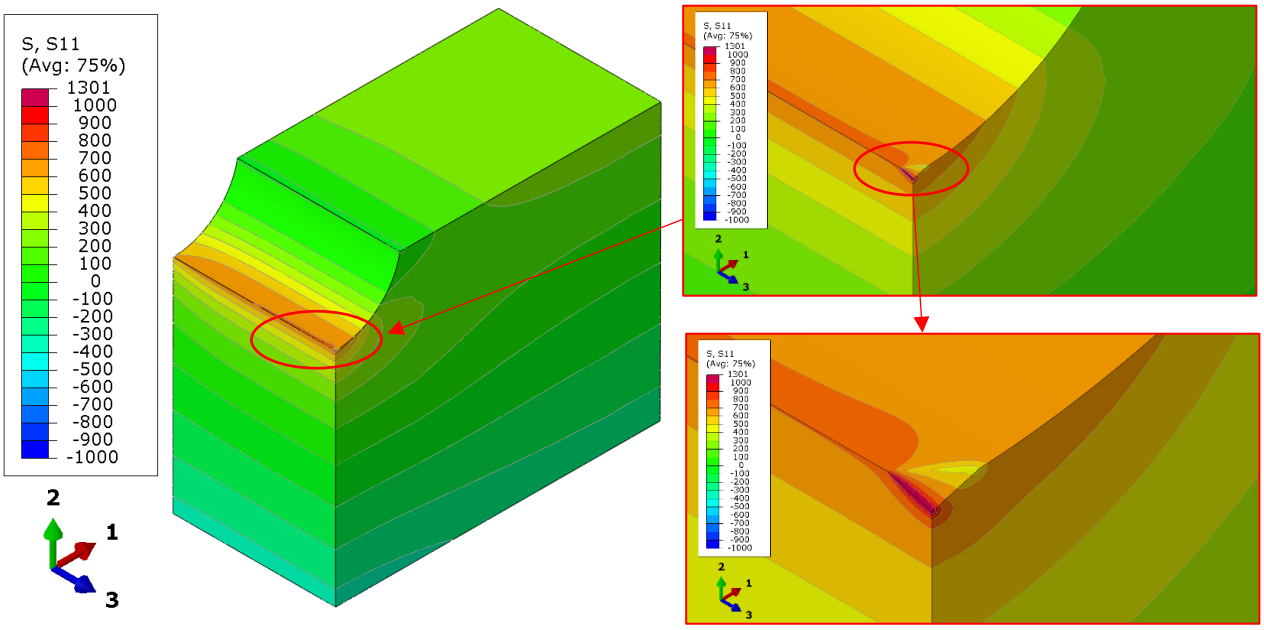

Figure 6. 60 S_{11} stress distribution after applying M_2=15391 N·mm

The PEEQ magnitude results are presented after applying the M_2 bending moment on the WoRS specimen. Figure 6.61 shows the area where the main plastic strain equivalents (PEEQ) ε_{PEEQ} were the greatest. In the red area the plastic strain was greater than 0.2%.

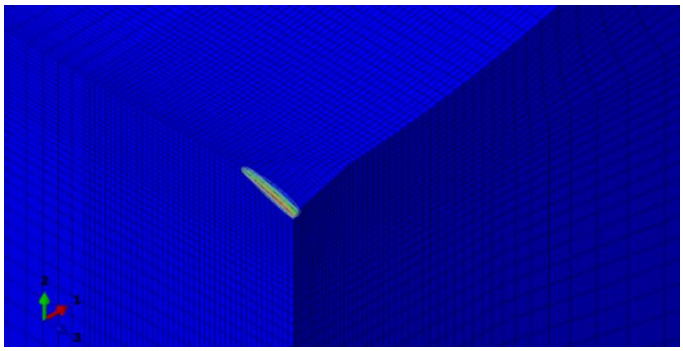

Figure 6. 61 The plastic strain equivalent (PEEQ) after applying the M_2 bending moment

The plot of the stress distribution in plane 23 in the s_{11} direction along the path distance for specimens without residual stresses conditions and the moment of loading with bending moment M_2 (above the endurance limit of WoRS condition) is presented n Figure 6.62 . The stress maximum value generated after applying bending moment M_2 was at the microdefect (Vickers Indentation). The stress started to stabilise along the distance to the level of the endurance limit σ_{eR}.

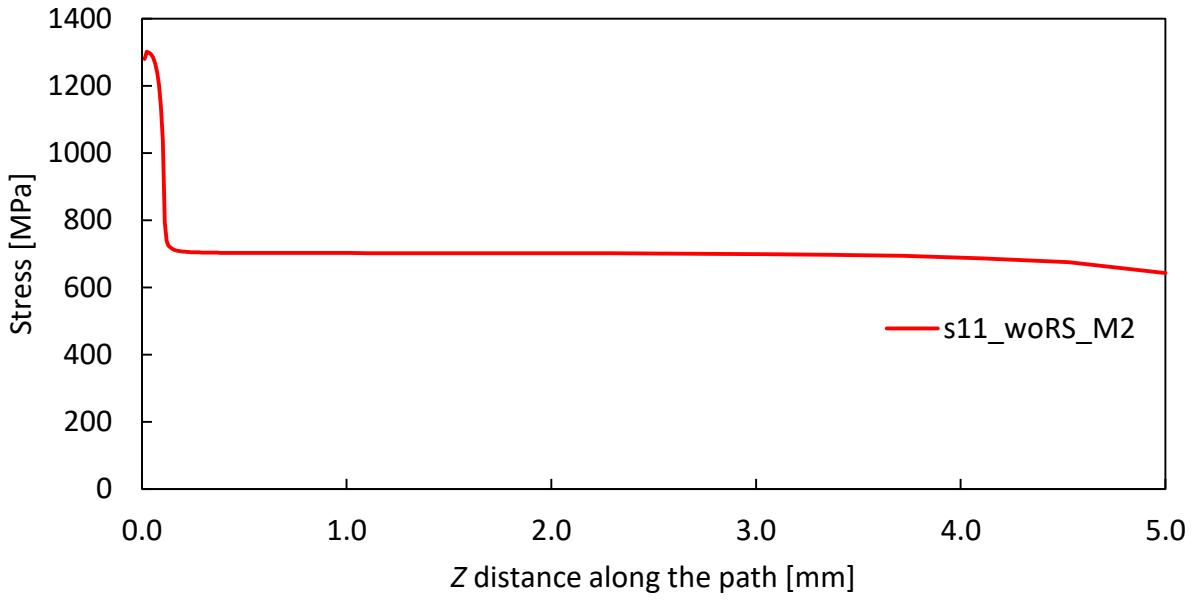

Figure 6. 62 Stress distribution along the path distance

6.9.6 S11 distribution in SMOOTH specimens

After loading the specimen to the fatigue limit σ_{eR} = 675 MPa, and the model with the bending moment of M_2 =15391 N·mm, which was ½ of the global bending moment of the specimen (30782 N·mm), the stress distribution was generated and concentrated mostly on the groove of the specimen.

The generated stress distribution along the groove/notch of specimen as it is shown in Figure 6.64.

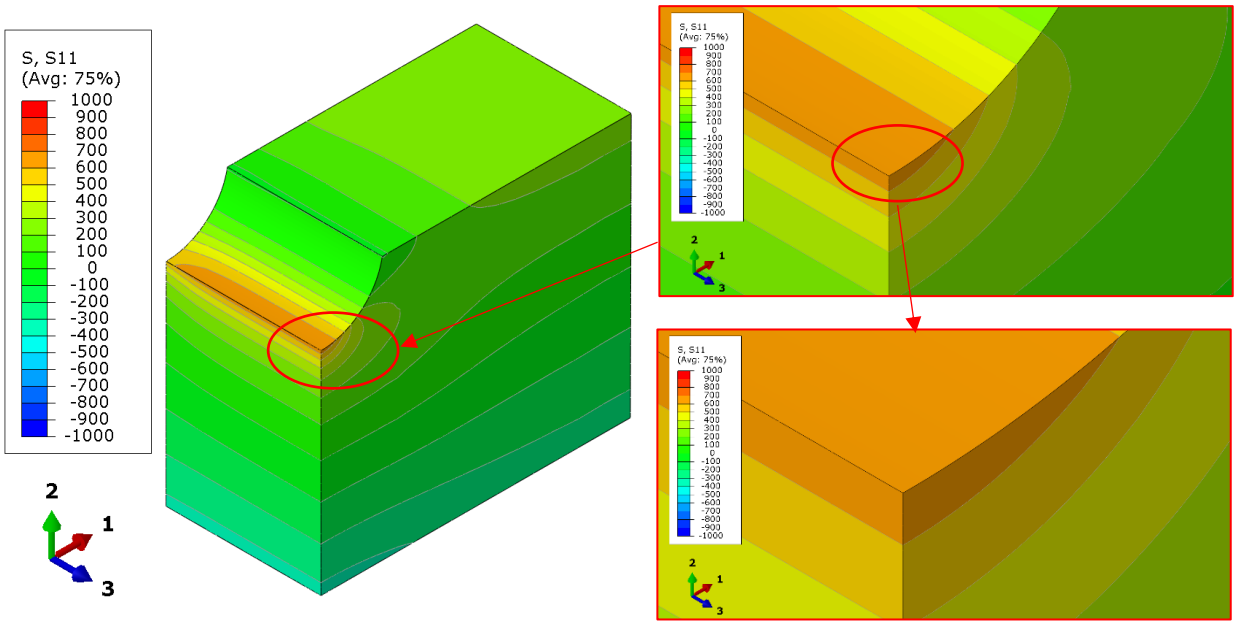

Figure 6. 63 s_{11} stress distribution after applying M_2 = 15391 N·mm on the SMOOTH specimens

For better visualization we adjusted the results legend from 700 MPa to -700 MPa and the generated stress distribution along the groove/notch of specimen is shown in Figure 6.64.

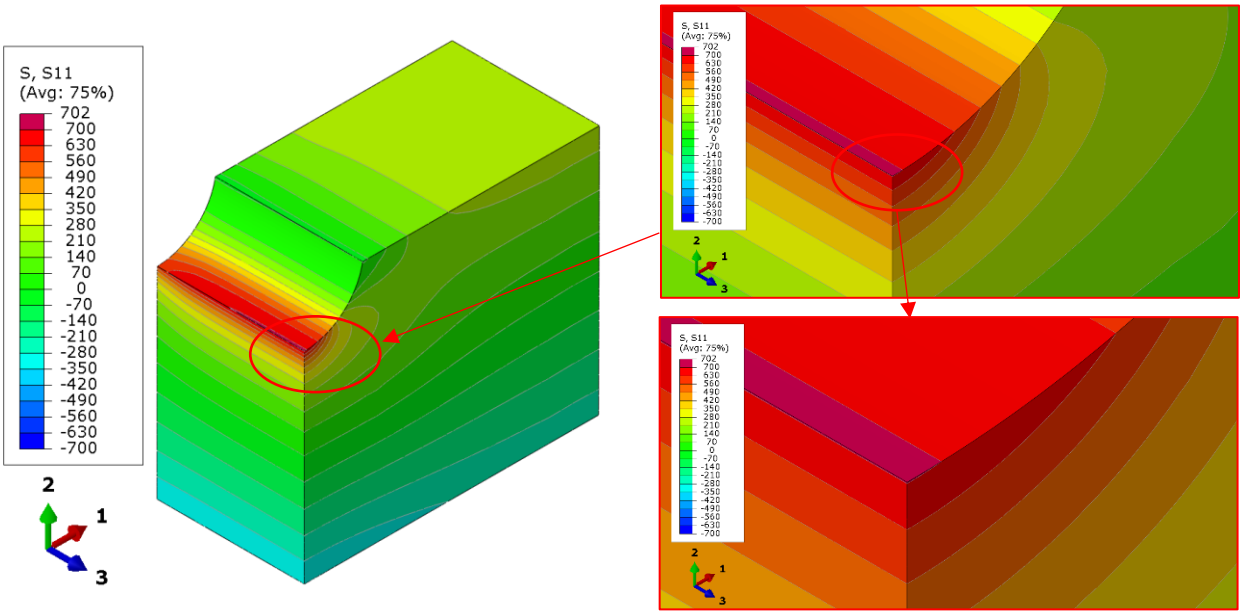

Figure 6. 64 S_{11} stress distribution after applying M_2 = 15391 N·mm at the SMOOTH specimens

The tensile stresses in the groove can a reach value of 702 MPa, and bigger than -700 MPa compressive stresses. This value has difference of approximately 4 % from the fatigue limit of specimens. This difference could be attributed to K_t or/and K_f factors.

The plot of the stress distribution along the path distance for SMOOTH specimens is presented in Figure 6.65. The stress generated after applying bending moment M_2 are tension in nature, and their distribution was constant along the path until the side of the specimen, where the value started to drop slightly.

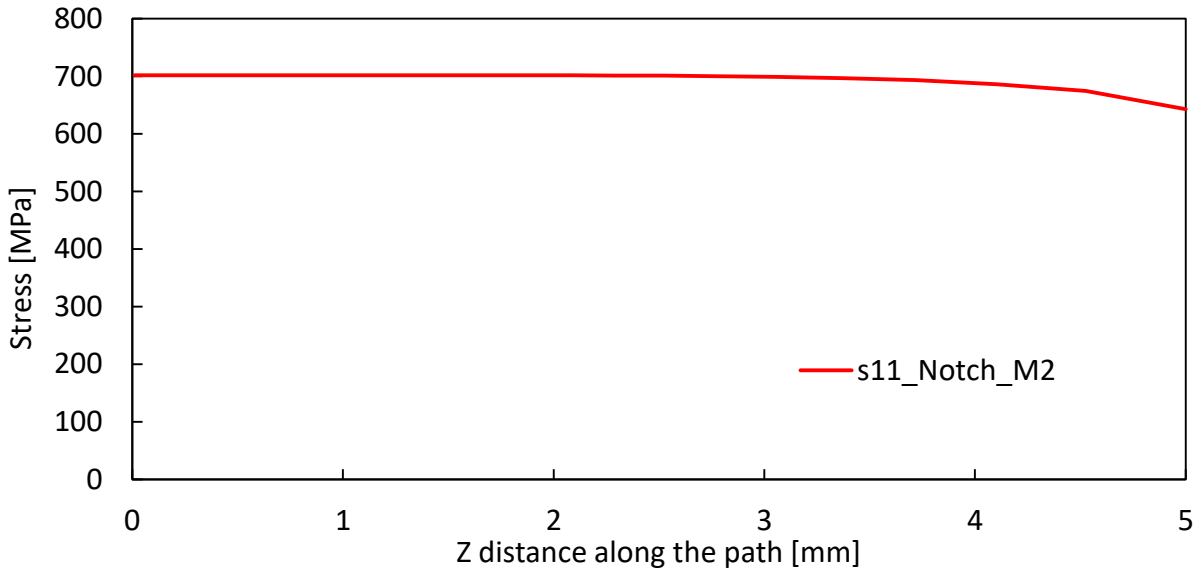

Figure 6. 65 Stress distribution along the path distance

6.9.7 Comparison of stress distribution for all types of specimens

Two alternative bending moments (M_1, M_2) were simulated and compared, in order to understand better what occurs during the loading of each type of specimen. Bending moments M_1 and M_2 were applied in tension.

Figure 6.71 shows the comparison of the stress distribution components at the maximum indentation depth, when the pyramid was in equilibrium with the material reaction for two different conditions (WRS-left side, WoRS- middle). For the third type of specimen (SMOOTH-right side), there was no indentation and a smaller stress concentration through the groove.

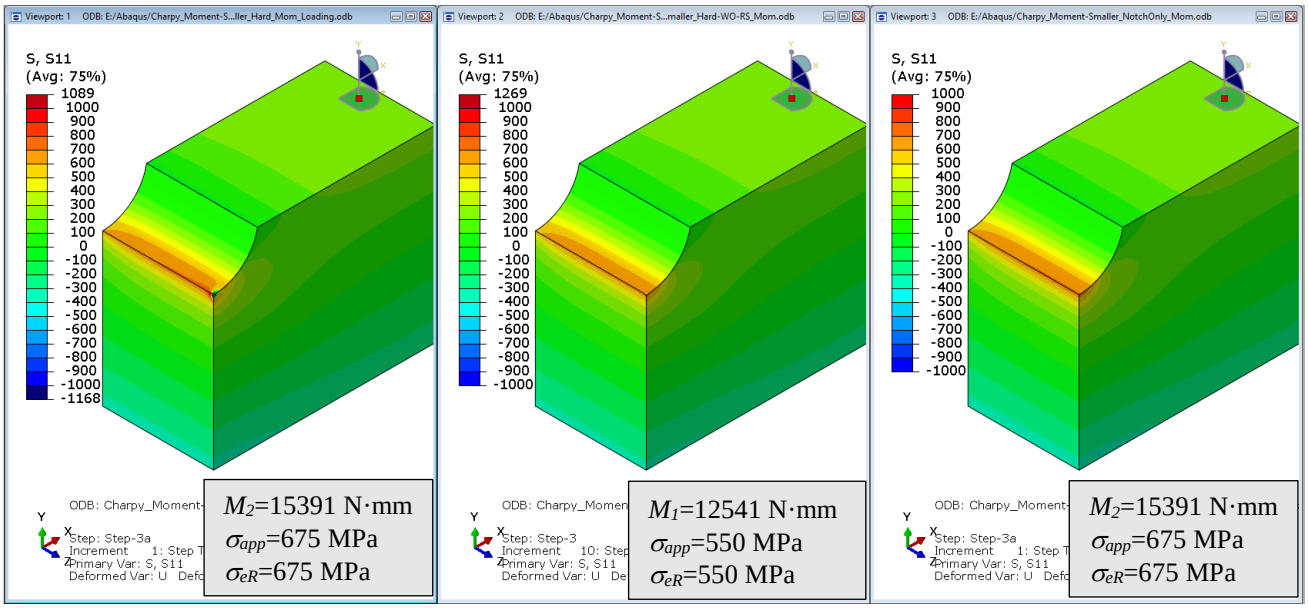

Figure 6. 66 Comparison of stress distribution for all types of specimens

The results shown in Figure 6.66 show that the maximum magnitude of the stress component destribution was in the specimens without residual stresses, with a value of 1090 MPa in tensile. On the other hand, the magnitude in the WRS specimens was 1089 MPa in tensile. Finally, the magnitude at the SMOOTH specimens was 702 MPa but the scale is adopted to other condition from -1000 to 1000 MPa for easier comparison.

A zoomed-in view of Figure 6.66 is shown in Figure 6.67, for the better vizualisation of the distribution of stress components when the Vickers pyramid was removed and the material had relaxed elastically. The stress component σ_{11} is the most important for crack initiation as it acts as tensile (stress mode I). The stresses shown in Figure 6.67 were in the material after the Vickers pyramid indentation, and represent the residual stresses due to the Vickers pyramid indentation. These stresses may be accelerating, or inhibiting the initiation and propagation of fatigue cracks, depending on their size and character (tensile-compressive).

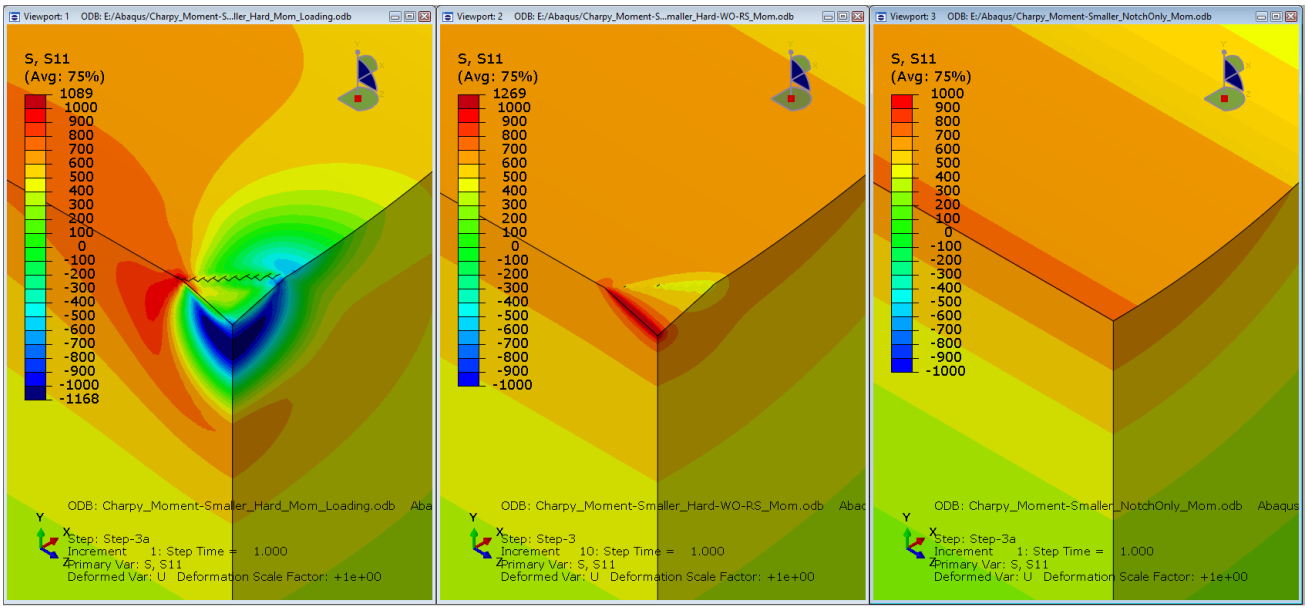

Figure 6. 67 Stress distribution in a cross-section of the impression of a Vickers pyramid when the pyramid was removed; (WRS, WoRS and SMOOTH)

6.10 Chapetti model including the FEA RS results

The effect of residual stress calculated by FEA and the estimation of the fatigue threshold for propagation and non-propagation cracks is explained with a Kitagawa-Takahashi diagram type for different types of specimens.

6.10.1 Chapetti model of AF+WQ of a SMOOTH specimen including local residual stresses (RS) calculated by FEM

The experimental data of stress threshold as a function of crack length were plotted including the RS from the FEM analysis, and are presented in Figure 6.68 and Figure 6.69. The thresholds for short crack and long crack propagation were calculated and the threshold limit was found. In the KT-diagram the black circles represent the threshold stress range in the function of the threshold for long crack propagation (known as a long crack regime), including the residual stress effect, while the blue circles represent the threshold stress range in the function of the threshold for long crack propagation (known as a long crack regime) excluding the residual stress effect. The vertical green dashed line represent the size area $\sqrt{area}$ of the artificial microdefect, which, for our case,

was calculated to be $\sqrt{area} = 0.047$ mm. This means that the microdefect size was larger than the a_i (the critical crack size to behave as a long crack), which was $a_i = 0.017$ mm, and the threshold ΔK_{thR} becomes critical for further propagation.

Fatigue crack propagation occurs only if the applied crack driving force ΔK_{appl} is higher than the threshold $\Delta K_{th,R,}$ and if the inclusion size (as $\sqrt{area} = 0.047$ in Figure 6.68) is higher than the value in the intersection between the threshold limit curve $\Delta K_{th,R}$ and the applied crack driving force line (fatigue limit). The fatigue crack is going to propagate until critical crack length a_c. The value of the critical crack length is determined by the fracture toughness of the material.

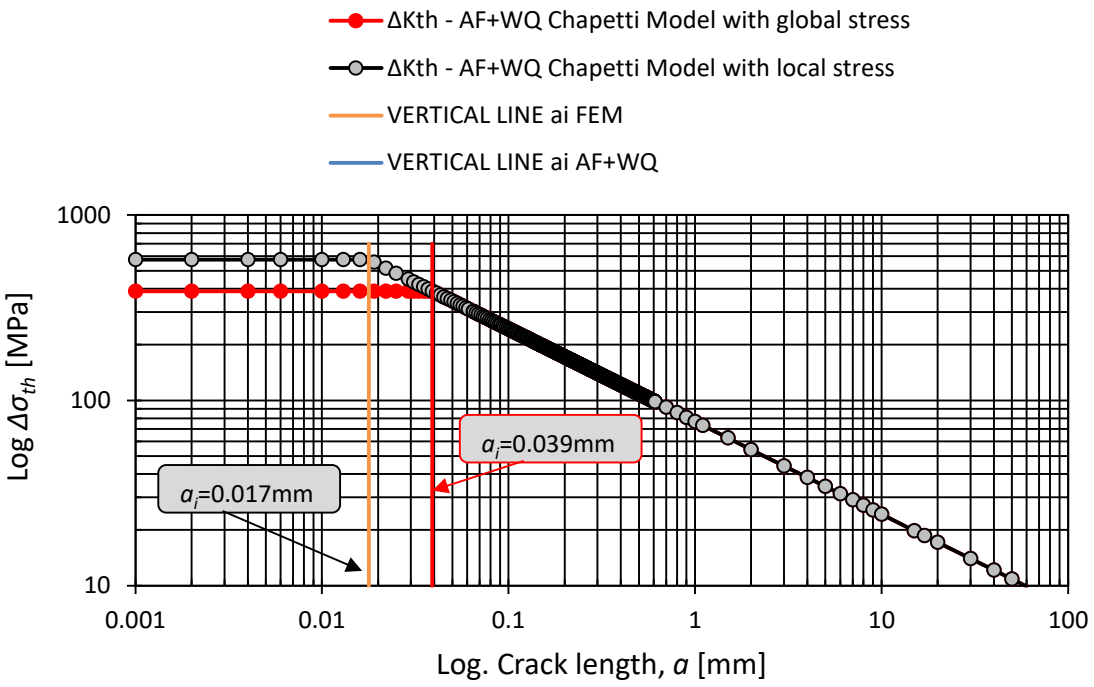

Figure 6. 68 KT-diagram of SMOOTH AF+WQ specimens with local and global RS from FEA

Figure 6.69 shows the fatigue crack driving force curves vs. the initial crack length for the constant applied stress $\Delta\sigma_n$. Based on Figure 6.69 it could be concluded that, when the global residual stress is taken into account, a smaller size of inclusion is predicted a_i=0.0178 mm. On the other hand, when the local residual stress is not taken into account, the size of the inclusion is predicted to be a_i = 0.0391 mm, and with a constant threshold value ΔK_{thR} = 4.3 MPa·m$^{1/2}$.

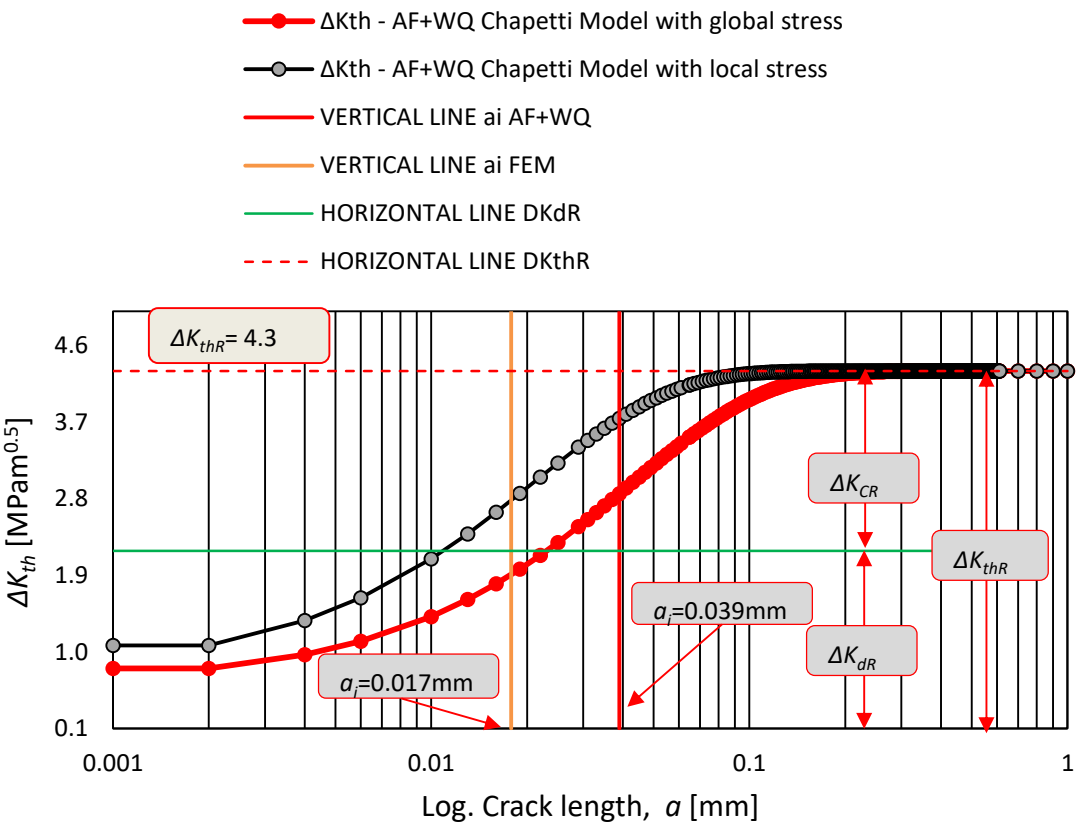

Figure 6. 69 Crack propagation threshold as a function of crack length (logarithmic scale) according to Chapetti's model

6.10.2 Chapetti model of AF+WQ of a WoRS specimen including residual stresses (RS) calculated by FEM

The experimental data of stress threshold as a function of crack length were plotted including RS from the FEM analysis, and are presented in Figure 6.70 and Figure 6.71. The thresholds for short crack and long crack propagation were calculated and the threshold limit was found. In the KT- diagram the black circles represent the threshold stress range in the function of the threshold for long crack propagation (known as a long crack regime) including the residual stress effect, while the blue circles represent the threshold stress range in the function of the threshold for long crack propagation (known as a long crack regime) excluding the residual stress effect . Also, the vertical green dashed line represents the size area $\sqrt{area}$ of the artificial defect, which, for our

case, was calculated to be $\sqrt{area} = 0.047$ mm. This means that the microdefect size was larger than the a_i (the critical crack size to behave as a long crack), which was $a_i = 0.014$ mm, and the threshold ΔK_{thR} becomes critical for further propagation.

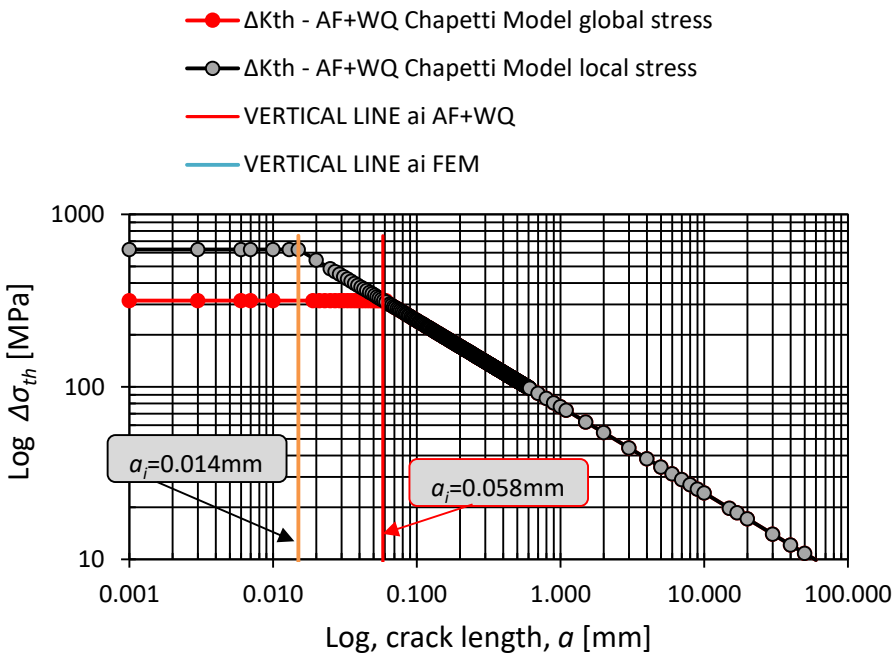

Figure 6. 70 KT diagram of WoRS AF+WQ specimens with and without RS from FEA

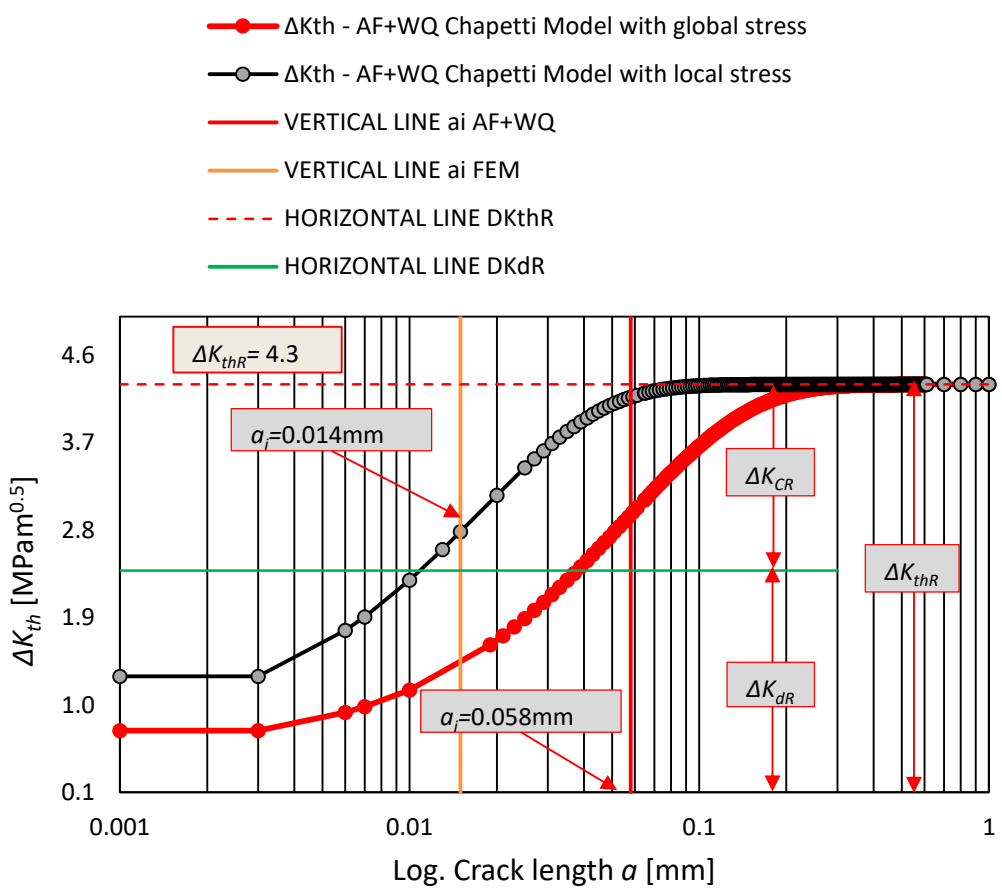

Figure 6. 71 Crack propagation threshold as a function of crack length (logarithmic scale) according to Chapetti's model

6.10.3 Chapetti model of AF+WQ of the WRS specimen including residual stresses (RS) calculated by FEM

The experimental data of the stress threshold as a function of crack length were plotted including the RS from the FEM analysis, and are presented in Figure 6.72 and Figure 6.73. The thresholds for short crack and long crack propagation were calculated and the threshold limit was found. In the KT-diagram the black circles represent the threshold stress range in the function of the threshold for long crack propagation (known as a long crack regime), including the residual stress effect, while the blue circles represent the threshold stress range in the function of the threshold for long crack propagation (known as a long crack regime), excluding the residual stress effect . Also, the vertical green dashed line represents the size area $\sqrt{area}$ of the artificial defect, which,

for our case, was calculated to be $\sqrt{area} = 0.047$ mm. This means that the microdefect size was larger than the a_i (the critical crack size to behave as a long crack) which was $a_i = 0.015$ mm, and the threshold ΔK_{thR} becomes critical for further propagation.

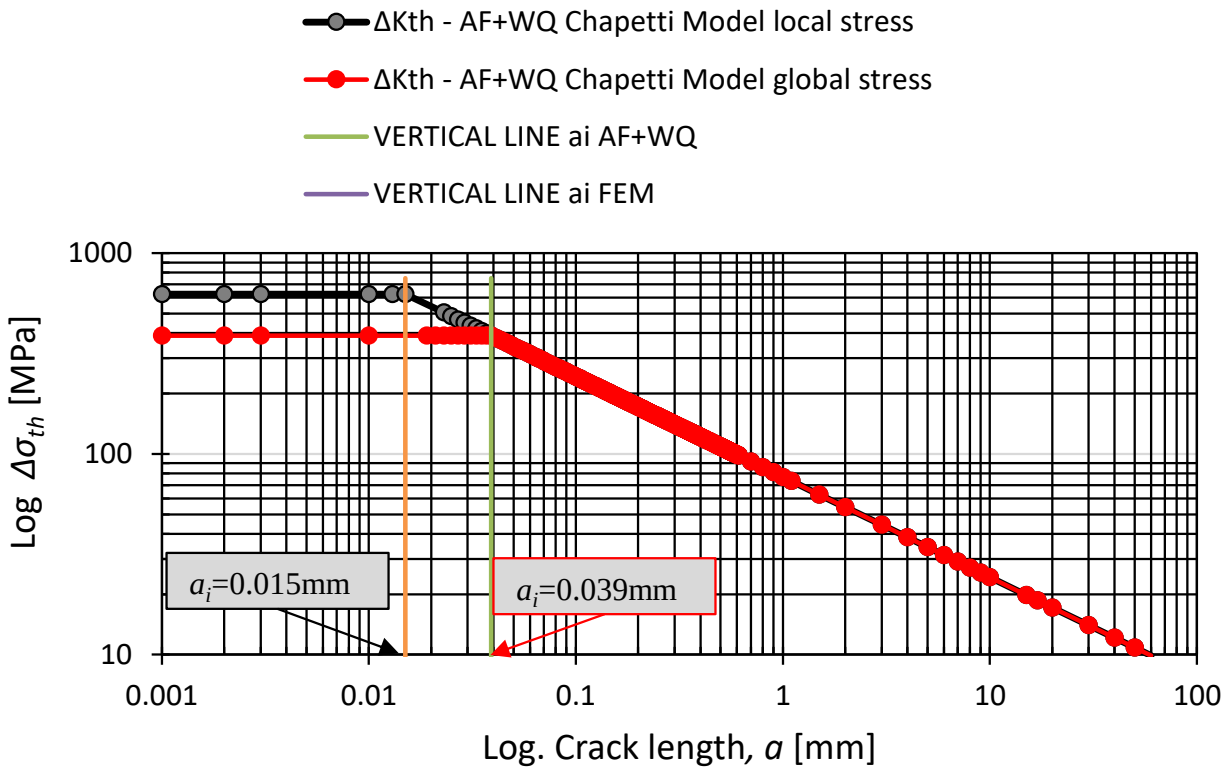

Figure 6. 72 KT-diagram of WRS AF+WQ specimens with and without RS from FEA

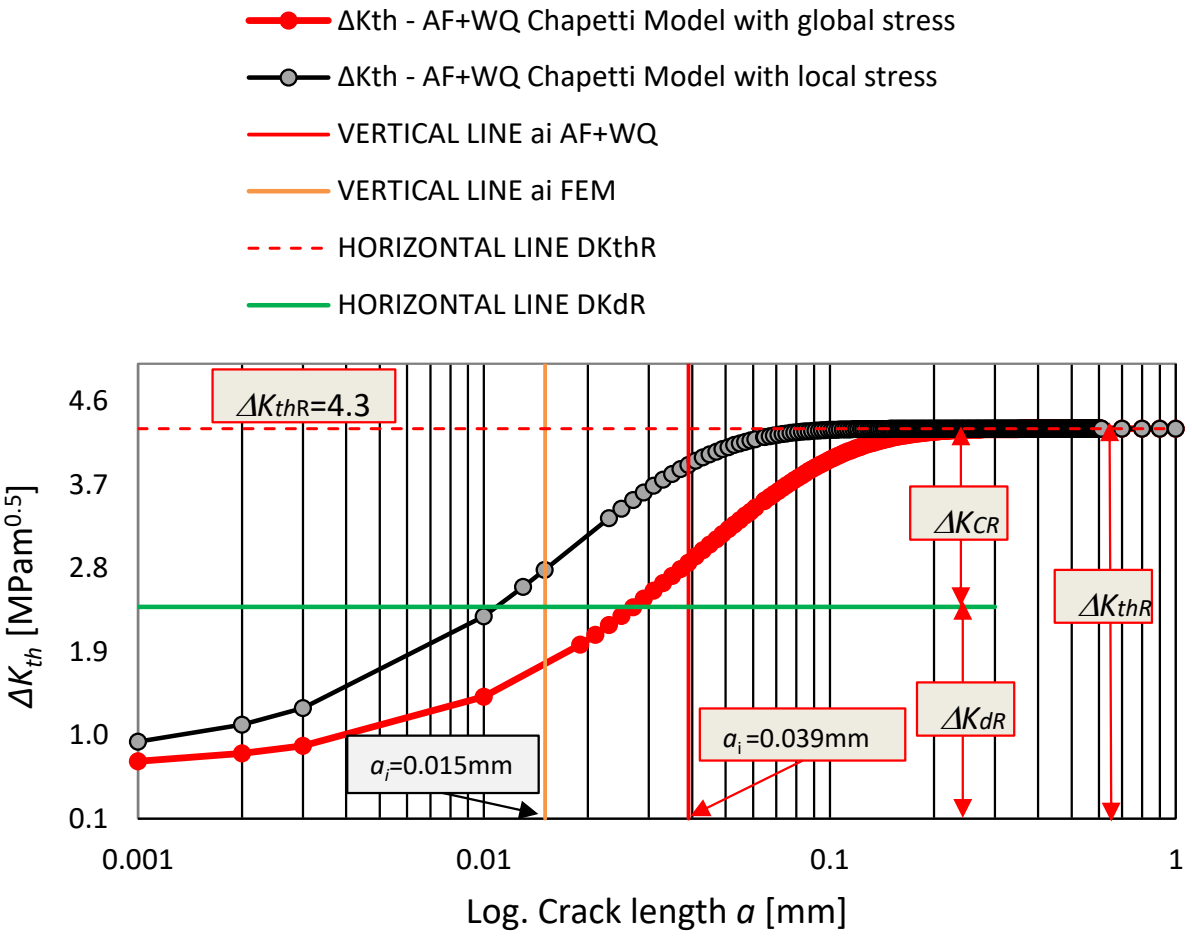

Figure 6. 73 Crack propagation threshold as a function of crack length (logarithmic scale) according to Chapetti's model

7 DISCUSSION

7.1 Fatigue behavior of steels with a martensitic microstructure

The S-N curve provides an overview demonstration of how different cyclic stresses affect the performance of steels having a martensitic microstructure.

There are two types of dynamic strength regions distinguished for steels having a martensitic microstructure: temporary (low cycle regime) and permanent (high cycle regime), Figure 2. 2 .

Only parts of the S-N curves close to the permanent dynamic strength of the steels with martensitic microstructure are considered in this thesis. The permanent dynamic strength is determined for different states of the material, with and without different artificial microdefects (Figure 6. 30 to Figure 6. 35). The above mentioned region was of interest for the study of the initiation and propagation of cracks.

Several factors affect how steels with a martensitic microstructure behave under fatigue:

- The presence of major defects,
- The crystal grain size,
- The crystal grain boundaries,
- The boundaries between martensite grains,
- The size of the martensite laths,
- The distribution of dislocations within and between the martensite laths,
- The hardness of the martensite,
- The global residual stresses due to cooling and alteration,
- The presence of microdefects,
- The local stresses around the microdefects.

If the microdefects are large enough in a steel with a martensitic microstructure, they will have a tendency to grow, and this is the beginning of fatigue cracks` formation.

Thus, the permanent dynamic strength of steels with defects of different magnitudes is best illustrated by the Kitagawa-Takahashi diagram [107], where the diagram depends on the macro and micro properties of the steel microstructure. That is implemented and illustrated in this investigation through (Figure 6. 36 to Figure 6. 47) by applying the modified Chapetti model [108].

Different types of martensitic microstructure have different permanent dynamic strengths (endurance limits), which are constrained by the Kitagawa-Takahashi diagram, and a different threshold for the propagation of large cracks.

The permanent dynamic strength and the threshold for propagation of large cracks are influenced by the macro and micro properties of the microstructure of the steel, and the macro and micro properties are also influenced by:

- The type of loading (bending, tension, tension-pressure, torsion,...),
- The cyclic stress ratio *R*,
- The residual stresses` magnitude in the vicinity of the microdefects.

7.1.1 Global residual stresses

Quenching from 870°C (Figure 3.5) in water results in the global residual stresses of the specimens. It is known from the literature that quenching produces compressive residual stresses at the surface [118] and tensile residual stresses in the core of the specimen.

Global compressive stresses inhibit the initiation and initial propagation of cracks, while the tensile global residual stresses accelerate crack initiation and initial crack propagation.

Due to the specimen's geometry, it was not possible to measure the residual stresses precisely experimentally using the blind hole drilling technique or X Ray in the groove of specimen, therefore, we decided to use FEM analysis to determine the residual stresses in the test specimen.

7.1.2 Local residual stresses

In addition to global residual stresses, local residual stresses can also exist around microdefects. The microdefects can occur during the production process of components. In the case of an artificial microdefect these stresses are due to the fabrication of the microdefect.

In this study it is crucial to consider how and when the artificial microdefect was created. If it was made after the heat treatment, the local residual stresses are present around the micro-defect, whereas, if it was made before quenching they are absent, as they have relaxed during heating to the austenitisation temperature. In this study, the local residual stresses are due to the production of the microdefect. With this in mind, we distinguished two types of test specimens in states with and without residual stresses, and the third type was smooth without artificial microdefects. It is also important to mention that two different ways of heat treatment (AF+WQ and WTCS) were applied during the preparation of these specimens.

7.1.3 Local residual stresses in the vicinity of the indentation of the Vickers pyramid

In order to clarify the mechanisms of crack initiation and initial crack propagation, we need to detail local residual stresses due to microdefect fabrication. These residual stresses cannot be measured directly experimentally, because the area in which these stresses act is too small, and, in addition, it is located at the bottom of the groove, which is difficult to access.

The local residual stresses after indentation of the Vickers pyramid were determined by FEM analysis of the corresponding numerical model.

In order to compare the Vickers pyramid indentation measurements on the instrumented hardness tester in the sample's groove and on a flat surface, we took the following approach:

a) The flat surface of the specimen with an FG HAZ microstructure was indented with an instrumented hardness tester Vickers pyramid with a load of 98.1 N. The force-depth diagram was recorded. This diagram was used to control the response of the applied numerical model.

b) The depth and the actual profile of the final Vickers indentation were measured using a KEYENCE microscope (Figure 6. 4).

c) A numerical model of the specimen was developed and analysed by FEM, and the Vickers pyramid indentation was simulated on a flat surface and in a groove (Subchapter 3.2.1 and Subchapter 3.2.2).

d) To obtain the same response as the actual indentation of the Vickers pyramid on the instrumented hardness tester, the model was optimised accordingly. There, it can be notified that, on the flat surface, the depth of the indentation was slightly smaller in comparison with the depth

of the groove. The depth of indentation on the flat surface, as it can be seen, was 25.38 μm, on the other hand, the depth of the indentation at the groove was 26.898 μm. The reason behind of such behaviour was the contact surface between the pyramid and the surface of the specimen (Subchapter 6.2).

e) We also developed a numerical model to simulate the indentation on the groove of the specimen. We have taken into account the findings obtained from the previous model.

f) Using the KEYENCE microscope (Subchapter 6.2), we also measured the depth of the test piece in the groove, and the actual profile of the indentation of the Vickers pyramid (Figure 6. 6).

g) In the simulation of the Vickers pyramid indentation we analysed the shape and depth of the indentation, and compared them with the actual results obtained by the measurements taken from the KEYENCE microscope (Figure 6. 53).

h) We analysed the stresses at the maximum indentation depth, when the Vickers pyramid is in equilibrium with the material reaction (Figure 7. 3 and Figure 7.3).

i) We analysed the stresses in the vicinity of the impression when the pyramid was removed, which represents local residual stresses after indentation.

For both numerical models, using FEM, the friction coefficient between the specimen and the diamond pyramid was 0.07. The coefficient of friction was varied.

To maximise the accuracy of the results the grid was densified accordingly. The response of the model was compared with a force-depth diagram of the indentation obtained on an instrumented hardness tester from experiments on the flat surface and at the groove of the specimen (Figure 6. 53).

The red and black curve in Figure 6.53 shows the indentation force versus displacement taken from FEA analysis. The blue curve shows the indentation force as a function of the displacement of the pyramid in the actual indentation of the Vickers pyramid (experiment). The three curves are almost identical. The only major difference was at the end, when the pyramid was removed. At that point, the material relaxed elastically.

By optimising the numerical model on a flat surface, we ensured the depth of the indentation, which was (25.38 μm), and the coefficient of friction, which was 0.07.

The shape of the grid used for the numerical model is shown in (Figure 3. 14). Due to the plane symmetry of the pyramid, only a 1/4 of the pyramid and the material were modelled. We were able to control the model of the impression of the Vickers pyramid on a flat surface by the depth of the impression.

Also, we found data on the size of the plastic zone. The results in Figure 7.2 and Figure 7.2 show the area of the main plastic deformations that were modelled numerically for the flat surface and for the groove on the specimens. The indentation was greater than 0,2% in both cases. The width of the region was almost the same in both cases, but the depth was not. The slightly larger plastic region (1.674) was on the flat surface compared to that on the groove (1.354).

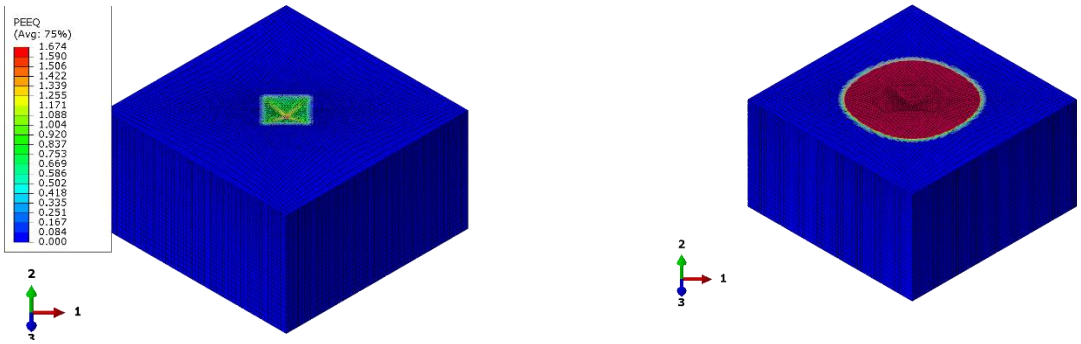

Figure 7.1 Size of the plastic zone at the flat surface

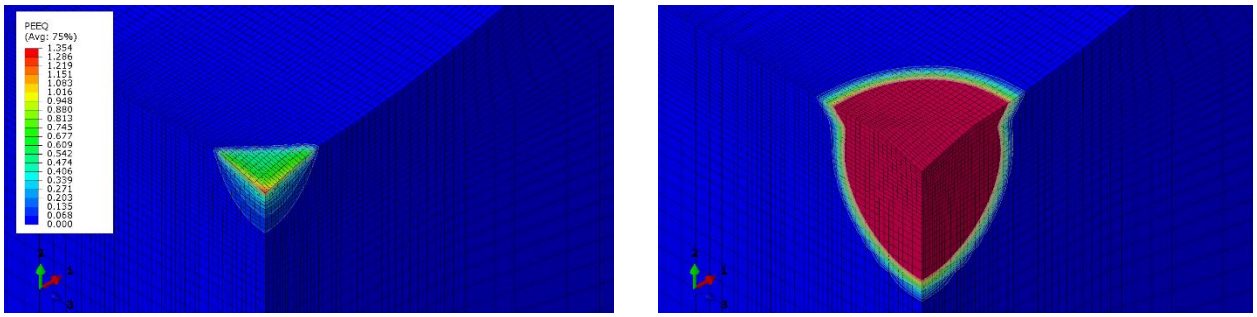

Figure 7.2 Size of the plastic zone at the indentation in the groove of the specimen

When the pyramid was removed, the residual stresses resulting from the microdefect`s fabrication of the Vickers pyramid indentation remained. They are shown in Figure 7. 3. After applying the F_{max}, the largest tensile residual stresses were at the top edge of the Vickers pyramid impression (almost 1000 MPa), and the largest compressive residual stresses (3402 MPa) in the bottom of indentation. At this point, the pyramid pushed the material apart. A peak of material appeared, which was tilted at the upper edge.

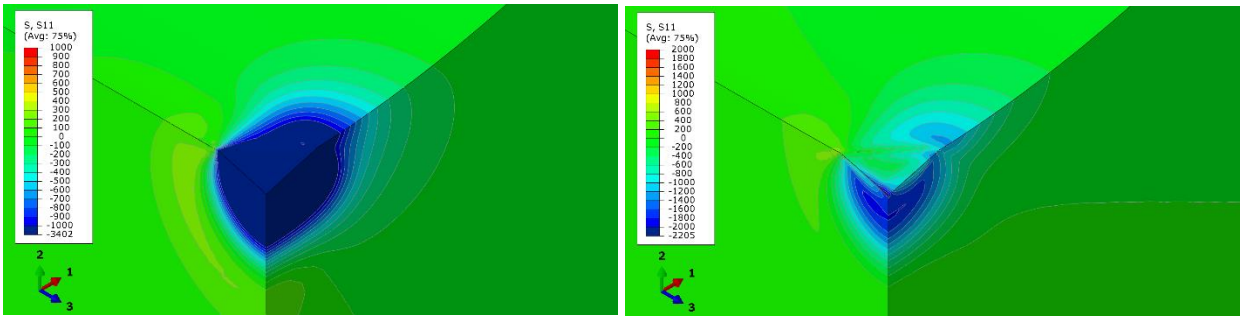

Figure 7. 3 Tensile and compressive residual stresses in the WRS specimen after applying the load at Fmax and at Fo

This is the reason for the existence of tensile residual stresses. It can be seen that, when the pyramid was removed, the compressive stresses decreased at the bottom of the Vickers pyramid indentation (2205 MPa), while the tensile stresses at the top edge remained unchanged.

7.1.4 The mechanism of initiation and propagation of a crack in a Vickers pyramid indentation without residual stresses (WoRS)

In Figure 7.4, we can see that, even in the case where there was no residual stress due to the manufacture of the Vickers pyramid impression, the crack propagated through the impression.

The residual stresses acting as result of the Vickers pyramid impression had been removed due to the heat treatment, because the impression was made before the heat treatment step (Figure 3.5). The residual stresses were relaxed when heated to 870°C. Without the existence of residual stresses the conditions for crack formation at the base of the Vickers pyramid impression are more favourable than at the edge of the impression (ΔK_{local} at that point is larger).

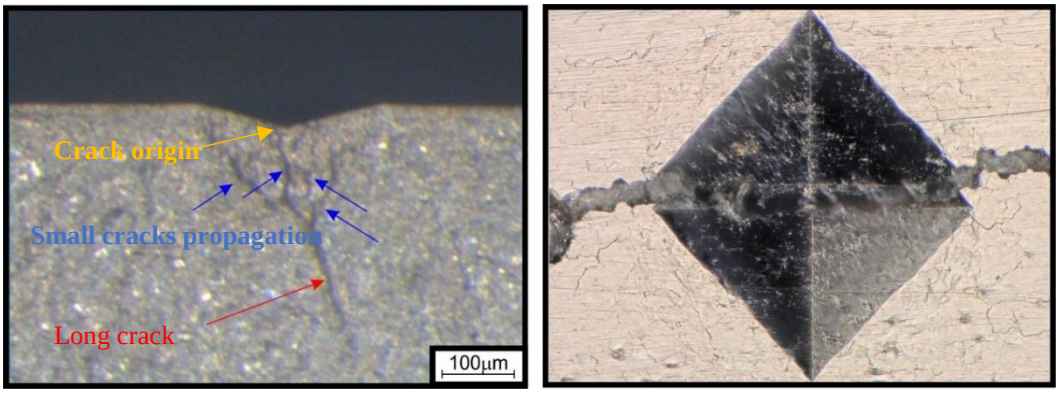

Figure 7.4 Fracture surface with propagation marks` crack (crack formed at the base of the impression of the Vickers pyramid).

For specimens (AF+WQ FG HAZ) in the WoRS condition, only one crack was formed at the bottom of the impression (see the red arrow on Figure 7.4). The initiation of cracks resulting from different planes of propagation is shown with the blue arrow in the same photograph.

The propagation front of the crack runs perpendicular to them. If we follow these traces in the opposite direction of the propagation of the crack, we find that the crack was formed at the base of the indentation of the Vickers pyramid.

The crack had extended from the bottom of the indentation in all directions, and also along the edge of the indentation. When the crack propagated across the entire indentation of the Vickers pyramid, it spread along the microdefect diagonals, and the final fracture occurred as is shown in Figure 7.4. The location of the crack initiation and the mechanism of the initial crack propagation in the plane and lateral sections of the indentation of the Vickers pyramid is illustrated schematically in Figure 7.5. It is shown in four stages. The site of formation was at the base of the indentation (stage 1), which was quite similar behaviour as at the CG HAZ [95].

The other stages (2,3,4) show the initial crack propagation from the bottom toward the edges of the indentation. Once the crack was large enough, propagation continued on the free surface outside the indentation the Vickers pyramid and into the depths.

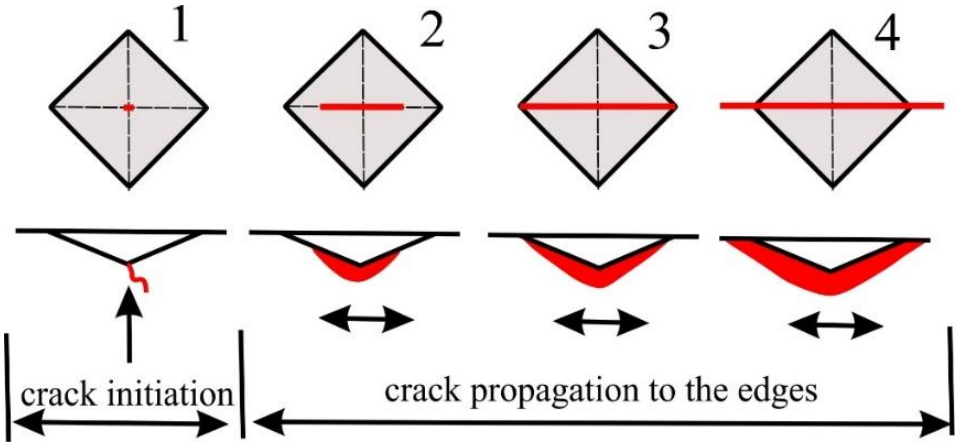

Figure 7. 5 Schematic representation of crack initiation on AF+WQ FG HAZ in WoRS condition.

7.1.5 Mechanism of initiation and propagation of a crack in a Vickers pyramid indentation with residual stresses (WRS)

There are large compressive residual stresses at the base of the Vickers pyramid impression and at the top edge of the pyramid, and tensile residual stresses at the top of the impression (Figure 6. 54). These residual stresses are important for crack initiation and propagation. The tensile region is the result of the expansion of the material in the indentation of the Vickers pyramid. When the pyramid is removed, the shape of the made impression prevents the material from relaxing elastically at this point. This results in tensile residual stresses at the edges of the impression, as shown by the analysis of the numerical model with FEM (Subchapter 6.9.2).

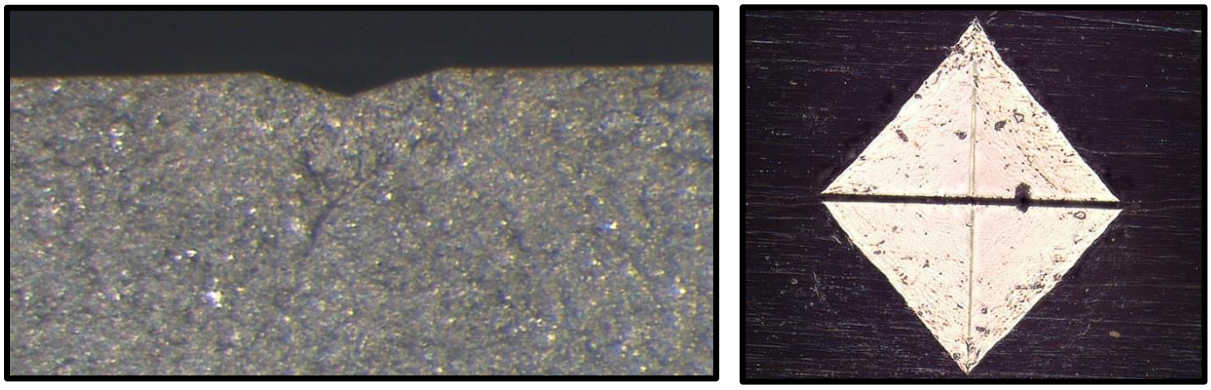

Figure 7.6 Fracture surface with propagation marks crack

Figure 7.7 shows the location of the cracks and the development of their initial propagation of cracks on AF+WQ FG HAZ in the WRS condition schematically, which was quite similar behaviour like for the CG HAZ [95].

To understand the mechanism of initial crack propagation we need to know the magnitude of the residual stresses around the defect. Why were two cracks formed along the upper edge of the indentation? Because in that location the tensile residual stresses are greater, and this helps cracks to be developed in that region. On the other hand, the compressive residual stresses blocked the crack opening in the vicinity of the defect, therefore the crack development started from the edges of the indentation in the WRS specimens.

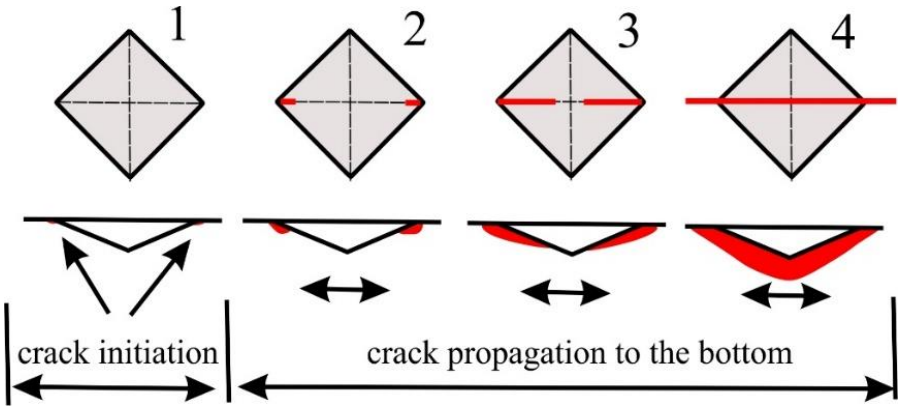

Figure 7.7 Schematic representation of crack initiation on AF+WQ FG HAZ in the WRS condition.

The plastic area around the Vickers pyramid indentation was several times the size of the larger indentation (Figure 6. 51), so there were large residual stresses in the vicinity of the indentation. These stresses changed the local stress ratio R_{local} (Subchapter 4.2.2). Tensile residual stresses at the edge of the Vickers pyramid`s indentation (Figure 7. 3) increased the local stress ratio R_{local}, which caused the crack formation at this location, because the formed crack at this location remained open for a longer time under cyclic loading. Such conditions are more conducive to crack formation.At the bottom of the indentation the compressive residual stresses were very high (Figure 7. 3 and Figure 6.58), therefore the local stress ratio R_{local} was lower, and this resulted in fatigue crack closure for a longer time. These are less favourable conditions for further propagation of the resulting crack.

Therefore, both cracks were formed at the upper edge of the Vickers pyramid indentation and extended towards the bottom of the indentation. The large compressive residual stresses around the base of the indentation prevented the cracks from merging at the base of the indentation. This occurred in the material below the indentation, where the compressive stresses were already smaller. After the two cracks had merged, the merged crack also propagates towards the free surface at the base of the Vickers pyramid indentation. At the base of the indentation the mode of merging is different. As the cracks propagated from the edge to the bottom of the indentation, the propagation occurred exactly along the diagonal of the Vickers pyramid indentation. As the crack propagated from the merging point towards the bottom of the indentation, it did not propagate exactly along the diagonal of the Vickers pyramid indentation, and the crack at this location was not quite straight.

7.1.6 Comparison of the experimental results of the AF+WQ and WTCS specimens

The results derived from the experimental and numerical methods were compared and discussed for two different conditions (AF+WQ and WTCS), and showed a similarity in their mechanical properties. Furthermore, in this chapter is also discussed the effect of residual stresses on the fatigue limit of a fine grain microstructure. Based on fact that the Chapetti model does not take into account the influence of residual stresses, the calculated residual stresses from FEA have been implemented into the model to get the KT-diagram to explain their effect.

7.1.7 Fatigue crack growth of AF+WQ vs WTCS specimens

Fatigue crack growth diagrams were plotted and compared for both types of prepared fine grain microstructure. According to *Figure 7. 8*, the red curve represents the data of the WTCS of the tested specimen, and the blue curve represents the data of the AF+WQ of tested specimen.

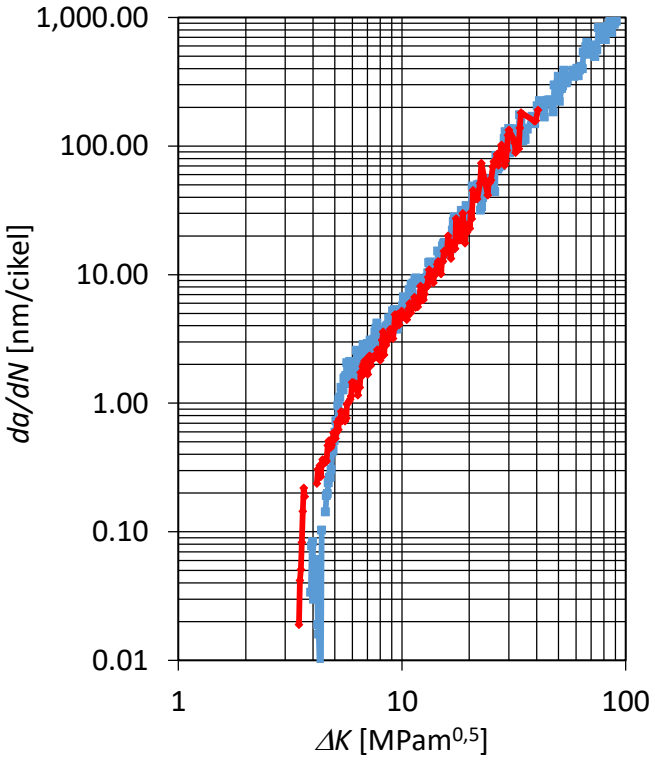

Figure 7. 8 Comparison of the results of an FCG test of AF+WQ vs WTCS

Although, the thresholds for long crack propagation have a small difference between them, the coefficients *C* and *m*, which were derived from the region II where the Paris law was valid, are quite similar in magnitude.

Based on the results of fatigue crack growth, we can derive that both types of prepared microstructure had similar behaviour on long crack propagation, besides that their threshold limit differed slightly.

7.1.8 S-N diagram of AF+WQ vs WTCS SMOOTH specimens

The S-N diagram of two different types of specimens created under the conditions AF+WQ and WTCS is shown in the picture below. The WTCS specimen is shown in red, while the AF+WQ specimen, which was produced in a lab furnace, is shown in blue circles. The fatigue limit for both types of specimens was determined to be σ_{eR} = 675 MPa and σ_{eR} = 675 MPa, respectively, based on an evaluation of the experimental data.

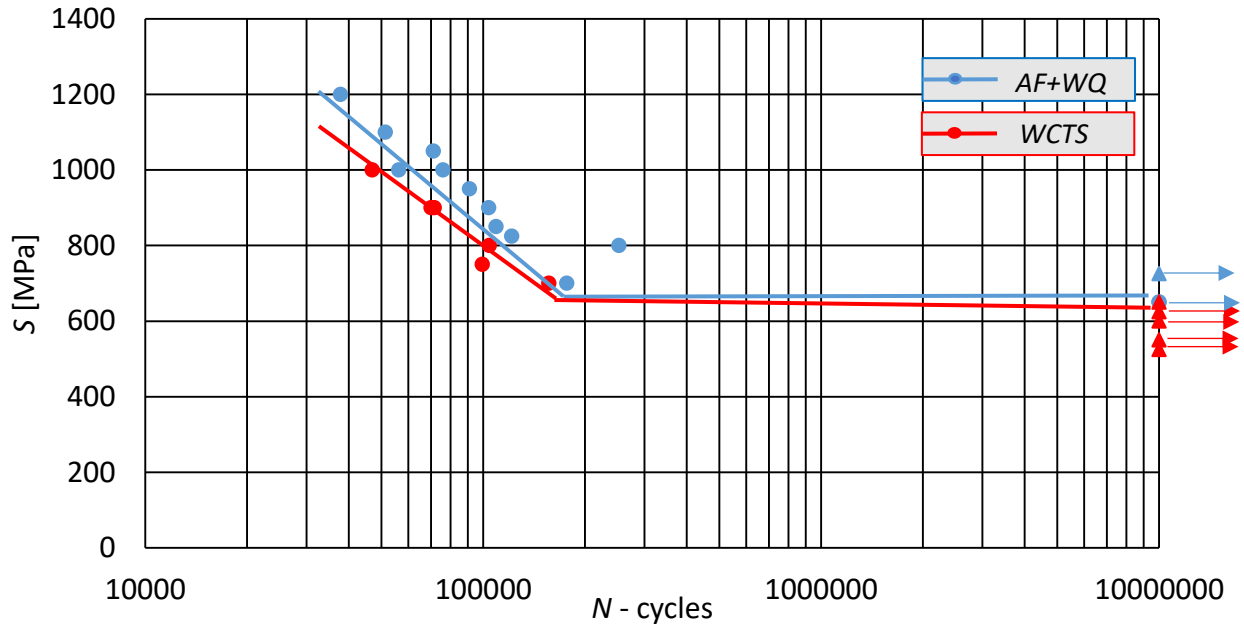

Figure 7. 9 S-N diagram comparison of AF+WQ (blue) vs WTCS (red) smooth specimens

7.1.9 S-N diagram of AF+WQ vs WTCS specimen (WoRS)

The figure below compares two different types of specimens made using the AF+WQ and WTCS heat treatment methods. The only difference in the specimens` conditions is the heat treatment

technique. The internal residual stresses were relaxed after the heat treatment, which resulted in the preparation of specimens without residual stresses (WoRS). The red circles represent the WTCS specimen, while the blue circles indicate the AF+WQ prepared specimen. The S-N diagram was plotted in a semi log scale, and, according to the evaluation of the experimental data, it was revealed that the fatigue limit of both types of specimens was σ_{eR} = 550 MPa and σ_{eR} = 550 MPa respectively.

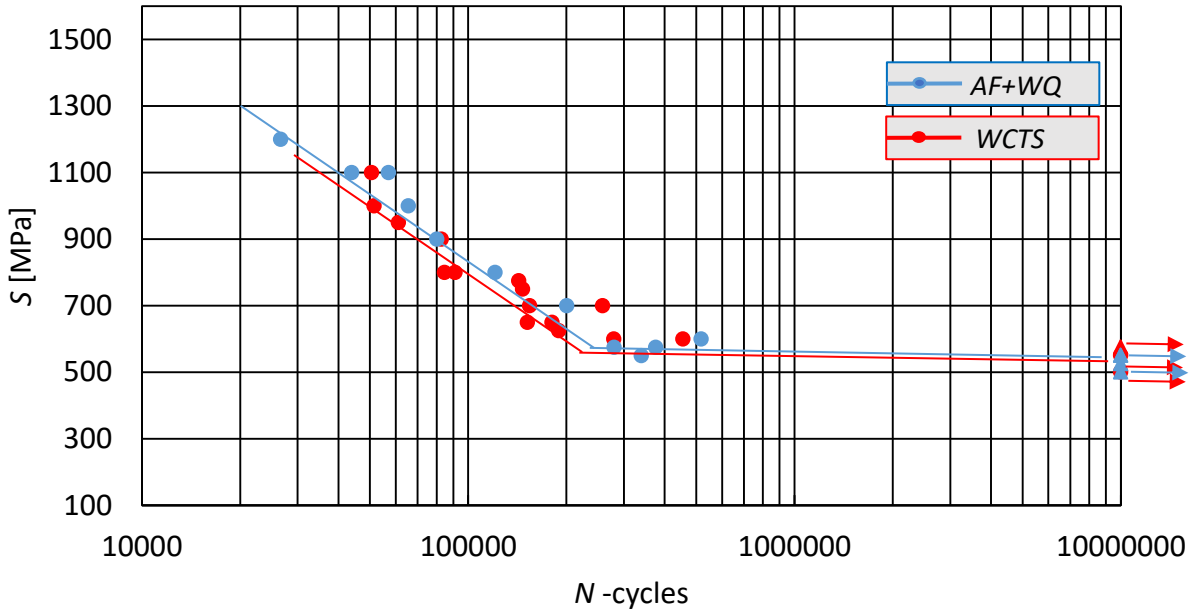

Figure 7. 10 S-N diagram comparison of AF+WQ (blue) vs WTCS (red) WoRS specimens

The experimental data on fatigue bending tests indicated that the fatigue limit (endurance limit) of the WTCS and AF+WQ specimen without RS were very close. Fractography of the specimens that failed during tests at higher stress levels provided proof that the crack began at the bottom of an artificial microdefect introduced to the specimen before the heat treatment. Also, is worth mentioning that the crack propagated through the diagonals of the Vickers pyramid.

The figure below depicts light microscope images showing crack initiation and propagation together with a loaded specimen schema. As shown in the micrographs, the crack initiated at the bottom of the indentation (Vickers indentation) and propagated through the diagonals of the artificially prepared microdefect after a number of cycles under a particular load which exceeds the endurance limit.

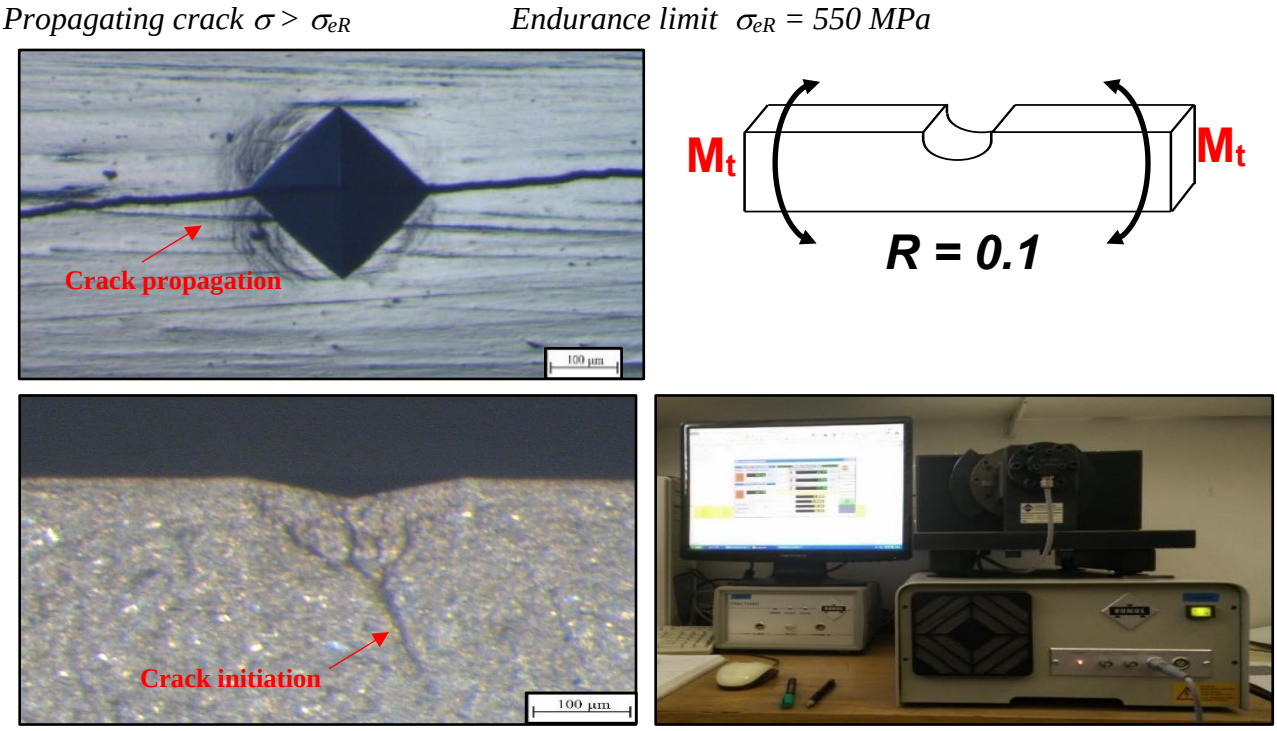

Figure 7. 11 Propagation of the crack through the physical defect and the testing machine

Figure 7.11 depicts the origin of the crack's initiation from the microdefect's bottom along with the crack's propagation through the Vickers pyramid's diagonals. The crack's propagation was as a result of load at a stress level of 700 MPa, with a fatigue life of 200 174 cycles.

7.1.10 S-N diagrams between AF+WQ vs WTCS specimens (WRS)

Two different types of specimens, prepared in a laboratory furnace and a welding simulator, are presented in Figure 7.12. Both of the specimens were in the same condition (with an artificial microdefect with residual stress), and the only difference was the environment of the heat treatment. The blue circles represent the AF+WQ specimen prepared in the laboratory furnace, and the red circles represent the WTCS specimen. *The* S-N diagram was plotted in a semi log scale, and, according to the evaluation of the experimental data, it was revealed that the fatigue limit of both types of specimens was σ_{eR} = 675 MPa and σ_{eR} = 675 MPa respectively.

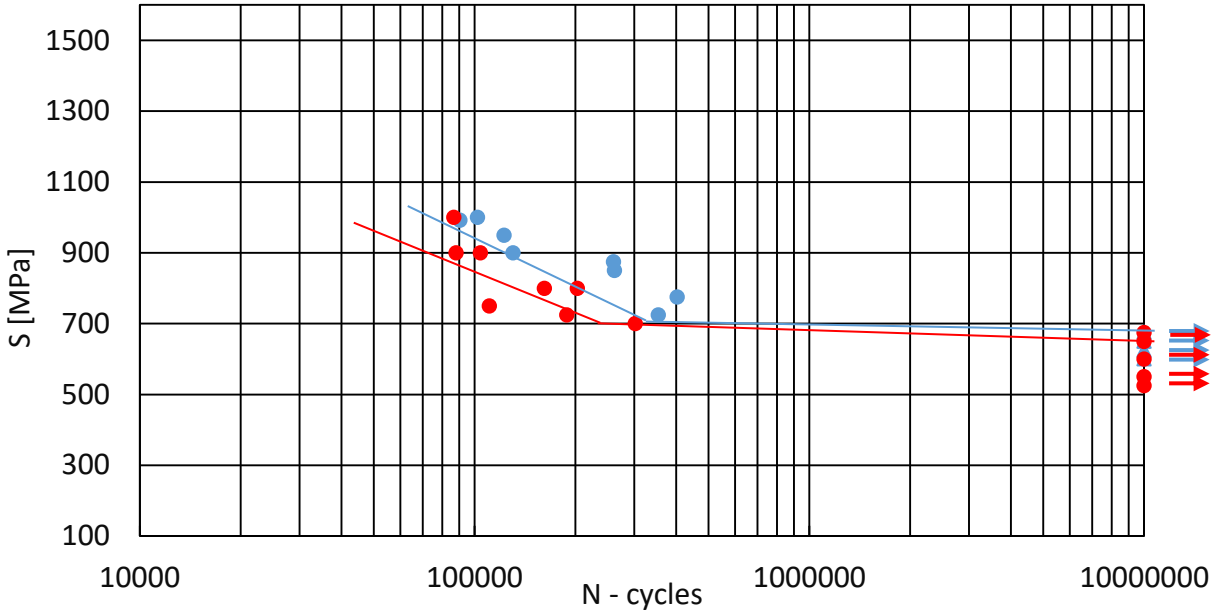

Figure 7. 12 Comparison of the S-N diagrams between AF+WQ (blue) vs WTCS (red) specimens

The experimental data on the fatigue bending tests revealed that the fatigue limits of the WTCS specimen without RS and the AF+WQ specimen were quite close (endurance limit). Fractography of the specimens that failed during tests at higher stress levels provided evidence that the crack initiated below the microdefect on the specimen, and moved toward the bottom of the artificial microdefect introduced before the specimen's heat treatment. Also, it is important to mention that the crack propagated through the diagonals of the Vickers pyramid.
If we compare the results of the fatigue endurance limit of WoRS to WRS specimens, the influence of the compressive residual stresses at the bottom created from the Vickers pyramid on fatigue endurance limit is also quite evident, and it can be seen clearly from Table 7.1.

Table 7. 1 Comparison of fatigue limit of specimens

Type of specimen	Smooth	WoRS	WRS
FG HAZ (AF+WQ)	675 MPa	550 MPa	675 MPa
FG HAZ (WTCS)	675 MPa	550 MPa	675 MPa

Based on the results presented in table 7.1 it is distinguished that in case of SMOOTH and WRS condition of specimens, there is practically no influence of small micro defect related to fatigue limit and in the early stage of crack initiation. In the other hand, in case of WoRS condition of specimens there is the influence of micro defect which has reflected to the early crack initiation and lower fatigue limit. This practically approved our first hypothesis which we have in the beginning of our investigation.

7.1.11 KT-diagram of smooth specimens AF+WQ vs WTCS

In order to compare the threshold for propagating and non-propagating cracks as a function of stress threshold, endurance limit, and critical crack size directly, KT-diagrams were drawn for both types of specimens. A Kitagawa-Takahashi diagram, or KT-diagram, depicts the relationship between the threshold stress intensity range and the crack length, and demonstrates the existence of a transition length value beyond which the threshold of fatigue crack growth is governed by linear elastic fracture mechanics.

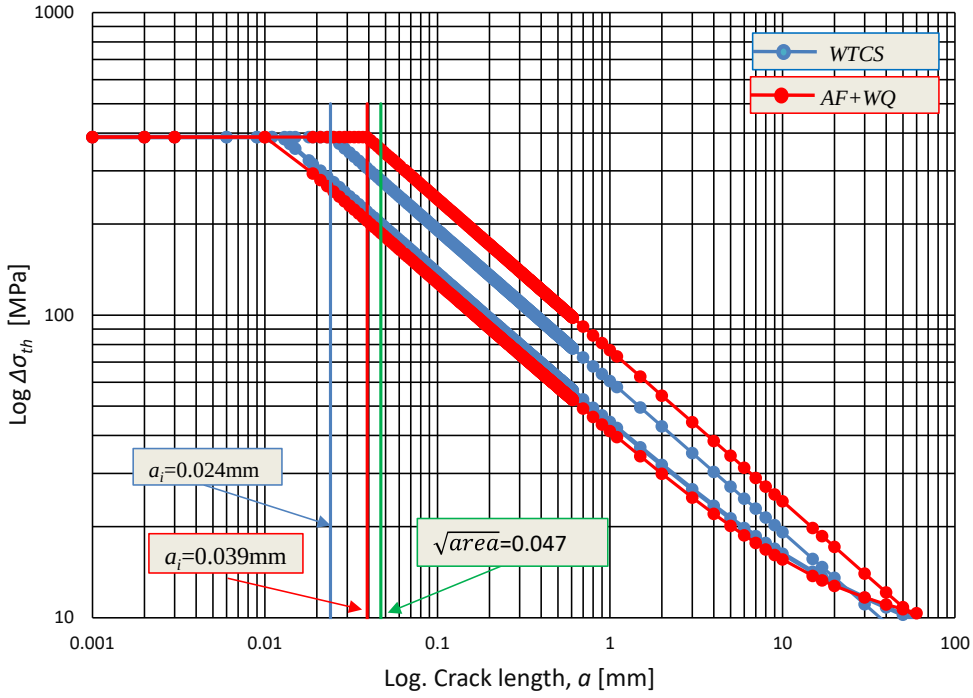

Figure 7. 13 Kitagawa-Takahashi diagram of AF+WQ vs WTCS smooth specimens

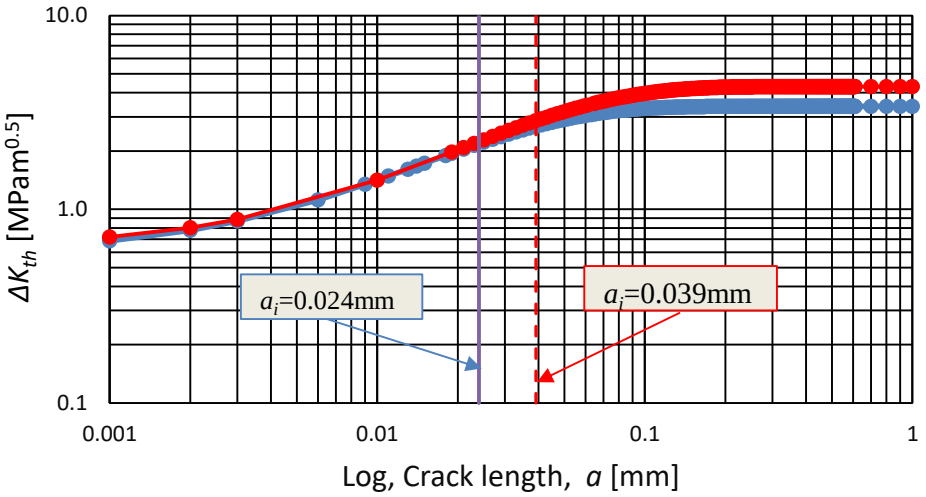

Figure 7. 14 Crack propagation threshold according to Chapetti's model

7.1.12 KT-diagram of AF+WQ vs WTCS specimens without residual stress

The threshold for propagating and non-propagating cracks as a function of stress threshold, endurance limit and critical crack size were compared directly using the KT-diagrams created for AF+WQ and WTCS specimens, and the plot of the data is presented in Figures 7.15-7.16.

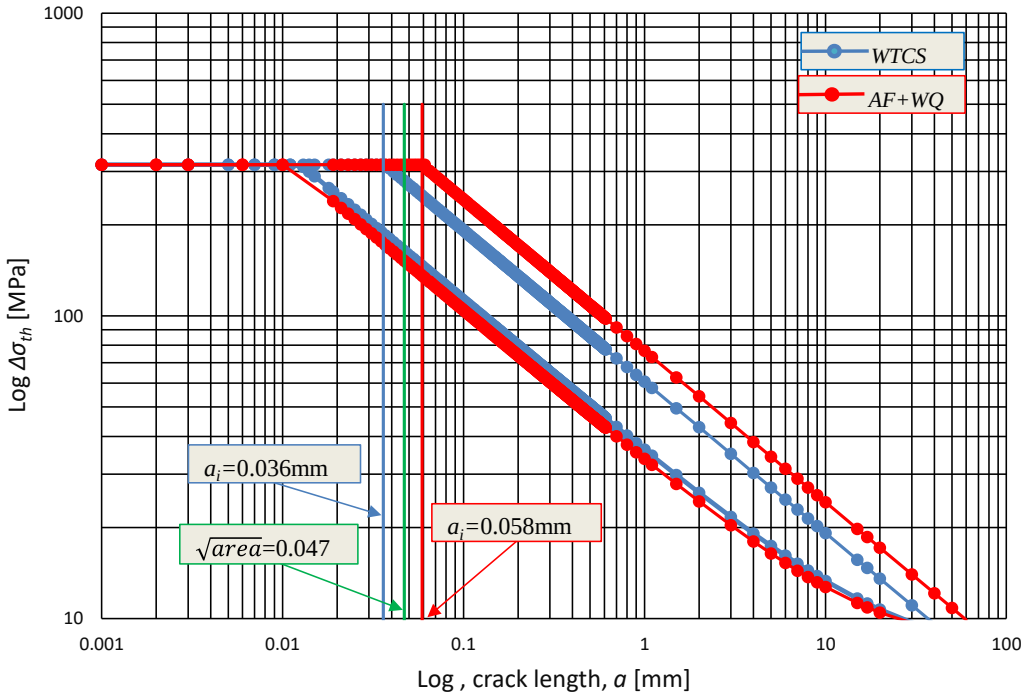

Figure 7. 15 Kitagawa-Takahashi diagram of AF+WQ vs WTCS WoRS specimens

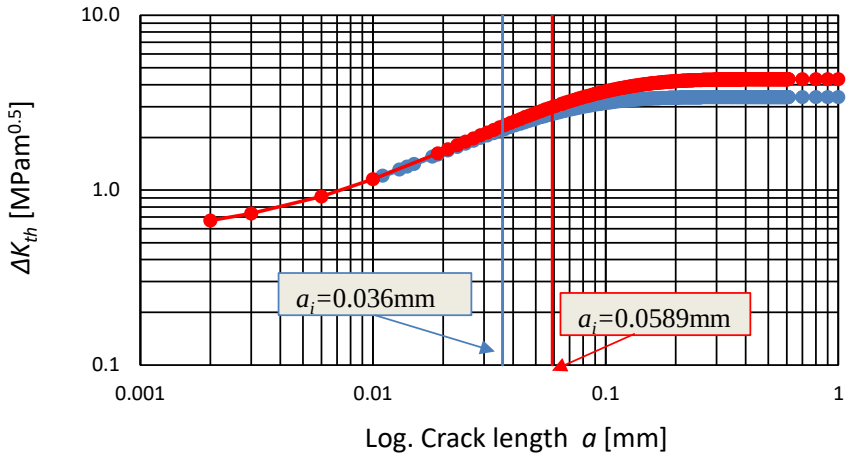

Figure 7. 16 Crack propagation threshold according to Chapetti's model

7.1.13 KT-diagram of AF+WQ vs WTCS specimens with residual stress

The KT-diagrams constructed for the AF+WQ and WTCS specimens were used to compare the threshold for propagating and non-propagating cracks as a function of stress threshold, endurance limit and critical crack size directly.

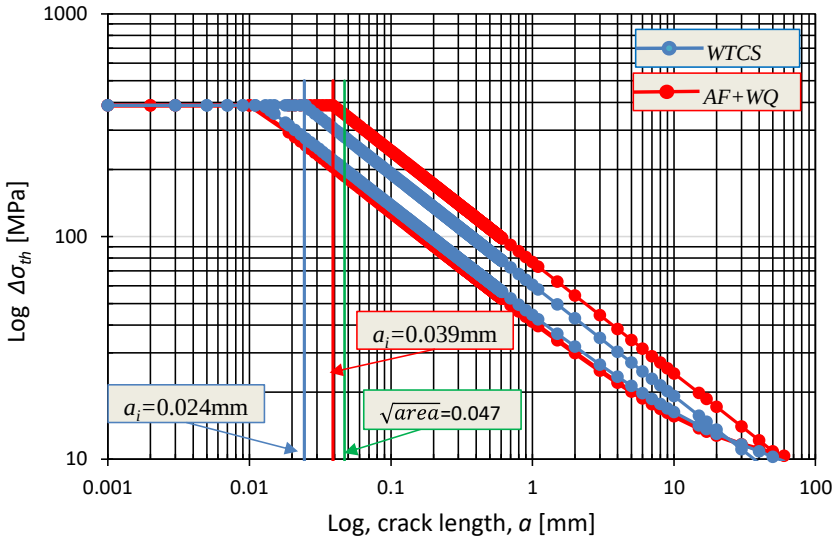

Figure 7. 17 Kitagawa-Takahashi diagram of the AF+WQ vs WTCS WRS specimens

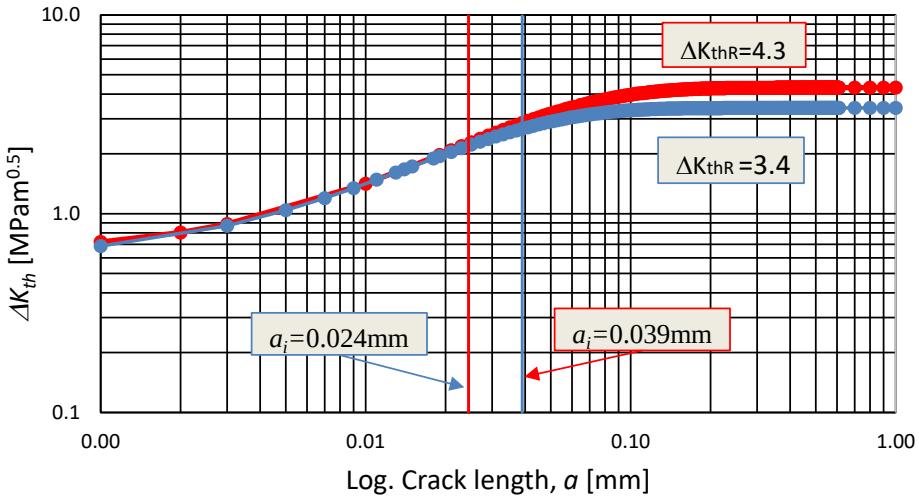

Figure 7. 18 Crack propagation threshold according to Chapetti's model

7.1.14 Comparison of the Chapetti model parameters for all AF+WQ specimens, including the FEM results of RS

The effect of the local residual stress and the groove on crack propagation is presented in Figure 7.19 as a comparison for all specimens.

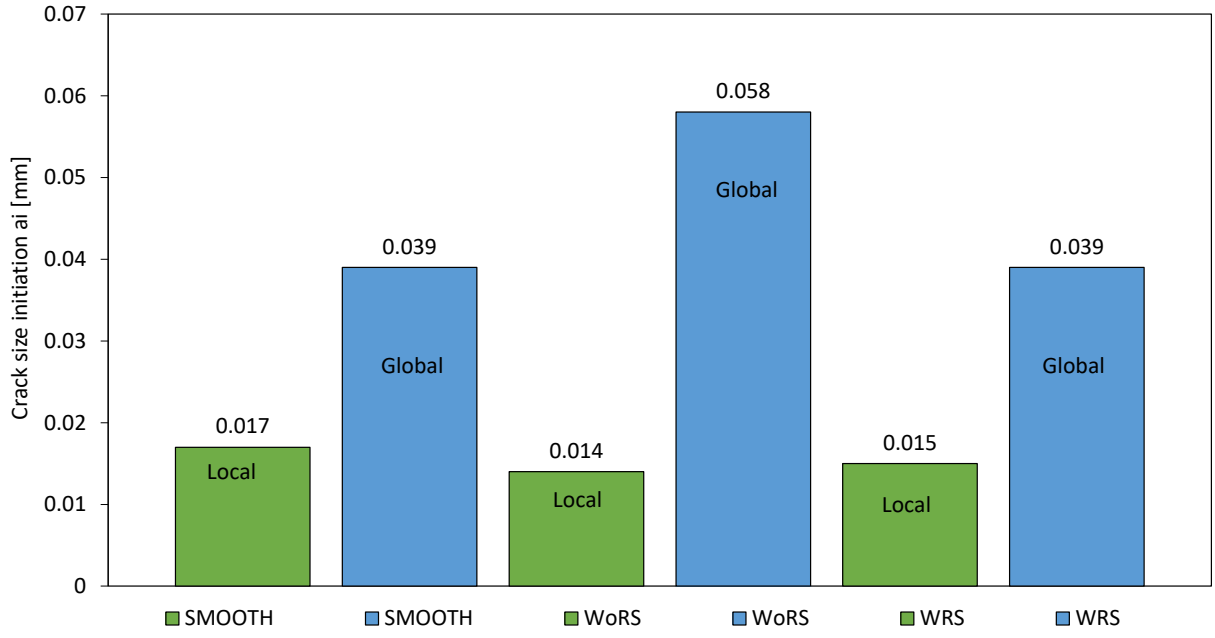

Figure 7. 19 Comparison of the groove contribution and the RS effect on crack size initiation

Based on the diagram presented in Figure 7.18 it can be derived that the effect of residual stress influenced the crack size initiation was significant, which reduced the crack initiation size. Also the influence of the groove was significant on the size of the crack initiation. The presence of the residual stress also deteriorated the extrinsic threshold component for crack propagation ΔK_{cR}, and a summary of the effect of residual stress is presented in Table 7.2.

Table 7. 2 Experimental results of Chapetti's model for the AF+WQ specimens

Designation	RS condition	*Crack length a_i [mm]*	ΔK_{dR}	ΔK_{CR}	$\Delta K_{dR}/\Delta K_{CR}$
S_{AF+WQ}	Local	0.017	2.19	2.11	1.03
	Global	0.039	1.48	2.82	0.52
$WoRS_{AF+WQ}$	Local	0.014	2.38	1.92	1.24
	Global	0.058	1.20	3.10	0.39
WRS_{AF+WQ}	Local	0.015	2.38	1.92	1.24
	Global	0.039	1.48	2.82	0.52

7.1.15 Comparison of the Chapetti model parameters for all WCTS specimens, including the FEM results of RS

The effect of the local residual stress and the groove on crack propagation is presented in Figure 7.20 as a comparison for all specimens.

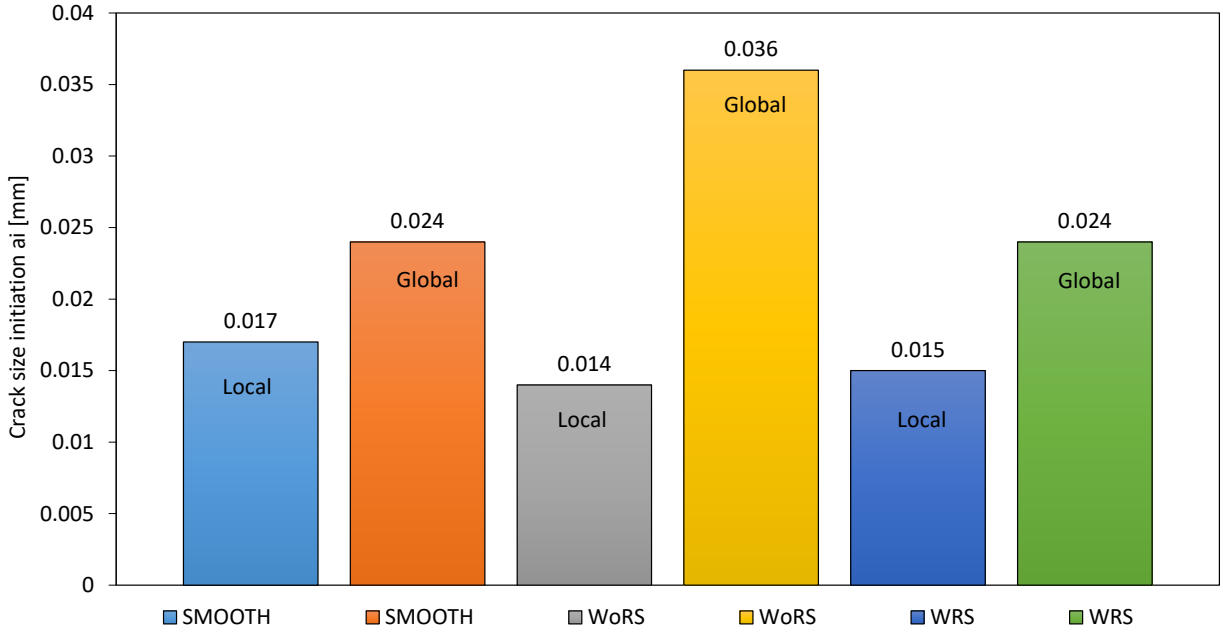

Figure 7. 20 Comparison of groove contribution and the RS effect on crack size initiation

Based on the diagram presented in Figure 7.20 it can be derived that the effect of residual stress (red bar) influenced the crack size initiation highly, which reduced the crack initiation size. Also, the influence of the groove (yellow bar) was significant on crack initiation size. The presence of the residual stress also deteriorated the extrinsic threshold component for crack propagation ΔK_{cR}, and a summary of the effect of residual stress is presented in Table 7.3.

Table 7. 3 Experimental results of Chapetti's model for WTCS specimens

Designation	Condition	*Crack length a_i [mm]*	ΔK_{dR}	ΔK_{CR}	$\Delta K_{dR}/\Delta K_{CR}$
S_{WTCS}	Local	0.017	2.19	2.11	1.03
	Global	0.024	1.59	1.81	0.87
$WoRS_{WTCS}$	Local	0.014	2.38	1.92	1.24
	Global	0.036	1.29	2.11	0.61
WRS_{WTCS}	Local	0.015	2.38	1.92	1.24
	Global	0.024	1.59	1.81	0.87

Based on the results which we abtained from the FEM simulation and after implementing Chapetti's model, there is found that the influence of local residual stresses in vicinity of the microdefect have a significant rol on crack initiation point. They reduced the crack length to both types of specimen. In case of AF+WQ we have decrease of 56.4% for SMOOTH, for WoRS 75.86% and for WRS 61.53%, in case of WCTS types of specimen the decrease was 29.1% for SMOOTH, for WoRS 61.11% and for WRS 41.66%. This actually approved our third hypothesis in the beginning of this investigation and also explain the phenomena that if a small crack exists in FG HAZ it propagate all the time until it reach next subzone of HAZ. In case of when the crack each CG HAZ it either propagate through the grain or through grain boundary depend of the crack driving force magnitude. This also approved the secand hypothesis of our investigation.

8 CONCLUSIONS

The conclusion and contribution of this Doctoral Thesis in scientific contribution can be written as:

The FG HAZ-microstructures were prepared artificially (simulated) in two different ways:

a) Austenitising in a laboratory Furnace followed by Water Quenching (AF+WQ), and

b) By using a Weld Thermal Cycle Simulator (WTCS).

The microstructures and mechanical properties of the prepared specimens were compared, to confirm that both the techniques used during this investigation were adequate and gave approximately same results. In order to validate the results of the prepared microstructure from both techniques, several steps were taken and the following conclusions were derived:

1) Photographs were also compared with a real weld photograph. To get a real weld photograph, a multi-pass single-V butt weld was made on a 15 mm thick preheated plate, in order to produce a reference microstructure. $\Delta t_{8/5}$ = 10 s was measured during welding. The same value was adopted for the simulations of the FG HAZ microstructures.

2) The width of individual HAZ subzones is very small. The results of mechanical tests of a real weld HAZ, apart from the hardness measurement, cannot be linked to only one certain type of microstructure. Therefore, only the hardness of the real weld FG HAZ was measured, while other mechanical tests were omitted. However, comparison of the hardness and microstructures indicated that other properties of the simulated specimens must also have been quite similar to those of the real weld FG HAZ.

3) The microstructures of both types of simulated specimens were very similar to the microstructure of the real weld FG HAZ. The grain size in all three cases was about 10 μm.

4) The hardness of all specimens was similar: AF + WQ specimens 425 HV, WTCS specimens 419 HV and the real weld FG HAZ 405 HV. The differences were less than 4 %, which is the required repeatability of measurements according to ISO 6507-2.

5) The absorbed impact energies of the WTCS specimens were higher (KV = 101.49 J) than the energies of the AF+WQ specimens (KV = 73.11 J). However, due to the utilisation of the WTC

simulator, the microstructure of the WTCS specimens was much less homogeneous than the microstructure of the AF+WQ specimens. Therefore, the more ductile material in the vicinity of the fracture surface of the WTCS specimens could influence the results. Consequently, the difference between the WTCS and AF+WQ specimens was less significant than indicated by the results of the Charpy impact tests. Both types of specimens absorbed substantially more energy for crack initiation E_i than for crack propagation E_p.

6) The results of the fatigue crack growth tests of both types of specimens were very similar. The WTCS specimens exhibited ΔK_{thR} = 3.40 MPa $m^{0.5}$, C = 1.64×10^{-11}, and m = 2.4465. The AF+WQ specimens exhibited ΔK_{thR} = 4.33 MPa $m^{0.5}$, C =1.73×10^{-11}, and m = 2.5114. The differences were insignificant, and indicated very similar resistance to the occurrence of long cracks and very similar propagation rates. Comparison of these results with the results of a previous investigation of a CG HAZ revealed that the CG HAZ had a slightly higher threshold ΔK_{thR} than the FG HAZ, but once a long crack formed in a CG HAZ it propagated significantly faster than in the FG HAZ.

7) Implementation of the Chapetti model on a AF+WQ specimen derived that the micro structural threshold ΔK_{dR} was in a range between 2.19-2.38 when the effect of residual stress are not included. On the other hand, when the residual stress were included, it was in a range between 1.20-1.48. This range is very small, and once a crack exists it could propagate and merge to behave as a long crack.

8) Implementation of the Chapetti model on the WTCS specimen derived that the micro structural threshold ΔK_{dR} was in a range between 2.19-2.38 when the effect of residual stresses were not included. On the other hand, when the residual stresses were included, it was in a range between 1.29-1.59. This range is also very small, and once a crack exists it could propagate and merge to behave as a long crack.

9) Compressive residual stresses around the induced microdefect played a significant role in the early stage of the initiation and propagation of the crack. They blocked the crack initiation at the bottom end of the microdefect, but that was not sufficient, because the crack started well below the indentation where the compressive residual stresses magnitude were lower and linked with the cracks formed from diagonals.

10) Tensile residual stresses in the vicinity of the microdefect promoted the initiation of the cracks from the diagonals of the indentation. Their presence around the microdefect is inevitable, and they deteriorate the service life of the component, and, at the same time, they accelerate the failure of structural components.

11) Comparison of the results for both types of simulated specimens between each other gives a significant contribution to reliabilty for a real weld FG HAZ. The similarity in microstructure and mechanical properties confirmed that both types of simulated specimens are suitable for mechanical tests of individual HAZ subzones.

SUGGESTIONS FOR FUTURE WORK

Based on the fact that the welding process is usually followed by microdefects in the microstructure, and the HAZ is heterogeneous, the possibility for future work exists in this field. It will be quite interesting, and, at the same time, a future challenge for any other Doctoral students to investigate mechanical properties during dynamic load of an inter-critical subzone of a HAZ under the presence of a microdefect. This part of a HAZ needs to receive attention, in order to know its behaviour in fatigue crack initiation and propagation. This information will be significant, and help engineers to predict the weld joint life, and, at the same time, prevent the catastrophic failures.

9 REFERENCES

[1] T. Vuherer, V. Gliha, L. Milovi´c, M. Dunder, I. Samardži´c, "Instruction of welding and review of steels for power plant equipment and possibility of using HAZ simulation in order improve weld joint quality," in *6th International Scientific-Professional Conference SBW 2011*, Slavonski Brod,Croatia, 26–28 October, 2011.

[2] B. Despotovi´c, T. Marseni´c, D. Baji´c, T. Vuherer, I. Samardži´c, "Weldability of modern 9-12 Cr martensitic steels for steam boiler components," *Welding & welded structures : Yugoslav Welding Association review*, vol. 58, no. 1, p. 5–14, 2013.

[3] G. Gnirs, "Zavarivanje modernih kotlovskih čelika," *Zavarivanje i zavarene konstrukcije*, vol. 47, no. 2, p. 103–113, 2002.

[4] K. Haarmann, J.C Vaillant, B. Vandenberghe, W. Bendick, A. Asbab, The T91/P91 Book, Duesseldorf: Vallourec & Mannesmann Tubes, 2002.

[5] G. Taniguchi, K. Yamashita, "Effects of Post Weld Heat Treatment (PWHT) Temperature on Mechanical Properties of Weld Metals for High-Cr Ferritic Heat-Resistant Steel," *Materials Science*, vol. 32, no. 1, pp. 33-39, 2013.

[6] T. Anderson, Fracture Mechanics: Fundamentals and Applications, Vols. 2nd ed.; CRC Press: Boca Raton, FL, USA,, 2017.

[7] P.C. Paris, F. Erdogan , "A Critical analysis of crack propagation laws," *Journal of Basic Engineering* , vol. 85, p. 528–533, 1963.

[8] S. Kou, Welding Metallurgy, Second edition, New York: John Wiley & Sons, Inc, 2002.

[9] K.E. Easterling, Introduction to Physical Metallurgy of Welding, London: Butterworth-Heinemann Ltd, 1983.

[10] W. Kurz and D.J. Fisher, Fundamentals of Solidification, Aedermannsdorf: TransTech. Publications, 1986.

[11] R. Trivedi, G. M. Pound, "Effect of Concentration-Dependent Diffusion Coefficient on the Migration of Interphase Boundaries," *Journal of Applied Physics,* vol. 38, no. 9, pp. 3569-3576, 1967.

[12] E.H. Roushdy, A.Y. Kandeil, "Influence of surface finish on fatigue life of steel specimens subjected to pure bending," *Engineering Journal of Qatar University,* vol. 3, pp. 25-35, 1990.

[13] P.R Frise, R. Bell,, "Fatigue crack growth and coalescence at notches," *International journal of fatigue,* vol. 14(1), pp. 51-56, 1992.

[14] S. Suresh, Fatigue of Materials, Cambridge University Press, 1998.

[15] T. Vuherer, P. Maruschak, I. Samardžić, "Behaviour of coarse grain heat affected zone (HAZ)," *Metalurgija,* vol. 51, pp. 301-304, 2012.

[16] F. Smaili, G. Lojen, T. Vuherer, "Fatigue crack initiation and propagation of different heat affected zones in the presence of a microdefect," *International Journal of Fatigue,* vol. 128, no. 105191, 2019.

[17] F. Smaili, T. Vuherer, I. Samaržić, "Resistivity during cycle loading of fine grain heat affected zone (HAZ) of 17CrNiMo7 steel prepared into laboratory furnace," *Metalurgija,* vol. 58, no. 1-2, pp. 87-90, 2019.

[18] F.Smaili, T. Vuherer, "Fatigue crack propagation initiated at artificially made small defect in two different microstructures," *Procedia Structural Integrity,* vol. 13, pp. 1347-1352, 2018.

[19] Z. Barsoum, Guidelines For Fatigue And Static Analysis Of Welded And Un-Welded Steel Structures, Stockholm: KTH Royal Institute of Technology, 2020.

[20] A. Cabrilo, A. Sedmak, Z. Burzic, S.Perkovic, "Fracture mechanics and fatigue crack propagation in armor steel welds," *Engineering Failure Analysis,* vol. 106, pp. 1-21, 2019.

[21] R. W. Hertzberg ,R. P. Vinci, J. L. Hertzberg, Deformation and Fracture Mechanics of Engineering Materials, 5th Edition, Denver : Wiley , 2020.

[22] J. Guo, Y. Zhou, C. Liu, Q. Wu, X.Chen, J. Lu, "Wire arc additive manufacturing of AZ31 magnesium alloy: Grain refinement by adjusting pulse frequency," *Materials,* vol. 9, no. 823, pp. 1-13, 2016.

[23] S.T. Lie, H.S Zhao, S.P. Vipin, "New weld toe magnification factors for semi-elliptical cracks in plate-to-plate butt-welded joints.," *Fatigue Fract. Eng. Mater. Struct.,* vol. 40, p. 207–220, 2016,.

[24] I.S. Raju, J.C. Newman, , "Stress-intensity factors for a wide range of semi-elliptical surface cracks in finite-thickness plates," *Engineering Fracture Mechanics* , vol. 11 , p. 817–829, 1979.

[25] H.S. Zhao, S.T. Lie,, "Determination of dimensionless stress intensity factor of plate-to-plate butt welds between axially aligned members of different thickness.," *Engineering Fracture Mechanics,* vol. 172, pp. 90-105, 2017.

[26] S. Maddox, "Applying Fitness-for Purpose Concepts to the Fatigue Assessment of Welded Joints.," *Proceedings of the International Conference on Fatigue,* p. 72–81, 3–7 May 1994.

[27] D. Bowness, M.M.K. Lee, "Prediction of weld toe magnification factors for semi-elliptical cracks in T-butt joints," *International Journal of Fatigue,* vol. 22, no. 5, p. 369–387, 2000.

[28] F.P. Brennan, W.D. Dover, R.F. Karé, A.K. Hellier , "Parametric equations for T-butt weld toe stress intensity factors," *Int. J. Fatigue,* vol. 21, p. 1051–1062 [CrossRef], 1999.

[29] Y. Nadot, "Fatigue from Defect: Influence of Size, Type, Position, Morphology and Loading," *International Journal of Fatigue,* vol. 154, p. 106531, 2022.

[30] E. Friedman, "Finite Element Analysis of Arc Welding; ReportWAPD-TM-1438," Department of Energy, West Mifflin, 1980.

[31] R. D. Henshell. K. G. Shaw., "Crack tip finite elements are unnecessary," *International Journal for Numerical Methods in Engineering,* vol. 9, p. 495–507, 1975.

[32] R. Barsoum, “Triangular quarter-point elements as elastic and perfectly-plastic crack tip elements,” *International Journal For Numerical Methods In Engineering,* vol. 11, p. 85–98, 1977.

[33] M. Erdogan, G. Ibrahim, The Finite Element Method and Applications in Engineering Using ANSYS, New York: Springer, 2006.

[34] S. Babu, “The mechanism of acicular ferrite in weld deposits,” *Current Opinion in Solid State and Materials Science,* vol. 8, p. 267–278, 2004.

[35] A. Hobbacher, “Comparison of fatigue verification procedures at a thick-walled welded component,” *Welding in the World,* vol. 61, p. 801–818, 2017.

[36] U. Zerbst, S. Beretta, G. Köhler, A. Lawton, M. Vormwald,H.T. Beier, “Safe life and damage tolerance aspects of railway axles – A review,” *Eng Fract Mech,* vol. 98, p. 214–71, 2013.

[37] T.X. Guang, L. Jian, Q.L. Feng, W. Gang, T.L. Hai, H.Zh. Ming , “Characterization of fracture toughness for surface-modified layer of 18CrNiMo7-6 alloy steel after carburizing heat treatment by indentation method,” *Engineering Fracture Mechanics,* vol. 269, 2022, 108508.

[38] Y. Zhang, Sh. Wang, G.T. Xu, G. Wang, M. H. Zhao, “Effect of Microstructure on Fatigue-Crack Propagation of 18CrNiMo7-6 High-Strength Steel,” *International Journal of Fatigue,* vol. 163, 2022.

[39] Sh. Qin, Ch. Zhang, B. Zhang, H. Ma, M. H. Zhao, “Effect of carburizing process on high cycle fatigue behavior of 18CrNiMo7-6 steel,” *Journal of Materials Research and Technology,* vol. 16, pp. 1136-1149, 2022.

[40] Paris PC, Erdogan F. , “ A critical analysis of crack propagation laws.,” *J Basic Eng* , vol. 85: , p. 528–33., 1963; .

[41] R. Jones, B. Farahmand, C.A. Rodopoulos, “Fatigue crack growth discrepancies with stress ratio,” *Theoretical and Applied Fracture Mechanics,* vol. 51, no. 1, p. 1–10, 2009.

[42] K.N. Smith,Th. Topper, P. Watson, "A stress–strain function for the fatigue of metals (stress-strain function for metal fatigue including mean stress effect)," *Journal of Materials Science,* vol. 5, p. 767–778, 1970.

[43] K. Walker, "The effect of stress ratio during crack propagation and fatigue for 2024-T3 and 7075-T6 aluminum.," *Materials Science,* vol. 462, p. 1–14, 1970.

[44] A.H. Noroozi, G. Glinka, S. Lambert, "A two parameter driving force for fatigue crack growth analysis," *International Journal of Fatigue,* vol. 27, no. 10–12, p. 1277–1296, 2005.

[45] X. Huang, T. Moan, "Improved modeling of the effect of R-ratio on crack growth rate," *International Journal of Fatigue,* vol. 29, p. 591–602, 2007.

[46] Y. Li, H. Wang, D.Gong, "The interrelation of the parameters in the Paris equation of fatigue crack growth," *Engineering Fracture Mechanics,* vol. 96, p. 500–509, 2012.

[47] W. Zhan, N. Lu , C. Zhang, "A new approximate model for the R-ratio effect on fatigue crack growth rate," *Engineering Fracture Mechanics,* vol. 119, no. , p. 85–96, 2014.

[48] K. Sadananda, A. Arcari, AK. Vasudevan, "Does a nucleated crack propagate?," *Engineering Fracture Mechanics 119: 85-96,* vol. 176, p. 144–160, 2017.

[49] W. Elber, "Fatigue crack closure under cyclic tension," *Engineering Fracture Mechanics,* vol. 2, p. 37–44, 1970.

[50] R. C. McClung, "The inflence of applied stress, crack length, and stress intensity factor on crack closure," *Metallurgical Transactions A,* vol. 22, p. 1559–1571, 1991.

[51] J. Newman, "A crack opening stress equation for fatigue crack growth," *International Journal of Fracture,* vol. 24, no. 4, p. 131–135, 1984.

[52] A. J. McEvily, R. O. Ritchie, "Crack closure and the fatigue-crack propagation threshold as a function of load ratio," *Fatigue and Fracture of Engineering Materials and Structures,* vol. 21, no. 7, p. 847–855, 1998.

[53] A. E647-15e1, In Standard Test Method for Measurement of Fatigue Crack Growth Rates, West Conshohocken: ASTM International, 2015.

[54] M. Skorupa, T. Machniewicz, A. Skorupa, "Applicability of the ASTM compliance offset method to determine crack closure levels for structural steel," *International Journal of Fatigue*, vol. 29, no. 8, p. 1434–1451, 2007.

[55] J. Donald, "Introducing the compliance ratio concept for determining effective stress intensity," *International Journal of Fatigue,* vol. 19, no. 93, p. 191–195, 1997.

[56] R. Jones, "Fatigue crack growth and damage tolerance," *Fatigue & Fracture of Engineering Materials & Structures,* vol. 37, p. 463–483, 2014.

[57] A. Hobbacher, Recommendations for fatigue design of welded joints and components. 2nd ed., Wilhelmshaven: Springer Cham, 2013.

[58] M. Lee, N. Kang, S. Liu, K. Cho, "Effects of inclusion size and acicular ferrite on cold cracking for high-strength steel welds of YS 600 MPa grade," *Science and Technology of Welding and Joining,* vol. 21, no. 8, p. 711–719, 2016.

[59] Q. Wang, X. Liu, W. Wang, C. Yang, X. Xiong, H. Fang, "Mixed mode fatigue crack growth behavior of Ni-Cr-Mo-V high strength steel weldments," *International Journal of Fatigue*, vol. 102, p. 79–91, 2017.

[60] Q. Wang, Zh. Yan, X. Liu, Zh. Dong, H. Fang, "Understanding of fatigue crack growth behavior in welded joint of a new generation Ni-Cr-Mo-V high strength steel," *Engineering Fracture Mechanics,* vol. 194, p. 224–239, 2018.

[61] A. E647-13a, Standard Test Method For Measurement Of Fatigue Crack Growth Rates, New York: ASTM International, 2006.

[62] D. V. Hutton, *Fundamentals of Finite Element Analysis,* McGraw-Hill: McGraw-Hill Science/Engineering/Math, 2004.

[63] Z. Mecitoglu, Finite element analysis in structures, Lecture notes, Istanbul: Istanbul Technical University, 2008.

[64] F. Williamson, "Richard courant and finite element method: A further look," *Historia Mathematica*, vol. 7, pp. 369-378, 1980.

[65] Yuri Kadin, Mehdi Mazaheri, Vadim Zolotarevskiy, Charlotte Vieillard, Mark Hadfield, "Finite elements based approaches for the modelling of radial crack formation upon Vickers indentation in silicon nitride ceramics," *Journal of the European Ceramic Society,* vol. 39, no. 14, pp. 4011-4022, 2019.

[66] Yuye Tang, Akio Yonezu, Nagahisa Ogasawara, Norimasa Chiba, Xi Chen, "On radial crack and half-penny crack induced by Vickers indentation," *Procedings of the Royal Society A,* vol. 464 , p. 2967–2984, 2008.

[67] Muchtar, A., Lim, L.C., Lee, K.H. , "Finite element analysis of vickers indentation cracking processes in brittle solids using elements exhibiting cohesive post-failure behaviour," *Journal of Materials Science,* vol. 38, no. 2, p. 235–243, 2003.

[68] K. Zeng, A.E. Giannakopoulos, D.J. Rowcliffe,, "Vickers indentations in glass—II. Comparison of finite element analysis and experiments," *Acta Metallurgica et Materialia,* vol. 43, no. Issue 5, pp. 1945-1954, 1995.

[69] Xi Chen, Jin Yan, Anette M. Karlsson, "On the determination of residual stress and mechanical properties by indentation," *Materials Science and Engineering: A,* vol. 416 , no. 1–2, pp. 139-149, 2006.

[70] T.N. Nguyen, M.A. Wahab, "A theoretical study of the effect of weld geometry parameters on fatigue crack propagation life," *Engineering Fracture Mechanics,* vol. 51, no. 1, pp. 1-18, 1995.

[71] T.N. Nguyen, M.A. Wahab, "The effect of residual stresses on fatigue of butt joints," *Weld. Res. Suppl.,* vol. 75, no. 2, pp. 55-61, 1996.

[72] M. Aygül, Fatigue Analysis of Welded Structures Using the Finite Element Method, Chalmer (Sweden) : ProQuest, 2012.

[73] António L.L. da Silva, José A.F.O. Correia, Abílio M.P. de Jesus, Grzegorz Lesiuk, António A. Fernandes, Rui Calçada, Filippo Berto, "Influence of fillet end geometry on fatigue behaviour of welded joints," *International Journal of Fatigue,* vol. 123, pp. 196-212, 2019.

[74] SIST EN 1011-2, *Welding - Recommendations for welding of metallic materials -Arc welding of ferritic steels,* Brussels: Europian Commity for Standartization, 2001.

[75] SIST ISO 18275, *In Welding consumables - Covered electrodes for manual metal arc welding of high-strength,* Geneva: International Organization for Standardization, 2018.

[76] Steelselector.sij.si. [Online]. Available: https://steelselector.sij.si/steels/CT781.html. [Accessed 18 05 2022].

[77] SIST ISO 6507-1, *In Metallic materials — Vickers hardness test — Part 1: Test method,* Geneva: International Organization for Standardization, 2018.

[78] SIST ISO 9015-1, *In Destructive tests on welds in metallic materials — Hardness testing — Part 1: Hardness test on arc welded joints,* Geneva: International Organization for Standardization, 2001.

[79] SIST ISO 6344-3, *In Coated abrasives — Grain size analysis — Part 3: Determination of grain size distribution of microgrits P240 to P2500,* Geneva: International Organization for Standardization, 2013.

[80] SIST ISO 6892-1, *In Metallic materials - Tensile testing - Part 1: Method of test at room temperature,* Geneva: International Organization for Standardization, 2019.

[81] SIST ISO 148-1, *In Metallic materials — Charpy pendulum impact test — Part 1: Test method,* Geneva: International Organization for Standardization, 2016, pp. pp 1-29..

[82] A. E1820-20, Standard Test Method for Measurement of Fracture Toughness, West Conshohocken: ASTM Standards, 2020.

[83] R. G. Budynas, Roark's Formulas for Stress and Strain 9th Edition, New York: McGrawHill Education, 2020.

[84] K. J. Miller, "The two thresholds of fatigue behaviour," *Fatigue & Fracture of Engineering Materials & Structures,* vol. 16(9), pp. 931-939, 1993.

[85] M. D. Chapetti, "Fatigue propagation threshold of short cracks under constant amplitude loading," *International Journal of Fatigue,* vol. 25, pp. 1319-1326, 2003.

[86] M.D. Chapetti, N. Katsura, T. Tagawa, and T. Miyata, "Static strengthening and fatigue blunt notch sensitivity in low carbon steels," *International Journal of Fatigue,* vol. 23, p. 207–214, 2001.

[87] R. I. Stephens, A. Fatemi, R. R. Stephens, H. O. Fuchs, Metal Fatigue in Engineering, 2nd Edition, Iowa City: John Wiley and Sons, Inc., 2000.

[88] W. Gerber, "Bestimmung der zula¨ssigen Spannungen in EisenConstructionen. [Calculation of the allowable stresses in iron structures]," *Z Bayer Archit Ing Ver,* vol. 6(6), p. 101–110., 1874.

[89] J. Goodman, *Mechanics Applied to Engineering,* London: Longman, Green & Company, 1899.

[90] B. Haigh, "Experiments on the fatigue of brasses," *Journal of the Institute of Metals,* vol. 18, p. 55–86, 1917.

[91] C. Soderberg, "Factor of safety and working stress," *Transactions of the American Society of Mechanical Engineers,* vol. 52, p. 13–28, 1930.

[92] J. Morrow, "Fatigue Properties of Metals," in *Fatigue Design Handbook, Soc. of Automotive Engineers*, Warrendale, 1968, pp. 1-132.

[93] K.N. Smith, P. Watson, T.H. Toper, "A Stress-Strain Function for the Fatigue of Metals," *Journal of Materials,* vol. 5, p. 767–778, 1970.

[94] K. Walker, "The Effect of stress ration during crack propagation and fatigue for 2024-T3 and 7075-T6 aluminium," in *Effects of environment and complex load history on fatigue life,* Lockheed-California, ASTM, 1970, pp. 1-14.

[95] Y.L. Lee, M. E. Barkey, K. Hong-Tae , Metal Fatigue Analysis Handbook, Practical problem-solving techniques for computer-aided engineering, Michigan: Butterworth-Heinemann, 2012.

[96] D. Arola, M. Ramulu, "Material removal in abrasive waterjet machining of metals. Part II: a residual stress analysis," *Wear,* vol. 211, no. 2, pp. 302 - 310, November 1997,.

[97] S. Gungor, L. Edwards, "Effect of surface texture on the initiation and propagation of small fatigue cracks in a forged 6082 aluminum alloy," *Materials Science and Engineering,* vol. 160, no. 1, pp. 17-24, 1993.

[98] W. Thomas, Effect of scratches and of various workshop finishes upon the fatigue strength of steel, Oxford: University of Oxford, 1923.

[99] M. Field, Koster,W. P. Kohls,J. B. Snider,R. E. Meranchik,John , Jr, "Machining of High Strength Steels with Emphasis on Surface Integrity," Air Force Machinability Data Center Cincinnati Ohio, Ohio, 1970.

[100] J.D. Fordham, R. Pilkington, C.C. Tang, "The effect of different profiling techniques on the fatigue performance of metallic membranes of AISI 301 and Inconel 718," *International Journal of Fatigue,* vol. 19, no. 6, pp. 487-501, 1997.

[101] W.L. Xiao, H.B. Chen, Y. Yin, "Effects of Surface Roughness on the Fatigue Life of Alloy Steel," *Key Engineering Materials,* pp. 417-420, November 2012.

[102] E.S. Dzidowski, E.S. Dzidowski, J. Banach,, "Working conditions and the potential damage of energy pipelines with respect to welding technology," in *Proceedings of 1-st scientific-technical conference PIRE -98*, Kudow a Zdrój, 1998.

[103] T. Jóźwik, "Steels CR -MO -V for work at elevated temperatures after long-term operation problems of welding," in *Proceedings of 1-st scientific-technical conference PIRE -98*, Kudowa Zdrój,, 1998.

[104] T. Vuherer, Analiza vpliva mikro napak na trdnost pri utrujanju grobozrnatega TVP na zvarih : doktorska disertacija, Maribor: University of Maribor, 2008.

[105] R. S. Funderburk, "A look at heat input," *Welding Innovation,* vol. 16, no. 1, pp. 8-11, 1999.

[106] T. Vuherer, "Different Methods For Haz Microstructure Preparation On High Alloy Steel CT781," in *VIII International Metallurgical Congress*, Ohrid, 2018.

[107] SIST ISO 6520-1, Welding and allied processes Classification of geometric imperfections in metallic materials Part 1: Fusion welding (ISO 6520-1:2007), Geneva: International Organization for Standardization, 2007.

[108] SIST ISO 5817, *Welding — Fusion-welded joints in steel, nickel, titanium and their alloys (beam welding excluded) — Quality levels for imperfections,* Geneva, Switzerland: International Organization for Standardization, 2014.

[109] SIST ISO 10042, Welding — Arc-welded joints in aluminium and its alloys — Quality levels for imperfections, Geneva, Switzerland: International Organization for Standardization, 2005.

[110] SIST ISO 148-1, *Metallic materials — Charpy pendulum impact test — Part 1: Test method,* Geneva: ISO, 2009.

[111] A. E2298-18, *Standard Test Method for Instrumented Impact Testing of Metallic Materials,* West Conshohocken, PA, 19428-2959 USA: ASTM International, 2018.

[112] Y. Murakami, M. Endo, "The behavior of short cracks," *Mechanical Engineering Publication,* vol. 1, pp. 275-294, 1986.

[113] Y. Murakami, M. Endo, "Effect of Hardness and Crack Geometries on dKth of Small Crack Emanating from Small Defects," *Mechanical Engineering Publication,* vol. 1, pp. 275-293, 1986.

[114] SIST ISO 12107, Metallic materials —Fatigue testing —Statistical planning and analysis of data, London: ISO, 2012.

[115] SIST ISO 12107, *Metallic materials —Fatigue testing —Statistical planning and analysis of data,* London: ISO, 2003.

[116] H. Kitagawa, S. Takahashi, "Applicability of Fracture Mechanics to Very Small Cracks or the Cracks in the Early Stage," in *Proceedings of Second International Conference on Mechanical Behaviour of Materials,* American Society for Metals, Metal Park, 1976. p. 627-631.

[117] M. D. Chapetti, "Fracture mechanics models for short crack growth estimation and fatigue strength assessment," *Matéria (Rio J.),* vol. 27, no. 3, pp. 1-17, 2022.

[118] F. Frerichs, U. Fritsching, T. Lübben, S.S ander, S. Schüttenberg , "Schalenhärtung mittels Hochgeschwindigkeits-Abschreckung* Teil 2," *HTM Journal of Heat Treatment and Materials,* vol. 70, no. 3, pp. 123-134, 2015.

[119] D. Kujawski, "A fatigue crack driving force parameter with load ratio effects," *International Journal of Fatigue,* vol. 23, p. 239–246, 2001.

[120] D. Kujawski, "A new (ΔK+Kmax)0.5 driving force parameter for crack growth in aluminum alloys," *International Journal of Fatigue*, vol. 23, p. 733–740, 2001.

[121] R. D. Cook, *Finite Element Modeling for Stress Analysis,* Illinois: John Wiley & Sons, Inc., 1994.

Fidan Smaili, Msc. in Mechanical Engineering Corriculum Vitae

Education

Doctoral study programme – University of Maribor, Faculty of Mechanical Engineering Oct. 2016-Current

Master study programme – University of Prishtina, Faculty of Mechanical Engineering
Calculation of weld parameters during welding with SAW method of the gaz tank

Work Experience

University teaching assistant – University of Prishtina, Faculty of Mechanical Engineering Oct. 2016-Current

University teaching assistant – UBT Kollegue, Faculty of Mechatronics Oct. 2019-Current

Important publications

Fidan SMAILI, Gorazd Lojen, Tomaz Vuherer, ″Fatigue crack initiation and propagation of different heat affected zones in the presence of a microdefect″ *International Journal of Fatigue*, vol. 128, 105191, 2019

Fidan SMAILI, Tomaz Vuherer, Samardžić Ivan, ″Resistivity during cycle loading of fine grain heat affected zone (HAZ) of 17CrNiMo7 steel prepared into laboratory furnace″ *Metalurgija*, 58(1), pp.87-90, 2019

Fidan SMAILI, Tomaz Vuherer, ″ Fatigue crack propagation initiated at artificially made small defect in two different HAZ microstructures″ *Procedia Structural Integrity*, 13, pp. 1347–1352, 2018

Tomaž Vuherer, Fidan SMAILI, Edvard Bjelajac, Mirza Manjgo, Gorazd Lojen, ″ Simulation and Mechanical Properties of Fine-Grained Heat-Affected Zone Microstructure in 18CrNiMo7-6 Steel″ *Materials*, 15(19), 6782, 2022

Bjelajac, Edvard ; Skumavc, Andrej ; SMAILI, Fidan ; Lojen, Gorazd ; Predan, Jožef ; Vuherer, Tomaž, ″Experimental study of crack propagation through cladded 316L/S355 steel produced by the hot-roll bonding process″ *Metals*, 13(7), 1273, 2023

Univerza v Mariboru

Fakulteta za strojništvo

(ime clanice UM)

IZJAVA O AVTORSTVU IN ISTOVETNOSTI TISKANE IN ELEKTRONSKE OBLIKE DOKTORSKE DISERTACIJE

Ime in priimek študenta/-ke: Fidan Smaili

Študijski program: Mechanical Engineering

Naslov doktorske disertacije: Influence of microdefect on fatigue properties in weld fine grain heat affected zone on nickel-molybdenum alloy steel

Mentor/-ica: Tomaž Vuherer

Podpisani/-a študent/-ka: Fidan Smaili

- izjavljam, da je zaključno delo rezultat mojega znanstvenoraziskovalnega dela;
- izjavljam, da sem pridobil/-a vsa potrebna soglasja za uporabo podatkov in avtorskih del v zaključnem delu in jih v zaključnem delu jasno in ustrezno označil/-a;
- na Univerzo v Mariboru neodplačno, neizključno, prostorsko in časovno neomejeno prenašam pravico shranitve avtorskega dela v elektronski obliki, pravico reproduciranja ter pravico ponuditi zaključno delo javnosti na svetovnem spletu preko DKUM in drugih informacijskih zbirk in ponudnikov; sem seznanjen/-a, da bodo dela deponirana/objavljena v DKUM dostopna široki javnosti pod pogoji licence Creative Commons BY-NC-D, kar vključuje tudi avtomatizirano indeksiranje preko spleta in obdelavo besedil za potrebe tekstovnega in podatkovnega rudarjenja in ekstrakcije znanja iz vsebin; uporabnikom se dovoli reproduciranje brez predelave avtorskega dela, distribuiranje, dajanje v najem in priobčitev javnosti samega izvirnega avtorskega dela, in sicer pod pogojem, da navedejo avtorja in da ne gre za komercialno uporabo;
- dovoljujem objavo svojih osebnih podatkov, ki so navedeni v zaključnem delu in tej izjavi, skupaj z objavo zaključnega dela;
- izjavljam, da je tiskana oblika zaključnega dela istovetna elektronski obliki zaključnega dela, ki sem jo oddal/-a za objavo v DKUM;
- Izjavljam, da sem seznanjen s pogoji Proquest-a za oddajo in javno objavo doktorske disertacije v podatkovno zbirko ProQuest Dissertations & Theses Global (http://contentz.mkt5049.com/lp/43888/382619/PQDTauthoragreement.pdf).

Uveljavljam permisivnejšo obliko licence Creative Commons: CC BY-ND 4.0 (navedite obliko)

Kraj in datum: 11.09.2023 Podpis študenta/-ke: